

Ministry of Education and Science of the Russian Federation
Federal State Educational Establishment of Higher Professional Education
Siberian State Industrial University
Advanced Materials Institute of Tsinghua University
Shanghai Jiao Tong University

**External fields processing and treatment technology and
preparation of nanostructure of metals and alloys**

Book of the International workshop articles

Russia-China
International workshop
1-7 October, 2014

Novokuznetsk
2014

UDK 669.419:621.778:539.4

BBK 34.232.4:34.5,3:34.206.22

E 43

Reviewers

Professor, Sc. D. (Engineering) Muraviov V.V.

Professor, Sc. D. (Phys.-math.) Danilov V.I.

External Fields processing and treatment technology and preparation of nanostructure of metals and alloys: Book of the International seminar articles, 1 – 7 October 2014/ Ed. by V. Gromov; Siberian State Industrial University – Novokuznetsk: Publishing Center SibSIU, 2014. – 348 p.

ISBN 978-5-7806-0399-3

The reports made at the Russian-Chinese International seminar are brought in this edition. The problems of the external energy fields action on the structure, phase composition, defect substructure of different metals and alloys during deformation are discussed.

The book of articles is intended for the material science and metallurgy specialists and can be useful for the post graduate student of corresponding specialist.

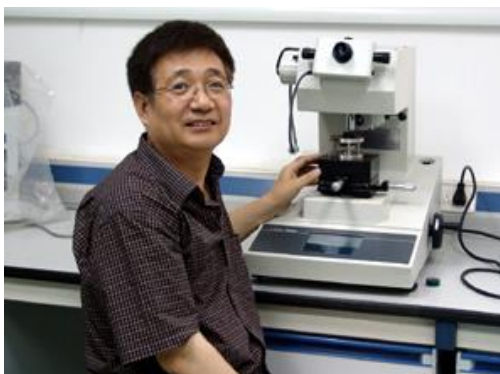
Dedicated to the 60th anniversary of professor G. Tang

This workshop was supported by Russian Foundation for Basic Research (project No 13-02-12009 ofi_m), Government state No 2708GS.

ISBN 978-5-7806-0399-3

Siberian State Industrial University, 2014

Curriculum Vitae



Name: Guoyi TANG Sex: Male

Place of birth: Heilongjiang Province, P. R. China

Citizenship: Chinese Present position: Professor, Executive director

Address: Advanced Materials Institute of Graduate School at Shenzhen, Tsinghua University.

Building J, 204, Tsinghua Campus, The University Town, Shenzhen, 518055, China

Tel and Fax: 86-755-26036752(O), 86-13530478111(Mobile)

E-mail: tanggy@mail.tsinghua.edu.cn

Education Background:

1986-1990 PhD Candidate: The Central Iron and Steel Research Institute, Beijing, P.R.China. (Doctoral Degree)

1983-1986 Post-graduate student: Dept. of Materials Science, Northeast Heavy-Machinery Institute, P.R.China. (Master's Degree)

1978-1982 undergraduate student: Dept. of Materials Science, Northeastern University, P.R.China. (Bachelor's Degree)

Experience :

Feb.2003-Present: Professor, Ph.D candidate supervisor, executive director, Advanced Materials Institute of Graduate School at Shenzhen, Tsinghua University.

Jan.2009-Mar. 2009, Visiting Professor, Dept. of Aerospace and Mechanical Engineering, Nanyang Technology University, Singapore.

Nov.2005-Feb. 2006, Visiting Professor, Dept. of Intelligent and Mechanical Engineering, Akita University, Japan.

Nov.2001 – Feb.2003: Visiting Professor, Dept. of Materials Science and Engineering, North Carolina State University, USA.

Major research fields: Nanomaterials, thin film materials, electron materials, Electroplastic processing for metal.

Dec. 2000 – Nov. 2001, Visiting Professor, Mechanical Engineering Department, University of Alaska Fairbanks, USA.

Graduate course taught: Arctic Materials Engineering.

Major research fields: Arctic materials, Nanomaterials.

Projects Head: Epsco project (\$20,000),

Project Title: Study on dynamic damage mechanism for a composite of fiber reinforcement concrete under arctic environmental service, supported by Alaska Science Foundation (Approval number: SG01-12), USA.

Oct. 1999 - Dec. 2000: Guest Professor, Institute For Theoretical and Applied Physics, Stuttgart University, Germany, and Max-Planck Institute for Metallforschung, Stuttgart, Germany.

Major research field: Nanomaterials.

June 1996 - Oct. 1999: Professor, Ph. D candidate supervisors, Deputy Director of Advanced Material Research Key Lab of Education Ministry in China, Head of Nanostructure Research Faculty, Head of Electron Microscope Laboratory of Materials Science & Engineering School, Tsinghua University, Beijing, P.R.China.

Undergraduate course taught: Electron Microscopy.

Graduate courses taught: Mechanical Metallurgy, Failure Analysis.

Major research fields: electron microscopy; nanomaterials; advanced metal materials (super-strength steels, New type petroleum engineering steels, and so on); surface super hard and wear resistance polymer materials; electroplastic processing and application in metal materials; composite materials; electrochemical processing and surface treatment of materials; new

manufacturing technology of nanomaterials (electrochemical manufacturing technology of nanomaterials and failure analysis (including mineral equipments, power station components, Bridges, airplanes, etc.).

Oct.1994 – Apr.1996: Research Scientist, Korea Atomic Energy Research Institute, Taejon, South Korea.

Research work: materials surface modification and microstructure analysis (including Zircaloy-4, Polymer, and magnetic film, metal, etc).

June 1992 – Oct. 1994: Associate professor, Dept. of Mechanical Engineering, Tsinghua University, Beijing, P.R. China.

Research work: failure analysis; dynamic fracture mechanism and its application in engineering; fracture mechanism of welding structure steel; extension the life of old steel bridges; microalloyed steel and thermo-mechanical treatment.

June 1990 - June 1992: Postdoctoral research fellow, Dept. of Mechanical Engineering, Tsinghua University. Beijing, P.R. China. Advisor: Prof. Qigong Cai and Prof. Jiluan Pan (both are members of the Chinese Academy of Sciences).

Research works: Dynamic fracture mechanism and its application in engineering; fracture mechanism of welding structure steel.

Oct. 1986 - June 1990: Ph.D. candidate, The Center Iron and Steel Research Institute, Beijing, P. R. China. Supervisor Prof. Qigong Cai and Prof. Jing Zhu (both are members of the Chinese Academy of Sciences). Thesis title: The study of physical metallurgy and fracture mechanism of V-Ti-N microalloyed steel.

Training skills: microscopic analysis (transmission electron microscope, scanning electron microscope); experimental and analysis techniques of fracture mechanics; data acquisition and analysis by computer.

Mar. 1986 -Oct. 1986: Lecturer, Dept. of Materials Science, Northeast Heave-Machinery Institute, P.R. China.

Aug. 1983 - Mar. 1986: Post-graduate student, Dept. of Materials Science, Dept. of Materials Science, Northeast Heavy-Machinery Institute, P.R. China.

Aug. 1982 -Aug. 1983: Assistant lecturer, Dept. of Materials Science, Northeast Heavy-Machinery Institute, P.R. China.

Sep. 1978 - Aug. 1982: Undergraduate student. Dept. of Materials Science and Engineering, Northeast University, P.R. China.

Nov. 1970 - Aug. 1978: steel production worker, metallographic and electron microscopy technician, Qiqihar special steel plant in China. Worked on defect analysis, quality control and failure analysis. Accumulated practical experiences for steel production.

Honors:

1. National Award for Technological Invention, second- class prize, China Government, 2010.
2. Science and Technology Advancement Award of The Education Ministry of China, 1995.
3. Science and Technology Advancement Award of The Education Ministry in China, 1996.
4. Science and Technology Advancement Award of The Railway Ministry of China, 1994.
5. Science and Technology Advancement Award of the Metallurgy Ministry of China, 1993.
6. Outstanding Young Professor Award. Tsinghua University, 1999.
7. Outstanding Student Award of Northeast University in 1979, 1980, 1981.

Major Research Interests:

1. Advanced materials and new processing technology (advanced metal materials, film materials, nanomaterials, electrical materials, composite materials).
2. Techniques of microstructure and microanalysis for materials (interface, boundary, crystal defects, Precipitate phase etc.).
3. Surface modification and its application (metal, polymer, diamond, nanoparticles, multiplayer film, electrochemical plating, high energy electro-pulse surface treatment).

4. Electroplastic processing and its application in the metal materials.
5. Phase change materials and its application in storage energy.
6. Fracture mechanism and application in engineering.
7. Failure analysis (metal, ceramics, electronic devices [MOS], composite materials, semiconductors, etc).
8. Nano-materials and Function materials.
9. Engineering polymer and Bio-degradable polymer composite.

Recent Research Projects (As responsible Supervisor):

1. ‘Fundamental study on the novel phase change materials (PCMs) and its applications in textiles and building materials’2008DFA51210, an international collaborative project of the national Ministry of Science and Technology (MOST), China, 2009-2011.
2. Bio-degradable polymer composite and its applications, 2010-2012, industrial funded project.
3. ‘Preparation of nano-sized magnesium hydroxide flame retardant and its application in thermal shrinkable materials’ (2008131), a Shenzhen Nanshan Science and Technology Bureau funded project in collaboration with Changyuan Group Ltd, 2009-2011.
4. Environmental-friendly flame retardant and smoke suppression material: its preparation and characterization, Shenzhen funded project, 2007-2010.
5. Physical nature of structural-phase transformations at electroblasting alloying of metals and alloys surface. National Science Foundation from NCSF, 2008-2010. (Approval No.50811120046)
6. Mg alloy electroplastic process and application, National Science Foundation from NCSF, 2006-2008. (Approval No.50571048)
7. Phase change materials and its application in engineering, National Science Foundation from NCSF, 2006-2008. (Approval No.50572045)
8. Deformation Mg alloy application research, Shenzhen government foundation, 2005-2007.

9. Nano- function material and its application, Shenzhen government foundation.
10. Study on dynamic damage mechanism for a composite of fiber reinforcement concrete under Arctic environmental service, Supported by Alaska Science foundation (Approval number: SG01-12), USA. Completed in 2002 (5/1/2001 - 4/30/2002).
11. Seed Grant to Establish Materials Research for the Arctic Region based on a Scanning Electron Microscope, Supported by Alaska Science foundation (E01-04), USA. Completed in 2002 (5/1/2001 - 4/30/2002).
12. Nanomaterials and application in Engineering, Continue research (1999-2002).
13. Advanced steel materials, The National Key Research Projects of China, (approval number: 973-15). Completed in 1999 (1998 -1999).
14. Superhard-surface and high wear resistant polymers, supported by The National Nature Science Foundation of China (approval number: 59673003). Completed in 1999 (1996 -1999).
15. Study of Mechanism and engineering application of electroplasticity, supported by The National Nature Science Foundation of China (approval number: 59475056). Completed in 1997 (1994-1997).
16. Electroplastic effects and fatigue property of metals. Supported by the Education Ministry of China. Completed in 1998 (1996-1998).
17. The study of ion implantation processing for Zircaloy-4 alloy to be used in nuclear reactor. Supported by Tsinghua University. Completed in 1996
18. The study of ion implantation processing for amorphous magnetic materials. Supported by Tsinghua University. Completed in 1996.

Representative Patents:

1. Environmental-friendly flame retarding and smoke suppression form stable phase change materials and its preparation method, Chinese Patent: CN200910106596.2.
2. A preparation method for nano-sized magnesium hydroxide, Chinese Patent:

CN101376511.

3. A surface modification method for nano-sized magnesium hydroxide, Chinese Patent: CN101368009.
4. A multi-functional ultrasonic reactor, Chinese Patent: 200720196712.
5. A method for preparing micro-encapsulated phase change materials, Chinese Patent: CN200610157343.4.
6. A method for preparing micro-sphere composite containing phase change materials, Chinese Patent: CN200710124055.3.
7. A rapid method for preparing microcapsules of phase change materials by UV initiated polymerization, Chinese Patent: 200910106965.8.
8. A electric plastic rolling method for the deformation of Mg alloy board, strips and wires and its equipments, Chinese Patent: CN200510080495.4.
9. A fast online treatment method for Mg alloy wires and strips by using high energy electric pulsing technique, Chinese Patent: CN200610061957.2.
10. A high energy electric pulsing treatment method for steel wires and strips, Chinese Patent: CN200510101148.5.

Representative Papers :

1. Yanbin Jiang, **Guoyi Tang**, Chanhung Shek, Yaohua Zhu, Zhuohui Xu On the thermodynamics and kinetics of electropulsing induced dissolution of b-Mg₁₇Al₁₂ phase in an aged Mg–9Al–1Zn alloy **Acta Materialia** 57 (2009) 4797–4808 (SCI and EI index, IF=3.92).
2. Sude Ma, Guolin Song, Wei Li, Pengfei Fan, **Guoyi Tang**. UV irradiation-initiated MMA polymerization to prepare microcapsules containing phase change paraffin. **Solar Energy Materials & Solar Cells**, 2010. 94 (10): 1643-1647 (SCI index IF=3.858).
3. Guolin Song, Sude Ma, **Guoyi Tang**, Zhansong Yin, Xiaowei Wang. Preparation and characterization of flame retardant form-stable phase change materials composed by EPDM, paraffin and nano magnesium hydroxide. **Energy**, 2010, 35, 2179-2183(SCI Index IF=2.952).
4. Guolin Song, Sude Ma, **Guoyi Tang**, Xiaowei Wang. Ultrasonic-assisted

synthesis of hydrophobic magnesium hydroxide nanoparticles. **Colloids and Surfaces A: Physicochemical and Engineering Aspects**, 2010. 364 (1-3): 99-104 (SCI index IF=1.988).

5. **Guoyi Tang**, Zhuohui Xu, et al, Effect of a pulsed magnetic treatment on the dislocation substructure of a commercial high strength steel. **Materials Science and Engineering A** 398 (2005) 108–112 (2005) (SCI and EI index IF=1.901).

ELECTRICAL PULSE ANNEALING IMPROVES SOFT MAGNETIC PROPERTIES OF NANOMETER CoNbZr FILMS IN GHz FREQUENCY RANGE

Guijie Hao, Huaiwu Zhang, Xiaoli Tang

State Key Laboratory of Electronic Thin Films and Integrated Devices,
University of Electronic Science and Technology, Chengdu 610054, People's
Republic of China

Abstract

We present a new method by using electrical pulse annealing to improve soft magnetic properties of nanometer CoNbZr thin films in this investigation. The variations of nanometer crystal film grain size, structure and ferromagnetic resonance (FMR) with different electrical pulse annealing parameters have been analyzed. The results show that the saturation magnetization ($4\pi M_s$) of the thin films increases from 15.93kGs to 20.79kGs, meanwhile, the anisotropy field H_k raise to 61Oe. Furthermore, the cutoff frequency (f_r) increases to 3.45GHz, after electrical pulse annealing process. Through electrical pulse annealing, not only the soft magnetic properties such as $4\pi M_s$, anisotropy field (H_k) rapidly improved but also the grain size was refined. Moreover, damping coefficient also changed because of electrical pulse annealing. This behavior may attribute to the competitive growth of the nanometer crystal and nuclei forming.

Introduction

Magnetic films are widely used in various fields of high speed electronics such as data transmission, spintronic devices, and micro inductors [1-4]. With the operational frequency of electronic devices approaching to GHz regime, a remarkable tendency on electronic device is to continue increasing the operational frequency and degree of integration. An important material parameter that must be considered in these applications is the cut-off frequency (f_r), which is proportional to the square root of saturation magnetization ($4\pi M_s$) multiplied by magnetic uniaxial anisotropy field (H_k), $f_r = (\gamma/2\pi)$.

CoZr alloy thin films with good soft magnetic properties are promising candidates due to their high saturation magnetization, tunable anisotropy, and high electric resistivity. However the saturation magnetostriction coefficient of the CoZr thin films is large, so that some other elements with negative magnetostriction coefficient such as Nb, Ta, Mn are added into CoZr to reduce the magnetostriction coefficient to near zero.

Since amorphous alloy phase is a kind of thermal metastable state, heat treatment may influence the magnetic anisotropy and $4\pi M_s$ in CoNbZr films. Therefore, searches for post annealing leading to an improvement of soft magnetic properties have been carried out. These methods frequently employed are situ annealing and the magnetic field annealing. However, either treatment mentioned above need vacuum chamber, and the process of heating and cooling cost too much time, so that it takes more time and energy for cycle annealing. In this work, we realized a new kind of electrical pulse annealing method for CoNbZr thin films without any vacuum equipment. The approach of electrical pulse annealing has also been seen to make a decrease both in the magnetic anisotropy H_a and coercivity H_c by adjusting the crystallite size [5]. Since the electrical pulse can effectively control the current through the films, the annealing temperature will be changed rapidly. Furthermore, there is interdiffusion during the annealing process, which results in changes of both microstructure and mechanical properties [6-9]. These factors all have important influence on the soft magnetic and electromagnetic properties of films. In this paper, a new method by using power controlling electrical pulse annealing is presented to improve microstructure, grain size and distribution of CoNbZr thin films, through this way the remaining ferromagnetic amorphous matrix phase surrounding ultrafine crystal grains was decreased.

Experimental details

CoNbZr thin films (~250nm) were deposited on single-crystal 5×10 mm silicon substrates with (100) surface orientation at room temperature by dc magnetron sputtering at ambient temperature. The background pressure was less

than 5×10^{-4} Pa. An external uniform magnetic field about 500 Oe, induced by the sintered NdFeB magnets, was fixed parallel to the film plane in order to obtain a uniform in-plane magnetic anisotropy during the deposition process. A $\text{Co}_{85.5}\text{Nb}_{8.9}\text{Zr}_{5.6}$ target was used to deposit CoNbZr soft magnetic films. The electrical pulse annealing method was carried out by an alternating current power supply system whose pulse waveform is rectangular wave. The thicknesses of these thin films were measured by using a step profiler, and the magnetic hysteresis loops were measured at room temperature with a vibrating sample magnetometer (BHV-525). The crystal structures were analyzed by an x-ray diffraction (XRD) (Bede TM 2000). The microwave permeability measurements were carried out by using an Agilent network analyzer (N5230A) with a shorted microstrip transmission-line perturbation method without any external magnetic field [10-11]. The ferromagnetic resonance (FMR) behaviors of the films were detected by the vector network analyzer method, which takes advantages of the capabilities for wide-range magnetic field scanning.

Results and discussions

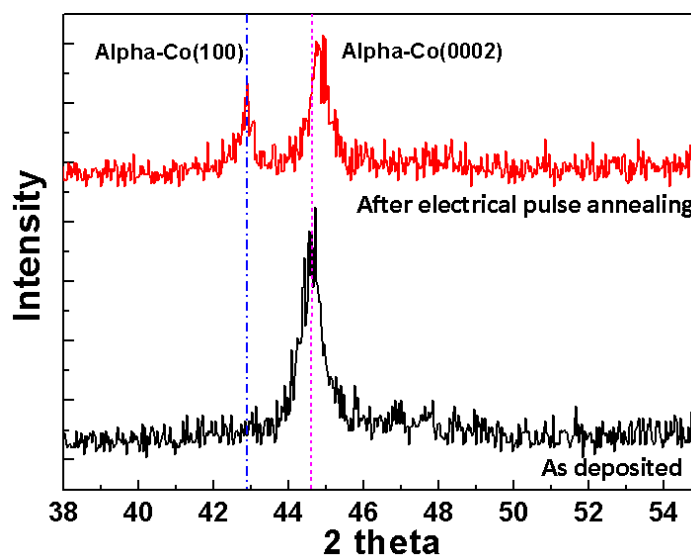


Fig. 1. XRD patterns of CoNbZr films.

Fig. 1 shows the x-ray diffraction patterns of CoNbZr thin films deposited at room temperature, and these then annealed at rectangle electrical pulse power.

The x-ray diffraction exhibit two main peaks, both the sharp (0002) peak around 44° and the (100) peak around 43° originating from the hcp α -Co nanocrystalline phase existing for CoNbZr films. This implies that the film is a nanocrystalline composite consists of nanocrystal grains surrounded by a remaining ferromagnetic amorphous matrix. Assisted with the Scherrer equation, the average grain size of these crystallization films was obtained to be 15 nm. The diffracted ray of the film as deposited, the (100) diffraction peak almost disappears. And the peak of α -Co gradually shifts from 44° to 45° after electrical pulse annealing, together with a variation in its intensity. The result confirms changes in both the nanocrystal phase and amorphous matrix. The shift roots in Zr and Nb atoms which gradually dissolve out of the metallic CoNbZr compound metal phase to form CoNb and CoZr₂ microcrystal due to the annealing temperature. The grains refined by electrical pulse annealing cause the intensity of the diffraction peak decreases.

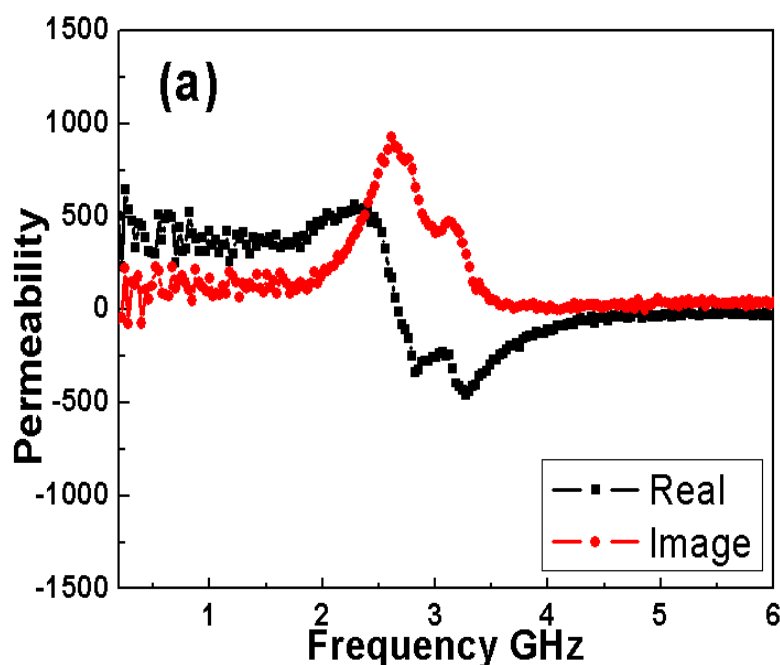


Fig. 2. Permeability spectra of the samples (a) as deposited 0.

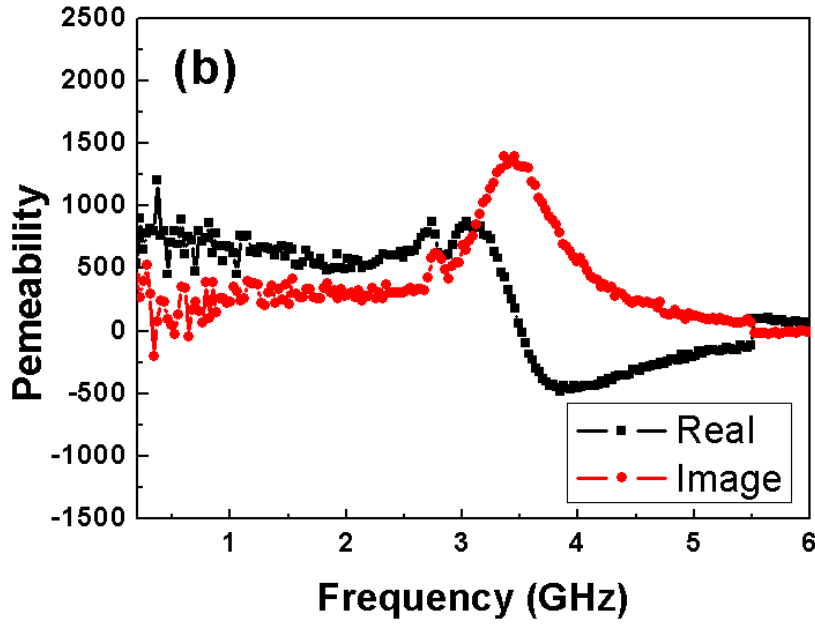


Fig. 2. Permeability spectra of the samples (b) post annealed by electrical pulse.

Fig. 2 presents the complex permeability spectra of the CoNbZr films (a) as deposited, (b) after post electrical pulse annealing. The scattering parameters S_{11} , which correspond to the microwave transmission through the coplanar waveguide with resonant reflection of the samples, were collected without any applied field. It can be clearly seen from Fig.2, the resonant magnetic frequency increases because of the electrical pulse annealing power. We also found that the initial permeability increases from 2.8GHz to 3.45GHz. Furthermore, the real parts of the permeability μ' have a different manner both in values and tendency. The full width at half maximum (FWHM, Δf) of the imaginary part is different from each other, from which we can obtain the effective damping factor (α_{eff}) using $\Delta f = \frac{1}{\alpha_{eff}}$. The minimum of α_{eff} is about 0.032. It is known that the effective damping parameter α_{eff} consists of both the intrinsic and the extrinsic contributions [12]. The intrinsic damping factor which can be measured from FMR studies is contributed to the fundamental property such as interaction of spin-orbit coupling with lattice [13]. And the extrinsic contributions are generally explained by various theories including the defect-induced two-magnon model [12] and the local resonance model [14] etc.

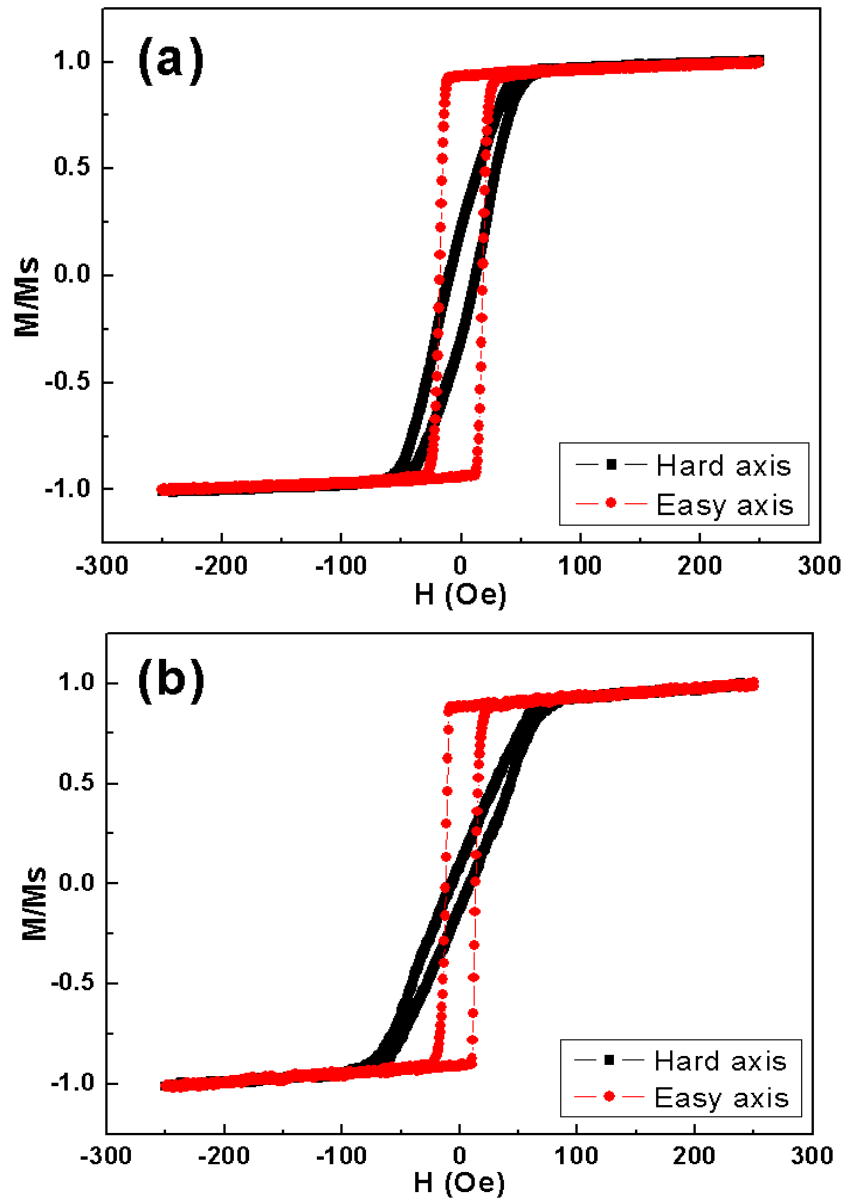


Fig. 3. The M-H loops along the easy and hard axes of CoNbZr films (a) as deposited (b) post annealed by electrical pulse.

The in-plane hysteresis loops of the thin CoNbZr films are shown in Fig.3. As it can be seen from Figure 3, coercivity of the films annealed is about 7.88, which is much smaller than the as deposited one H_c 180Oe. And the change of saturation magnetization $4\pi M_s$ and anisotropy field both have a contrary trend. It is known that the saturation magnetization of the nanocrystalline phase is higher than that of the amorphous phase [15]. The increase of saturation magnetization is caused by the presence of more and more nanocrystalline phase in the films. As the temperature gradient which is the driving force of nucleation moderately increasing, the current through the films during the electrical pulse

annealing can lead to an increase in the number of nucleation in magnitude. According to the well known Kittel formula for magnetic thin films, the resonant magnetic field is inversely proportional to the saturation magnetization. Therefore, nanocrystalline phase can lead to a decrease in the resonant magnetic field. Both grain refinement and release of intrinsic stress contribute to uniform distribution of the magnetic domains, which conduce towards increasing anisotropy field H_k as long as cutoff frequency f_r .

The results of the static magnetic measurements revealed that the electrical pulse annealed CoNbZr thin films possess a well-defined uniaxial anisotropy with an in-plane static uniaxial anisotropy field H_k of 61 Oe, and a saturation magnetization of 20.79 kGs. The cutoff frequency reaches 3.45 GHz while the real part of the permeability remains constant at about 700 up to 3 GHz. These excellent soft magnetic properties in the CoNbZr films can be explained by Herzer's random anisotropy model (RAM) theory [16-17]. When particle size along with the distance between particles is reduced to the critical exchange length L_{ex} , the magnetic exchange coupling interacts among grains, which forces the magnetic moments of neighboring grains to be aligned parallel, lead to a demagnetization effect of individual grains and a cancellation of local anisotropies [18]. Therefore the thin CoNbZr films annealed under electrical pulse display good soft magnetic properties.

Conclusion

In this work, a kind of nanometer CoNbZr thin films were fabricated by DC magnetron sputtering and then treated by an electric pulse annealing method. It was showed that good high frequency properties have been obtained with high ferromagnetic resonant frequency. Meanwhile the ferromagnetic resonant frequency could be effectively tuned by this kind of post annealing. Through electric pulse annealing the f_r ascended to 3.45 GHz and a μ' 350 was obtained. The physical origin of this phenomenon is suggested to be based on the changes of microstructure as well as composition in films.

Acknowledgements

The authors would like to acknowledge financial support from the Foundation for Innovative Research Groups of the National Natural Science Fund of China under Grant No. 61021061, the National Basic Research Program of China under Grant No. 2012CB933104 and National Natural Science Foundation of China (Grant Nos. 61271037, 61071028, 51171038 and 61271038).

References

- [1]. Y. Hayakawa, A. Makino, H. Fujimori, and A. Inoue, *J. Appl. Phys.* 81, 3747 (2002).
- [2]. E. Salahun, P. Quéffélec, G. Tanné, A. Adenot, and O. Acher, *J. Appl. Phys.* 91, 5449 (2002).
- [3]. K. Seemann, H. Leiste, and V. Bekker, *J. Magn. Magn. Mater.* 283, 310 (2004).
- [4]. Y. W. Zhao, X. K. Zhang, and J. Q. Xiao, *Adv. Mater. (Weinheim, Ger.)* 17, 915 (2005).
- [5]. V. Edon, S. Dubourg, and J. Vernières, *J. Appl. Phys.* 107, 09A321 (2010).
- [6]. Jiang Xiangdong Zhang HuaiWU and Wen Qiye *Materials Science and Engineering B*, 103(1), 32 (2003).
- [7]. P. Gorria, J. S. Garitaonandia, and J. M. Barandiaran, *J. Phys. :Condens. Matter* 8, 5925 (1996).
- [8]. Y. Yoshizawa, S. Oguma, and K. Yamauchi, *J. Appl. Phys.* 64, 6044 (1988).
- [9]. G. Herzer, *IEEE Trans. Magn.* 25, 3327 (1989).
- [10]. V. Bekker et al., *J. Magn. Magn. Mater.* 270, 327 (2004).
- [11]. Y. Liu et al., *Rev. Sci. Instrum.* 76, 063911 (2005).
- [12]. R. Arias and D. L. Mills, *Phys. Rev. B* 60, 7395 (1999).
- [13]. Yicheng Wang, Huaiwu Zhang, and Dandan Wen, *J. Appl. Phys.* 113, 17A316 (2013)
- [14]. C. Chappert, K. L. Dang, P. Beauvillain, H. Hurdequint, and D. Renard, *Phys. Rev. B* 34, 3192 (1986).

- [15]. D. S. Schmool, J. S. Garitaonandia, and J. M. Barandiaran, *Physical Review B*, 58(18), 159 (1998).
- [16]. G. Herzer, *IEEE Trans. Magn.* 25, 3327 (1989).
- [17]. G. Herzer, *IEEE Trans. Magn.* 26, 1397 (1990).
- [18]. Guangduo Lu, Huaiwu Zhang, and John Q. Xiao, *J. Appl. Phys.* 109, 07A308 (2011).

**STRUCTURE-PHASE STATES AND WEAR RESISTANCE OF
DEPOSITION SURFACE FORMED ON STEEL BY ELECTRIC ARC
METHOD**

**S.V. Raikov¹, E.V. Kapralov¹, E.S. Vashchuk¹, E.A. Budovskikh¹,
V.E. Gromov¹, Yu.F. Ivanov^{2,3}, K.V. Sosnin¹**

¹ Siberian state industrial university, 654007, Novokuznetsk, Russia

² Institute of high current electronics Sib. branch RAS, 634055, Tomsk, Russia

³ National research Tomsk polytechnical university, 634050, Tomsk, Russia

E-mail: budovskih_ea@physics.sibsiu.ru

Abstract

Investigations of elementary and phase structure, state of defect structure and tribological characteristics of a deposition, formed on a low carbon low-alloy steel by a welding method were carried out. It was revealed that a deposition, formed on a steel surface is accompanied by the multilayer formation, and increase of wear resistance of the layer w deposition as determined.

Key words: steel Hardox 400, structure, hard facing, phase composition, wear resistance.

Introduction

Electric arc deposition takes strong positions in the improvement of structure of machine parts and mechanisms in different branches of industry. As a result of deposition and in a manufacture of machine parts it is possible to obtain a working surface possessing a necessary complex of properties: wear resistance, heat stability, heat resistance, corrosion resistance, etc.¹

Using a deposition, it is possible to reduce the consumption of the expensive nonferrous metals and alloys and high carbon steels. Besides, repeated restoration of the worn parts decreases to a large extent the consumption of metal for the manufacture of spare parts of the equipment. The increase of service life of equipment parts is especially important, if the performance of high efficient equipment depends on their reliability and durability. A high economical and technical efficiency of deposition in metallurgical machine building is specified by it. The efficiency of structure improvement by deposition is determined by the right choice of deposited metal composition based on the conditions of work of a part and a main type of wear. The choice of the deposited material is done with regard to exploitation conditions of the part being restored, type of protection, design features of a part and the equipment available. At present a large number of electrode materials has been developed on the base of iron for arc deposition.

Material and research method

Steel Hardox 400 was used as the test material, its element composition is shown in Table 1. Thick deposited layers (3 -5 mm in thickness) were formed on steel surface by welding method. Element composition of welding wire used for formation of a layer is shown in Table 1.

Investigation of element and phase composition, state of defect substructure of deposited layer were done by methods of optic (metallographic

¹ The research was done with financial support of RFFI in frames of research project №13-02-12009 ofi_m, Ministry of education and science, 2708 GZ, project FNI SO RAS (project № II.9.5.2).

microvisor mVizo-MET-221), scanning (scanning electron microscope Philips SEM-515 with microanalyzer EDAX ECON IV) and transmission (transmission electron microscope EM-125) electron microscopy, X-ray structural analysis (X-ray diffractometer DRON-7). Tribological characteristics of coating were revealed by wear resistance and friction coefficient determination (tribotester Tribotechnic). Tribological tests were done under the following conditions: a ball with diameter of 3 mm from a hard alloy VK-8 was used as a counterbody. A counterbody was shifted on the sample surface along the circle of 4 mm diameter at linear velocity 2 cm/sec under normal load 5 N. The total number of revolutions of counterbody was 5000.

Table 1. Chemical composition of test materials (the remainder Fe, weight%).

Chemical element	C	Si	Mn	P	N	B	S	Mo	Cr	Nb
Steel Hardox 400	0,18	0,70	1,60	0,01	0,004	0,025	0,01	0,25	----	
Welding wire SKA 70 - G	2,6	0,6	1,7	-----	-----	2,2	-----	-----	14,8	4,7

Results of investigations and their discussion

Tribological test has shown that the formation of deposition on the surface of steel Hardox 400 results in the increase of wear resistance of material surface layer by a factor of ~ 2.25 and friction coefficient – by a factor of – 1.05.

To establish the physical mechanisms of wear resistance increase of steel with deposited material the studies of structure, phase and element composition of deposition/steel system were carried out. Structure and element composition analyses were done in two sections: in section parallel to the surface of deposition and in section perpendicular to the deposited layer.

Structure of deposition is shown in Fig. 1. A large number of inclusions are of edged shape. Inclusion sizes vary within 1 mcm to 5 mcm. The second

morphological element of the deposited layer is a structure of dendritic (Fig. 1, b, c) and cellular (Fig. 1, c, d) crystallization. The cell sizes vary within 0.3 μm to 0.8 μm . The cells are separated by interlayers of 50 to 100 nm thickness.

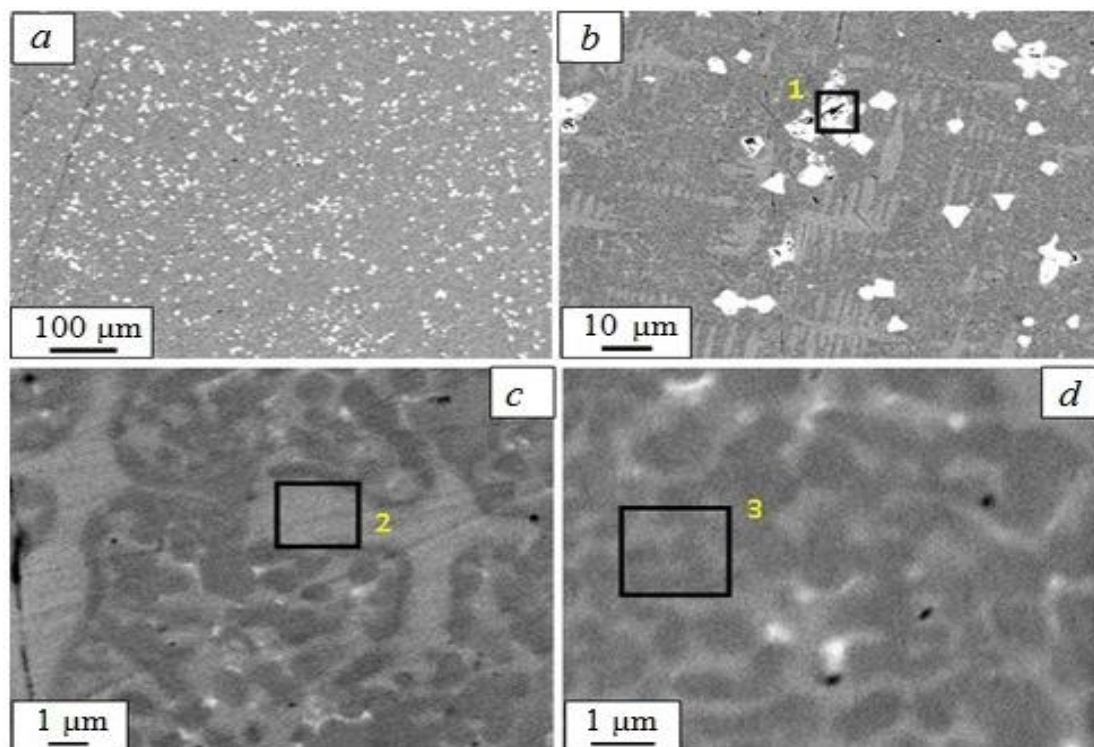


Fig. 1. Structure of deposition being formed on the surface of steel. Section is parallel to the surface of deposition. Frames show the sites of X-ray spectrum analysis of the material.

Table 2. Results of X-ray microspectrum analysis of deposition structure formed on the surface of steel.

Spectrum	Alloying elements, weight %							Result
	C	Si	Ti	Cr	Mn	Fe	Nb	
Zone 1	0,0	0,0	1,02	6,50	0,0	7,07	85,42	100.00
Zone 2	3,74	1,40	0,0	7,89	1,44	85,53	0,0	100.00
Zone 3	4,11	0,71	0,0	13,07	1,71	80,40	0,0	100.00

X-ray microspectrum analysis of deposition sites, designated by frame in Fig. 1, has shown that particles of the edged shape are enriched by atoms of

niobium (Fig. 1, b, zone 1); zones of dendritic crystallization (Fig. 1, c, zone 2) are enriched by atoms of iron, chromium and carbon. A characteristic feature of the cellular crystallization structure being formed largely by atoms of iron is the presence of carbon and chromium atoms of large concentration (Fig. 1, c, zone 3). The given results are shown in Table 2 in a quantitative ratio.

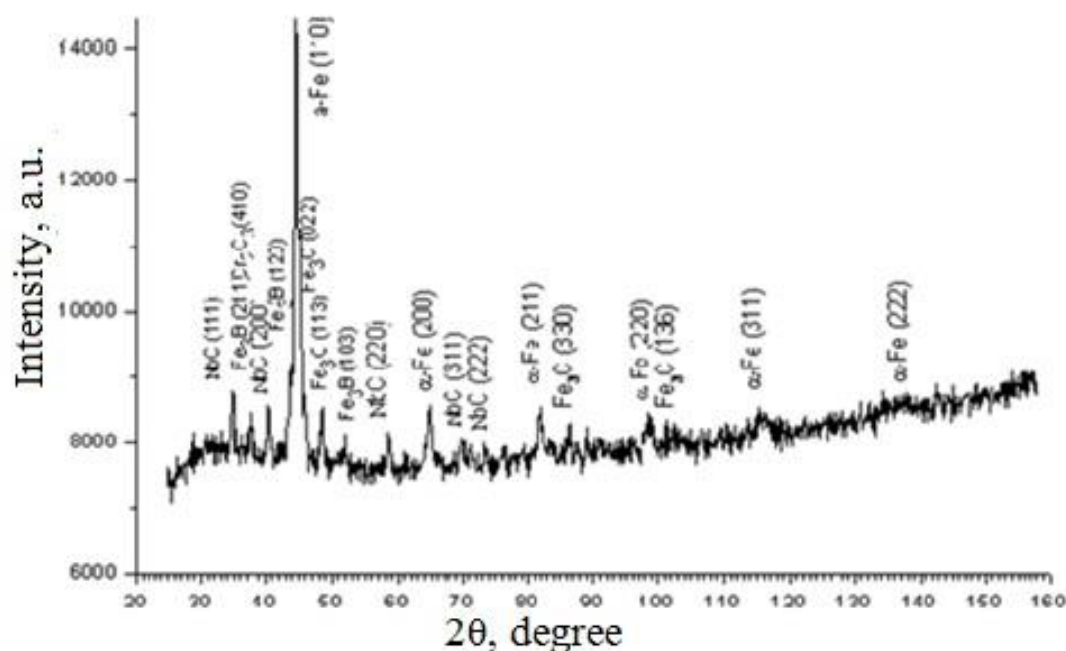


Fig. 2. Part of X-ray photograph obtained from the surface layer of deposition.

Table 3. Results of phase analysis of surface deposition layer.

Volume fraction, %			
α -Fe	Fe_3C	NbC, Cr_3C_2	Fe_3B
60	10	20	10

Table 4. Results of α -Fe structure analysis of surface deposition layer.

Parameter of crystal lattice, a , nm	Sizes of coherent scattering, D , nm	Microdistortions of crystal lattice ($\Delta d/d$)
$0,2874 \pm 0,0001$	30,0	$0,0010 \pm 0,0005$

Phase composition of surface deposition layer was analyzed by X-ray diffraction method. X-ray photograph obtained from the surface deposition layer is shown in Fig. 2, the results of its analysis are shown in Table 3 and Table 4.

When analyzing the results shown in Table 3 and 4, it can be noted that the basic phase of the tested deposition is α -iron, the average size of coherent scattering zone of which is $D = 30\text{nm}$. The revealed parameter of α -iron crystal lattice is somewhat higher than that of α -iron containing no admixture ($a_0 = 0.28668\text{ nm}$ [1]). Suppose the increase of crystal lattice parameter of deposition α -phase is caused by formation of solid solution oversaturated by carbon atoms. In this case, using the estimation expression (1), given in [2, 3] it can be shown that carbon concentration ΔC located in crystal lattice on the base of α -iron is 0.018 weight %.

$$\Delta C = (\alpha - a_0/39 \pm 4) \cdot 10^3, \quad (1)$$

where $a_0 = 0.28668\text{ nm}$, $\alpha = 0.28740\text{ nm}$.

The hardness phase of test deposition is iron carbide of composition Fe_3C (cementite), volume fraction of which is 10%, carbides of niobium and chromium of composition NbC and Cr_3C_2 (sum volume fraction of the given carbides is 20%) and boride of iron of composition Fe_3B , volume fraction of which is 10% (Table 3). It should be noted that these phases are expectable because they are in the deposition composition in comparatively large quantities, in addition to iron, carbon, boron, niobium and chromium (Table 1).

Cross-section analysis of deposition/substrate system made it possible to reveal the multilayer structure which according to morphological characteristics can be presented by deposition layer (Fig 3, a, layer 1), transition layers (Fig. 3, a, layer 2 and 3) and a layer of thermal transformation of steel (Fig. 3, layer 4). Deposition layer (Fig. 3, layer 1) has principally a structure of cellular crystallization and is characterized by the presence of particles, enriched by niobium (Fig. 3, a, b). Sizes of crystallization cells vary within 0.5 μm to 1 μm ; a thickness of interlayers separating them is 0.1 – 0.3 μm .

The first transition layer (Fig. 3, layer 2) has an island-type structure. Islands of sizes 5 – 10 μm are separated by extended interlayers having a complex substructure, the element sizes of which vary within 300 – 600 nm (Fig. 3, c). The second transition layer, directly adjacent to steel interface is comparatively thin 10 – 20 μm and is characterized by column dendritic structure being formed from the steel interface (Fig. 3, d). In specific cases, microcracks and comparatively large 0.9 – 1 μm second phase precipitates are located along the interface of layers 2 and 3.

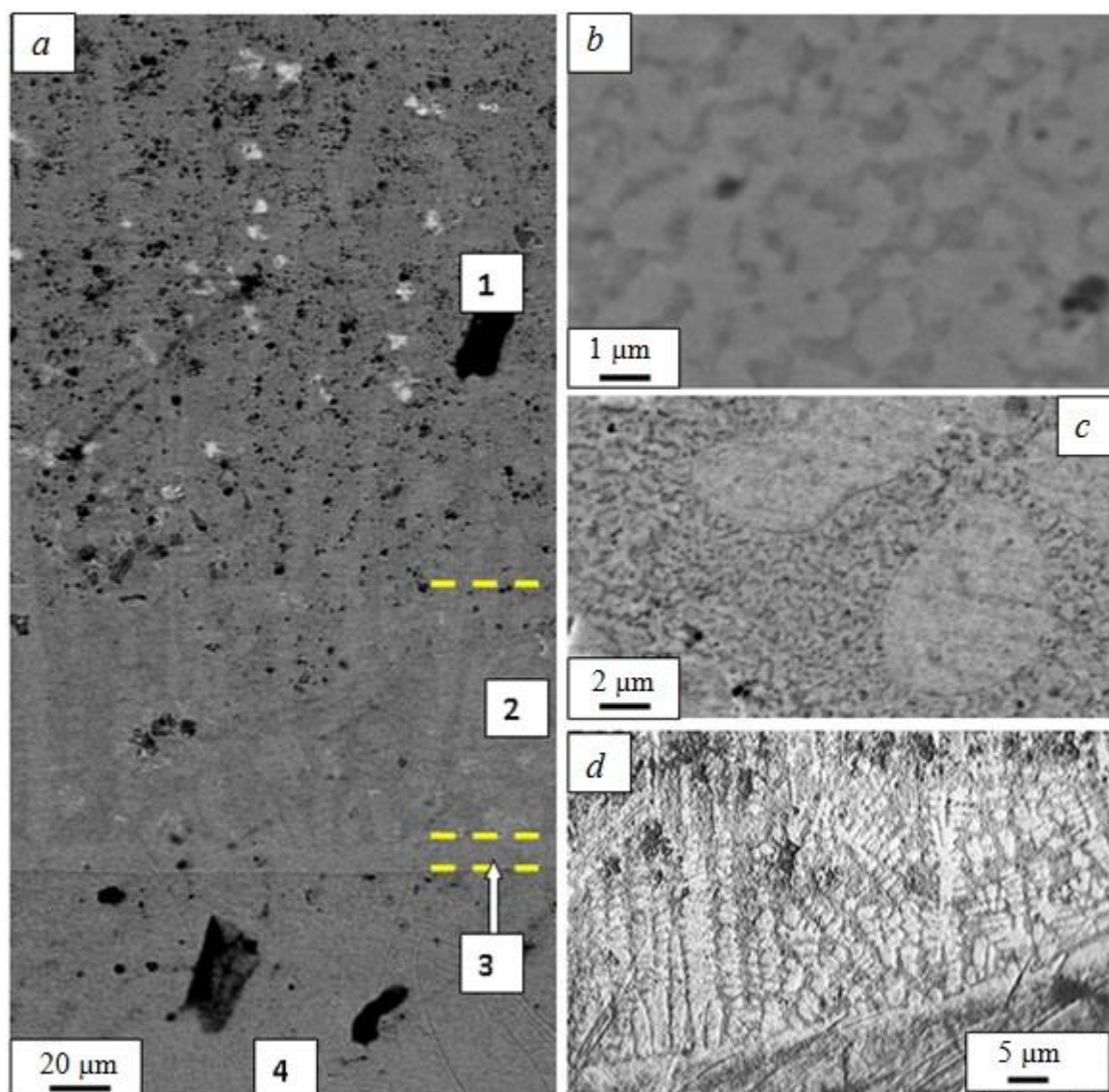


Fig. 3. Structure of transversal metallographic section of deposition, formed on steel.
Designation: 1 – deposition layer; 2, 3 – transition layers; 4 – layer of thermal influence of steel; b- structure of zone 1; c – zone 2; d – zone 3.

Structure of deposition formed on steel is characterized by the presence of macro and microcracks, micropores (Fig. 4, cracks are designated by arrows). Macrocracks are detected in all deposition layers, the most extended from them being present in layer 1 are located, largely, parallel to deposition surface (Fig. 4, a). The sources of cracks are large 1 - 2 mcm inclusions of the second phase (Fig. 4, b), dendrites of crystallization (Fig. 4, c), zones of island crystallization (Fig. 4, d).

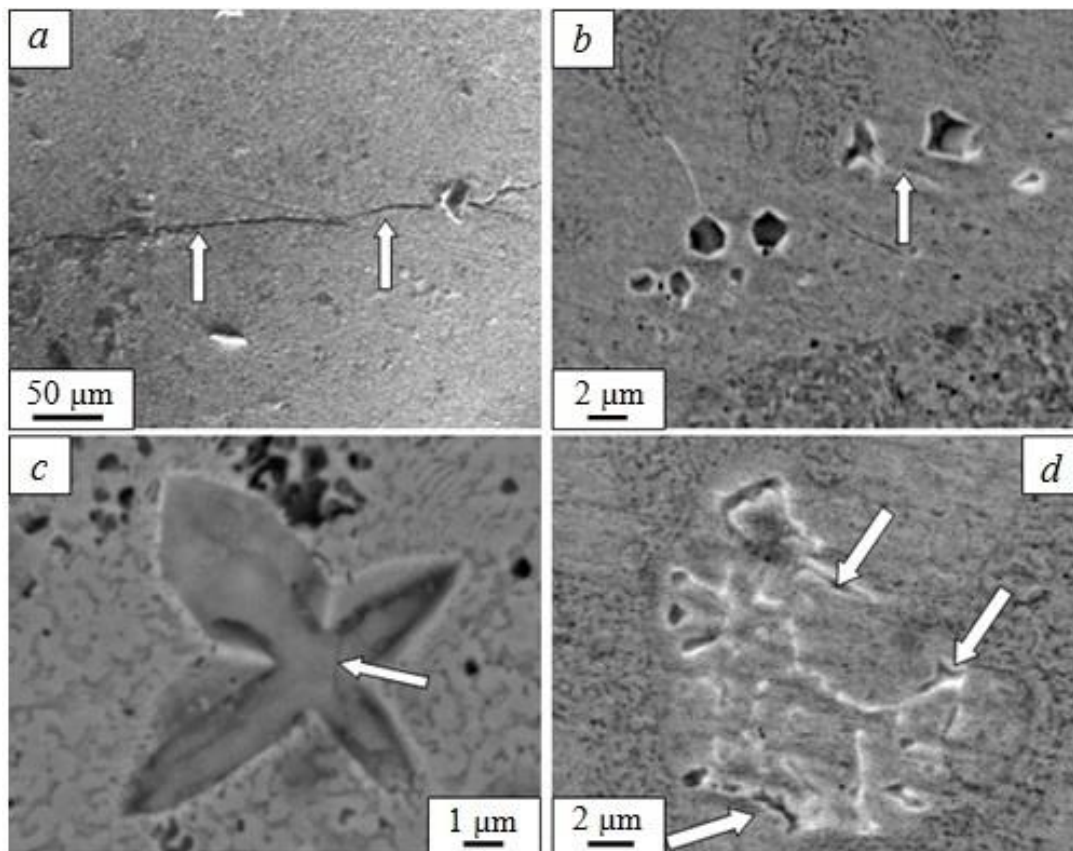


Fig.4. Defects of structure (shown by arrows), being present in deposition, formed on steel.

The carried out studies of defect substructure, phase and element composition of deposition make it possible to consider the revealed fact by the following way: increase of wear resistant surface layer. Namely: formation in the deposited layer a submicrosize structure of crystallization, precipitation of large number (~40%) of high strength particles of carbide and boride phases facilitates a significant increase of deposition strength as a whole.

Conclusions

The carried out studies of structure, element and phase composition of deposition formed on the low carbon low-alloyed steel Hardox 400 make it possible to make the following conclusion:

1. Formation of deposition on the surface of steel is accompanied by the formation of multi-layer structure, the layer of which differ in the morphology of element substructure.

2. Deposition is a multi-phase material and is presented by solid solution grains on the basis of α -iron, by particles of iron carbide of composition Fe_3C (cementite), the volume fraction of which is 10%, of niobium and chromium carbides NbC and Cr_3C_2 (sum volume fraction of carbides is 20%) and of boride of iron Fe_3B , the volume fraction of which is 10%.

3. The revealed multiple (more then twice) increase of wear resistance of deposited layer (para to volume of steel) is specified by formation of submicro- and nanosize structure of α -phase crystallization and precipitation of large volume (~40%) of particles of high strength of carbide and boride phases.

Electric arc deposition with powder wire is used for strengthening the excavator's buckets and bodies of large-size automobiles.

References

- [1]. A.P. Babichev, N.S. Babushkin, A.M. Bratkovskii et al; edited by I.S. Grigoriev, E.Z. Meilikhov. Physical magnitudes: Reference book. M. Energoatomizdat, 1991. 1232 p.
- [2]. V.G. Kurdyumov, L.M. Utevsikii, R.I. Entin Transformation in iron and steel. Nauka, 1977. 236 p.
- [3]. E.J. Fasiska, H. Wagenblat. Dilatation of alpha-iron by carbon // Trans.Met.Soc. AIME. 1967. V.239. №11. pp. 1818 – 1820.

EFFECT OF ELECTRIC PULSES ON THE ANNEALING BEHAVIORS OF SUBMICRON GRAINED METALS

Wei Li, Yao Shen, Wei Zeng

State Key Lab of Metal Matrix Composites, School of Materials Science and
Engineering, Shanghai Jiao Tong University, Shanghai 200240, People's
Republic of China

Email: yaoshen@sjtu.edu.cn

Abstract

Submicron grained (SMG, $0.1\mu\text{m} < D < 1\mu\text{m}$) Al, Ti and Cu were fabricated by heavy cold rolling and then subjected to annealing either by electric pulse or by traditional air furnace. An abnormal increase in the strength of SMG Al and Ti occurred by a moderate airfurnace annealing (AFA) due to the occurrence of a dislocation source-limited hardening mechanism. Moreover, the hardening rate was substantially enhanced by electric pulse annealing (EPA) at the same or slightly lower temperatures. However, the usual annealing induced softening was observed in SMG Cu by AFA and was promoted by EPA. Detailed microstructural characterization suggests that the enhanced hardening rate is related to the enhanced rate of dislocation recovery and the accelerated softening of Cu is caused by promoted recrystallization.

Introduction

Submicron grained (SMG, $0.1\mu\text{m} < D < 1\mu\text{m}$) materials have attracted much attention for decades due to their high strength[1-3]. However, the poor ductility of these materials limited their industrial application[4, 5]. Just like other materials, the unique mechanical properties of SMG materials are determined by their characteristic microstructures. SMG metals produced by severe plastic deformation have dislocation densities in the order of $10^{12}\sim 10^{14}\text{m}^{-2}$ for face-centered cubic (fcc) and body-centered cubic (bcc) crystal structure with high to medium stacking fault energy (SFE) [2, 6-8], which are much lower than those ($10^{14}\sim 10^{15}\text{m}^{-2}$) in deformed coarse grain metals (CG, $D > 1\mu\text{m}$) [8,

9]. These dislocations are present in the form of individual dislocations or loose dislocation tangles. The low density of dislocation, and the high volume fraction of grain boundary in SMG metals may cause the unexpected annealing behaviors, such as annealing induced hardening [2, 6, 7, 10-15]. This abnormal hardening by annealing was suggested to be caused by a new strengthening mechanism, i.e. dislocation source-limited strengthening [2, 6, 15], which occurs in SMG or even nanocrystalline (NC, $D < 0.1 \mu\text{m}$) metals if they lack mobile dislocations and easy dislocation sources. While in most cases the strength of SMG metals decreases when annealed due to the decrease of interior dislocation density and the increase of grain size, which is the same as the usual annealing induced softening observed in CG metals. One may expect that the hardening or softening kinetics can be manipulated if the rate of decrease of dislocation density can be changed somehow, e.g. by different annealing treatments.

It has often been reported that the mobility of dislocations can be increased by application of electric pulses during plastic deformation or during annealing although the exact mechanisms by which the mobility of the dislocations is increased by electric pulses is still open to debate [16-18]. Therefore an enhancement of dislocation annihilation is expected during electric pulse annealing (EPA) as compared to conventional annealing at similar temperatures. If this is the case, an enhanced hardening and softening kinetics can also be expected. In this study, we prepared three kinds of SMG metals: Al (fcc, high SFE), Cu (fcc, medium to high SFE) and Ti (hexagonal close-packed, hcp) to investigate the effects of EPA treatment on the kinetics of annealing induced hardening or softening

Experimental

Fully recrystallized commercial pure (CP) Al (99.7% purity) plate, hot rolled CP Ti (98.95% purity) and as-cast CP Cu (97.53% purity) were used as starting materials, whose chemical compositions are shown in Table 1.

Table 1. Chemical composition of CP metals studied.

(a) Chemical composition of CP Al

Element	Cu	Fe	Mg	Mn	Ni	Si	Ti	Zn	Al
Content (wt %)	0.0007	0.1063	0.0025	0.0013	0.0029	0.0333	0.0041	0.0024	Balance

(b) Chemical composition of CP Ti

Element	O	N	Fe	Si	Al	Ti
Content (wt %)	0.2	0.03	0.2	0.06	0.56	Balance

(c) Chemical composition of CP Cu

Element	C	O	Si	P	S	Cr	Mn	Fe	Zn	As	Cu
Content (wt %)	0.49	0.37	0.14	0.20	0.07	0.74	0.13	0.14	0.02	0.17	Balance

To prepare a submicron grained microstructure, heavy cold rolling was employed. A 40 mm thick CP Al plate was symmetrically rolled (SR) to 0.6 mm by 12 rolling passes (named as Al-SR, equivalent von Mises strain $M=4.85$). Considering the limited starting thickness of CP Ti and Cu plates (9 mm and 15 mm respectively), asymmetrically rolling (ASR) was applied instead for a M higher than that would be available by SR. The CP Ti and Cu plates were asymmetrically rolled to 1.5 mm by 15 and 27 rolling passes respectively with a roll speed ratio of 1.5 between the two rollers.

Electric pulse was used for the heat treatment of rolled pure metals and, for comparison, air furnace annealing (AFA) was conducted for 30 minutes at the temperatures same as the highest reached in the electric pulse heating. Dog-bone shaped specimens were machined by electric discharge machining from the rolled sheets, then they were annealed by electric pulses under different annealing conditions: a) The Al-SR specimens were electric pulse annealed at 150 and the total EPA treatment duration was varied from 0.5 to 5 minutes. b) The Ti-ASR specimens were electric pulse annealed at 200 for 2 minutes. c) The Cu-ASR specimens were electric pulse annealed in the temperature range 50 to 300 for 2 minutes. The temperature rise due to Joule heating was monitored by a thermocouple well attached to the surface of the specimens. To be noted, after reaching the targeted annealing temperature, the specimens were

kept at a temperature close to but not exceeding the target temperature by well controlled air cooling conditions.

The mechanical properties of these samples were characterized by tensile or microhardness test. The tensile tests were performed at a strain rate of 4×10^{-4} /s on a Zwick/Roel testing machine for CP Al samples. At least 3 tensile specimens were tested to obtain the mean value of yield strength in each group. For the CP Ti and Cu samples, microhardness was measured at a loading of 200g and 500g respectively for 15s on a Buehler Micromet Hardness Tester. To minimize the errors, at least 15 data points were obtained to calculate the mean value for each group and all the measured data points were near the central line along the longitudinal direction of rolling surface, as shown in Fig. 1.

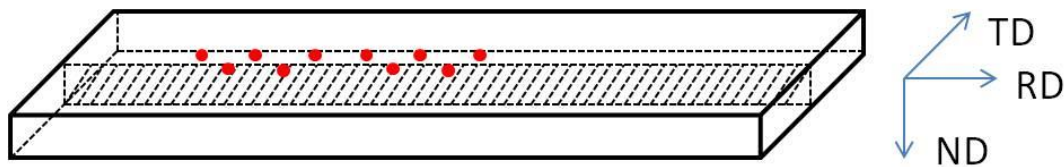


Fig. 1 Sketch of rolling sheet and the locations and geometry for experimental measurement and observation. RD, TD and ND stands for rolling direction, transverse direction and normal direction respectively. The red solid dots indicate where the microhardness was measured. The shadow is the observed section for TEM.

Microstructure morphologies and statistics including average grain sizes, interior dislocation densities and distributions of grain boundary misorientation were obtained from transmission electron microscopy (TEM) performed with a JEM-2100 microscope operating at 200kV. The observed sections for TEM were RD-TD plane cut from the central part of the rolled sheets, as shown in Fig. 1. Average grain sizes were calculated from 250 to 320 grains by the line interception method. Interior dislocation densities were calculated by grid line method and at least 30 grains or subgrains in more than 2 zones were measured for each sample. Visualization of interior dislocations were obtained by multiple-beam condition (e.g. $B // \langle 001 \rangle$ or $\langle 011 \rangle$ for fcc metals and $B // \langle 11-20 \rangle$ for hcp metals), at which almost all interior dislocations are visible. The thickness,

which was used in calculation of the dislocation densities in the observed zones, were measured by convergent beam electron diffraction (CBED). Misorientations of grain boundary were measured by a hand-operated Kikuchi line analysis and more than 70 misorientations were analyzed in this study.

Results

Changes in strengths of Al-SR, Ti-ASR and Cu-ASR after annealing

Annealing induced hardening occurred in Al-SR and Ti-ASR after AFA at 150 and 200 for 30 minutes respectively and a more pronounced hardening was observed after EPA at the same temperatures in a shorter time. Figure 2, a shows the tensile curves of CP Al samples in the as-cold-rolled state and after annealing by AFA at 150C for 30 minutes or by EPA for 0.5, 1, 2 and 5 minutes. Compared with the as-cold-rolled sample, all the annealed samples show an increase in the yield strength and a decrease in elongation, similar to previous observations in annealed nanostructured Al processed by ARB [2, 6] or ECAP [19, 20] or cold rolling [21]. In the case of EPA, peak hardening is observed after 2 minutes EPA treatment. After 5 minutes EPA treatment the stress-strain curve shifts down, although the yield strength is still higher than that for the as-cold-rolled sample. When comparing the hardening behavior of the samples treated by EPA with those by AFA, two remarkable differences are found. The first is the substantially enhanced hardening rate by EPA compared to AFA; the annealing time required to reach the peak hardening is 2 minutes for the EPA treatment, whereas it is 30 minutes for the AFA treatment. The second is the higher maximum yield strength achieved by EPA than by AFA (190.2 versus 179.7 MPa). Figure. 2b shows the microhardness of CP Ti-ASR before and after AFA or EPA. Similarly annealing hardening was observed to occur by AFA or EPA, but EPA induced larger increase in microhardness is shorter time.

However, annealing induced hardening was not observed in Cu-ASR after either AFA or EPA in any temperatures; instead, softening was observed when the annealing temperatures were elevated. Figure 2, c displays the microhardness of Cu annealed in a wide temperature range, 50 to 350 by air

furnace and 50 to 300 by electric pulse, along with those before annealing for comparison. The strength of Cu-ASR remains almost unchanged when annealed in the temperature range of 50 to 250 by either electric pulse or air furnace annealing, but decreased to different values at 300. The decrease of strength in Cu-ASR at 300 by EPA is much larger than that by AFA at the same temperature and is as much as that at 350 by AFA. This is an indication of acceleration of softening by EPA, which have already been reported for other metals[22-25].

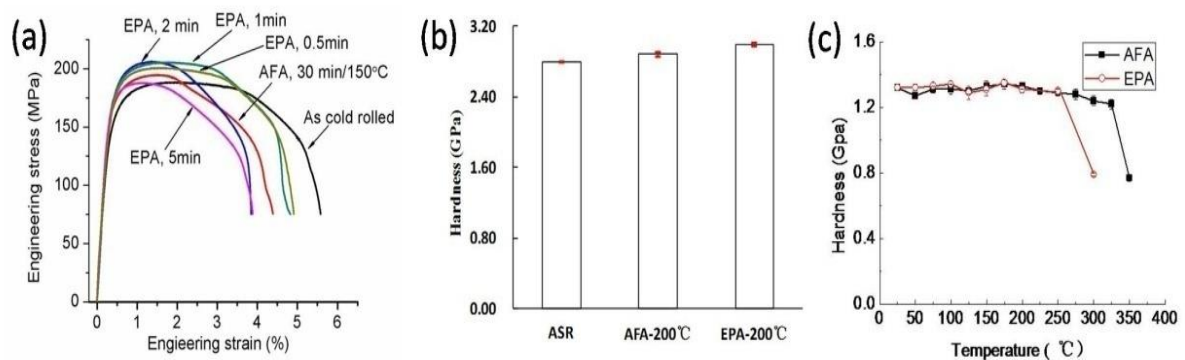


Fig. 2. (a) Stress-strain curves of CP Al-SR before or after EPA or AFA. (b) Microhardness of CP Ti-ASR before or after annealing at 200. (c) Microhardness of CP Cu-ASR as a function of annealing temperature.

Microstructures of CP Al-SR, Ti-ASR and Cu-ASR before and after annealing

Microstructures of rolled metals

Figure 3 and Table 2 show the TEM microstructures and the statistics including average lamellar boundary spacing, interior dislocation densities and distributions of grain boundary misorientation angles in Al-SR, Ti-ASR and Cu-ASR. The rolled samples all exhibited a typical submicron grained structure (50 to 500 nm) but with different morphological details and grain boundary features. Microstructures of Al-SR are only composed of lamellar grains with their extended lamellar boundaries parallel to the rolling plane and short transverse boundaries interconnecting the lamellar boundaries. The fraction of high-angle boundaries ($>15^\circ$) in Al-SR is about 50%, which is very similar to those

observed in nanostructured Al sample processed by ARB [2,6] or ECAP [19,20]. But in Ti-ASR, both submicron grained lamellar grains and equiaxed grains in the size range of 50 to 200 nm appeared. The selected area electron diffraction (SAED) obtained from a disc of 2 μm diameter shows a wide spreading of SAED pattern, indicating a high proportion of high-angle grain boundaries in Ti-ASR. This is consistent with the measured proportion (47%) of high-angle grain boundaries by the Kikuchi line analysis. While microstructures of Cu-ASR are composed of lamellar grains with much longer and more curved extended lamellar boundaries. The single crystal-like diffraction pattern with streaking of spots suggested a dominating proportion of low-angle grain boundaries, consistent with the measured proportion of 94.7%. No deformation twins were observed by TEM in both Cu-ASR and Ti-ASR. This simplifies our interpretation of the microstructure-strength relationship.

Microstructure changes after annealing

Figure 3 and Table 2 also show the changes of microstructures and their statistics in these rolled metals after AFA or EPA. Microstructure morphologies and distributions of grain boundary misorientation angles in Al-SR, Ti-ASR and Cu-ASR almost remained unchanged after annealing at 150, 200 and 175 respectively, which implied that only recovery process occurred at these temperatures.

Table 2. Microstructure statistics for different samples. DL, is the lamellar spacing; ρ_0 , the interior dislocation density; $f_{<3^\circ}$, the fraction of boundaries with misorientation angles less than 3° ; f_{3-15° , between 3 and 15° ; $f_{>15^\circ}$, more than 15° .

Sample	DL (nm)	ρ_0 (10^{14}m^{-2})	$f_{<3^\circ}$ (%)	f_{3-15° (%)	$f_{>15^\circ}$ (%)
Al-SR	280	8	23.0	27.0	50.0
Al-AFA for 30min/150°C	356	5	–	–	–
Al-EFA for 2min/150°C	310	5	–	–	–
Ti-ASR	186	19	28.3	23.9	47.8
Ti-AFA for 30min/200°C	210	8.8	27.7	19.1	53.2
Ti-EFA for 2min/200°C	191	9.2	26.5	20.4	53.1
Cu-ASR	209	30	63.2	31.6	5.3
Cu-AFA for 30min/175°C	221	26	61.9	33.3	4.8
Cu-EFA for 2min/175°C	216	28	62.5	33.3	4.2

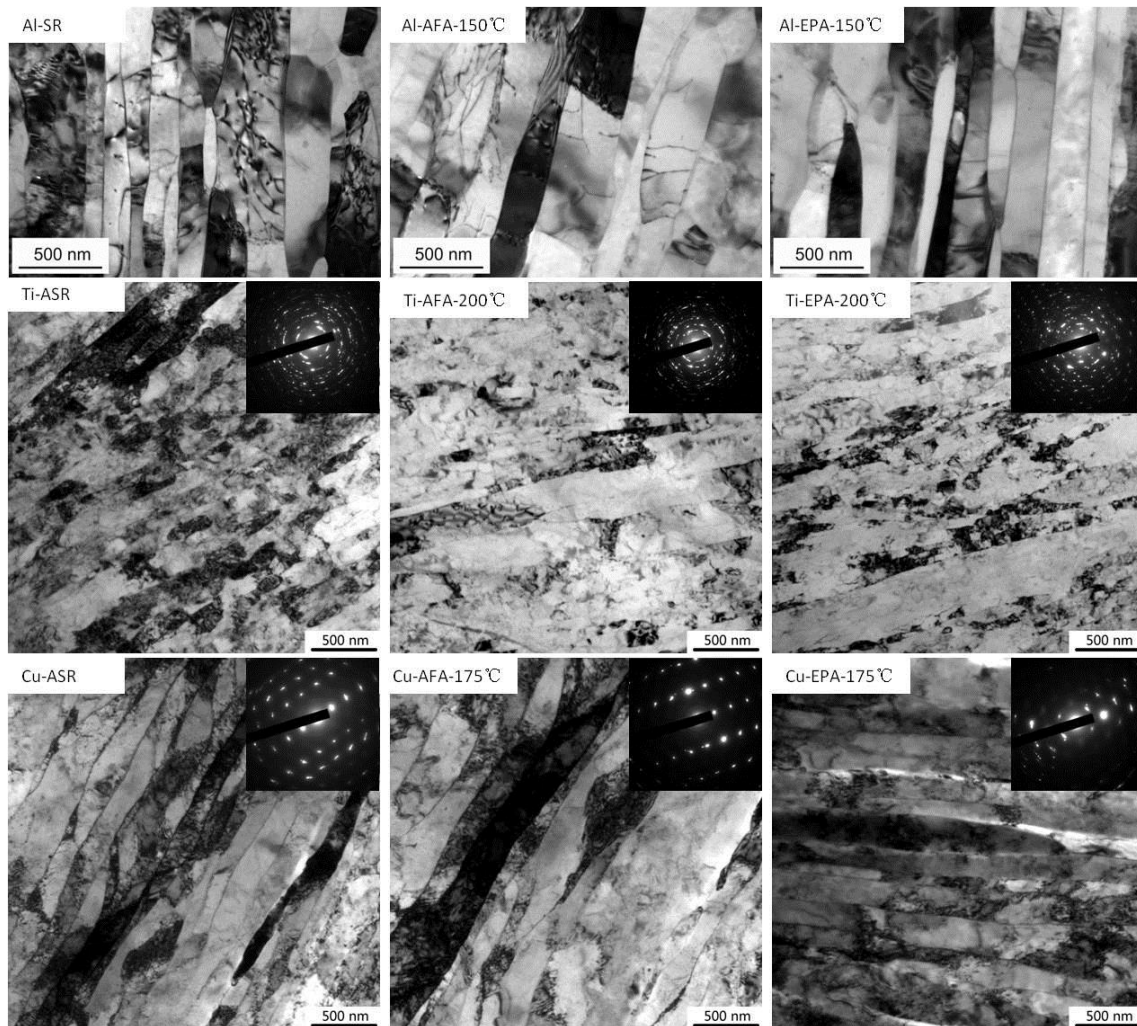


Fig. 3. TEM microstructures of Al-SR, Ti-ASR and Cu-ASR before or after AFA or EPA. The SAED showing that dominated high proportion of high angle boundaries or low-angle boundaries exist in SMG Ti and Cu respectively.

Although the morphological features in CP Al-SR and Ti-ASR remained the same, their statics underwent changes after annealing. It's observed that a moderate structural coarsening occurred in Al-AFA and Ti-AFA samples, with the lamellar boundary spacing increased by 27% (280 to 356 nm) and 13% (186 to 210 nm) respectively, while it is negligible in the EPA samples (increased by 11% and 2% respectively). However, the dislocation density measurements show a clear decrease after AFA or EPA; the extent of the reduction is about the same by AFA or EPA both for Al and Ti, but the rate is much higher by EPA than by AFA. In the case of Cu-ASR, only a tiny increase of lamellar boundary spacing and a negligible decrease of interior dislocation density occurred after

AFA or EPA at 175. This indicates that neither recrystallization nor obvious recovery process occurred in Cu-ASR during annealing at 175. However, fully recrystallizations occurred after EPA at 300, while it was still in the recovering process when AFA at 300, as shown in Fig. 4.

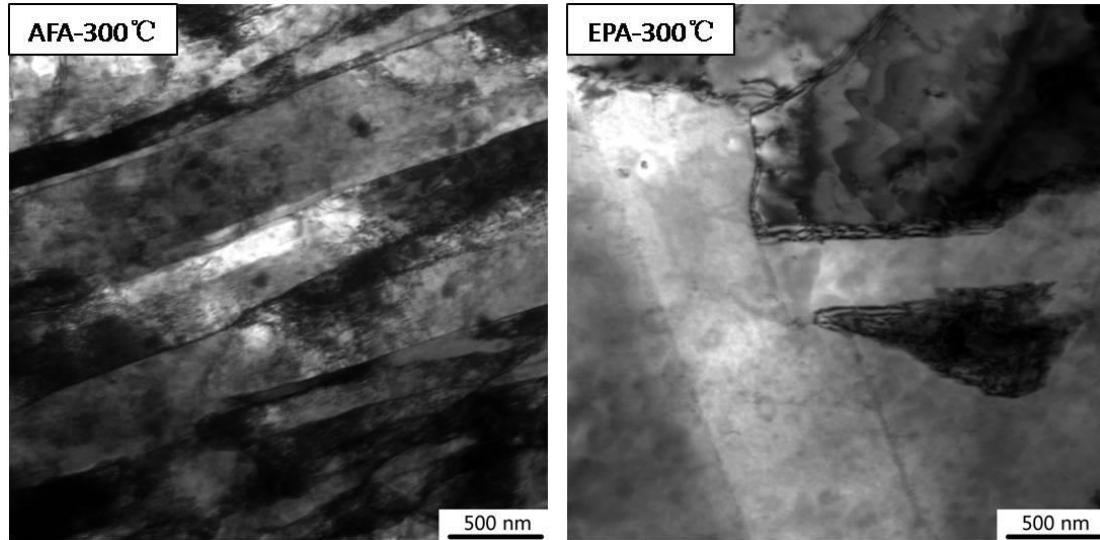


Fig. 4. TEM microstructures of annealed Cu at 300°C by both AFA or EPA.

Discussions

Strength and microstructural changes by annealing

The changes in microstructures and the resulting changes in mechanical strength follow the same trends when annealed either by AFA or EPA. Annealing induced hardening are both observed for heavy cold rolled Al and Ti, which are directly linked with the feature of the microstructural changes that substantial reduction in dislocation but with grain sizes nearly unchanged. This feature has led Huang et al to propose a dislocation source hardening mechanism for such abnormal hardening by annealing [2, 6]. However, softening was observed for Cu when the temperature is reaching 300°C. In this case, the softening is caused by recrystallization, indicating recovery is not active or suppressed.

Enhanced hardening rate in Al-SR and Ti-ASR and accelerated softening in Cu-ASR induced by EPA

The kinetics of the microstructural change are accelerated by EPA, seen from the fact that both the reduction in dislocation density and recrystallization

happen in a shorter time. The EPA-accelerated dislocation reduction is directly linked to the increased mobility of dislocations caused by the “electron wind” force on the dislocations [16]. As a result, the enhanced rate of dislocation density decrease during EPA causes the enhanced hardening rate in Al-SR and Ti-ASR where dislocation source-limited strengthening mechanism works.

The enhancement in recrystallization kinetics was not caused by changes in activation energy but mainly by the enhanced nucleation rate. Conrad et al suggested that the electric pulse had essentially no effect on the activation energy of the combined nucleation and growth of the new strain-free grains and the major effect of the electric pulse on the recrystallization is on the nucleation rate of new grains [22-24]. Moreover, these accelerated effects are much higher at the elevated temperatures [25].

The above accelerations in kinetics of microstructural change induced by the EPA treatment are not directly related to the annealing parameters. This can be seen from a comparison of annealing parameters (temperature and heating rate) between AFA and EPA. For instance, in the case of annealing process in CP Al-SR, the highest temperature for the EPA treatment was measured to be in the range of 120 - 150°C, with the average temperature well below 150°C for AFA. In this case, the maximum heating rate during EPA can be calculated to be 2.8°C/s by assuming adiabatic heating. For AFA, because of the small thickness of the tensile specimen (0.6 mm), it takes less than 2 min for the temperature of the specimen to reach the preset annealing temperature of 150°C after the sample is put into the furnace. This corresponds to an average heating rate of about 1°C/s, which is similar to the heating rate estimated for EPA. Thus the differences of thermal history between the two annealing processes can be neglected.

Tailoring microstructures by EPA treatment

Compared to AFA, the short time EPA treatment can change microstructures differently, to reduce the interior dislocation density rapidly but induce negligible grain growth. This suggests a novel annealing process for tailoring microstructures in a wider spectrum. It has been demonstrated that this

strategy works for Al and Ti in their heavy rolled state which are characterized by submicron lamellar structures with a large proportion of high-angle grain boundaries (~50%). However, it does not work for heavy rolled Cu; the reason might be due to the low proportion of high-angle grain boundaries (less than 10%), which in turn might be attributed to a stacking fault energy lower than those of Al and Ti. It remains to clarify if this strategy can be extended to a wider context, i.e. Al and Ti with wider features of microstructures and more materials.

Conclusions

1. The EPA treatment enhanced the hardening rate and the maximum strength in CP Al-SR and Ti-ASR due to the enhanced rate of dislocation recovery. While EPA accelerated the softening in Cu-ASR resulted from the premature occurrence of recrystallization.

2 EPA treatment led to the rapid decreases of interior dislocation density to the same level compared to AFA while with much less grain growth, suggesting a novel annealing process to tailor microstructures in a wider spectrum.

References

- [1]. Y. Estrin, A. Vinogradov. Extreme grain refinement by severe plastic deformation: A wealth of challenging science. *Acta Materialia*. 2013; 61: 782-817.
- [2]. N. Kamikawa, X. Huang, N. Tsuji, N. Hansen. Strengthening mechanisms in nanostructured high-purity aluminium deformed to high strain and annealed. *Acta Materialia*. 2009; 57: 4198-208.
- [3]. JR. Weertman Hall-Petch strengthening in nanocrystalline metals. *Materials Science and Engineering: A*. 1993; 166: 161-7.
- [4]. D. Jia, Y.M. Wang, K.T. Ramesh, E. Ma, Y.T. Zhu, R.Z. Valiev. Deformation behavior and plastic instabilities of ultrafine-grained titanium. *Applied Physics Letters*. 2001; 79: 611.

- [5]. X. Huang. Tailoring dislocation structures and mechanical properties of nanostructured metals produced by plastic deformation. *Scripta Materialia*. 2009; 60: 1078-82.
- [6]. X. Huang, N. Hansen, N. Tsuji. Hardening by annealing and softening by deformation in nanostructured metals. *Science*. 2006; 312: 249-51.
- [7]. N. Kamikawa, X. Huang, N. Hansen. Dislocation-Source Hardening in Nanostructured Steel Produced by Severe Plastic Deformation. *Materials Science Forum*. 2010; 638-642: 1959-64.
- [8]. R. Kapoor, A. Sarkar, R. Yogi, S.K. Shekhawat, I. Samajdar, J.K. Chakravartty. Softening of Al during multi-axial forging in a channel die. *Materials Science and Engineering: A*. 2013; 560: 404-12.
- [9]. Z.N. Yang, F.C. Zhang, Y.Y. Xiao, Z.G. Yan. Dynamic recovery: The explanation for strain-softening behaviour in Zr–2.3Nb alloy. *Scripta Materialia*. 2012; 67: 959-62.
- [10]. R. Valiev. The effect of annealing on tensile deformation behavior of nanostructured SPD titanium. *Scripta Materialia*. 2003; 49: 669-74.
- [11]. D. Terada, H. Houda, N. Tsuji. Effect of strain on “hardening by annealing and softening by deformation” phenomena in ultra-fine grained aluminum. *Journal of Materials Science*. 2008; 43: 7331-7.
- [12]. Y.M. Wang, S. Cheng, Q.M. Wei, E. Ma, T.G. Nieh, A. Hamza. Effects of annealing and impurities on tensile properties of electrodeposited nanocrystalline Ni. *Scripta Materialia*. 2004; 51: 1023-8.
- [13]. J.R. Bowen, P.B. Prangnell, Juul Jensen D, N. Hansen. Microstructural parameters and flow stress in Al–0.13% Mg deformed by ECAE processing. *Materials Science and Engineering: A*. 2004; 387-389: 235-9.
- [14]. N. Jia, X. Zhao, D. Song, M.H. Zhou, Y.D. Wang. On the anomalous hardening during annealing of heavily deformed f.c.c. metals. *Materials Science and Engineering: A*. 2010; 527: 1143-50.

- [15]. X. Huang, N. Kamikawa, N. Hansen. Strengthening mechanisms in nanostructured aluminum. *Materials Science and Engineering: A*. 2008; 483-484: 102-4.
- [16]. A.F. Sprecher, S.L. Mannan, H. Conrad. Overview no. 49 On the mechanisms for the electroplastic effect in metals. *Acta Materialia*. 1986; 37: 1145-62.
- [17]. L.B. Zuev, V.E. Gromov, L.I. Gurevich. The effect of electric current pulses on the dislocation mobility in zinc single crystals. *Phys stat sol (a)*. 1990; 121: 437-43.
- [18]. Z. Suo. Dislocation climb in the electron wind. *Mat Res Soc Symp Proc*. 1994; 338: 379-90.
- [19]. J.R. Bowen, P.B. Prangnell, D.J. Jensen, N. Hansen. Microstructural parameters and flow stress in Al-0.13% Mg deformed by ECAE processing. *Materials Science and Engineering: A*. 2004; 387: 235-9.
- [20]. C.Y. Yu, P.W. Kao, C.P. Chang. Transition of tensile deformation behaviors in ultrafine-grained aluminum. *Acta Materialia*. 2005; 53: 4019-28.
- [21]. N. Zhang. Master thesis. Shanghai Jiao Tong University. 2009.
- [22]. H. Conrad, Z. Guo, A.F. Sprecher. Effect of an electric field on the recovery and recrystallization of Al and Cu. *Scripta Materialia*. 1989; 23: 821-4.
- [23]. H. Conrad, N. Karam, S. Mannan, A.F. Sprecher. Effect of electric current pulses on the recrystallization kinetics of copper. *Scripta Materialia*. 1988; 22: 235-8.
- [24]. X.N. Du, S.M. Yin, S.C. Liu, B.Q. Wang, J.D. Guo. Effect of the electropulsing on mechanical properties and microstructure of an ECAPed AZ31 Mg alloy. *Journal of Materials Research*. 2011; 23: 1570-7.
- [25]. H. Conrad, N. Karam, S. Mannan. Effect of prior cold work on the influence of electric current pulse on the recrystallization of copper. *Scripta Materialia*. 1984; 18: 275-80.

STRESS RELAXION IN Ni_3Ge SINGLE CRISTALS WITH THE ANOMALOUS TEMPERATURE STRENGTHENING

V.A. Starenchenko, Yu.V. Solov'eva, S.V. Starenchenko

Tomsk State University of Architecture and Building, Solyanaya sq.2,

634003, Tomsk, RUSSIA

E-mail: star@tsuab.ru; sve-starenchenko@yandex.ru.

Abstract

This paper presents the results of a study of stress relaxation in Ni_3Ge single crystals with the $L1_2$ structure oriented along the [001] axis. The anomalous temperature dependence of the strain rate at relaxation has been determined.

Key words: creep, intermetallics, stress relaxation, a single crystal, temperature anomaly of the mechanical properties.

Introduction

Metal or alloy deformed under the influence of the static, dynamic loads or in creep and then left under the stress so that there will not be further change of its form and the total deformation remains constant demonstrates stress relaxation, e.i. the load required to maintain the constant state of the alloy will decrease over time.

Stress relation is used as the standard technology to obtain the value of the rate sensitivity being directly connected with the amount of activation volume in the course of thermoactivation analysis. The focus of attention is on the adjustment of activation volume values calculated using standard formulae of the thermoactivation analysis in order to obtain values more accurately reflecting the thermoactivated motion of the dislocation in a crystal. Efforts are focused on the methodological details in order to consider the impact of machine hardness and the deformaion strengthening of the material in the relaxation process.

Study on the change of the activation volume with the temperature, deformation, different temperature ranges (below the temperature peak anomaly above temperature peak anomaly) for different orientations of the deformation axis of single crystals and various kinds of slip (multiple, single, cubic) in alloys exhibiting an anomaly of the mechanical properties was not carried out. The values of the activation volumes and other characteristics are obtained for alloy Ni₃Al [1 - 4], other alloys of the same superstructure are not investigated in this respect. Alloy Ni₃Al mentioned above and alloy Ni₃Ge having received extensive information on the different types of deformation [5 - 17] appeared to be the most studied ones among alloys demonstrating temperature anomaly of the mechanical properties. Plastic behavior of alloys with the L1₂ superstructure in stress relaxation tests remains insufficiently researched. There are no data on changes of deformation rate in relaxation process and impact of temperature and stress on it.

Thus the aim of this paper is to examine the plastic behavior of single crystals of alloy Ni₃Ge under the stress relaxation in a wide range of temperatures and stresses. Therefore the analysis of creep curves, deformation rate in the process of stress relaxation was carried out. The effect of temperature and stress on creep rate of relaxation has been studied.

Experimental details

Single crystals of the Ni₃Ge were grown using a Chokhralski technique in a purified Ar atmosphere with the gradient zone movement rate of 1 mm/min. Samples with the size of 3.0×3.0×6.0 mm³ were cut from single crystal ingots using the spark erosion method. The facet orientations were determined by XRD Laue method. The samples were homogenized at T=953° C for 48 hrs, followed by furnace cool down to room temperature (T_{room}). The uniaxial compression tests were carried out with the constant rate of 3.3×10⁻⁴s⁻¹ using an Instron type test machine in the 4.2-1000 K temperature interval in vacuum under the pressure of 10⁻² Pa. The shear stresses in the octahedral slip planes were

calculated using the $\tau=m\times\sigma$ relationship, where m is the Schmid factor of the primary octahedral slip system, σ is flow stress. The critical resolved shear stress, τ , was considered equal to the flow stress value at $\varepsilon=0.2\%$. The stress (τ) - strain (ε) dependencies were obtained at temperatures of 4.2 K, 77 K, 293 K, 523 K, 673 K, 873 K. 10-12 samples were tested at each temperature. To obtain a 3-dimensional picture of the dislocation structure in the investigated alloy, different foil sections were examined, particularly in [111], [100], [110] and other orientations near these zone axes. The foils were cut using spark erosion to thickness of 0.3-0.4 mm and mechanically thinned down to 0.1 mm. Final thinning was done in electrolyte. The dislocation structure was studied in electron microscope, at accelerating voltage of 125 kV, with a goniometer capable of up to $\pm 30^\circ$ tilt angle. The scalar dislocation density and straight dislocation density were measured by the secant method. The active slip systems were identified using slip trace analyses.

Research results

Relaxation curves

The stress relaxation tests were carried out within the frame of the work. The obtained relaxation curves for different temperatures of deformation and the first 300 seconds are shown in Fig. 1 and Fig. 2.

The experimental relaxation curves show a drop of stress over time. The rate of stress decrease having maximum value at the first seconds of relaxation process gradually decreases over time. Such relaxation is well marked at temperatures close to room temperature. The depth of stress relaxation decreases while the temperature of study increases from 293 K to 573 K (Fig. 1). Regardless of the temperature the higher the strain value the greater the depth of relaxation is. However the depth of relaxation is not monotonous with temperature increase. When the temperature increases up to 673 K and above the rapid decrease of the stress during relaxation has been observed (Fig. 2). The significant dependence of stress on deformation degree was revealed also.

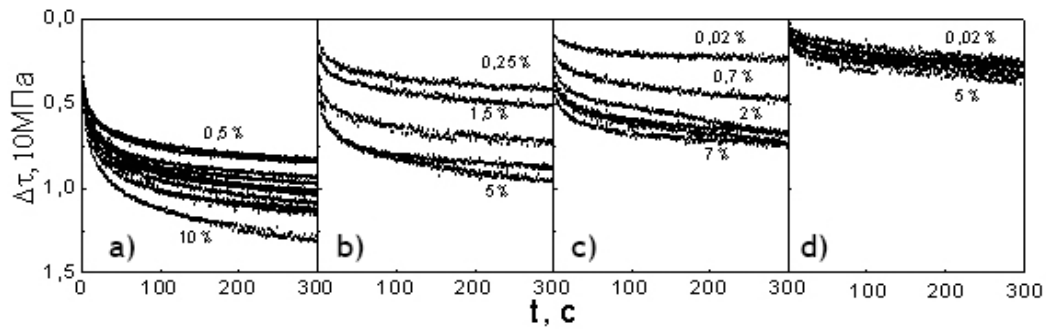


Fig. 1. Alloy single crystals Ni_3Ge relaxation curves of [001] orientation tested at different temperatures: (a) 293 K, (b) 373 K, (c) 473 K (d) 573 K.

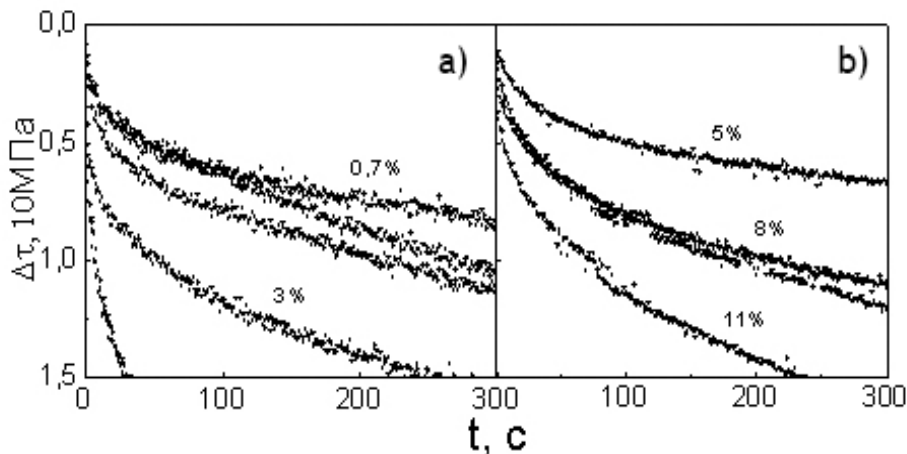


Fig. 2. Relaxation curves of single crystals of alloy Ni_3Ge of [001] orientation tested at different temperatures: (a) 673 K, (b) 773 K.

Strain rate in relaxation

Differentiation of relaxation curves - $\tau(t)$ gives the chance to receive the dependences of the deformation rate on time $\dot{\varepsilon}(t)$ for different applied stresses and the temperatures of the test. Relaxation curves obtained at different temperatures but having the same meaning of the primary stress from which the relaxation started were considered to determine the effect of temperature on creep rate at relaxation. The analysis illustrated in Figure 3 showed that the temperature increase from 293 to 573K resulted in anomalous temperature dependence on creep rate under stress relaxation. Especially significant is the decrease of strain rate with temperature being appeared in the first 20-40 seconds of relaxation. It is at the beginning of relaxation when deformation rate is high and comparable with the rate of active deformation anticipating the relaxation. For relaxation time above 100 seconds, deformation rate becomes

very low of 10^{-8} - 10^{-9} s $^{-1}$ at all temperatures, and there is no effect of temperature. The temperature increase up to 673 K leads to normal temperature dependence, i.e. leads to the increase of creep rate with temperature (Fig. 4). That rate increase of stress fall occurring with temperature rise is connected with the phenomenon of recovery.

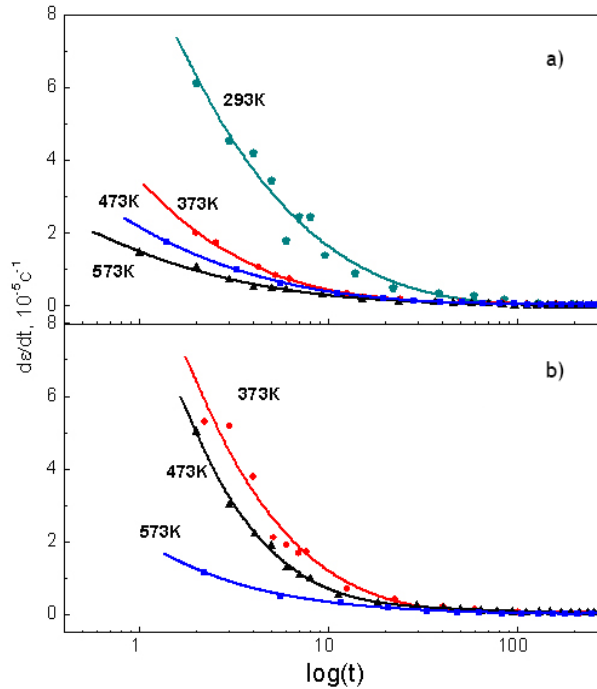


Fig. 3. The influence of temperature on strain rate in stress relaxation in single crystals of Ni₃Ge of [001] orientation having equal primary applied stress: (a) $\tau_1=300$ MPa, (b) $\tau_1=400$ MPa.

Thus, rapid strain rate decrease at temperature rise from room temperature to 373 K is characteristic for Ni₃Ge and the transition to normal temperature dependence for single crystals Ni₃Ge is at $T > 573$ K. Normal temperature dependence on strain rate starts with temperature of $0.4T_{\text{melt}}$. The obtained results of temperature behavior of strain rate in stress relaxation, i.e. the observed stages of value change in strain rate in stress relaxation with temperature change, are correlated with the temperature dependence behavior of anomalous component of stress jump in strain rate variation [18]. Therefore, it is possible to believe that mechanisms of anomaly behavior of strain rate and mechanisms influencing the change character of strain rate in relaxation are the same.

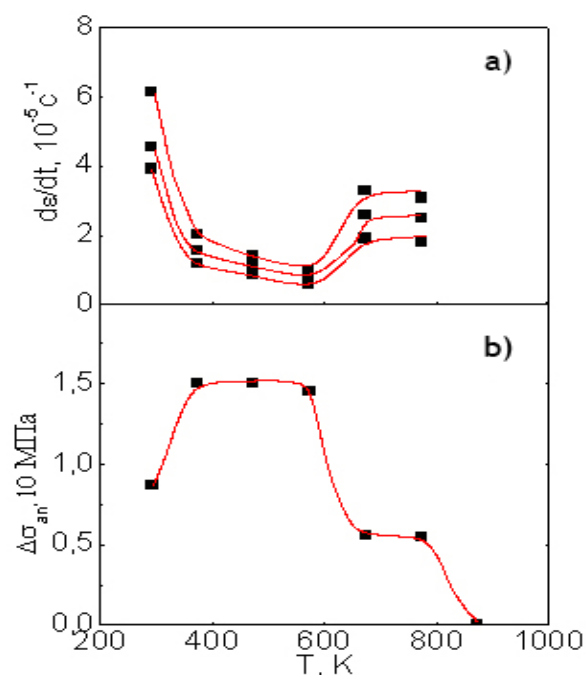


Fig. 4. Temperature dependence on deformation rate in stress relaxation of single crystals of Ni_3Ge of [001] orientation at the first three seconds of relaxation (a). Temperature dependence of anomalous component of stress jump ($\Delta\sigma_{an}$) at strain rate variation of (5%) [13] (b).

Thus, the results of the experiment given in the paper testify that self-locking mechanisms exist not only in experiments with active load, but play a significant role in stress relaxation experiments reducing the mobility of dislocations and strain rate with the temperature rise.

References

- [1]. J.R. Nicholls, R.D. Rawlings. Phys. Stat. Sol. (a). 1978. V.49. P. K85-K89.
- [2]. J. Bonneville, P. Spatig, J.L. Martin. Solid State Phenomena. 1994. V. 35-36. P. 461-466.
- [3]. K.J. Hemker, W.D. Nix, M.J. Mills Acta Metall. Mater. 1991. № 8. P. 1901.
- [4]. A. Orlova, J. Bonneville, P. Spatig. Materials Science and Engineering. A. 1995. V. 191. P. 85-89.
- [5]. V.A. Starenchenko, E.V. Kozlov, Yu.V. Solov'eva, Yu.A. Abzaev, N.A. Koneva. Materials Science and Engineering. A. 2008. 483-484. № 1-2. P. 602-606.

- [6]. Yu.V. Solov'eva, M.V. Gettinger, S.V. Starenchenko, V.A. Starenchenko. Russian Physics Journal. 2009. 52. № 4. P. 390-397.
- [7]. Yu.V. Solov'eva, V.A. Starenchenko, S.V. Starenchenko, M.V. Gettinger, T.A. Shalygina. Steel in translation. 2009. № 12. P. 1043-1048.
- [8]. Yu.V. Solov'eva, S.V. Starenchenko, V.A. Starenchenko et al. Izv. Vyssh. Uchebn. Zaved. Chern. Met. 2009. № 12. P. 28.
- [9]. Yu.V. Solov'eva, S.V. Starenchenko, M.V. Gettinger, V.A. Starenchenko. Izv. Vyssh. Uchebn. Zaved., Fiz. 2009. № 9/2. P. 98-107.
- [10]. Yu.V. Solov'eva, S.V. Starenchenko, V.A. Starenchenkoю Fundament. Probl. Sovr. Materialoved. 2009. 6. № 3. P. 41-54.
- [11]. Yu.V. Solov'eva, S.V. Starenchenko, V.A. Starenchenko. Bulletin of the Russian Academy of Sciences:Physics. 2011. **75**. № 2. P. 202–206.
- [12]. V.A. Starenchenko, O.D. Pantyukhova, S.V. Starenchenkoю Fiz. Tverd. Tela. 2002. 44. № 5. P. 950.
- [13]. V.A. Starenchenko, O.D. Pantyukhova, S.V. Starenchenkoю Physics of the Solid State. 2002. 44. № 5. P. 994-1002.
- [14]. V.A. Starenchenko, O.D. Pantyukhova, Yu.V. Solov'eva, S S.V. Starenchenko. Izv. Vyssh. Uchebn. Zaved., Fiz. 2009. № 9/2. P. 118.
- [15]. Yu.V. Solov'eva, S.V. Starenchenko, O.D. Pantyukhova, V.A. Starenchenkoю Bulletin of the Russian Academy of Sciences. Physics. 2012. 76. № 7. P. 788-781.
- [16]. Yu.V. Solov'eva, V.A. Starenchenko, B.I. Burtsev, M.V. Gettinger, T.A. Kovalevskaya. Izv. RAN. Seriya Fizicheskaya. 2006. 70. № 11. P. 1683-1685.
- [17]. Yu.V. Solov'eva, S.V. Starenchenko, V.A. Starenchenko. Bull. Russ. Acad. Sci. Phys. 2011.75. № 2. P. 202.
- [18]. Yu.V. Solov'eva, M.V. Gettinger, V.A, Starenchenko, S.V. Starenchenko. Fundament. Probl. Sovr. Materialoved. 2012. 9. № 4/2. P. 646-653.

INVESTIGATION ON THE AGGLOMERATION BEHAVIOR OF PRIMARY SILICON IN HYPEREUTECTIC Al-Si ALLOY MELT UNDER ELECTROMAGNETIC VIBRATION

Zhang Tengfei^{1,2} Li Qiulin^{1,*}, Han Yecong^{1,2}, Gao Minrui^{1,2}, Liu Wei²

¹ Advanced Materials Institute, Graduate School at Shenzhen, Tsinghua University, 518055, Shenzhen, PR China.

² Laboratory of Advanced Materials, School of Materials Science and Engineering, Tsinghua University 100084, Beijing, PR China.

* Corresponding author at: Room 304A, Building J, Tsinghua Campus, The University Town, 518055, Shenzhen, China. Tel.: +86 755 26036424; fax: +86 755 26036424. E-mail: liql@sz.tsinghua.edu.cn

Abstract

The collision and agglomeration behavior of primary silicon particles in hypereutectic Al-Si alloy was investigated by imposing an electromagnetic vibration induced by simultaneously applying an alternating electric field and a stationary magnetic field. The results showed that the silicon particles collided with each other and agglomerated into clusters with the application of the electromagnetic vibration. With the increase of the current and the magnetic field intensity, the number of silicon particles in one cluster and the sizes of the clusters decreased. The clusters also became compacter. Increase of frequency had nearly no effect on the compacting degree of the clusters. The sizes of the clusters increased with an increasing frequency no more than 200 Hz, while not increased with an increasing frequency not less than 400Hz.

Key words: hypereutectic Al-Si alloy; primary silicon particles; collision and agglomeration; electromagnetic vibration; cluster

Introduction

The non-metallic inclusions in the metal have harmful effects on the metal's strength, elongation, toughness, corrosion resistance and service life [1]. With the increasing need of high purity steel and non-ferrous metal products,

there are stricter requirements on the controlling of the size and content of the inclusions in the metal. There are some conventional purification methods used to purify the melt, such as sedimentation, flotation and filtration. But they all have limited ability to remove the small size inclusions [2-3]. Electromagnetic purification, as a method using the directional electromagnetic force to cause directional migration of the non-metallic inclusions, could remove the inclusions with a similar density comparing with the melt. It has a high efficiency to remove large inclusion particles but its efficiency to reomove the small inclusion is still very low. One feasible route is to agglomerate the small inclusions into clusters of a large size, which is easy to be removed.

Miki Yuji et al. studied the buoyancy effect of a rotating magnetic field on the inclusion particles in the steel melt. The results showed that a rotating magnetic field can promote the collision and agglomeration of the inclusion particles in the steel melt, thus accelerated the flotation behavior of the inclusion particles with a smaller density than the surrounding melt [8]. He et al. found that the combined magnetic field consisting of a traveling magnetic field and a rotating magnetic field can promote the primary silicon particles to agglomerate into clusters in the hypereutectic Al-Si alloy melt, having a better separating effect than any single magnetic field [9-10].

Numerous studies on the effect of the electromagnetic vibration on metal mainly focused on the areas such as refining of organizations and grain [11-14]. But the study on its effect on the movement of non-metallic inclusions in metallic melt is not deep enough. Radjai et al. have pointed out that the primary silicon particles in the hypereutectic Al-Si Alloy locally agglomerated during the solidification process under electromagnetic vibration [15], but did not have a further study on this agglomeration behavior. In this study, the primary silicon particles in the Al-20%Si alloy melt are regarded as non-metallic inclusions need removing. The collision and agglomeration behavior of primary silicon particles under different electromagnetic vibration parameters was investigated.

Experimental apparatus and methods

Fig. 1 shows the schematic view of the experimental apparatus. Electromagnetic vibration is induced by the simultaneous application of an alternating electric field and a stationary magnetic field. The material used in our experiment is Al-20%wt Si and the chemical composition is shown in Table 1. The Al-Si rod sample is fixed in a quartz tube by two graphite electrodes and placed in the experimental apparatus. The sample is then heated to 730°C and kept at this temperature for 4 minutes. Then the magnetic and electric fields are imposed on the sample simultaneously and the cooling air is blown out to cool the sample to room temperature at a constant cooling rate of 30 °C/s. Finally, the microstructure of the samples is observed after polishing carefully.

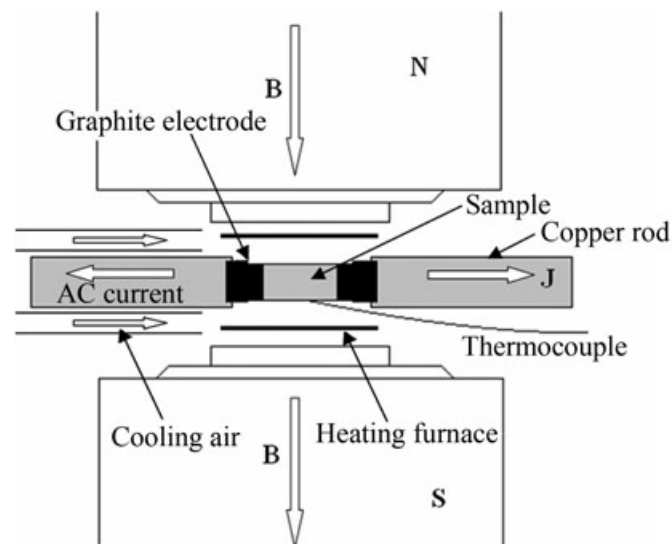


Fig. 1. Schematic view of the experimental apparatus (top view).

Table 1. Chemical composition of hypereutectic Al-Si alloy (wt%).

Si	Cu	Fe	Mg	Zn	Ti	Al
18~20	<0.1	<0.1	<0.1	<0.1	<0.1	balance

Results

Effect of current on the agglomeration behavior of primary silicon

Figure 2 shows the macrostructure and microstructure of the samples under different currents. As is seen in figure 2(a, b), primary silicon particles distribute uniformly and separately on the upper part of the sample without any magnetic

field. As is shown in figure 2(c, d), primary silicon particles agglomerate into loose clusters under the condition that $B=0.43T$, $I=20A$. The clusters are of large size and include many silicon particles. As is shown in figure 2(e, f), when the current increases to 60A, the clusters distribute uniformly on the cross-sections of the sample. The silicon particles in the clusters agglomerate more closely and the sizes of the clusters become smaller. As is shown in figure 2(g, h), when the current increases to 100A, both the number of silicon particles in one clusters and the sizes of clusters continue to decrease. The silicon particles also agglomerate more closely than those under the condition that $I=60A$.

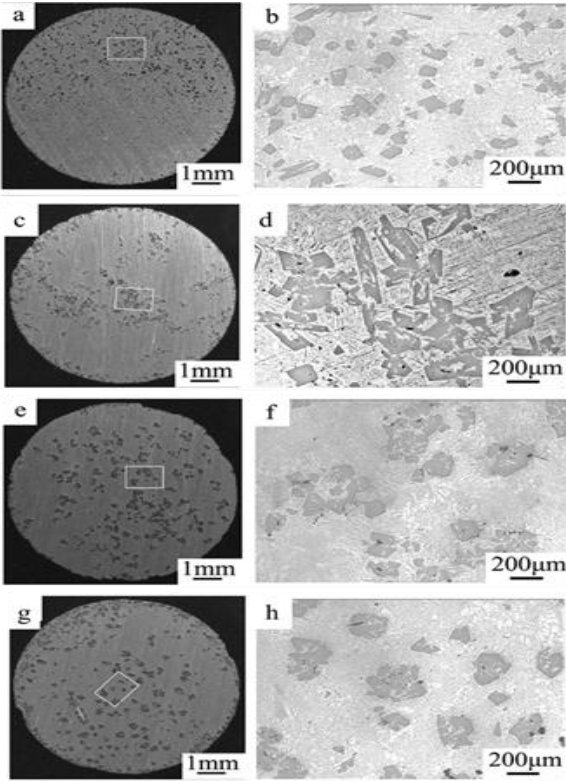


Fig. 2. the macrostructure and microstructure of the samples under different current ($f=50Hz$).

- | | |
|--------------------------------|------------------------------|
| (a) (b) without magnetic field | (c) (d) $I=20A$, $B=0.43T$ |
| (e) (f) $I=60A$, $B=0.43T$ | (g) (h) $I=100A$, $B=0.43T$ |

Effect of magnetic field intensity on the agglomeration behavior of primary silicon

Figure 3 shows the macrostructure and microstructure of the samples under different magnetic field intensity. When the magnetic field intensity is 0.18T

(Fig. 3 a, b), the silicon particles distribute uniformly on the transverse section of the sample. Metallographic figure shows that the silicon particles have agglomerated in some degree, but the clusters including many silicon particles are loose and large. When the magnetic field intensity increases to 0.31T (Fig. 3 c, d), the silicon particles also distribute uniformly on the transverse section of the sample on a macroscopic scale. It can be seen from the microstructure that the silicon particles in the clusters agglomerate more closely and the sizes of the clusters become smaller. With increasing the magnetic field intensity to 0.43T (Fig.3 e and f), the silicon particles agglomerate much more closely. Both the number of silicon particles in one cluster and the sizes of clusters continue to decrease. When the magnetic field intensity increases up to 0.55T (Fig. 3 g, h), the number of silicon particles in one cluster and the clusters size decrease continuously, and very compactable silicon aggregations are obtained as expected.

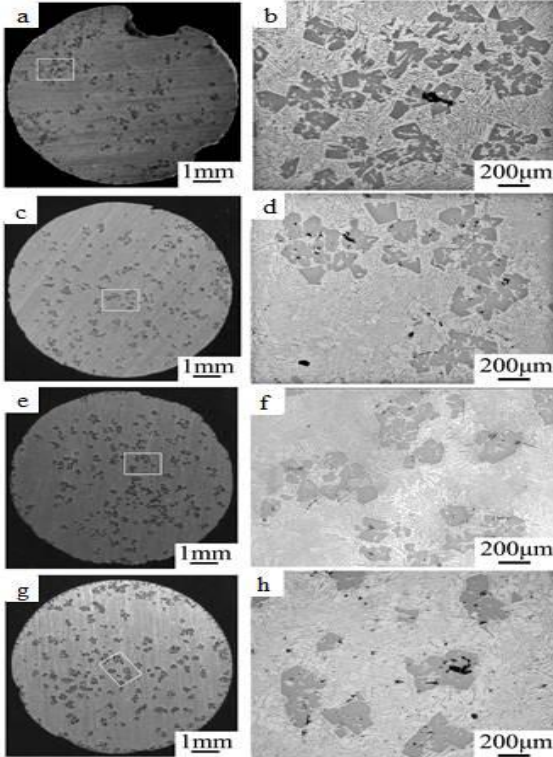


Fig. 3. the macrostructure and microstructure of the samples under different magnetic field intensity $f=50\text{Hz}$.

- (a) (b) $I=60\text{A}$, $B=0.18\text{T}$ (c) (d) $I=60\text{A}$, $B=0.31\text{T}$
(e) (f) $I=60\text{A}$, $B=0.43\text{T}$ (g) (h) $I=60\text{A}$, $B=0.55\text{T}$

Effect of frequency on the agglomeration behavior of primary silicon

Figure 4 shows the macrostructure and microstructure of the samples under different frequency. When the frequency is 50Hz (Fig. 4 a, b), the silicon particles distribute uniformly on the transverse section of the sample and agglomerate into clusters, which can also be observed when the frequency increases to 100Hz (Fig. 4 c, d). With increasing the frequency up to 200Hz (Fig. 4 e, f), the distribution of silicon clusters becomes looser and the number of silicon particles in one cluster increases compared with that of 50Hz and 100Hz while the compacting degree of primary silicon particles in the clusters changes a little. When the frequency is up to 400Hz (Fig. 4 g, h), the sizes of clusters and the number of silicon particles in one cluster have not obviously changed compared with that of 200Hz. The compacting degree of primary silicon particles in the clusters also changes a little.

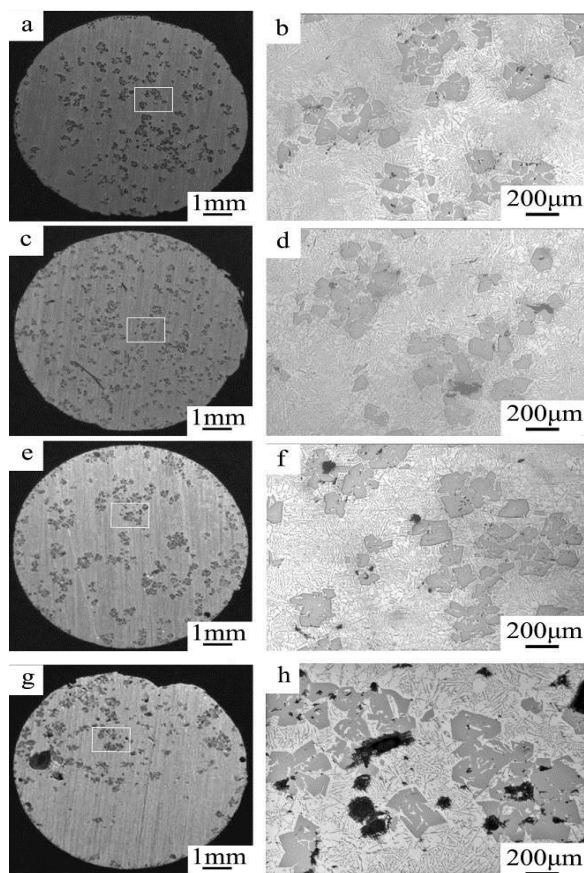


Fig. 4. the macrostructure and microstructure of the samples under different frequency ($I=60A$, $B=0.43T$).

(a) (b) $f=50Hz$ (c) (d) $f=100Hz$ (e) (f) $f=200Hz$ (g) (h) $f=400Hz$

Discussions

An alternating electric field (J) and a stationary magnetic field (B) are applied to the sample at the same time during the solidification of Al-Si alloy melt, resulting in an electromagnetic vibration force which has the same frequency with the alternating electric field. The electromagnetic vibration force can be expressed as the non-metallic primary silicon particles, whose electronic conductivity is at nearly zero, are affected by an electromagnetic extrusion force with an opposite direction to the electromagnetic vibration force. The electromagnetic extrusion force on a particle of a diameter d can be expressed as where d represents the diameter of the particle.

It can be seen that the electromagnetic extrusion force on a particle is proportional to the volume and the electromagnetic vibration force. Thus a large particle has the large electromagnetic force, resulting in a large velocity. Different particles of different sizes have different velocities. According to the model by Saffman, the possibility of collision is improved by the velocity gradient between the particles. In addition, primary silicon particles under the vibrating magnetic field may move in different directions, also improving the collision possibility.

It is also clear that the electromagnetic vibration force increases with the increase of the current when the stationary magnetic field intensity is fixed. The increase of the electromagnetic vibration force makes the electromagnetic vibration extrusion increase, resulting in the increase of velocity gradient between silicon particles. So the agglomeration behavior of particles is more obvious with the increase of current. The electromagnetic extrusion force will also increase with the increase of the stationary magnetic field intensity when the current is fixed, resulting in the larger velocities of the primary silicon particles. The larger velocities improve the collision possibility of particles of different sizes, promoting them to agglomerate into clusters.

Under the electromagnetic vibration, a large particle has a large velocity because of the large electromagnetic extrusion force. Particles of different sizes

have different velocities, which causes the velocity gradient and collision behavior between the particles. The electromagnetic extrusion force on a particle increases with the increase of current and the stationary magnetic field intensity, so the particle has a larger velocity, promoting the behavior of collision and agglomeration of particles. Particles with larger velocities agglomerate into clusters more closely since they have enough moving energy to overcome the resistance force from the melt [17]. So the clusters are closer with the increase of current and the stationary magnetic field intensity.

Electromagnetic vibration promotes the collision and agglomeration behavior while the vibration electromagnetic extrusion force and vibration flow can also broke the silicon particles which have agglomerated into clusters [18-19]. So the number of silicon particle in one cluster and the sizes of clusters will decrease with the increase of the stationary magnetic field intensity.

The frequency of electromagnetic vibration has no relationship with the electromagnetic vibration force, so the compacting degree of the clusters in the melt has nearly no change with the increase of frequency.

The vibration times of primary silicon particles increases with the increase of the frequency of electromagnetic vibration, so the times of collision increase and there are more particles colliding and agglomerating with each other. It is obvious that the sizes of clusters and the number of primary silicon particles in one clusters increase with the increase of frequency. However, the electromagnetic vibration force also increase with the increase of the sizes of the clusters and electromagnetic vibration has a dispersing effect on the clusters in which primary silicon particles agglomerate not very closely, so the clusters will not continue to grow when they reach a constant size.

Conclusions

The effect of current, magnetic field intensity and frequency on the agglomeration behavior of primary silicon in hypereutectic Al-Si alloy melt is investigated, and the following results are obtained. With the increase of the current and magnetic field intensity, the number of silicon particles in one

cluster and the sizes of the clusters decrease and the clusters becomes compacter. With the increase of the frequency, the compacting degree of primary silicon particles in the clusters changes a little. When the frequency is lower than 200Hz, the number of silicon particles in one cluster and the sizes of the clusters increase with the increase of the frequency. But it does not continue to increase when the frequency increases to 400Hz.

Acknowledges

This research was supported through grants from the National Nature Science Foundation of China (no. 50904042).

References

- [1]. FU Gao-sheng, Kang Ji-xing, Chen Wen-zhe, Qian Kuang-wu. Interactive mechanism between inclusions and hydrogen in molten aluminum [J]. The Chinese Journal of Nonferrous Metals, 1999, 95(1): 51-56.
- [2]. Zheng Xian-Shu, LI Zhao-xia, Wang Yi-cheng. Experimental study of concavity of large EMC slab [J]. Science and Technology of Advanced Materials, 2001, 2: 113-116.
- [3]. FU Gao-sheng, Chen Wen-zhe, Qian Kuang-wu. Synthetical technique of high-efficient melt-treatment of aluminum and its effect. The Chinese Journal of Nonferrous Metals, 2002, 12(2): 269-274.
- [4]. EL-Kaddah N. A comprehensive mathematical model of electromagnetic separation of inclusion in molten metals [C].Industry Applications Society Annual Meeting, 1988., Conference Record of the 1988 IEEE. IEEE, 1988: 1162-1167.
- [5]. WU Jia-xiong, Ren Zhong-ming, Zhang Bang-wen, Zhong Yun-bo, Deng Kang. Electromagnetic purification of aluminum alloy melts only by alternating current [J]. The Chinese Journal of Nonferrous Metals, 2004, 14(3): 354-358.
- [6]. XU Zhen-ming, LI Tian-xiao, Zhou Yao-he. Continuous Removal of Nonmetallic Inclusions from Aluminum Melts by Means of Stationary Electromagnetic Field and DC Current [J]. Metallurgical and Materials Transactions A, 2007, 38(5): 1104-1110.

- [7]. Shu Da, Sun Bao-de, Li Ke, LI Tian-xiao, XU Zhen-ming, Zhou Yao-he. Continuous separation of non-metallic inclusions from aluminum melt using alternating magnetic field [J]. *Materials Letters*. 2002, 55:322-326.
- [8]. Y. Miki, H. Kitaoka, T. Skuraya, T. Fujii. Mechanism for separating inclusions from molten steel stirred with a rotating magnetic field [J]. *ISIJ International*. 1992, 32:142-149.
- [9]. HE Yan-Jie, LI Qiu-Lin, LIU Wei. Effect of combined magnetic field on the eliminating inclusions from liquid aluminum alloy. *Materials Letters [J]*, 2011, 65 (8):1226.
- [10]. HE Yan-jie, LI Qiu-lin, Liu Wei. Separating Effect of a Novel Combined Magnetic Field on Inclusions in Molten Aluminum Alloy [J]. *Metallurgical and Materials Transactions B*, 2012, 43(5): 1149-1155.
- [11]. A. Radjai, K. Miwa. Structural refinement of gray iron by electromagnetic vibrations [J]. *Metallurgical and Materials Transactions A*, 2002, 33(9): 3025-3030.
- [12]. C. Vives. Effects of forced electromagnetic vibrations during the solidification of aluminum alloys: Part I. Solidification in the presence of crossed alternating electric fields and stationary magnetic fields [J]. *Metallurgical and Materials Transactions B*, 1996, 27(3): 445-455.
- [13]. C. Vives. Effects of forced electromagnetic vibrations during the solidification of aluminum alloys: Part II. solidification in the presence of colinear variable and stationary magnetic fields [J]. *Metallurgical and Materials Transactions B*, 1996, 27(3): 457-464.
- [14]. YU Jian-bo, Ren Zhong-Ming, Deng Kang, Ren Wei-Li, Li Xi, Wang Jun. Effects of simultaneously imposing high magnetic field and alternative current on solidification structures of pure aluminum [J]. *The Chinese Journal of Nonferrous Metals*, 2007(1): 92-97.
- [15]. A. Radjai, K. Miwa, T. Nishio. An investigation of the effects caused by electromagnetic vibrations in a hypereutectic Al-Si alloy melt [J]. *Metallurgical and Materials Transactions A*, 1998, 29(5): 1477-1484.

- [16]. D. Leenov, A. Kolin. Theory of electromagnetophoresis. I. Magnetohydrodynamic forces experienced by spherical and symmetrically oriented cylindrical particles [J]. Journal of Chemical Physics, 1995, 22(4): 683
- [17]. Lu De-Hong, Jiang Ye-Hua, Guan Gui-Sheng, Zhou Rong-Feng, Li Zhen-Hua, Zhou Rong. Refinement of primary Si in hypereutectic Al–Si alloy by electromagnetic stirring [J]. Journal of Materials Processing Technology, 2007, 189: 13-18.
- [18]. I. Grant, A. Klyukin, G. Gerbeth. Instability of the melt flow in VGF growth with a traveling magnetic field [J]. Journal of Crystal Growth, 2009, 311: 4255-4264.
- [19]. S. Mckee, R. Watson, J.A. Cuminato, P. Moore. Particle-tracking within turbulent cylindrical electromagnetically-driven flow [J]. International Journal of Numerical Method Fluids, 1999, 29:59-74.

FEATURES OF ELECTROPLASTIC DEFORMATION AND ELECTROPULSE TREATMENT FOR TiNi ALLOYS

V. Stolyarov, A.A. Blagonravov

Institute of Machines Science, Russian Academy of Sciences, Maly
Kharitonievsky Lane, 4, Moscow, 101990, Russia.

E-mail: vlstol@mail.ru

Abstract

The influence of the combined action of severe plastic deformation (SPD) and pulse current on the microstructure and mechanical behaviour of TiNi alloys in austenitic and martensitic states is investigated. The dependence of the electroplastic effect on the initial phase composition of the alloys is demonstrated. It is established that electropulse treatment (EPT) after SPD

promotes the acceleration of stress relaxation during recovery, polygonization and recrystallization of deformed TiNi alloys.

Keywords: strength, ductility, deformability, current, structure

Introduction

The sequential or simultaneous action of plastic deformation and electric current in different alloys, including shape memory TiNi alloys, leads to a number of interesting phenomena. An increase of deformability, suppression or acceleration of phase transformations, formation of nano- or ultrafine-grained structure and improvement of mechanical and functional properties can be observed during the simultaneous action of electric current and deformation [1, 2]. The influence of the initial phase composition has been investigated during electroplastic rolling (EPR) in martensite and austenite states. It has been shown recently that conventional post-deformation annealing for stress relaxation or recrystallization can be substituted by electropulse treatment (EPT) [3, 4]. Therefore, we investigated in this work the possibility of applying a pulse current instead of thermal annealing for the deformed shape memory TiNi alloy.

Experimental procedure

Investigations of EPR were performed on $\text{Ti}_{50-x}\text{Ni}_{50+x}$ ($x=0; 0.7; 0.8$) rods $\text{Ø}6.1 \times 135$ mm after quenching from 800 °C in water. Multipass EPR was executed with the simultaneous introduction of a unipolar pulse current with density $j=100$ A/mm², pulse duration 1×10^{-4} s and frequency of 10³ Hz. Accumulated strain and deformability were estimated using the value of true strain $e = \ln t_i / t_f$, where t_i and t_f are the initial and final strip thickness, respectively. For the study of EPT processing, $\text{Ti}_{49.3}\text{Ni}_{50.7}$ alloy was used in the form of a $0.41 \times 10 \times 50$ mm³ strip processed by the EPR technique with $e=1.5$ [5]. EPT was performed at current density of $j=100$ A/mm² with exposure duration $t=1-10$ s. Structure examinations and mechanical tests were executed on samples after annealing at temperatures of 450 and 600 °C. At these temperatures appreciable structural changes like stress relaxation, recrystallization or ageing

took place. The microstructure was investigated by transmission electron microscopy (TEM) using a JEM-2000 microscope at an acceleration voltage of 100 kV. The mechanical behaviour was studied by tension with a rate of 0.5 mm/min by MTS testing machine (without a current) and horizontal set IM-5081 (with a single and multipulse current). Microhardness was evaluated on a PMT-3 device at load of 100 g.

Electroplastic rolling

Data presented in Table 1 show that cold rolling in the presence of a pulsed current for both alloys increases the deformability 6-10 times in comparison with cold rolling without a current. Thus the deformability of $\text{Ti}_{50.0}\text{Ni}_{50.0}$ alloy with a current and without a current is higher than for the $\text{Ti}_{49.2}\text{Ni}_{50.8}$ alloy. Application of a pulse current allows the deformation of stoichiometric alloy up to $e > 3.6$. Most probably, the raised deformability of an alloy in the martensite state is connected with the twinning deformation mechanism of B19' phase. The additional twin's formation in B2 during the reversal martensite transformation may be important. Most probably it also makes an additional contribution to the deformability [6] since the twin grain boundaries are very sensitive to the influence of temperature and impurities.

Table 1. Deformability of alloys at rolling with and without current

Alloy	Phase composition	True strain without current, e	True strain with current, e
$\text{Ti}_{49.2}\text{Ni}_{50.8}$	austenite	0.1	1.2
$\text{Ti}_{50.0}\text{Ni}_{50.0}$	martensite	0.6	$> 3.6^*$

*- real value limited by the minimal calibre size

Microhardness measurements during EPR showed significant differences in both the microhardness level and the type of deformation strengthening of alloys (Fig. 1). $\text{Ti}_{49.2}\text{Ni}_{50.8}$ alloy has a much higher level of microhardness and deformation strengthening during EPR. This is explained by the presence of additional Ni atoms in a solid solution in the $\text{Ti}_{49.2}\text{Ni}_{50.8}$ alloy and different

deformation mechanisms in the austenite grains and martensite plates. The essential contribution to the hardening also brings the elastic modulus, which for austenite phases is almost two times higher than that for the martensite [7]. More intensive hardening of an off-stoichiometric alloy during EPR can be connected with the hardening of the matrix by Ti_3Ni_4 particles [8]. They precipitated due to local heating during the passing of current. Since the microstructure of deformed alloys is not uniform, post-deformation annealing is required. It has been shown recently that the optimal combination of strength and ductility in off-stoichiometric $Ti_{50-x}Ni_{50+x}$ alloys after EPT can be obtained after annealing at $500^\circ C$ [9, 10].

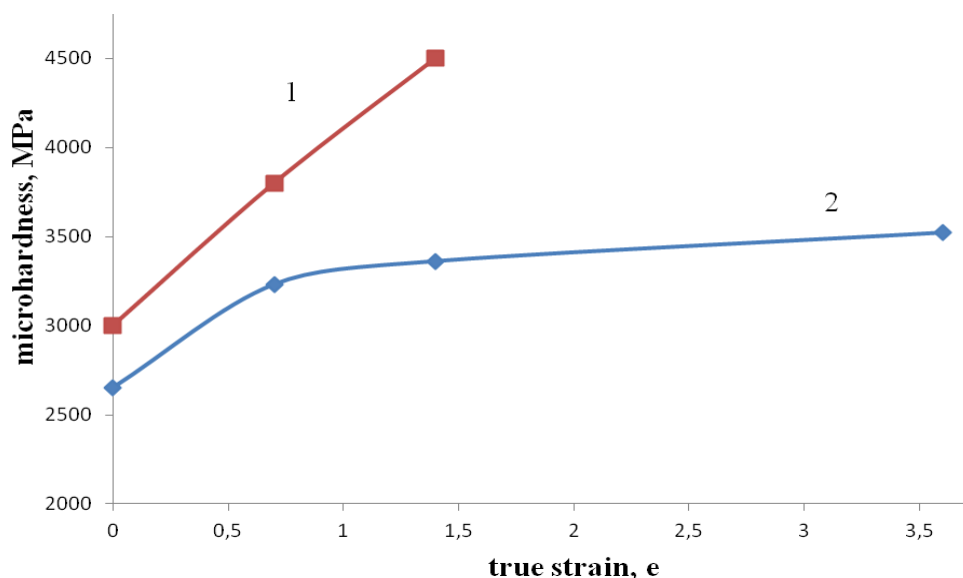


Fig. 1. Dependence of microhardness on true strain: 1- $Ti_{49.2}Ni_{50.8}$, 2- $Ti_{50.0}Ni_{50.0}$, $j=100$ A/mm².

In Fig. 2 the TEM images of deformed alloys after annealing are presented. In the austenitic alloy after EPR ($e=1.2$) annealing at $500^\circ C$ forms the nanograined structure with a mean grain size of 80 nm (Fig. 2a). In the martensitic alloy the same annealing leads to a grain size of 100 nm (Fig. 2b). However, a smaller grain size of 60 nm can begin to form at $450^\circ C$ (Fig. 2c). Analysis of SAEDP allows us to conclude that $Ti_{49.2}Ni_{50.8}$ alloy after annealing remains mainly in an austenitic state while a mixed austenite-martensite structure is formed in the $Ti_{50.0}Ni_{50.0}$ alloy.

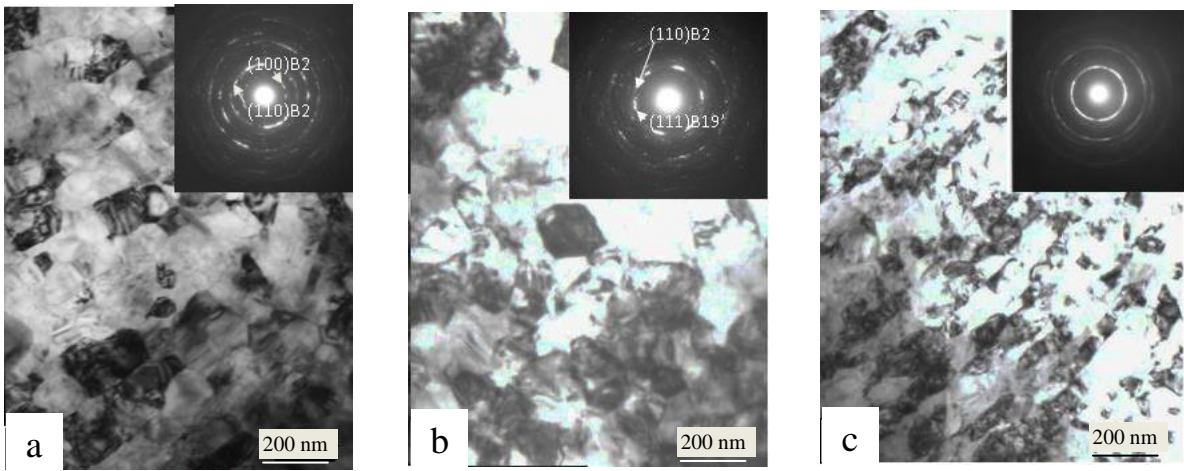


Fig. 2 Microstructure of deformed alloys after annealing: (a) $\text{Ti}_{49.2}\text{Ni}_{50.8}$, $e = 1.2$ + annealing at $500\text{ }^\circ\text{C}$; (b) $\text{Ti}_{50.0}\text{Ni}_{50.0}$ $e = 1.4$ + annealing at $500\text{ }^\circ\text{C}$; (c) $\text{Ti}_{50.0}\text{Ni}_{50.0}$ $e = 1.4$ + annealing at $450\text{ }^\circ\text{C}$. Insets show the respective patterns of selected area electron diffraction (SAEDP).

Electropulse treatment

In Fig. 3 a the dependence of microhardness on the current duration at $j=100\text{ A/mm}^2$ is shown. The initial microhardness decreases more than twice, to a value of 2000 MPa , corresponding to an undeformed state. Another feature in Fig. 3 a is hardening at duration $t=5-7\text{ s}$, caused by ageing. Similar ageing effects in the deformed alloy of the same composition were observed with traditional annealing in the furnace [10].

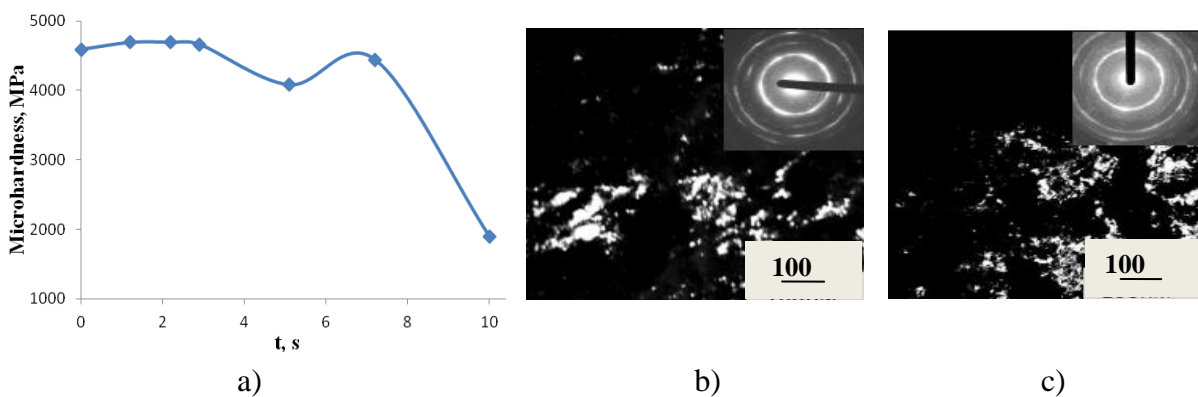


Fig. 3 Dependence of microhardness of deformed ($e=1.5$) $\text{Ti}_{49.3}\text{Ni}_{50.7}$ alloy on current duration (a) and its dark-field (DF) TEM micrographs after EPT (b) or furnace annealing at $450\text{ }^\circ\text{C}$, 1h (c). Insets show the respective SAEDP patterns.

TEM investigations showed that the nanogained structure is formed after EPT with $t=3s$, $j=100 \text{ A/mm}^2$ (see rings in SAEDP and the DF image, Fig. 3 b). Comparison of the dark fields in Figs. 3b and 3c confirms the similarity of the microstructures after EPT and conventional furnace annealing (450°C , 1h).

The mechanical properties given in Table 2 for the samples from EPR strip before and after EPT correlate with microhardness data (Fig. 3 a). The yield stress (YS) and ultimate tensile stress (UTS) to failure first increase weakly with the current duration, but then they sharply decrease. The elongation (El) also increases.

Table 2. Mechanical properties of EPR alloy before EPT, after EPT and after annealing

№	treatment/ EPT regime	YS, [MPa]	UTS, [MPa]	El, [%]
1	EPR	1320	1500	5
2	EPR+ EPT, 100 A/mm^2 , 3 s	1350	1550	10,6
3	EPR+ EPT, 100 A/mm^2 , 10 s	550	640	18,3
4	EPR + annealing at 450°C , 1h	1150	1350	14

Conclusions

Introduction of a pulse current during rolling increases the deformability of $\text{Ti}_{49.2}\text{Ni}_{50.8}$ and $\text{Ti}_{50.0}\text{Ni}_{50.0}$ alloys. This increase is more pronounced in the stoichiometric $\text{Ti}_{50.0}\text{Ni}_{50.0}$ alloy.

The deformation hardening during EPR is higher in the $\text{Ti}_{49.2}\text{Ni}_{50.8}$ alloy than in the $\text{Ti}_{50.0}\text{Ni}_{50.0}$ alloy.

The postdeformation annealing leads to the formation of a nanogained structure. The average grain size in the $\text{Ti}_{50.0}\text{Ni}_{50.0}$ alloy is lower than that in the $\text{Ti}_{49.2}\text{Ni}_{50.8}$ alloy.

Pulse current in specified EPT regimes can replace thermal annealing due to the accelerated stress relaxation during recovery, polygonization or recrystallization.

The financial support of the Russian Foundation for Basic Research (grant 13-08-12222 ofi_m).

References

- [1]. V. Stolyarov, Mater. Sci. Forum, V. 683 (2011) 137-148.
- [2]. V. Stolyarov, Mater. Sci. Eng. A V. 503 (2009) 18-20.
- [3]. Z.H. Xu, G.Y. Tang, S.Q. Tian, J.C. He: Research on the engineering application of multiple pulses treatment for recrystallization of fine copper wire. Mater.Sci.Eng.A. 424, 300 (2006).
- [4]. Yu.V. Baranov, O.A. Troitsky, Yu.S. Avraamov, A.D. Shlyapin, Physical base of electropulse and electroplastic treatment and new materials, MSIU, Moscow, 2001.
- [5]. V. Stolyarov, U. Ugurchiev, I. Trubitsyna et al., J. High Pressure Phys. Tech. V. 4, 16 (2006) 64-67.
- [6]. N.S. Surikova, A.N. Tumensev, O.V. Evtushenko, Izv.vyshikh uchebnykh zavedeniy. Physics, v. 52, no. 5 (2009) 58-67.
- [7]. T.W. Duerig, A.R. Pelton, Ti-Ni Shape memory alloys, Advanced Materials, Materials Properties. In: Handbook: Titanium Alloys, editors R. Boyer, G. Wesch, E.W. Collings, ASM International, (1994) 1035-1048.
- [8]. E. Hornbogen, V. Mertinger, D. Wurzel, Scr. Mater., 44, 1 (2001) 171-178.
- [9]. A.A. Potapova, V.V. Stolyarov, Chernaya metallurgiya, no. 10 (2010) 68-71, in Russian.
- [10]. A.A. Potapova, V.V. Stolyarov, Metalloved i termicheskaya obrabotka metallov, 11 (2011) 41-45, in Russian.

METHOD OF CURRENT AMPLITUDE ESTIMATION OF PULSE GENERATOR

V.E. Gromov, V.A. Kuznetsov, S.V. Konovalov, G. Tang, G. Song,
K.V. Alsaraeva, A.P. Semin

Siberian state industrial university, 654007, Novokuznetsk, Russia.

E-mail: gromov@physics.sibsiu.ru,

Abstract

Method of estimation of current amplitude (~ 10 kA) pulses constructed by powerful current pulse generator is suggested. It bases on the solution of differential equation current and voltage change on capacitor. The final formula consists of maximum value of capacitor charge, maximum negative voltage value, pulse duration and capacitor value.

Keywords: pulse generator, current amplitude, thyristor switch.

In recent years the attention of investigators in the field of physical materials science has been paid to the study of the effect of electro-pulse treatment on structure, phase composition and defect substructure of different metals and alloys in rolling and drawing [1-5].

For intensification of these process the high-power current pulse generators [6, 7] are used, whose basic block diagram is shown in Fig. 1.

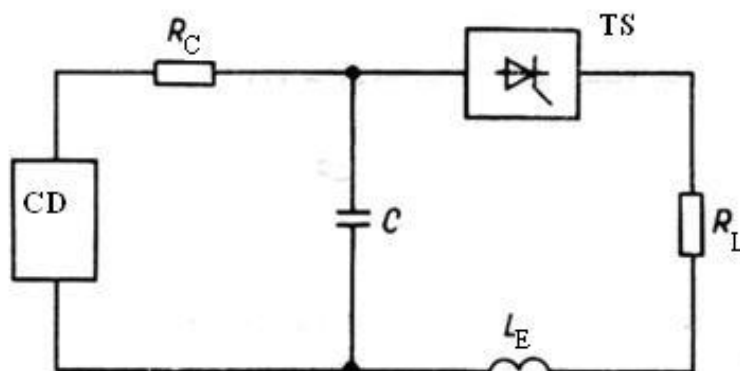


Fig. 1. Basic block diagram of current pulse generator.

CD – charging device, R_C – current limiting resistance, R_L – load resistance, C – bank of capacitors, TS – thyristor switch, L_E – equivalent inductance.

The prospects for justified application of these generators in studying of the electrostimulated plasticity and in metal pressure working should first of all be based on correct procedures of amplitude value of current pulses measurement.

Low-inductive shunts or transformers with integrators are usually used for current measuring through load [8]. The essential drawback of these procedures is the problem of calibration of manufactured shunt and current transformer in the absence of standard measuring instrument and a corresponding power supply. At high rates of amplitude rise of current pulses there is also a great error being introduced in indications by the value of electromotive force (e.m.f.) of self-induction.

The description of simple and accurate procedure of current measuring and calibration of current meter is given below, generator itself being used as a current supply.

Fig. 2 illustrates the process of current i change through load R_L and voltage on capacitor C provided that current limiting resistance R_C has a big value and charging current I_C does not influence on the process of pulse formation in power circuit C, L_E, R_L .

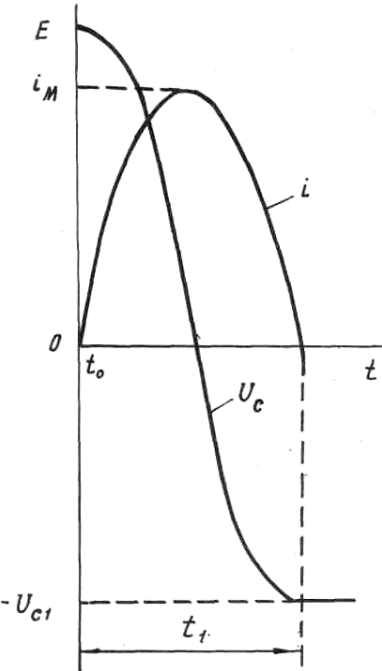


Fig. 2. Process of current change through load and voltage on capacitors.

For estimation of peak current i_M , the generator is switched on workable load and forms current pulses with minimum permissible frequency. The largest calibration accuracy is reached when R_C is large in the process of current pulse passage. With the help of high-precision instruments the following values are measured: maximum voltage E of charged capacitor, the largest negative voltage ($-U_{C1}$) on the capacitor C after current pulse passage, and also time t_1 counted from the beginning of capacitor C discharge to the moment when the voltage on capacitor will be maximum ($-U_{C1}$).

It is known that current and voltage change on capacitor is estimated as [9]:

$$i = \frac{E}{\omega' L_E} e^{-\beta t} \sin(\omega' t), \quad (1)$$

$$U_C = E \frac{\omega_0}{\omega'} e^{-\beta t} \cos(\omega' t - \gamma), \quad (2)$$

$$\beta = \frac{R_L}{2L_E}; \quad \omega' = \sqrt{\frac{1}{L_E C} - \left(\frac{R_L}{2L_E}\right)^2}, \quad (3)$$

$$\omega_0 = \frac{1}{\sqrt{L_E C}} \operatorname{tg} \gamma = \frac{\beta}{\omega'} \quad \text{and } E \text{ is a maximum value of capacitor charge.}$$

For finding the time t_1 , when voltage on capacitor reaches maximum negative value ($-U_{C1}$), we equate the derivative U_C to zero, whence it follows

$$\operatorname{tg}(\omega' t - \gamma) = \frac{\beta}{\omega'}, \quad (4)$$

When comparing (3) and (4) we have

$$\omega' = \frac{\pi}{t_1}, \quad (5)$$

From the first crossing of current curve with time axis (Fig. 2), when

$$i = \frac{E}{\omega' L_E} e^{-\beta t} \sin(\omega' t_n) = 0 \quad \text{we obtain}$$

$$\omega' t_n = \pi \quad (6)$$

It is seen from (5) and (6) that maximum voltage ($-U_{C1}$) takes place in the moment of time $t_1=t_n$, when $i=0$.

We shall take the ratio $U_C/t=0 = E$ $U_C/t=t_1 = -U_{C1}$. Solving the obtained equation relatively β we obtain

$$\beta = \frac{1}{t_1} \ln \frac{E}{U_{C1}}, \quad (7)$$

In terms of equations (3)-(5) and (7)

$$\frac{1}{L_E} = (\omega'^2 + \beta^2)C = \frac{\pi^2 + \ln \frac{E}{U_{C1}}}{t_1^2} C, \quad (8)$$

For estimating the time t_M , when current pulse is maximum, we equate the derivative to zero. Then

$$\lg(\omega' t_M) = \frac{\omega'}{\beta} = \frac{\pi}{\ln \frac{E}{U_{C1}}}, \quad t_M = \frac{t_1}{\pi} \operatorname{arctg} \frac{\pi}{\ln \frac{E}{U_{C1}}}, \quad (9)$$

Conclusively, in terms of (2), (4), (8), (9) we obtain the value of maximum current

$$i_M = \frac{\pi EC}{t_1} (1 + x^2) e^{\frac{\operatorname{arctg} x}{x}} \sin(\operatorname{arctg} x), \quad (10)$$

where $x = \frac{\pi}{\ln \frac{E}{U_{C1}}}$. The values $i_M \left(\frac{U_{C1}}{E}, t_1 \right)$ were calculated at fixed t_1 in the range

of 50-200 μs and U_{C1}/E change from 0.7 to 1.0, which is characteristic of working conditions of current generators [1, 3, 6, 7]. The obtained table of values allowed to make a conclusion about the possibility of formula changing (10) by the approximate polynomial of type

$$i_M = \frac{C}{t_1} (a_0 E + a_1 U_{C1}) \quad (11)$$

Here C is measured in μf , and E, U_{C1} – in V $a_0 = 1,60$; $a_1 = 1,54$ (Fig. 3)

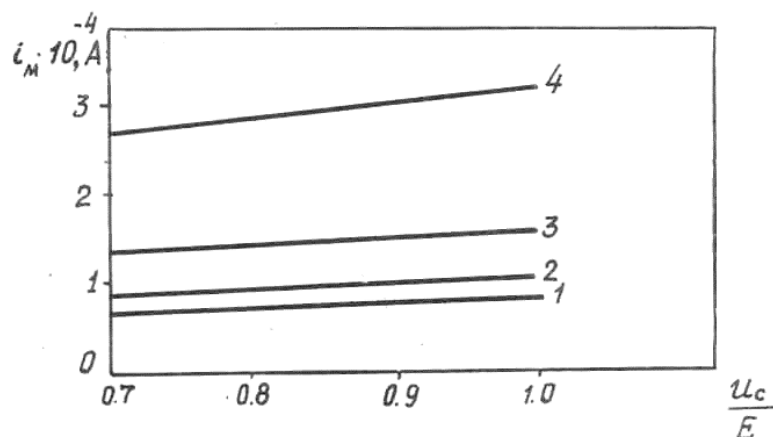


Fig. 3. The U_C/E relation of maximum current at different pulse duration μs :

1 - 50, 2 - 100, 3 - 150, 4 - 200.

Values of coefficients $a_0 = 1,60$ and $a_1 = 1,54$ are obtained by least square procedure. The derived mathematical model estimated by Fisher criterion [10] may be considered to be adequate at value level of $\alpha = 0,01$.

References

- [1] Electroplastic effect in metals Proceeding of China – Russia Symposium / Ed. By V. Gromov, G. Tang. Novokuznetsk: SibSIU, 2007. 319 p.
- [2] Electromagnetic fields effect on the structure and characteristics of materials Book of the International seminar articles / Ed. By Yu. Baranov, V. Gromov, G. Tang. Novokuznetsk: “Novokuznetskii Polygraphic Center”, 2009. 380 p.
- [3] Fundamental Aspects of External Fields Action on Materials Book of the International seminar articles / Ed. By V. Gromov. Novokuznetsk: “Novokuznetskii Polygraphic Center”, 2010. 613 p.
- [4] Properties, microstructure and texture evolution of cold rolled Cu strips under electropulsing treatment / R.F. Zhu, J.N. Liu, G.Y. Tang, S.Q. Shi, M.W. Fu // Journal of Alloys and Compounds, 2012. V. 544. P. 203-208.
- [5] R.F. Zhu, G.Y. Tang, S.Q. Shi, M.W. Fu, V.E. Gromov. Effect of electropulsing treatment on the microstructure and superelasticity of TiNi alloy. Applied Physics A, 2013, V. 111. № 4. P. 1195-1201.
- [6] V.A. Kuznetsov, V.E. Gromov, V.P. Simakov et al. Generator of powerful single-pole impulses of current. Technical electrodynamics. 1981. №5. P. 46-49.
- [7] V.A. Kuznetsov, V.E. Gromov, V.P. Simakov et al. Thyristor generator of powerful unipole current pulses. Electron treatment of materials. 1981. № 3. P. 72-73.
- [8] Levin G.I. Shunt for measuring of current pulses // Instruments and technique of experiment. 1975. № 5. P. 113-114.
- [9] V.E. Gromov, L.B. Zuev, E.V. Kozlov, V.Ya. Tsellermaer. Electrostimulated plasticity of metals and alloys. M.: Nedra. 2006. 293 p.
- [10] F.S. Novik, L.B. Arsov. Optimization process of metal technology by methods of experiment planning. M.: Mashinostroenie. 1980. 305 p.

INTERATOMIC POTENTIALS IN THE SYSTEMS Pd – H AND Ni - H

G.M. Poletaev^{1*}, N.A. Kulabukhova¹, M.D. Starostenkov¹, S.V. Dmitriev²

¹ Altai State Technical University, Lenin Str. 46, 656038 Barnaul, Russia.

² Institute for Metals Superplasticity Problems, Khalturin Str. 39, 450001 Ufa, Russia.

*E-mail: gmpoletaev@mail.ru

Abstract

Interatomic potentials are developed to model hydrogen impurities in Pd and Ni. The H-H potentials are constructed taking into account the results of ab initio simulations reported in the literature. The Pd-H and Ni-H potentials are fitted to the experimental data such as the absorption energy, the activation energy of over-barrier diffusion of H in metals, and the H-vacancy binding energy.

Keywords: interatomic potential, molecular dynamics, metal, hydrogen, absorption energy, diffusion activation energy.

Introduction

Interaction of hydrogen with metals remains a topic of active studies in the last century [1]. This is because of practical importance of metal-hydrogen systems, they find applications as radiation resistant materials, materials for extra-pure hydrogen filters and isotope fractioning, for accumulation and storage of light gases, for hydrogen transportation, etc. On the other hand, hydrogen can have undesirable effects on metallic materials, for instance, hydrogen embrittlement, corrosion, stress corrosion cracking [2].

Hydrogen atom is the smallest one in the periodic table both in terms of mass and size, it has high solubility and a uniquely high diffusivity in metals [3-5]. Hydrogenation of metals results in their dilatation, but even for large hydrogen concentrations the type of crystal lattice is typically unchanged and thus, the effect of dissolved hydrogen on metals is relatively soft. Metals completely restore their properties after evacuation of hydrogen and this fact

opens the possibilities of controllable change of properties of metals by reversible hydrogenation or, in other words, hydrogen treatment of metals [3].

There exist a number of experimental approaches to study the metal-hydrogen systems. However, the information provided by the experimental methods is very often incomplete, the measured properties may have a large dispersion, and interpretation of the experimental results is not obvious because they typically do not uncover the physical nature of many phenomena observed in hydrogenated metals [1, 3]. This is true especially for metals with low hydrogen solubility.

More detailed information can be obtained with the help of theoretical and computational methods such as the first-principle calculations and atomistic modeling based on the use of empirical interatomic potentials. The first-principle simulations are physically more justified but they are highly demanding on computer power and time. Because of this, they cannot be directly applied to the studies of dynamical processes in materials in the nanometer scale related to the evolution of defect structures and thermal fluctuations of atoms. The study of the absorption and diffusion of hydrogen in the crystal lattice and in the vicinity of defects, investigation of the effect of hydrogen on the mobility of defects, as well as prediction of mechanical properties of the hydrogenated materials can be done considering dynamics of relatively large number of atoms. Such molecular dynamics simulations are typically based on semi-empirical interatomic potentials constructed with the help of first-principle calculations taking into account experimental data.

It is well-known that diffusion of hydrogen and helium in metals differs from that of heavier interstitial atoms by exceptionally small diffusion activation energy and by quantum character of diffusion at low temperatures that, for hydrogen in pure metals, remains up to room temperature [2, 3, 6]. At very low temperatures the quantum mechanism of diffusion prevails which occurs through under-barrier quantum tunneling of hydrogen atoms between nearest interstitials. With increase in temperature and in the degree of imperfection of

crystal lattice the contribution of under-barrier diffusion sharply decreases and the classical over-barrier diffusion mechanisms start to operate. At temperatures above the room temperature the diffusion of hydrogen is mainly of over-barrier nature [2, 3, 6]. This makes it possible to investigate the diffusion of light interstitial atoms at sufficiently high temperatures in frame of classical molecular dynamics.

By now there exist several types of potentials describing the interaction of atoms in the metal-hydrogen system that differ by the methodology of fitting their parameters to the experimental data and by the form of the potential functions. Most of the potentials developed so far are built on the basis of various first-principle models, and, as a rule, they do not take into account experimental data such as hydrogen diffusion activation energy, binding energy with trapping defects, dilatation, etc. These characteristics are calculated afterwards and very often all of the abovementioned characteristics are not well described simultaneously by one type of interatomic potentials.

In this work the interatomic potentials are developed for the Pd-H and Ni-H systems taking into account the known potentials and the experimental data on the absorption energy, hydrogen diffusion activation energy, binding energy with point defects of crystal lattice, etc. The choice of metals is motivated by the popularity of these fcc metals among researchers of metal-hydrogen systems and by relatively large amount of experimental data reported for them in the literature.

H-H interaction in metals

The H_2 molecules adhered to the metal surface dissociate into separate hydrogen atoms due to the weakening of the covalent bond [3]. Inside the crystal lattice and in the defects of crystal lattice hydrogen exists in the atomic form. In the second half of the last century two models of the charge of hydrogen in metals existed, the H^+ (proton) and the H^- (anion) models. In the 80th it was found that the real situation has in fact the features of both models. By means of *ab initio* simulations it has been demonstrated that a proton in metals is screened

by the electrons even stronger than in vacuum and it has a charge different from the elementary charge because the hydrogen's electron contributes to the metallic bonding [3].

Semi-empirical potentials describing the interaction of hydrogen atoms embedded into a metal with each other can be divided into two groups. In both cases the parameters of the potentials are fitted to the results of *ab initio* simulations. In the first group, the H-H interactions are calculated in the electron gas of certain density that depends on the type of metal [7-11]. In the work [9] it has been demonstrated that this interaction is considerably weaker than in vacuum. The second group of H-H potentials is constructed based on the consideration of the metallic hydrogen characteristics, typically, the lattice parameter, the sublimation energy, and the bulk modulus, found from the first-principle simulations [12-14]. The potentials of the second group differ considerably from that of the first group by a deeper potential well shifted to the right, meaning a stronger interaction and a larger interatomic distance (see Fig. 1). It is worth noting that solid monoatomic metallic hydrogen having fcc lattice exists at temperatures close to 0 K and extremely high pressures, of order of 100 GPa [15]. At smaller pressures solid hydrogen has hcp lattice with H₂ molecules in the lattice points and interaction between them is weaker.

One of the most popular potentials describing H-H interaction in metals is the Daw-Baskes potential constructed by the embedded atom method [7, 8]. In Fig. 1 the repulsive part of the potential is shown by the curve 1. The authors claim that in the derivation of the potential they tried to use minimal number of assumptions and to take into account all the aspects of the electronic structure [7]. At the same time, the cut-off radius of the potential is limited to the first coordination sphere of the fcc lattice. Such a small cut-off radius does not seem realistic and only the repulsive part of the potential can be trusted.

In Fig. 1 the H-H potentials reported in the works [7-14] are reproduced: the repulsive part of the Daw-Baskes potential for H-H bond in Pd and Ni obtained by the embedded atom method (curve 1) [7, 8]; pair potential of the

work [10] for the H-H bond in Al (curve 2); H-H potential in Ni used in [11] (curve 3) (according to the authors, for the repulsive part of their potential they used the repulsive part of the Daw-Baskes potential, however, as it can be seen from the figure, they have shifted it to the right for the reason not explained in their work); potential of the work [12] that takes into account only the repulsive force for the H-H interaction in Pd and Ag (curve 4); H-H potential in Al from the work [13] (curve 5); the H-H potential in several hcp metals from the work [14] (curve 6). Potentials 4 to 6 belong to the second group, i.e., they are constructed with the use of the solid hydrogen characteristics. They are shifted to the right in comparison to the potentials of the first group. They also have a deeper potential well, as it has been mentioned.

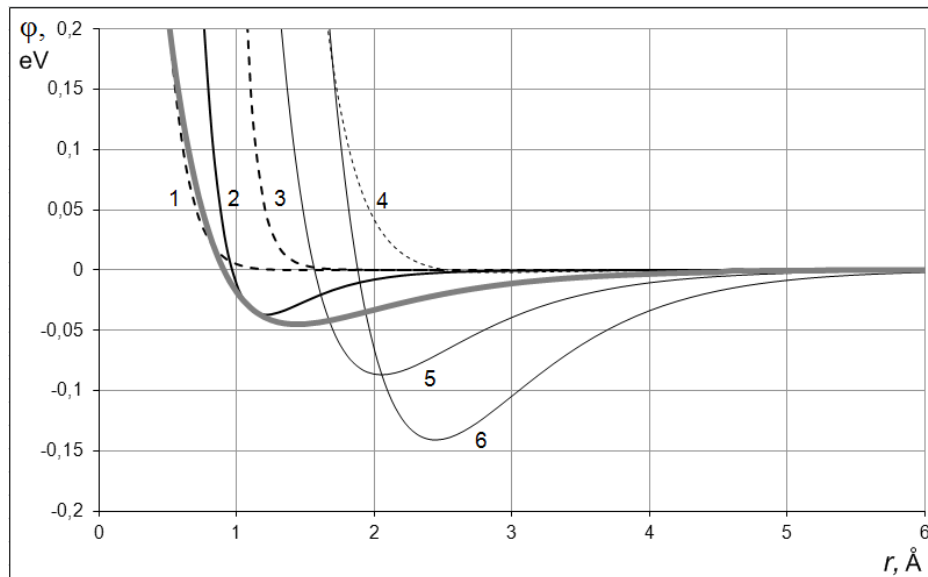


Fig. 1. H-H potentials in metals: 1 – in Pd and Ni [7,8]; 2 – in Al [10]; 3 – in Ni [11]; 4 – in Pd and Ag [12]; 5 – in Al [13]; 6 – in several hcp metals [14]. Potential developed in the present work is shown by the bold grey line.

The H-H potential shown by the curve 5 in Fig. 1 has been tested in the work [16]. In this work was found that due to the relatively deep potential well of the potential, hydrogen atoms tend to coagulate thus reducing the total energy of the system. The hydrogen absorption energy for the potentials of the second group is rather low and this contradicts to the experimental data. For example, at 70% hydrogen concentration in Al the average hydrogen absorption energy was

found to be -0.8 eV [16], which is eight times smaller than in Pd, for which the solubility of hydrogen, as it is well-known, is exceptionally high. In view of this, in the present work, we were oriented on the potentials of the first group, namely, on the potentials shown by the curves 1 and 2 in Fig. 1.

Parameters of the H-H potential offered in this work take into account the results of first-principle calculations obtained by other authors. In the work [9] it has been shown that the H-H potential is relatively soft and it has minimum at about $r=1.5$ Å. The authors of the works [17] and [18] have found that the binding energy between two hydrogen atoms located in the nearest octahedral holes of iron and tungsten (i.e. at the distances 2.03 Å and 2.22 Å, respectively) are equal to 0.044 eV and 0.02 eV, respectively.

To model the H-H, Pd-H, and Ni-H interactions in this work the Morse interatomic potentials is chosen,

$$\varphi(r_{ij}) = D\beta e^{-\alpha r_{ij}} \left(\beta e^{-\alpha r_{ij}} - 2 \right), \quad (1)$$

where α , β , and D are the potential parameters and r_{ij} is the distance between atoms i and j . Morse potentials, in spite of their simplicity and pairwise nature, are capable of describing many properties of metals and alloys [19]. Morse potentials are often used by researchers to describe interatomic interactions in metal hydrogen systems, e.g., [10, 12-14, 20]. Many-body potentials are more realistic for metals but, taking into account error in some experimental parameters they are fitted to, the choice of the pairwise potentials seems to be justified as an alternative approach. Moreover, because of the small atomic weight of hydrogen, its characteristic vibration frequency is much higher than that of metallic atoms, and one has to use one order of magnitude smaller integration time step in molecular dynamics simulations. The use of pair interatomic potentials softens this problem because they are less time consuming.

The H-H potential offered in the present study is depicted in Fig. 1 by the bold grey line.

Pd-H and Ni-H interactions

Potentials describing the metal-hydrogen interaction are usually built with the help of the first-principle simulations or/and experimental data, but sometimes they are defined as the average of the H-H and Me-Me potentials (Me meaning metal) [10, 11]. Thus developed potentials, in most cases, do not simultaneously describe with a good accuracy such experimental parameters as hydrogen absorption energy, the activation energy of over-barrier hydrogen diffusion in metal (at normal and higher temperatures), the binding energy of hydrogen with a defect (e.g., with vacancy), the dilatation, etc. One of the main goals of the present study is to construct the interatomic potentials capable of reproducing these experimental parameters.

The Me-Me interactions are described by the Cleri-Rosato many-body potentials constructed in frame of the strong bond approximation. Potential energy of i -th atom is defined as follows.

$$U_i = \sum_j A \exp\left(-p\left(\frac{r_{ij}}{r_0} - 1\right)\right) - \sqrt{\sum_j \xi^2 \exp\left(-2q\left(\frac{r_{ij}}{r_0} - 1\right)\right)}, \quad (2)$$

Here A , p , q , ξ , and r_0 are parameters, r_{ij} is the distance between i -th and j -th atoms. Parameters of the Cleri-Rosato potentials were taken from the work [21]. These potentials were successfully applied for solving some problems with the use of molecular dynamics [22].

Hydrogen absorption energy is the energy required for insertion of a hydrogen atom into metal taking into account the energy needed for the H-H bond breaking to dissociate the H_2 molecule. The absorption energy was calculated from

$$E_{ab} = (U_H - U_0) + \frac{1}{2} E_{dis}, \quad (3)$$

where U_0 is the ideal metal crystal potential energy, U_H is the potential energy of crystal containing a hydrogen atom taking into account the structure relaxation, E_{dis} is the hydrogen molecule dissociation energy ($E_{dis} = 4.485$ eV [1,3,9]). To

evaluate U_H , a hydrogen atom was introduced into a octahedral hole of a computational cell of fcc Pd or Ni followed by relaxation and then quenching to 0 K.

The binding energy between a hydrogen atom and a vacancy, E_{bv} , was calculated as the difference between potential energy of the computational cell containing a vacancy and a well separated octahedral hole with a hydrogen atom and potential energy of the computational cell with a hydrogen atom in the vacancy. In both cases the dynamic relaxation of the computational cells was carried out followed by quenching to 0 K.

The migration activation energy of a point defect can be found in molecular dynamics simulations by the static or dynamic method [22]. In the static method the energy barrier is calculated along the trajectory of the point defect. Dynamic method relies on the determination of the diffusion coefficient as the function of temperature $D(T)$ considering one defect in the computational cell (a hydrogen atom in our case). The migration activation energy of hydrogen atom, E_m , can be found from the dependence $\ln D(T^{-1})$, after estimating the slope $tg\alpha$, as follows

$$E_m = -k\alpha = -k \frac{\partial \ln D}{\partial (T^{-1})}, \quad (4)$$

k is the Boltzman constant and T is temperature.

The dynamical method can be also used to find the pre-exponent multiplier in the corresponding Arrhenius equation. The multiplier is proportional to the defect concentration

$$D = \frac{c}{c'} D' = D'_0 N c \exp\left(-\frac{E^m}{kT}\right), \quad (5)$$

where c is the concentration of the considered defects, c' is the concentration corresponding to one defect in a computational cell, D'_0 is the coefficient found from simulations for one defect in the computational cell, N is the number of atoms in the computational cell. The coefficient D'_0 in the Arrhenius equation

(5) can be found as the intersection point of the function $\ln D(T^{-1})$ with the ordinate [22].

In this work the migration activation energy of hydrogen over-barrier diffusion in Pd and Ni was calculated by both methods. It was found that the over-barrier diffusion of hydrogen in fcc metals takes place through successive penetration of hydrogen through the octahedral and tetrahedral holes, and that the migration activation energy for transition from the octahedral to the tetrahedral hole is nearly zero. That is why, in the static method, the migration activation energy was calculated as the difference of the energies of the computational cells with the hydrogen atom in the center of the triangle formed by the three neighboring atoms of (111) plane (pass point) and with the hydrogen atom in the octahedral hole. Before the calculations the computational cell was subjected to dynamic relaxation followed by quenching to 0 K.

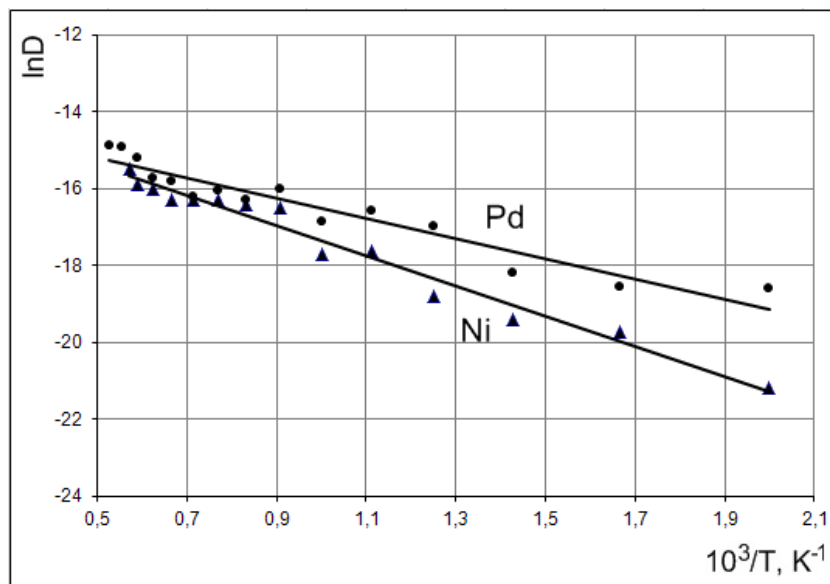


Fig. 2. $\ln D$ as the function of T^{-1} for Pd and Ni for a single hydrogen atom in the computational cell.

In the dynamical calculation of the migration activation energy, one hydrogen atom was introduced into the computational cell. The hydrogen diffusion coefficient in metals was estimated for different temperatures. Each computational run was at least 200 ps long with the time step of 1 fs. The diffusion coefficients were calculated from

$$D = \frac{1}{6tN} \sum_{i=1}^N \left((x_{0i} - x_i)^2 + (y_{0i} - y_i)^2 + (z_{0i} - z_i)^2 \right), \quad (6)$$

where x_{0i} , y_{0i} , z_{0i} are the initial coordinates of the hydrogen atom and x_i , y_i , z_i are the coordinates at time t . To exclude the effect of thermal fluctuations, at the end of the computational run the computational cell was quenched to 0 K.

In Fig.2 the dependencies $\ln D(T^{-1})$ calculated for a single hydrogen atom in the computational cell are given for Pd and Ni.

The concentration of hydrogen atoms in metals can be, of course, different. In order to have the possibility to compare the obtained simulation results with the experimental data, when calculating the the pre-exponent using (5), we took the hydrogen concentration as in the works [3, 17, 23-26], on average, 0.5% for Pd and Ni.

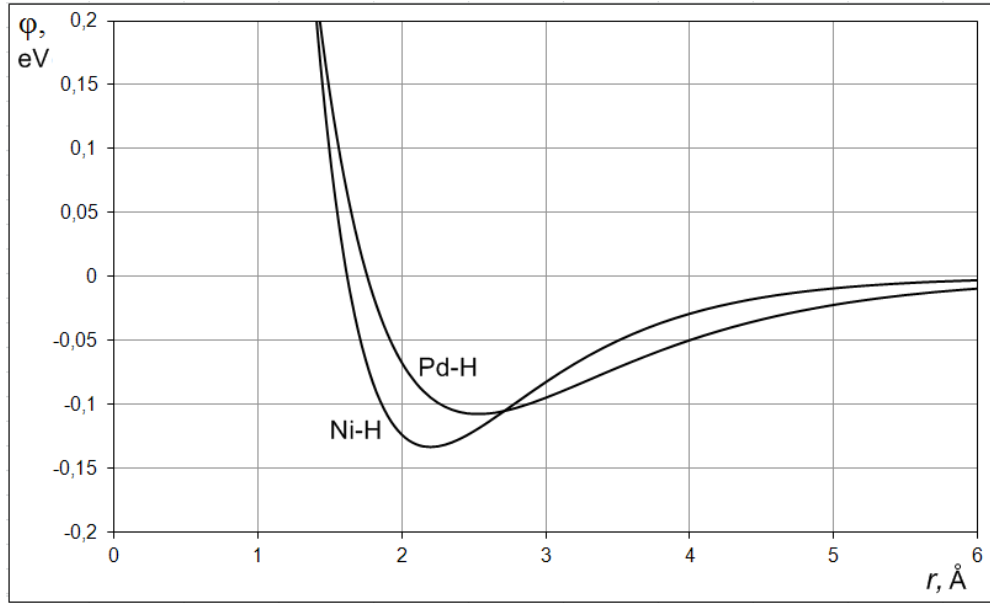


Fig. 3. Pd-H and Ni-H potentials

In Fig. 3 we plot the Pd-H and Ni-H potentials developed in this work. In Table 1 the experimental data used for fitting the potential parameters are presented together with the values found from molecular dynamics simulations based on the offered potentials. The cut-off radius of the H-H, Pd-H and Ni-H Morse potentials was set to take into account the first five coordination shells (i.e, approximately, $6 \div 6.5 \text{ \AA}$). Table 2 gives the potential parameters.

Table 1. The hydrogen absorption energy E_{ab} , the vacancy-hydrogen binding energy E_{bv} , the diffusion activation energy E_m and the pre-exponential factor D_0 for Pd-H and Ni-H systems. Experimental data is compared to the molecular-dynamics simulations based on the potentials constructed in this work.

		E_{ab} , eV	E_{bv} , eV	E_m , eV		D_0 , m ² /s
				Static method	Dynamic method	
Pd-H	Experiment	-0,08 ÷ -0,12 [1,9,27]	0,25÷0,27 [28-30]	0,22÷0,25 [3,17,23,24]		2 · 10 ⁻⁷ ÷8 · 10 ⁻⁷ [3,17,23,24]
	Simulations	-0,100	0,262	0,235	0,23	9,2 · 10 ⁻⁷
Ni-H	Experiment	0,15÷0,17 [3,7,8]	0,32÷0,54 [7,31]	0,33÷0,42 [24,25,26]		5 · 10 ⁻⁷ ÷9 · 10 ⁻⁷ [24,25,26]
	Simulations	0,160	0,401	0,375	0,34	15,1 · 10 ⁻⁷

Table 2. Morse potential parameters for the H-H, Pd-H, and Ni-H interactions.

	α , Å ⁻¹	β	D , eB
H-H	1,3	6,5	0,045
Pd-H	0,9	9,76	0,10737
Ni-H	1,2	14	0,1331

Conclusion

The potentials developed in the present study to describe the interaction of hydrogen with palladium and with nickel describe well such experimentally measured quantities as the absorption energy, the over-barrier hydrogen diffusion energy in metals (at room and higher temperatures), the vacancy-hydrogen binding energy. The H-H interactions were constructed taking into account the results of first-principle simulations obtained by other authors.

The developed potentials can be used for molecular dynamics and molecular quasi-static simulations of the Pd-H and Ni-H systems that include large number of atoms and various defects of crystal lattice. Acknowledgements

The reported study was partially supported by RFBR, research projects No. 12-08-98046-r_sibir_a, No. 12-02-98000-r_sibir_a, No. 13-02-00301_a.

References

- [1]. G. Alefeld, J. Volkl, eds. Hydrogen in Metals. Mir, Moscow, 1981.
- [2]. Yu.K. Tovbin, E.V. Votyakov. Physics of the Solid State. 42 (2000) p.1192.
- [3]. A.P. Zakharov, eds. The interaction of hydrogen with metals. Nauka, Moscow, 1987.
- [4]. A.V. Gapontsev, V.V. Kondrat'ev. Physics-Uspekhi. 46 (2003) p. 1077.
- [5]. R.A. Andrievski. Physics-Uspekhi. 50 (2007) p. 691.
- [6]. Yu.A. Kashlev. Theoretical and Mathematical Physics. 145 (2005) p. 1590.
- [7]. M.S. Daw, M.I. Baskes. Phys. Rev. B 29 (1984) p. 6443.
- [8]. M.S. Daw, M.I. Baskes. Phys. Rev. Letters. 50 (1983) p. 1285.
- [9]. O.B. Christensen, P.D. Ditlevsen, K.W. Jacobsen, P. Stoltze, O.H. Nielsen, J.K. Norskov. Phys. Rev. B 40 (1989) p. 1993.
- [10]. M.A. Baranov, A.Yu. Drozdov, V.G. Chudinov, V.Ya. Bayankin. Technical Physics. The Russian Journal of Applied Physics. 45 (2000) p. 427.
- [11]. M. Katagiri, H. Onodera, Materials Transactions. 40 (1999) p. 1274.
- [12]. H. Kurokawa, T. Nakayama, Y. Kobayashi, K. Suzuki, M. Takahashi, S. Takami, M. Kubo, N. Itoh, P. Selvama, A.Miyamoto. Catalysis Today. 82 (2003) p. 233.
- [13]. G.Zhou, F. Zhou, X. Zhao, W. Zhang, N. Chen, F. Wan, W.Chu. Science in China. 41 (1998) p. 176.
- [14]. S.J. Liu, S.Q. Shi, H. Huang, C.H. Woo. Journal of Alloys and Compounds. 330-332 (2002) p. 64.
- [15]. E.G. Maksimov, Yu.I. Shilov. Physics-Uspekhi. 42 (1999) p. 1121.
- [16]. N.A. Kulabukhova, G.M. Poletaev, M.D. Starostenkov, V.V. Kulagina, A.I. Potekaev. Russian Physics Journal. 54 (2012) p. 1394.
- [17]. L.V. Spivak, N.E. Skryabina, M.Y. Kats. Hydrogen and mechanical aftereffect in metals and alloys. Perm State University, Perm, 1993.
- [18]. Liu Y., Zhang Y., Zhou H., Lu G. Phys. Rev. B 79 (2009) p. 172103.
- [19]. G.M. Poletaev, A.B. Yuryev, V.E. Gromov, M.D. Starostenkov. Atomic mechanisms of structural-energetical transformations near tilt grain boundaries

in fcc metals and intermetallide Ni₃Al. Sybirian State Industrial University, Novokuznetsk, 2008.

[20]. D.V. Shalashilin, B.Jackson. Faraday Discussions. 110 (1998) p. 287.

[21]. F. Cleri, V. Rosato. Physical Review. B 48 (1993) p. 22.

[22]. G.M. Poletaev, M.D. Starostenkov. Physics of the Solid State. 52 (2010) p. 1146.

[23]. P. Kamakoti, D.S. Sholl. Fuel Chemistry Division Preprints. 47 (2002) p. 818.

[24]. L.N. Larikov, V.I. Isaychev. Diffusion in metals and alloys. Naukova dumka, Kiev, 1987.

[25]. K. Tanaka, T. Atsumi, M. Yamada. Journal de physique. 42 (1981) p. 139.

[26]. V.M. Sidorenko, I.I. Sidorak, Physicochemical Mechanics of Materials. 9 (1973) p. 52.

[27]. F.A. Lewis. Platinum Metals Rev. 26 (1982) p. 20.

[28]. S.M. Myers, S.T. Picraux, R.E. Stoltz. J. Appl. Phys. 50 (1979) p. 5710.

[29]. S.V. Eremeev, S.S. Kulkov, S.E. Kulkova, Physical Mesomechanics 13 (2010) p. 81.

[30]. T.B. Flanagan, R. Balasubramaniam, R. Kirchheim. Platinum Metals Review 45 (2001) p. 114.

[31]. F. Besenbacher, J.Bottiger, S.M. Myers. J. Appl. Phys. 53 (1982) p. 3547.

POSSIBILITIES OF APPLICATION OF CARBON-FLUORINE CONTAINING ADDITIONS IN SUBMERGED-ARC WELDING

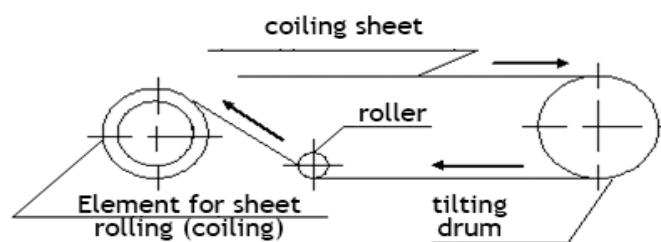
N.A. Kozyrev¹, N.E. Kryukov², R.E. Kryukov¹,
V.F. Igushev³, I.I. Kovalevskii³

¹ Siberian State Industrial University, Novokuznetsk, Russia.

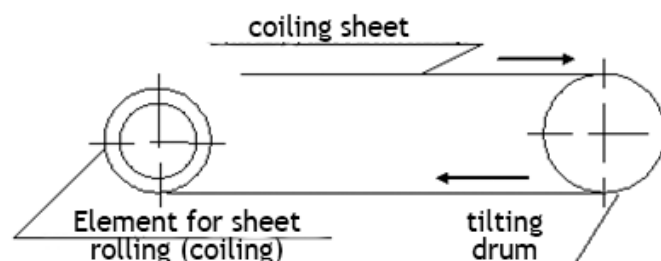
² Novokuznetsk reservoir metal structure plant, Novokuznetsk, Russia.

³ Baltic ship-building college, Kaliningrad, Russia.

A development of oil deposits in the North regions (in conditions of low temperatures) is connected with the necessity of oil tank manufacture for negative temperature exploitation. According to the “Rules of installation of vertical cylindrical steel tanks for oil and oil products”, Safety rules 03-605-03 and Construction codes 23-81, the increased demands are made on welded joints, with particular attention to the impact strength at negative temperatures. At Russian enterprises a submerged-arc welding (SAW) has been widely used, and technological process of assembling, welding, controlling and rolling of tank wall sheets into coils is done on special rolling unit with upper and lower rolling.



a)



b)

Fig. 1 Diagram of stsnd installation for rolling of reservoirs with upper (a) lower rolling (b).

Reservoir metal structure plant in Novokuznetsk has developed and mastered the reservoir manufacture technology for oil products for negative temperature exploitation [1 – 4]. In the given technology a two-side welding of butt joints of wall sheets is done automatically in SAW first on the top layer, then, after drawing the sheet by the drum, on the lower layer. To ensure a high productivity in manufacturing, crack formation elimination and to increase the mechanical properties we have developed and patented in Russia [5, 6] a technology of welding for tanks wall sheets. According to the technology a welding of tank is done with the welding wire **СВ-08ГА** under the mixture of fluxes **AH-348A** and **AH-67Б** with the ratio of 1:1. Welding is done without bevel to the sheet thickness of 16 mm. On the top layer the butt joints are welded at reduced power conditions, ensuring a weld metal penetration up to 0.55 of sheet thickness. On the lower layer a welding is done at high power conditions, permitting to get a weld metal penetration up to 0.7 of sheet thickness.

However, the required level of mechanical properties is not always ensured when using some flux grades, namely, the impact strength at lower temperature due to the formation of a large number of nonmetallic inclusions in the welded joints. Most of the nonmetallic inclusions in the joints are oxide, irrespective of whether they are exogenic or endogenic. A content of nonmetallic inclusions in a joint, in turn, depends on the quantity of total oxygen. As the oxygen solubility in a solid metal is small, the total oxygen content in a joint characterizes the level of its contamination by nonmetallic inclusions. The existing fluxes for low alloy steel welding show the increased total oxygen content, and, consequently, the increased number of nonmetallic inclusions in the joints. Today the reduction of nonmetallic inclusion content in welded joints in automatic SAW is reached with low oxidizing flux application. But these fluxes have unsatisfactory welding and technological properties and are rarely used in low alloy steel welding. In the case of oxidizing flux application the metal of a joint

is saturated by oxygen at the expense of silicon and manganese reduction process.

At present the alloying systems employed in welding at the expense of silicon and manganese reducing processes {1 – low carbon electrode wire and high manganese flux with high silica content; 2 – low carbon wire and high silicon (acid) flux; 3 – medium manganese electrode wire and medium manganese acid flux} have a number of disadvantages.

1) The use of silicon and manganese as deoxidizers results in the formation of different oxide inclusions, which, due to the short duration of the process, do not always have time to rise to the surface and assimilate with slag, therefore a concentration of free and bound oxygen in the metal of joint is rather high, in this connection, the reduction of impact toughness values of joint metal is observed, especially at negative temperatures. Thus, the use of carbon is optimal, from the point of view of elimination of nonmetallic inclusions formation in the welded joint, because the compounds CO and CO₂, being formed with carbon participation, are in gaseous state, in this connection they are removed easily and do not contaminate the joint metal by nonmetallic inclusions. However, use of carbon as a deoxidizer results in carburization of metal that, in turn, impair the mechanical properties and structure of welded joints.

2) The insufficient concentration of fluorine-containing components in fluxes for hydrogen removal, which allow to obtain the active fluorine as a result of dissociation, removing hydrogen from welded joint.

3) The absence of potassium and sodium in most grades of flux elements facilitating the ionization and ensuring a stable arcing.

We have tested the carbon and fluorine additions as flux additives [7 – 12]. Wastes of metal production in the form of dust of chemical composition mass %: Al₂O₃ = 25 – 30; Na₃AlF₆ = 30 – 5-; CF_x = 25 – 35 (1 ≥ x > 0) were taken as a base of carbon and fluorine containing addition.

In theory the given addition should permit:

1) to do the removal of hydrogen at the expense of fluorine containing compounds {like Na_3AlF_6 ; $\text{CF}_x = 25 - 35$ ($1 \leq x > 0$) etc.}, disintegrating at temperatures of welding processes with the liberation of fluorine, which, in turn, reacts to hydrogen dissolved in steel with the formation of gaseous compound HF;

2) to carry out the intensive carbon boiling at the expense of CO and CO_2 being formed in interaction of carbon fluoride CF_x ($1 \leq x > 0$) with the dissolved oxygen in steel, and as carbon is in a bound state a carbonization of steel should not practically occur;

3) to increase the arc stability at the expense of the elements facilitating the potassium and sodium ionization in the arc column.

The addition to flux was prepared in the following way: a carbon and fluorine containing components was mixed with glass, and after it a drying, cooling and crushing was done. Then the addition was mixed with a flux in a special mixer in a strictly prescribed ratio. For investigation the flux grades **AH-348A**, **AH-60**, **AH-67** and **OK 10.71** were taken as base variant and their mixtures with admixture of flux-additions.

Experiments were carried out on the specimens made from **09Г2С** steel, 16 mm thick and of size 200x500 mm. Welding of butt joints without edge preparation was done from two sides, as in welding of sheets of walls on the stand for rolling. A wire **СВ-08ГА** of 5 mm diameter was used as a filler metal.

Submerged-arc welding of specimens was done in identical conditions. Specimens were cut from welded plates and the following investigations were carried out: X-ray spectroscopic analysis of composition of joint metal, metallographic analysis of welded joints, determination of total oxygen content in joints, mechanical properties, hardness of welded joints and impact toughness of joints at temperatures of 20⁰C, minus 40⁰C and minus 70⁰C.

The metal chemical composition determination of welded joints by carbon, sulphur and phosphorus content was done by chemical methods according to State Standard 12344-2003, State Standard 12345-2001, State Standard 12347-

77 respectively. Content of alloying elements in a metal of joint, calcium oxide, sodium and fluorine compounds in fluxes with additions and slags obtained after welding was determined on X-ray fluorescence spectrometer XRF-1800 by SHIMADZU firm.

The test showed that the carbon concentration in a joint corresponding to the carbon concentration in the initial metal (Fig. 2) is insured upon use of carbon and fluorine containing addition in quantity up to 6%.

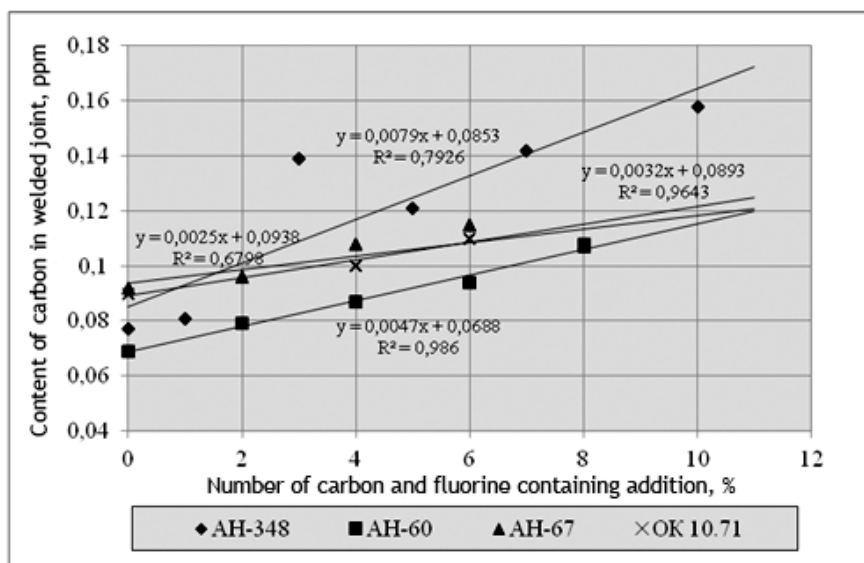


Fig. 2. Influence of carbon and fluorine containing addition on carbon content in welded joint.

Sulphur and phosphorus content in a metal of joint obtained in submerge-arc welding with additions and without additions did not change and was in the range of S = 0.015 – 0.019%, P – 0.013 – 0.015%, i.e. the application of fluxes with additions had no effect on the transition of sulphur and phosphorus from the formed slag into metal.

Determination of oxygen by method of reduction smelting on gas analyzer TC-600 by LECO firm showed that mass fraction of the given gas with the increase of addition content in flux has decreased (Fig. 3), and a fractional gas analysis has showed that depending on a state of oxidation and basicity of a slag system a redistribution of oxygen in inclusions occurs. Distributions of oxygen in silicates, aluminates, aluminosilicates is likely to be connected with basicity of

the obtained slag and assimilation of nonmetallic inclusions by slag depending on the obtained slag viscosity.

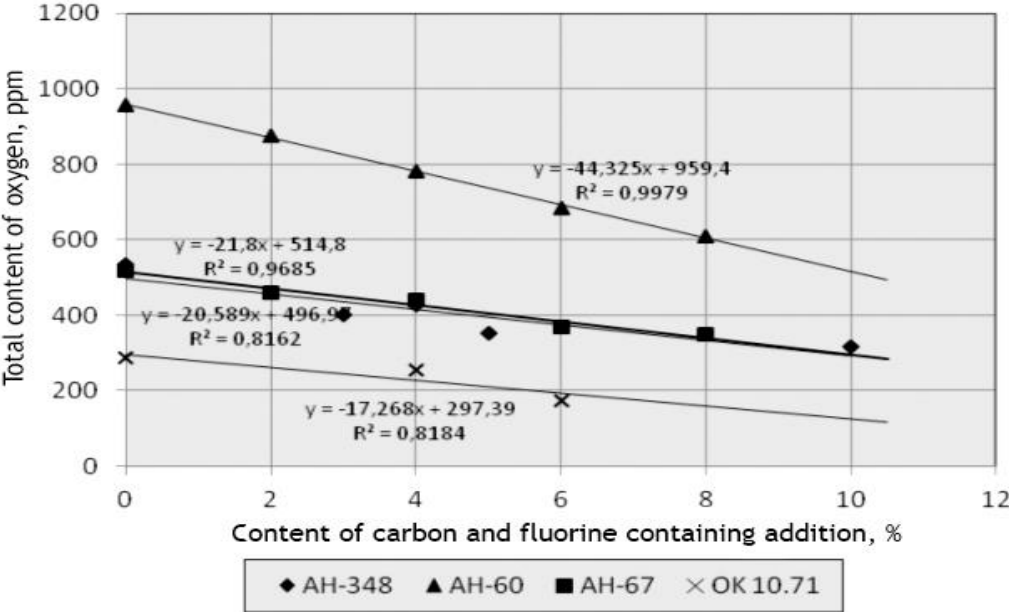


Fig. 3. Change of total oxygen in fluxes depending on the introduction of carbon and fluorine containing addition.

The largest number of aluminates and aluminosilicates, effecting adversely the physical and chemical properties of the welded joint, was contained in submerged-arc welding with flux **AH-60**, when the addition was introduced the decrease in number of these compounds was observed. In fluxes **AH-348** and **AH-67** the changes were negligible (Fig. 4).

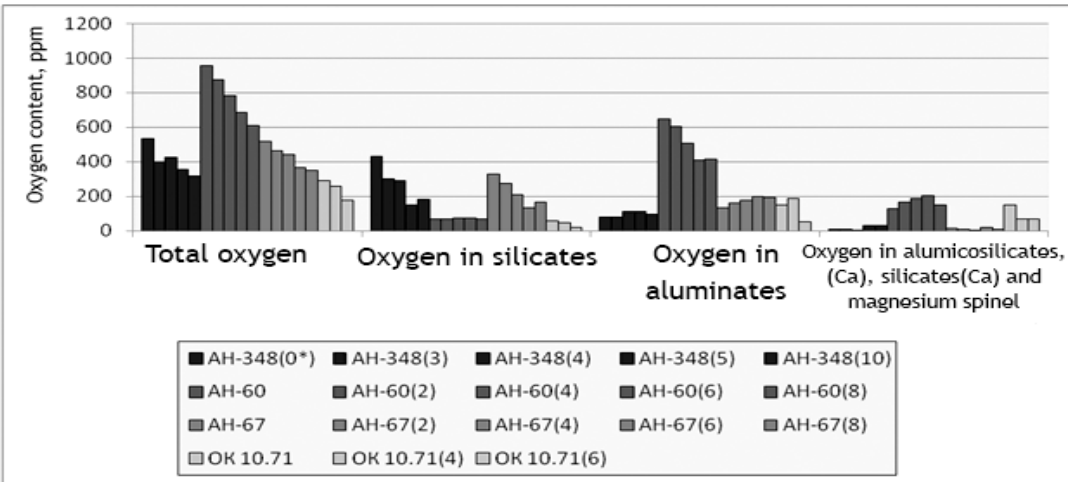


Fig. 4. Change of total and fractional oxygen concentration depending on the quantity of carbon and fluorine containing addition.

The carbon and fluorine containing addition influenced the reduction of the hydrogen in the welded joint according to the mechanism described above at the expense of fluorine (Fig. 5), and sodium concentration was slightly decreased (Fig. 6).

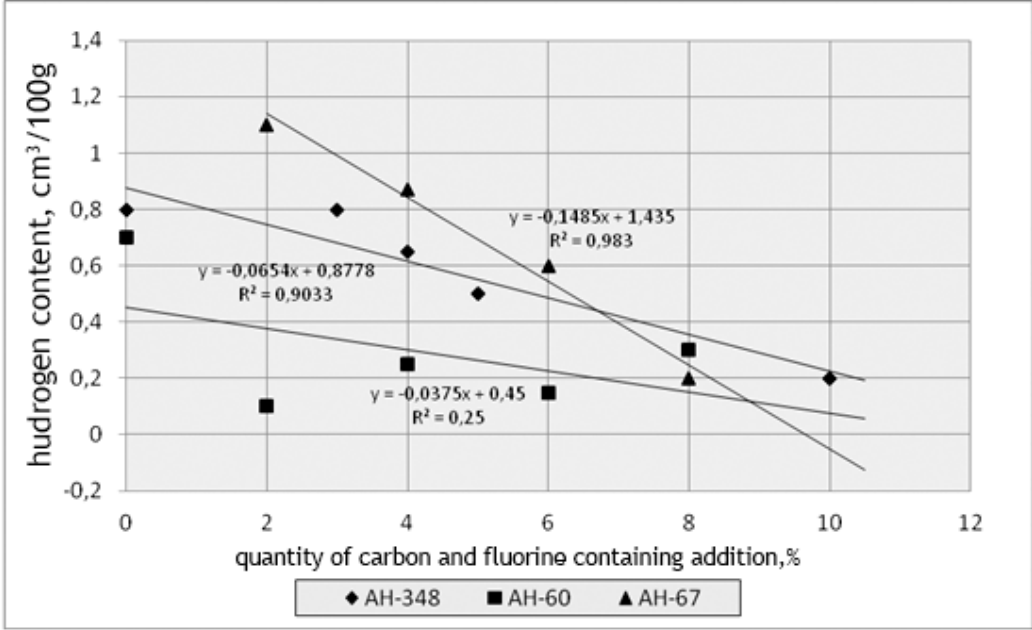


Fig. 5. Change of hydrogen content depending on quantity of carbon and fluorine containing addition.

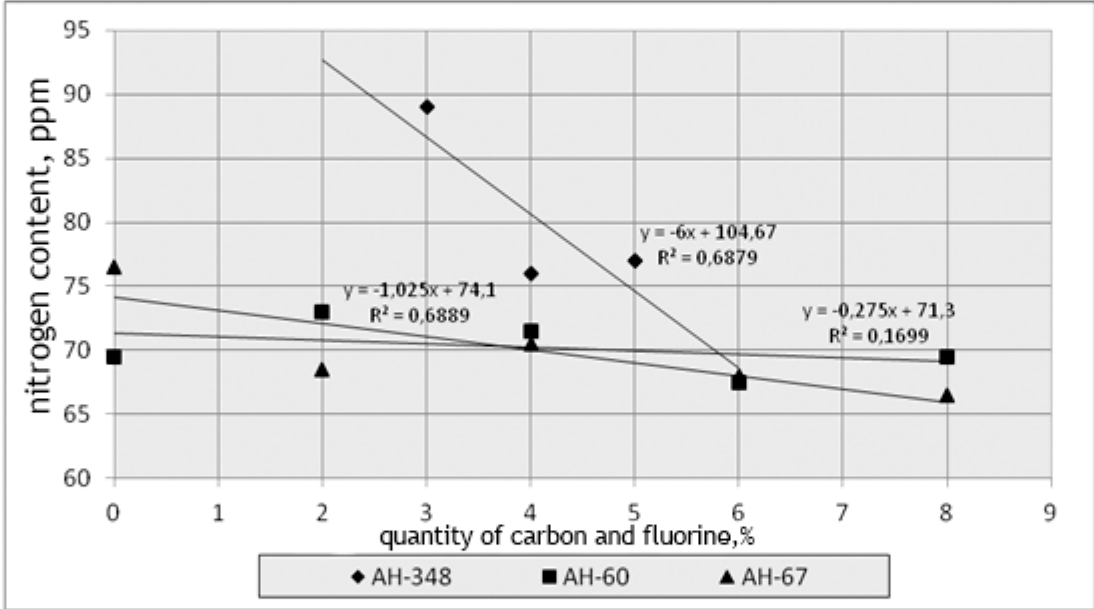


Fig. 6. Change of nitrogen content depending on quantity of carbon and fluorine containing addition.

A metallographic examination of polished microsections of welded joints were done with the help of optical microscope OLYMPUS GX-51 in a light field at magnifications $\times 100$, $\times 500$. Metal microstructure was revealed by etching in a solution of 4% HNO_3 in ethyl alcohol. A structure of base metal of all specimens consists of ferrite grains and lamellar pearlite (4 – 5 μm). In the transition zone from the base metal to the deposited one a fine-grained structure is observed (1 – 2 μm), being formed as a result of recrystallization on heating in welding process. Ferrite grains elongated in the direction of heat removal due to heating and accelerated cooling are present in the microstructure of welded joint. A detectable difference in structure of joints welded under different fluxes was not revealed. In specimens welded by submerged-arc welding with carbon and fluorine containing additions a decrease of contamination level by nonmetallic inclusions, connected with the decrease of total oxygen content was observed.

Study of mechanical properties (yield point, strength, unit elongation and impact toughness at negative temperatures) of specimens, cut according to State Standard 6996-66, has shown that a level of properties exceeds significantly the required values of State Standard 32385-2008 and normative values of Safety Rules 03-605 (rules for manufacture of vertical cylindrical tanks for oil and oil products) and rises with the increase of carbon and fluorine containing addition (Fig. 7). The increase of impact toughness values at negative temperatures (Fig. 8) should be especially noted.

Thus, upon introduction of the developed carbon and fluorine containing addition to the fluxes AH-60, AH-67, OK 10.71 the gas saturation of welded joint is increased, contamination by oxide nonmetallic inclusions is decreased, a complex of the required mechanical properties and impact toughness (especially at negative temperatures) is enhanced.

The production of carbon and fluorine containing addition protected by the patent [13], is mastered in the conditions of the joint-stock company N.E. Kryukov Novokuznetsk reservoir metal structure plant.

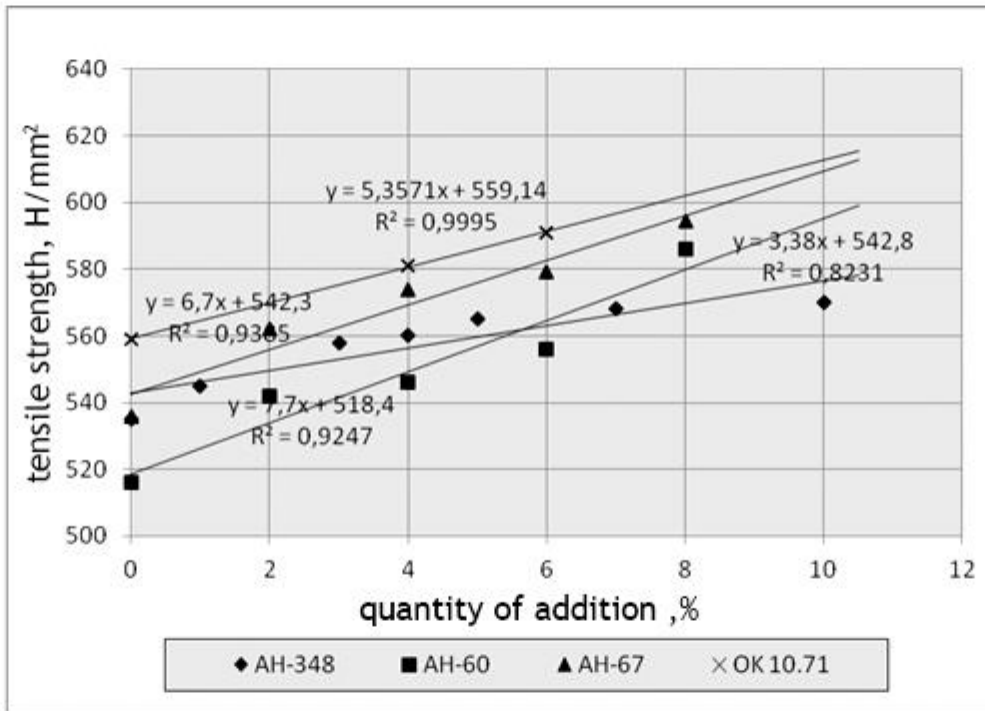


Fig. 7. Change of tensile strength depending on quantity of carbon and fluorine containing addition.

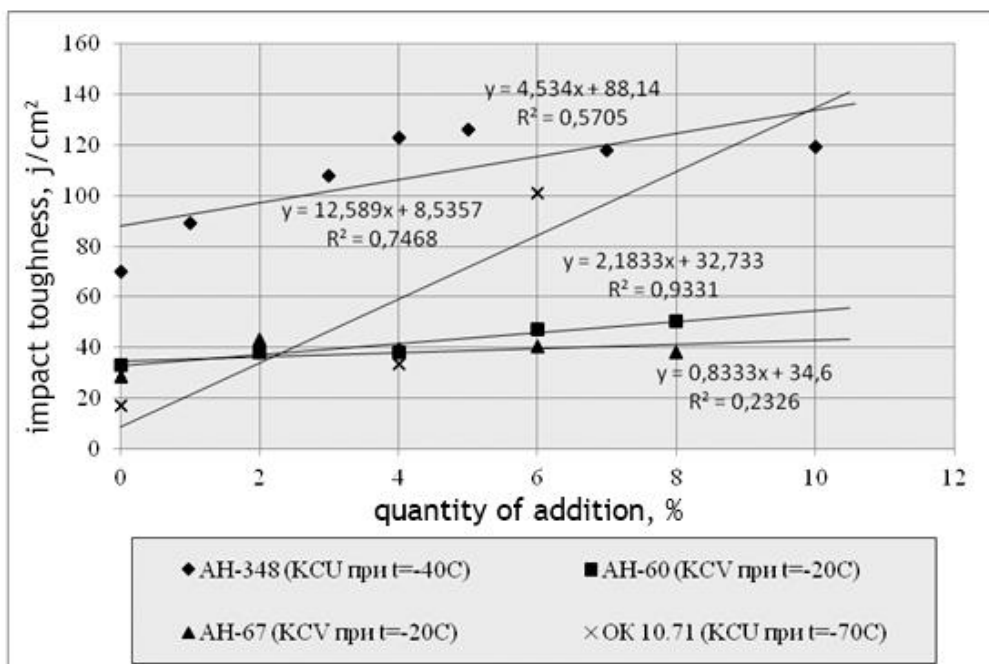


Fig. 8. Change of impact toughness depending on quantity of carbon and fluorine containing addition.

References

- [1]. N.E. Kryukov, I.N. Kovalskii, N.A. Kozyrev, V.F. Igushev, R.E. Kryukov. Electrometallurgiya. 2011. № 10. P. 28 – 31.

- [2]. N.E. Kryukov, I.N. Kovalskii, N.A. Kozyrev, V.F. Igushev, R.E. Kryukov. Izvestiya vuzov. Chernaya metallurgiya. 2012. № 2. P. 49 – 52.
- [3]. N.E. Kryukov, I.N. Kovalskii, N.A. Kozyrev, V.F. Igushev, R.E. Kryukov. Svarochnoye proizvodstvo. 2012. № 5. p. 35 – 38.
- [4]. N.E. Kryukov, I.N. Kovalskii, N.A. Kozyrev, V.F. Igushev, R.E. Kryukov. Steel in translation. 2012. V. 42. № 2. P. 118 – 120.
- [5]. Patent 2465108 RF, MPK⁸ V 23 K9/18, B23 K35/362 Method of submerged-arc welding / Kryukov N.E., Kovalskii I.N., Kozyrev N.A., Igushev V.F., Kryukov R.E.; Joint-stock company N.E. Kryukov Novokuznetsk reservoir metal construction plant. - № 2011123342/02(034573), applied 08.06.2011.
- [6]. Patent 2467853 RF, MPK⁸ V 23 K35/362 Ceramic flux-addition/ Kryukov N.E., Kovalskii I.N., Kozyrev N.A., Igushev V.F., Kryukov R.E.; Joint-stock company N.E. Kryukov Novokuznetsk reservoir metal construction plant. - № 201112341602(034573), applied 08.06.2011.
- [7]. N.A. Kozyrev, V.F. Igushev, S.N. Starovatskaya, R.E. Kryukov. Z.V. Goldun. Izvestiya vuzov. Chernaya metallurgiya. 2012. № 6. P. 26– 29.
- [8]. N.A. Kozyrev, V.F. Igushev, Z.V. Goldun, R.E. Kryukov. V.M. Shurupov. Izvestiya vuzov. Chernaya metallurgiya. 2012. № 10. P. 35– 38.
- [9]. N.A. Kozyrev, V.F. Igushev, R.E. Kryukov, Z.V. Goldun, I.N. Kovalskii. Svarochnoye proizvodstvo. 2012. № 12. – P. 3 – 6.
- [10]. N.A. Kozyrev, V.F. Igushev, R.E. Kryukov, S.N. Starovatskaya, A.V. Roor. Izvestiya vuzov. Chernaya metallurgiya. 2013. № 4. P. 30– 33.
- [11]. N.A. Kozyrev, V.F. Igushev, R.E. Kryukov, A.V. Roor, I.N. Kovalskii. Svarochnoye proizvodstvo. 2013. № 4. P. 30 – 33.
- [12]. N.A. Kozyrev, V.F. Igushev, R.E. Kryukov, A.V. Roor. Izvestiya vuzov. Chernaya metallurgiya. 2013. № 8. P. 33– 36.
- [13]. Patent 2484936 RF, MPK⁸ V 23 K35/362 Ceramic flux-addition/ Kozyrev N.A., Igushev V.F., Kryukov R.E.; Goldun Z.V.; FGBOU VPO Siberian State Industrial University - № 2012104939/02(007484), applied 13.02.2012.

HYDROGEN ABSORPTION EFFECT ON THE PLASTIC DEFORMATION LOCALIZATION OF LOW CARBON STEEL

S.A. Barannikova^{1,2}, D.A. Kosinov³, S.V. Kononov³,

O.A. Stolboushkina³, V.E. Gromov³

¹ Institute of Strength Physics and Materials Science SB RAS, Tomsk,
Russia.

² Tomsk State University, Tomsk, Russia.

³ Siberian State Industrial University, Novokuznetsk, Russia.

E-mail: gromov@physics.sibsiu.ru

Abstract

In the present study, the features of plastic strain localization and structure of polycrystalline low carbon steel 08pc were investigated after hot rolling and electrolytic hydrogen saturation. The method of double-exposure speckle photography have been used for identification of main types and parameters of plastic flow localization at different stages of strain hardening. Shown the effect of hydrogen on changing of defect substructure and cementite morphology by using optical and electron microscopy.

Keywords: hydrogen, speckle photography, strain localization, plasticity, wavelength.

Introduction

Increasing of reliability and extending the life of steel products is dependent on the content of harmful impurities. The hydrogen is one of such impurities that enters the metal, not only at all stages of the manufacturing process, but also during operation of articles thus significantly reducing their technological properties and service properties [1-3]. The equilibrium concentration of hydrogen in α -Fe is small, but it may be increased by electrolytic saturation [4, 5]. The combination of high hydrogen diffusibility and possibility of its transport by moving dislocations over long distances, which considerably exceeding the

length of the lattice diffusion paths is one of the difficulty for explanation of hydrogen effects [6].

There are many microscopic models based on the theory of dislocations [1, 2] developed to explain hydrogen effects. However, these approaches are insufficient because they do not include that the plastic deformation of solids localizelly develop during whole flow process [7-9]. Especially effectively this process manifests at the macroscale level when forming localization patterns are uniquely related with the laws of the strain hardening $\theta(\varepsilon)$ in force at the relevant stage of the process.

In this case, the patterns take the form of different types autowaves (autowaves of switching, phase autowaves etc.) [7-9]. In this regard, in the present study we attempted to figure out the effect of hydrogenation on macroscopic localization and structure of low-carbon steel.

Experimental procedure (Materials and methods)

Complex investigations of the nature of the plastic deformation inhomogeneity performed on samples of steel 08pc: after hot rolling (condition 1), and after laboratory electrolytic hydrogen saturation of the samples after hot rolling (condition 2). The initial average grain size in the cross section of the sample was $\sim 14 \pm 6$ microns and longitudinally $\sim 12 \pm 5$ microns. Samples with dimensions of the working part $50 \times 10 \times 2$ mm have been tensiled with testing machine "Instron-1185" at 300 K with velocity of 0.1 mm / min. The method of double-exposure speckle photography was used for investigation of macrolocalization plastic flow [10]. Hydrogen-charging of the samples was carried out within the three-electrode electrochemical cell with the 323 K temperature during 24 hours [4, 5] under the action of the constant controlled cathode, with potential -600 mV relative to a silver chloride electrode in 1 Normal sulfuric acid solution supplemented with 20 mg / l of thiourea. Current-voltage curves were recorded using potential tsio stata IPC-Compact. The hydrogenated samples were stored in liquid nitrogen before the mechanical

testing. The absolute concentration of hydrogen in the samples was determined by melting in an inert atmosphere at 602 RHEN analyzer. The method of atomic emission spectrometry was used for stratified analysis of the hydrogen distribution over the sample thickness by glow-discharge spectrometer (Profiler-2). Studies of the microstructure was conducted using optical microscopy (Neophot-21). Investigation of the phase composition and defect substructure of the samples was performed by electron diffraction microscopy (EM-125).

Experimental results

The yield plateau degenerates on plastic flow curves (Fig. 1) after hot-rolling (without hydrogen) after electrolytic hydrogen saturation (condition 2) within 24 hours as compared to initial state (condition 1). Also the decrease of the yield value and the tensile strength by ~ 25 MPa and decrease of the relative elongation after breaking by $\sim 5\%$ is observed. Using of the speckle imaging techniques has been revealed that character of development of the plastic flow localization patterns on the yield plateau is significantly different in the both of conditions. Data of velocity of single fronts localized deformation corresponding to Chernov-Luders lines are given in the Table 1.

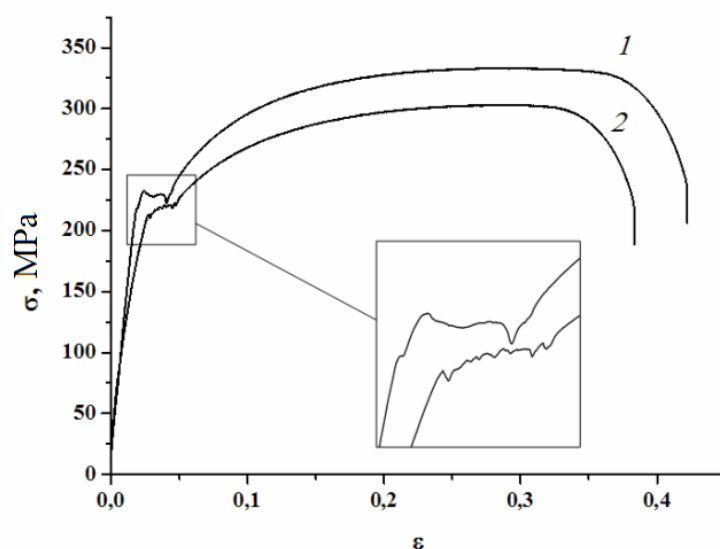


Fig. 1. Curves loading steel 08ps within the temperature of 300 K:
1 - samples in the initial condition (without hydrogen), 2 - hydrogenated in a three-electrode cell samples at a constant potential during the 24 hours; the yield plateau is highlighted for the initial and hydrogenated samples.

Table 1. Basic specifications about localization deformation of sheet steel 08pc during tensile.

Condition	Strainhardeningstages	Deformation localizationpatterns
1	Yieldplateau	Opposite traffic of single deformation localization zones ($V_{aw} \approx 8.5 \cdot 10^{-5}$ m/s; $3.8 \cdot 10^{-5}$ m/s; $6.8 \cdot 10^{-5}$ m/s; $8.5 \cdot 10^{-5}$ m/s)
	line stage	Travelling autowave of deformation localization ($V_{aw} \approx 5.3 \cdot 10^{-5}$ m/s; $\lambda \approx 8$ mm)
	Parabolic stage	Stationary system of deformation localization zones ($\lambda \approx 7.5$ mm)
2	Yieldplateau	Opposite traffic of single deformation localization zones ($V_{aw} \approx 1.3 \cdot 10^{-4}$ m/s; $5.5 \cdot 10^{-5}$ m/s)
	line stage	Travelling autowave of deformation localization ($V_{aw} \approx 6.3 \cdot 10^{-5}$ m/s; $\lambda \approx 6$ mm)
	Parabolic stage	Stationary system of deformation localization zones ($\lambda \approx 6$ mm)

Note. Convergence of the focus of localized plastic flow appears before the prefracture stage in the neck formation area (for the two conditions of steel 08pc).

The phase autowave of the localized plasticity is formed in the sample at the linear strain hardening stage. It is characterized not only by the propagation velocity V_{aw} , but also spatial period - long autowaves λ . These data can be obtained from Fig. 2 in the form of distributions of local elongations (component ε_{xx} of the tensor ε_{ij}) of the axes of the samples.

In the condition 1, $\lambda = 8$ mm, and $V_{aw} \approx 5.3 \cdot 10^{-5}$ m/s; in the 2th state, $\lambda = 6$ mm, and the propagation velocity $V_{aw} \approx 6.3 \cdot 10^{-5}$ m/s. The structure of localization focus in the condition 2 is difficult in contrast to condition 1. In this case, the high-amplitude peaks of local deformations, divided by the aggregate of low-amplitude peaks was revealed [11]. Earlier formed system of equidistant zones of strain localization becomes stationary at the stage of parabolic work hardening. Autowaves spatial period of the deformation localization is 7.5 mm for the condition 1 and it is 6 mm for the condition 2.

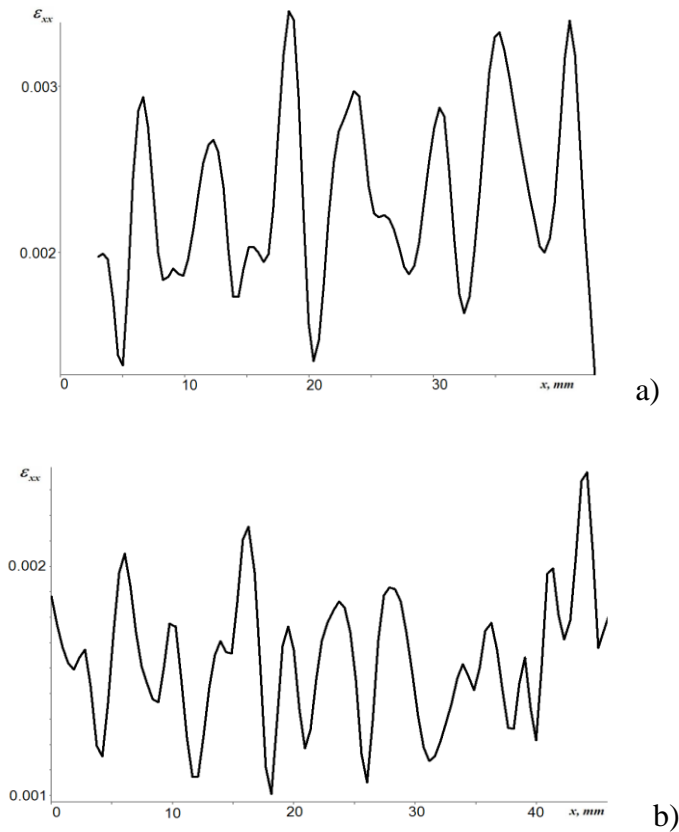


Fig. 2. Localization patterns of the plastic deformation of steel samples 08ps on the strain hardening stage is shown as distributions local elongation: in the initial condition (without hydrogen), $\varepsilon = 6.5\%$ (a); and in the hydrogenated condition within the three-electrode cell using the constant potential during for 24 h, $\varepsilon = 7.5\%$ (b).

At the pre-fracture stage, the stationary system of focus localized deformation, which qualify for the parabolic hardening stage, is changed by the gradually increasing stationary maximum. It is characterized by large amplitude of the local extension components ε_{xx} of plastic distortion tensor. This maximum indicates of the future site of ductile fracture of steel samples 08pc in condition 1 and 2, and since its inception almost all deformation is localized in the narrow zone of the sample.

It was found that hydrogen enhances the deformation localization and alters the quantitative parameters of the plastic strain localization pictures: the length and autowaves velocity of plastic strain localization. Summary results of the propagation velocity and lengths of the autowaves of plastic flow localization was shown in Table 1.

Investigation of the phase composition and dislocation substructure of steel samples 08pc was performed using diffraction electron microscopy techniques [12].

Analysis of the fragmented pattern, formed in the steel 08pc in condition 1 (after hot-rolling), showed that the relative area of the grain, occupied fragments with non-equiaxed and quasi-equiaxed forms is 0.7 and 0.1, respectively (the rest ~ 0.2 , grains are containing no fragments). The average cross dimensions of the quasi-equiaxed form fragments is ~ 1.6 μm and non-equiaxed form is ~ 0.6 μm .

There are two types of dislocation substructure within the fragments volume, and also into the grain volume, which does not contain low angle boundaries: mesh-type dislocation substructure (0.6 from the grain volume) and (0.4 from the grain volume). Scalar dislocation density averaged over all types of substructure is $\sim 2.4 \cdot 10^{10} \text{ cm}^{-2}$. There are bending extinction contours on electron microscopic images of the steel structure with dislocation density $\sim 1.3 \cdot 10^5 \text{ mm}^{-2}$ and average lateral dimension of ~ 190 nm. Such contours indicate the bending-torsion of the crystal lattice $\alpha\text{-Fe}$ in the condition 1, i.e., on the internal stress field formed in the steel during its thermomechanical processing. The grain boundaries and fragments are main sources of these fields. Electrolytic hydrogenation of the samples within 24 hours does not lead to a substantial changing of the steel structure. The fragmented substructure was found inside the grains (in condition 1) by electron microscopic methods. There are also mesh – type dislocation substructure or dislocation chaos type, the grain boundaries and fragments are sources of curvature – torsion of the steel crystal lattice, as evidenced by bending extinction contours. The quantitative analysis of the structure had shown the differences between two conditions of the structure, after hot rolling (condition 1) and after electrolytic hydrogenation (condition 2). As can be seen from Table 2, the electrolytic hydrogenation leads to a slight increase in average size of the fragments and also leads to significant expansion of the fragment sizes range. At the same time, steel hydrogenation accompanied

by the formation sites with quasi-equiaxed fragmented substructure in grain boundaries junctions. The range of fragment size of such fields is 100 - 550 nm. Presence of large amount of nanoscale fragments reflected in the structure of the electron diffraction pattern, which reflexes tend to the formation of the diffraction rings. It should be noted that before the hydrogen exposure (condition 1) such area is not detected. The forming of areas with nanoscale fragments were caused relaxation processes internal stress fields formed at the junctions of the grain boundaries of hydrogenated steel. It was revealed the slight decrease in the scalar density of dislocations due to the electrolytic hydrogenation. The insignificant (at ~ 1.14 time) reduction of the average size of the transverse bending extinction contours was found, which corresponds to a proportional increase of the amplitude of the internal stress fields. Evidently, this effect due to the hydrogenation processes of the steel crystal lattice. It has been found the insignificant increasing of the azimuthal component of the angle of complete disorientation of steel defect substructure (in ~ 1.2 times).

Table 2. Quantitative parameters of substructure of steel 08pc.

Condition	Fragments, μm		$\langle\rho\rangle, 10^{10}, \text{sm}^{-2}$	Contours		$\Delta\alpha, \text{deg.}$
	H	L		h, nm	$\eta, 10^5, \text{mm}^{-1}$	
1	0.6 ± 0.31	> 2.5	2.4	188.6	1.3	2.8
2	0.37 ± 0.16	0.85 ± 0.37	2.8	172.5	2.2	4.3

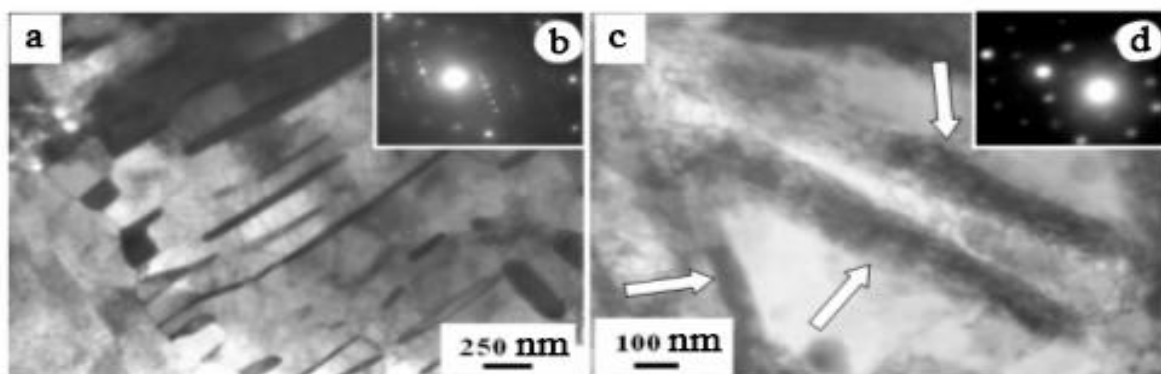


Fig. 3. EM pictures of the steel structure 08pc: initial condition without hydrogen (a, b) and prehydrogenated conditions (c, d); a, c - the bright-field pictures; b, d - microelectron pictures; (c) - the cementite plates are indicated by arrows.

This effect may be caused the influence of hydrogen on the steel defect substructure, located on the fragments subboundaries. The hydrogenation of steel has a significant impact on the carbide phase of the test material. It was found that the cementite plates lose facet and the speckled contrast revealed in the volume of plates (Fig. 3). Such morphology and structure changes of the plates may indicate decomposition of cementite during its interaction with the hydrogen atoms, namely, a "departure" of carbon atoms from the crystal lattice of cementite. Preferred sites of carbon atoms localization may be boundaries and grain boundary junctions.

The basic amount of hydrogen is concentrated in the surface layer after the electrolytic saturation of the sample. Simultaneously, there are two acting mechanisms of the hydrogen effect on structure and properties of the steel. The one mechanism leads to changes associated with hardening and the formation of micropores (hairline cracks in sufficient concentrations), and the other it leads to the changes due to the decomposition of cementite to form hydrocarbons (methine CH or methane CH₄ at high concentrations of hydrogen) [13, 14]. Upon decomposition of cementite under action of dissolved atomic hydrogen formed unsaturated hydrocarbon methine CH, which molecules have a sufficiently small size. It may be in the crystal lattice defects, including the subgrain boundary dislocations. In this case, the chemical reaction is $\text{Fe}_3\text{C} + \text{H} = \text{CH} + 3 \text{Fe}$. The heating for dehydriding shifts the chemical equilibrium towards the formation of cementite, because the reaction proceeds with a decrease in volume in this direction [14].

In the present paper, metallographic examination of samples was carried out by optical microscope. The microstructural investigation of the steel 08pc in the initial condition showed that ferrite is the main structural component, there is also perlite (Fig. 4 a), that is typical for low-carbon steels after hot rolling. As can be seen from Fig. 4, the structure of the steel in dependence of the sample thickness in the different conditions: (Fig. 4 a) - without hydrogen (condition 1) and (Fig. 4 b, c) after electrolytic hydrogenation (condition 2).

The structure observed slightly in the core after hydrogenation (Fig. 4b), while near the surface layer there is less pearlite structure (Fig. 4). This effect is identified as a partial decarburization at hydrogenation of carbon steel [14]. The average microhardness values for sample thickness were measured by PMT 3 microhardness tester. In the initial longitudinal section, within the core samples (condition 1), the microhardness was 1130 ± 10 MPa and near the surface - 1100 ± 15 MPa. After electrolytic hydrogenation (condition 2) the microhardness was 1330 ± 20 MPa and near the surface - 1250 ± 10 MPa. The data statistical processing showed that the microhardness values in the steel are significantly different before and after hydrogenation.

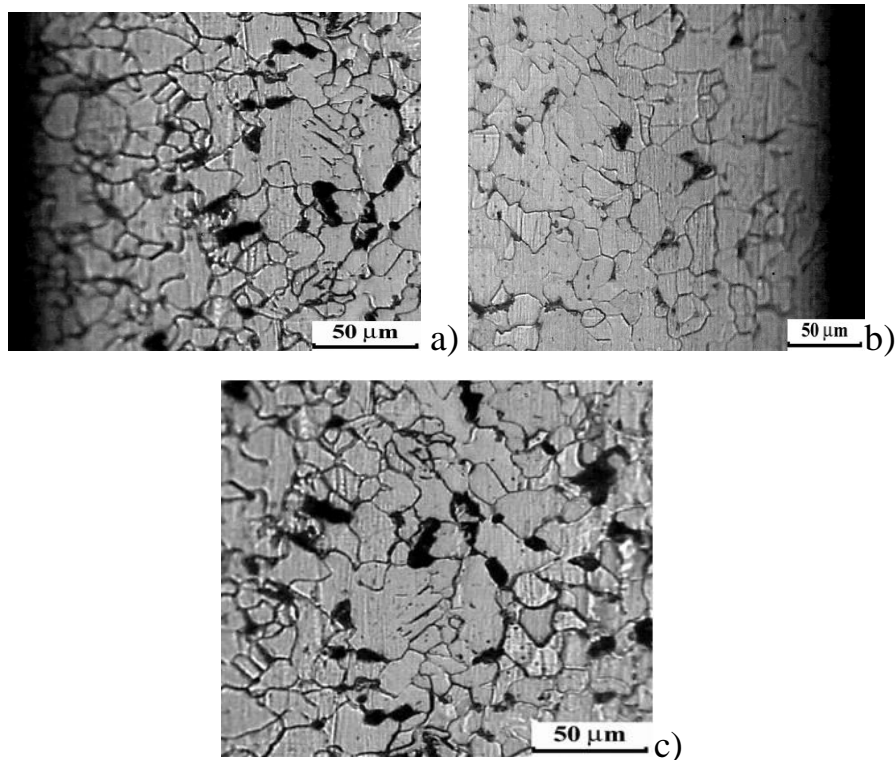


Fig. 4. Structure of steel 08ps: optical microscopy of the microsection thickness in the initial condition near the surface (a); in the hydrogenated condition near the surface (b); within the core (c).

Conclusion

Electrolytic hydrogen saturation of the low carbon steel 08pc samples leads to the change of the defect substructure, morphology and cementite plates and also it accompanied by the formation of the sites with nanoscale fragments in grain boundaries junctions. The hydrogen is reacted with cementite to form

hydrocarbon compounds in the phase boundary [13, 14], the pressure of it compounds reaches the critical values may lead to breakage. Thus, during subsequent deformation of the prehydrogenated steel, the area with a high level defects, which have been identified in the grain boundaries (the nanoscale fragmented substructure, the methine formation) subsequently will be as a microcracks sites formation. Change in the microstructure of steel affects on the stress-strain curves and also affects on the plastic strain localization patterns. Comparison of the data for the two conditions (initial condition and after hydrogenation) of steel 08pc showed that the localized plasticity sites have been formed and evolved throughout of the plastic flow process during tensile. Hydrogen enhances localization and changes the quantitative parameters of the macroscopic plastic strain localization: the length and the velocity of autowaves plastic strain localization [11, 15].

References

- [1]. H.K. Birnbaum, P. Sofronis. Hydrogen-enhanced localized plasticity-a mechanism for hydrogen-related fracture. *Mater. Sci. & Eng. A*. 1994. V. 176. pp. 191-202.
- [2]. P. Sofronis, Y. Liang, N. Aravas. Hydrogen induced shear localization of the plastic flow in metals and alloys. *J. Mech. A. Solids*. 2001. V. 20. pp. 857-872.
- [3]. V.P. Ramunni, De Paiva Coelho T., de Miranda P.E.V. Interaction of hydrogen with the microstructure of low-carbon steel. *Mater. Sci. Eng. A*. 2006. V. 435–436. pp. 504–514.
- [4]. Yu. Yagodzinsky, O. Tarasenko, S. Smuk, P. Aaltonen and H. Hänninen. A new method for studying thermal desorption of hydrogen from metals based on internal friction technique. *Physica Scripta*. 2001. V. 94. pp. 11-120.
- [5]. Y. Yagodzinsky, O. Todoshchenko, S. Papula, H. Hänninen. Hydrogen solubility and diffusion in austenitic stainless steels studied with thermal desorption spectroscopy. *Steel Res. Int.* 2011. 82. pp. 20–25.

- [6]. I.M. Robertson. The effect of hydrogen on dislocation dynamics. *Eng. Frac. Mech.* 2001. V. 68. pp. 671-692.
- [7]. L.B. Zuev, V.I. Danilov, S.A. Barannikova, V.V. Gorbatenko. Autowave model of localized plastic flow of solids. *Phys. Wav. Phen.* 2009. V. 17. pp. 1–10.
- [8]. L.B. Zuev, S.A. Barannikova, Evidence for the existence of localized plastic flow auto-waves generated in deforming metals. *Natur. Sci.* 2010. V. 2. pp. 476-483.
- [9]. L.B. Zuev, S.A. Barannikova, Plastic flow macrolocalization: autowave and quasi-particle. *J. Mod. Phys.* 2010. V. 1 pp. 1-8.
- [10]. L.B. Zuev, V.V. Gorbatenko, K.V. Pavlichev. Elaboration of speckle photography techniques for plastic flow analyses. *Measur. Sci. & Technol.* 2010. V. 21. pp. 1-5.
- [11]. S.A. Barannikova, D.A. Kosinov, M.V. Nadezhkin, A.G. Lunev, L.B. Zuev, V.E. Gromov. Investigation of the plastic strain localization patterns by the electrolytic hydrogenation of low carbon steels. *Fund.Probl.of Mod. Mater.* 2013. V.10. №. 3. pp. 329-333.
- [12]. D.A. Kosinov, V.E. Gromov, Y.F. Ivanov, S.V. Konovalov, N.S. Derbicheva. Evolution of the structure and phase composition of low carbon steel during hydrogenation. *Nanoengineering.* 2013. № 8. pp. 12 -14.
- [13]. J.V. Grdina, L.B. Krepysheva. About floken formation mechanism. *Proceed. of the Univ. Ferr. Metall.* 1961. № 10. pp. 94-103.
- [14]. M.M. Krishtal, A.A. Karavanova, A.A. Jeremic, I.S. Yasnikov. Reversibility decomposition effect of cementite during hydrogenation of carbon steel. *Acad.Sci. Rep.* 2009. V. 425. № 6. pp. 754-756.
- [15]. G.V. Shlyahova, S.A. Barannikova, L.B. Zuev, D.A. Kosinov. Localization of plastic deformation in the single crystals doped by Fe during electrolytic hydrogenation. *Proceed. of the Univ. Ferr. Metall.* 2013. № 8. pp. 37 -42.

FEATURES SURFACE TOPOLOGY OF FE-SI ALLOY IN THE LASER RADIATION EXPOSURE

V.A. Feodorov, P.M. Kuznetsov

Department of General Physics, Tambov G.R. Derzhavin State University,

Internatsionalnaya, 33. Tambov 392622, Russia.

E-mail: feodorov@tsu.tmb.ru, kuznetsov1985@list.ru

Abstract

The action laser radiation on a metal surface on the latter formed an wavy-like topography which can be divided into three stages of the spatial growth of the waves (the region stabilize, surface area of exponential growth and nonlinear waves) are shown. Wavy-like topography of the crater formation is associated with the appearance of thermocapillary instability. Breaking waves on nonlinear stage of growth could be related to the difference of the phase velocities.

Keywords: thermocapillary instability, laser, surface topology, waves.

The appearance of lasers has provoked intense development of research in the field of pulsed energy effects. Due to the special properties of laser light (coherence, polarization, high energy density, etc.) is made possible to manage internal processes in the solid state and to produce surface modification of materials [1], in particular metals.

Experimental technique

In the experiments, the polycrystalline plate alloy Fe-Si (Si ~ 3.4%) a thickness of 0.25 mm average particle size of 10 mm, prepared as metallographic grinding. Treatment of samples was performed on laser installation LTA-4-one with the active element based on yttrium-aluminum garnet ($\lambda = 1.064$ mm). Topological research surface after laser irradiation was performed on a metallographic microscope, as well as non-contact profilometer Wyko NT 9080 (Bruker AXS) (wavelength $\lambda \sim 670$ nm).

Experimental results

The critical energy density of radiation, the excess of which leads to melting of the surface $\approx 1.07 \cdot 10^5$ W·cm⁻² for a rectangular pulse with a duration of $3 \cdot 10^{-3}$ s.

The results are presented in Fig. 1. It is seen that by irradiating the surface with an intensity of $1.07 \cdot 10^5 \text{ W} \cdot \text{cm}^{-2}$ (Fig. 1 a) melt which is characterized by formation of a single wave. In the area of fusion after exposure to laser radiation with an intensity of $\sim 1.1 \cdot 10^5 \text{ W} \cdot \text{cm}^{-2}$ (Fig. 1 b) on the surface of Fe-Si Alloy begins to form a quasi-periodic wave is formed, this intensity is the threshold for the formation of a wave of relief.

Height above equilibrium melt surface at low intensities does not exceed 3-4 microns (Fig. 1 a-c), whereas irradiation of the surface Fe-Si alloy high intensity rise of the melt is up to 8 microns (Fig. 1 d-f). It is accompanied by a change in the total curvature of the surface. At low intensity laser power (Fig. 1 a) relief wave is absent, the surface is smooth. In the central part of the crater formed "jet". As there is a considerable increase in the intensity of curvature of the surface (Fig. 1 d-f), which indicates the formation of the molten bath and the existence of surface melt convection. Because of this surface area exposure to radiation takes a toroidal-like shape, which is formed by wavy relief (Fig. 1 d-f). In the central part of the crater formed depression by vapor recoil.

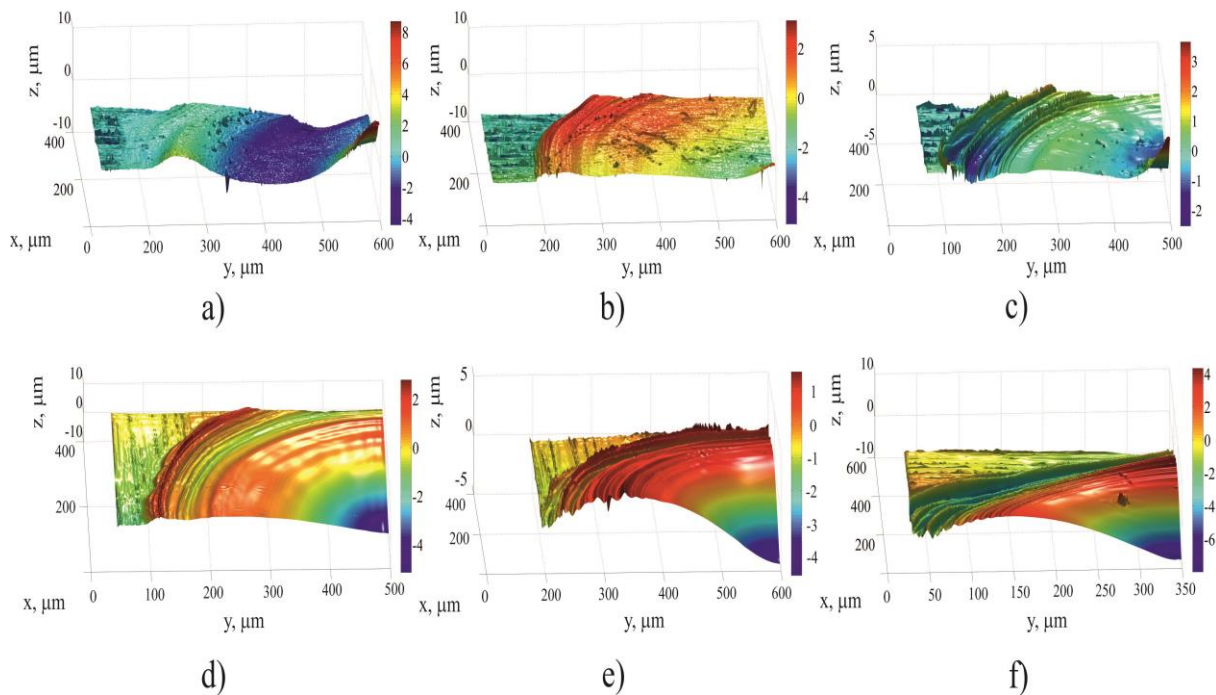


Fig. 1. The evolution of topology of the crater with variety of the laser power density:

- a) $1.07 \cdot 10^5 \text{ W} \cdot \text{cm}^{-2}$; b) $1.10 \cdot 10^5 \text{ W} \cdot \text{cm}^{-2}$; c) $1.16 \cdot 10^5 \text{ W} \cdot \text{cm}^{-2}$;
d) $1.3 \cdot 10^5 \text{ W} \cdot \text{cm}^{-2}$; e) $1.53 \cdot 10^5 \text{ W} \cdot \text{cm}^{-2}$; f) $1.7 \cdot 10^5 \text{ W} \cdot \text{cm}^{-2}$.

Based on the results of the melt surface at the time of laser radiation [2-4] can be concluded that the disturbance appearing on the surface of the melt stream is carried away from the center to the periphery. Applying this to our case, it can be argued, the formation of relief caused by convective instability surface capillary wave propagation.

Thus, the relief of the crater formed by the impact of the laser radiation is the result of the movement of the capillary waves on the surface of the melt, which provides information about the evolution of capillary waves in space. For this purpose, it is advisable to study profilograms crater.

Profilogram showing the characteristics of the formation of the wave of relief, shown in Fig. 2. As a typical example of the wave of relief chosen crater produced by irradiation with an intensity of $2.21 \cdot 10^5 \text{ W} \cdot \text{cm}^{-2}$. The inset shows the dependence of the wave amplitude (the difference between the amplitudes of neighboring) distance from the center of the crater.

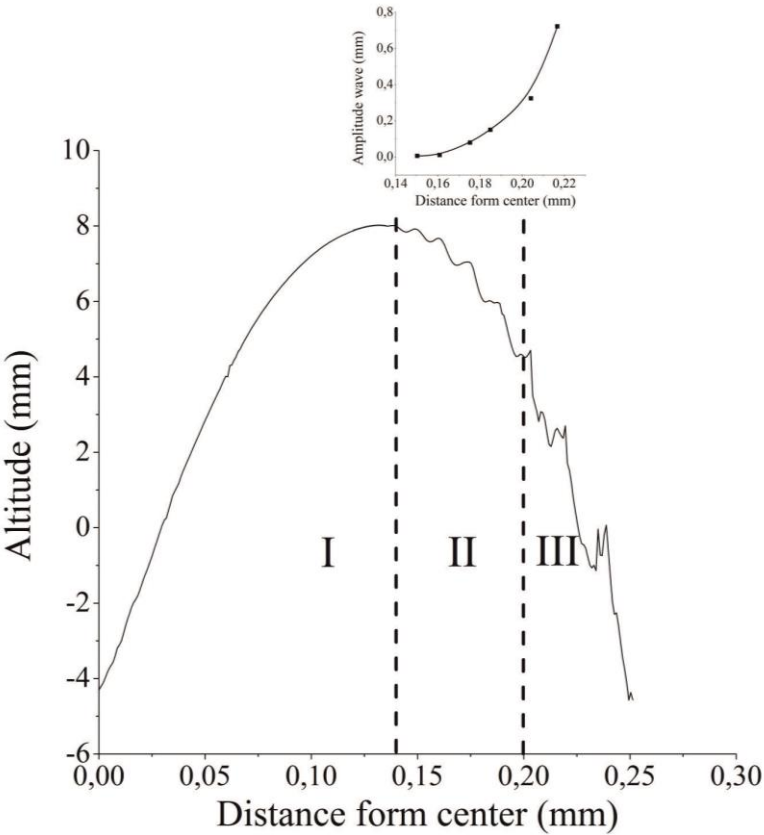


Fig. 2. The dependence height rise of the melt on distance to center of the crater for $(2.21 \cdot 10^5 \text{ W} \cdot \text{cm}^{-2})$.

Formation relief in the crater, as seen from Fig. 2 has three distinct zones:

- I. stabilizing the surface area ($\sim 0-0.15$ mm), waves formation does not occur;
- II. exponential growth region waves ($\sim 0.15-0.2$ mm), in the inset of the amplitude of the distance to the center of the crater;
- III. zone of non-linear growth of waves ($\sim 0.2-0.25$ mm).

The presence of these regions characterize the surface of the melt, as a non-linear medium - amplifier.

In the field of non-linear growth of waves a division into two separate waves. This may be due to the emergence of secondary instabilities in excess of the initial wave amplitude of the critical value [5], which is due to the difference in their phase velocities.

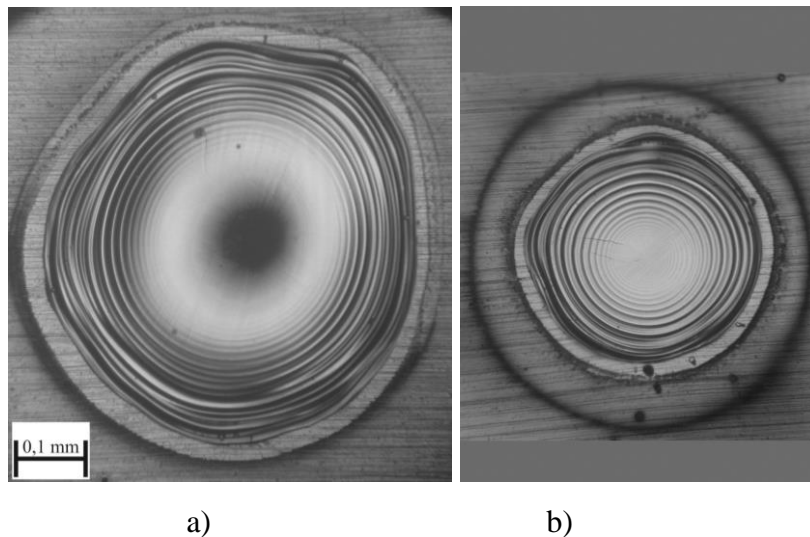


Fig. 3. View of the typical fracture surface of iron when exposed to laser light with an intensity of $2.9 \cdot 10^5 \text{ W} \cdot \text{cm}^{-2}$, a) front side, b) bottom side.

Increasing power density of up to $\sim 2.64 \cdot 10^5 \text{ W} \cdot \text{cm}^{-2}$ is on the opposite side of the plate (thickness = 0.3 mm) the formation of zones similar to the impact area on the front side (Fig. 3 a, b). On the reverse side, as can be seen from Fig. 3 b, there is a more pronounced relief. Detailed topology of the output characteristic of the crater on the other side, with irradiation of a metal surface with a power density of $2.9 \cdot 10^5 \text{ W} \cdot \text{cm}^{-2}$ is shown in Fig. 4.

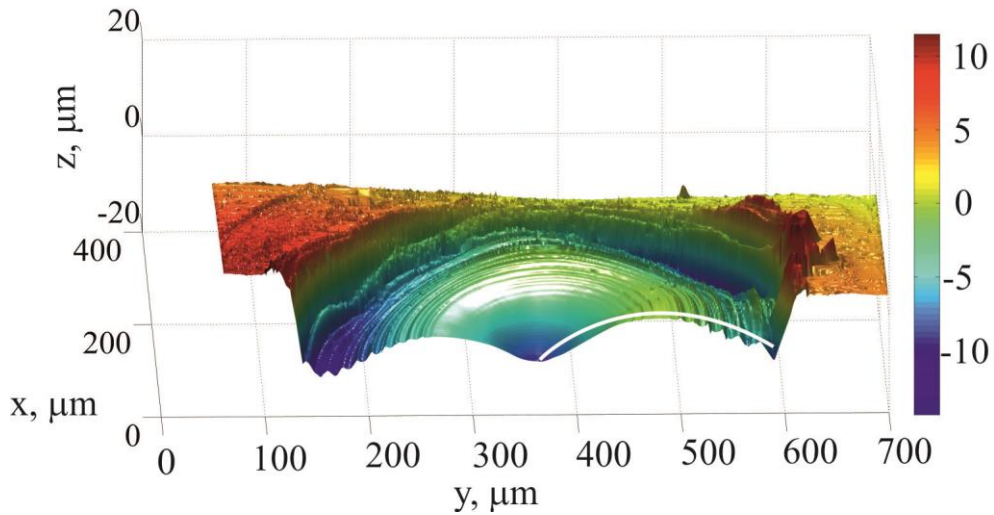


Fig. 4. A typical topology crater on bottom side of the plate, resulting from exposure to laser radiation ($2.9 \cdot 10^5 \text{ W} \cdot \text{cm}^{-2}$).

As can be seen from Fig. 4 performs the melt volume oscillations with an amplitude greater than 10 microns. Relief profile of the crater is shown in Fig. 5 marked by a white stripe on Fig.4). One can see the formation of the three areas, with the width of the non-linear growth is $\sim 0.075 \text{ mm}$.

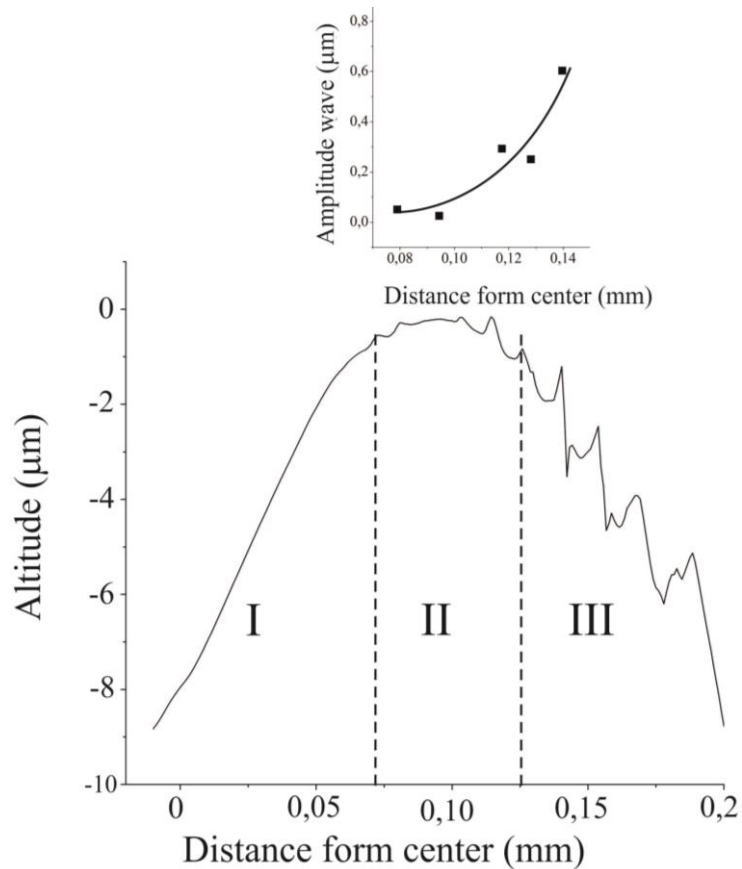


Fig. 5. Profilogram crater on the bottom side of the plate.

Discussion of results

Shape of the central part of the crater (Fig. 4) shows the appearance of the cavity (hollow channel) during exposure to laser radiation. Partial collapse of the cavity leads to a depression in the center of the crater.

It is known [6, 7] that the thermocapillary instability accompanied by the formation of a ring of the periodic relief on the surface of metal with a characteristic period of about 10^5 - 10^4 m⁻¹. To compare the observed structures with this mechanism were calculated wave- wave numbers. The wave numbers, the resulting wave-like structures for the front and back respectively: to the front of the $k_1 = 5.2 \cdot 10^5$ m⁻¹ for the reverse side $k_2 = 10^6$ m⁻¹. These values are of the same order with the structures formed by the thermocapillary mechanism. Sufficient conditions appearance thermocapillary instability are: the formation of the melt at the sample surface (which occurs at about $1 \cdot 10^5$ W·cm⁻²) there is a significant radial temperature gradient in the molten bath ($\sim 10^6$ K · m⁻¹), the existence of the thermal flow directed normal to the surface of the melt (e.g., by thermal radiation). Time increment thermocapillary instability is $\sim 10^3$ s⁻¹ for the wave numbers $\sim 10^5$ m⁻¹ [6], which is comparable with the effect of laser radiation and the characteristic parameters of the resulting structures.

Conclusion

Thus, the topography of the crater is undergoing significant changes with increasing power density. Revealed the existence of three growth areas of waves that describes the surface of the melt, as a non-linear medium - amplifier [5]. It is shown that the formation of undulating topography of the crater due to the appearance of thermocapillary instability and action of vapor recoil.

References

[1]. P.M. Kuznetsov, V.A. Fedorov. Formation of the relief of the crater by the laser radiation on the surface of the alloy Fe-Si. Izvestiya of the University of Tambov. Series: Natural and Technical Sciences. 2010. V. 15. № 6. p. 1790-1793.

- [2]. V.G. Prokoshev. Micro-and nanostructure of hydrodynamic instabilities induced by laser radiation on the surface of solids, and their methods of laser diagnostics and scanning probe microscopy. The Abstract. Novosibirsk, (2008) 41 p.
- [3]. V.G. Prokoshev and e.t. Non-stationary laser thermo-chemical processes on the surfaces of metals and their visualization by means of laser intensifier. "Quantum Electronics", 25. № 4 (1998) pp. 337-340.
- [4]. D.V. Abramov et al. Melting carbon heated concentrated laser radiation in air at atmospheric pressure and a temperature not exceeding 4000 K. JETP Lett. M. 84. № 5. pp. 315-319.
- [5]. E. Infeld, G. Rowlands. Nonlinear waves, solitons and chaos. "Fizmatlit", Moscow, 2006. 480 p.
- [6]. Laser Materials Processing Technologies: Modern problems of fundamental research and applications // Ed. Panchenko V.Y. "Fizmatlit", Moscow. 2009. 664 p.
- [7]. A.F. Banishev, V.S. Golubev, O.D. Khramova. Study of the Keyhole-Formation Dynamics. Laser Physics. V.3. № 6. 1993. pp. 1198-1202.

MATERIALS STRUCTURE DESCRIPTION BY FRACTAL COMPLEX

S.N. Starovackaya, L.P. Myshlyaev, I.V. Tsiryapkina

Siberian state industrial university, Kirov str., 42, Novokuznetsk, Russia.

Traditional views on the structure formation processes often do not meet modern creating materials requirements with desired properties. Representation of nonlinear dynamics (synergetic, self-organization) are adequate when materials are represented as hierarchically organized multiscale systems [1, 2]. Informative materials' structure descriptions based on model fractals, on physical representations about structures' dynamics transformation and

presented research areas have been obtained in this direction nowadays. It also points interdisciplinary researches' necessity using achievements of both science of material and control theory. The identification of natural (real) materials' structures by fractals is one of the priorities and also noted the expediency of interconnecting fractals identification and the expediency of using the traditional statistical concepts methods to describe the discrepancies of fractals identification [1,3].

Depending on the goal of creation materials' structure models and the initial information, the following statements of problems could be made [4].

Problem I

Given:

1. Natural materials' structures

$$St_j; \quad j = \overline{1, J},$$

where j –structure's number; J – structures' quantity.

2. Typical fractals' set

$$Fr_l; \quad l = \overline{1, L},$$

where l - typical fractal's number; L - fractals' quantity.

3. Identification criterion

$$Q_{j,l} = \sum_{m;n;l=1}^{M,N,L} |St_j(m,n) - Fr_l(m,n)| \rightarrow \min,$$

where m, n – quantity of pixels in the image structure.

4. Constraint $M \in \overline{1, M^{max}}$, $N \in \overline{1, N^{max}}$, где M^{max} , N^{max} – maximum quantity of pixels.

Required:

1. Choose a fractal with minimum Q from fractals' set Fr_l .

Problem II

Given:

1. Natural materials' structures

$$St_j; \quad j = \overline{1, J},$$

where l – structure's number; J – structures' quantity.

2. Typical fractals' set

$$Fr_l; \quad L = \overline{1, L},$$

where l – typical fractal's number; L - fractals' quantity.

3. Material's structure model

$$St_j^M = \sum_{j,l=1}^{J,L} \alpha_{lj} * Fr_l + \varepsilon_j,$$

where ε_j - model's discrepancy (disturbance interference), α_{lj} - required weighted coefficients.

4. Identification criterion

$$a) \quad Q_j = \sum_{j=1}^J |St_j(m, n) - St_j^M(m, N)| \rightarrow \min$$

$$b) \quad \tau_{r\varepsilon\varepsilon} \rightarrow \min,$$

where $\tau_{r\varepsilon\varepsilon}$ – autocorrelation dip of discrepancy.

5. Constraint $M \in M^{max}, N \in N^{max}$

Required:

1. To figure out optimum weighted coefficients α_{lj} .
2. To figure out the dominant typical fractal.

Problem III

Given:

1. Natural materials' structures

$$St_j; \quad j = \overline{1, J},$$

where j – structure's number; J – structures' quantity.

2. Typical fractals' set

$$Fr_l; \quad L = \overline{1, L}$$

where l – typical fractal's number; L - fractals' quantity.

3. Material's structure model

$$St_j^M = \cup \{Fr_l / S_{kl}\} + \varepsilon_j,$$

where S_{kl} - attracting space of natural structure for 1 - fractal model; k - number of attractive space; ε_j - model's discrepancy.

4. Identification criterion

$$Q_j = \sum_{k=1}^K S_{kl} \sum_{m,n=1}^{M,N} |St_j(m,n) - St_j^M(m,n)| / S_{kl}(m,n) \rightarrow \min,$$

where K - attractive spaces' quantity

5. Constraint

$$M \in M^{max}, N \in N^{max}, K \in K^{max}.$$

Required:

1. Figure out the size of attracting space S_{kl} for Fr_l .
2. Make structure model using Fr_l/S_{kl} combinations.

Problem IV

Given:

1. Natural materials' structures

$$St_j; \quad j = \overline{1, J},$$

where j –structure's number; J -structures' quantity.

2. Mathematical notation of forming fractals procedure [3]

$$a) \quad x_{n+1} = f(x_n) = (1 + r)x_n - rx_n^2,$$

where r –increment rate.

$$b) x_{n+1} = x_n^2 + C,$$

where C –complex variable.

3. Generator fractals' algorithm $Fr_l(r, c), l = \overline{1, L}$ - mathematical notations' quantity.

4. Identification criterion

$$Q_j = \sum_{m,n=1}^{M,N} |St_j(m,n) - Fr_l(m,n,c)| \rightarrow \min$$

5. Constraint

$$M \in M^{max}, N \in N^{max}, L \in L^{max}.$$

Required:

1. Determine the parameters r, C , minimizing Q .

Choice of specific statements of problems is based on natural materials' structures and stated objectives.

Satisfactory description in the first statement of problem is possible only in the simplest cases and good agreement model fractals with natural structures. That is why the more complicated task solution is better than easier one. Model fractals which fractal dimension close to natural structure dimension should be pre-selected to solve the second statement of problem (Table 1).

Table 1. Characteristics of Natural structures and model fractals.

Natural structures and theirs fractal dimension D_{St}	Model fractals and theirs fractal dimension D_{Fr}
Structure 1 $D_{St_1} = 1,6527$	Fractal 1.1 $D_{Fr_{1.1}} = 1,6667$ Fractal 1.2 $D_{Fr_{1.2}} = 1,6131$ Fractal 1.3 $D_{Fr_{1.3}} = 1,6131$ Fractal 1.4 $D_{Fr_{1.4}} = 1,6131$
Structure 2 $D_{St_2} = 1,6847$	Fractal 1,1 $D_{Fr_{1.1}} = 1,6667$ Fractal 2 $D_{Fr_2} = 1,7227$
Structure 3 $D_{St_2} = 1,7327$	Fractal 2 $D_{Fr_2} = 1,7227$ Fractal №3 $D_{Fr_3} = 1,7373$

The first variant solution of the second problem statement is made up of interconnecting fractals with the same weighted coefficients α_{ij} for the whole structure. The obtained values of the identification criteria for different combinations of model fractal pairs are presented in Tables 2 and 3 and complex examples describe in figures 1 and 2 respectively for the first and second natural structures.

Table 2. The obtained values of the identification criteria.

Model fractals	Fractal 1.1	Fractal 1.2	Fractal 1.3	Fractal 1.4
Fractal 1.1	-	$Q_{j,l} = 105,6$	$Q_{j,l} = 100$	$Q_{j,l} = 104,7$
Fractal 1.2	$Q_{j,l} = 105,6$	-	$Q_{j,l} = 128,3$	$Q_{j,l} = 114,9$
Fractal 1.3	$Q_{j,l} = 100$	$Q_{j,l} = 128,3$	-	$Q_{j,l} = 108,1$
Fractal 1.4	$Q_{j,l} = 104,7$	$Q_{j,l} = 114,9$	$Q_{j,l} = 108,1$	-

Table 3. The obtained values of weighted coefficients.

Model fractals	Fractal 1.1	Fractal 1.2	Fractal 1.3	Fractal 1.4
Fractal 1.1	-	$\alpha_{1.1} = 0,8$ $\alpha_{1.2} = 0,2$	$\alpha_{1.1} = 0,6$ $\alpha_{1.3} = 0,4$	$\alpha_{1.1} = 0,8$ $\alpha_{1.4} = 0,2$
Fractal 1.2	$\alpha_{1.1} = 0,8$ $\alpha_{1.2} = 0,2$	-	$\alpha_{1.2} = 0,7$ $\alpha_{1.3} = 0,3$	$\alpha_{1.2} = 0,3$ $\alpha_{1.4} = 0,7$
Fractal 1.3	$\alpha_{1.1} = 0,6$ $\alpha_{1.3} = 0,4$	$\alpha_{1.2} = 0,7$ $\alpha_{1.3} = 0,3$	-	$\alpha_{1.3} = 0,5$ $\alpha_{1.4} = 0,5$
Fractal 1.4	$\alpha_{1.1} = 0,8$ $\alpha_{1.4} = 0,2$	$\alpha_{1.2} = 0,3$ $\alpha_{1.4} = 0,7$	$\alpha_{1.3} = 0,5$ $\alpha_{1.4} = 0,5$	-

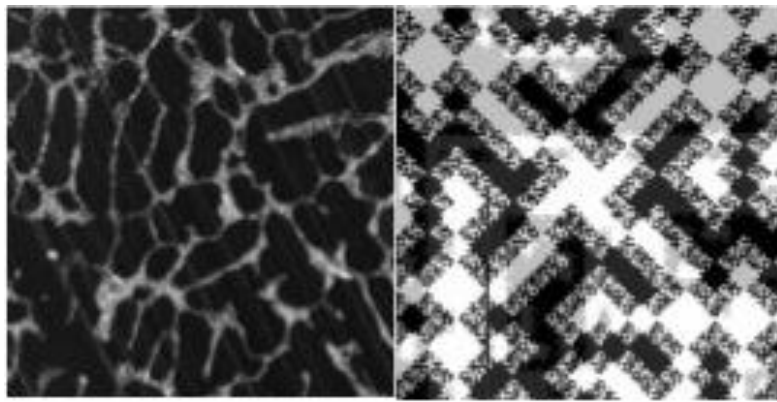


Fig.1. The Example of the first structure's complex description by fractal 1.1 and fractal 1.3 with the same weighted coefficient value α_{ij} for the whole structure.

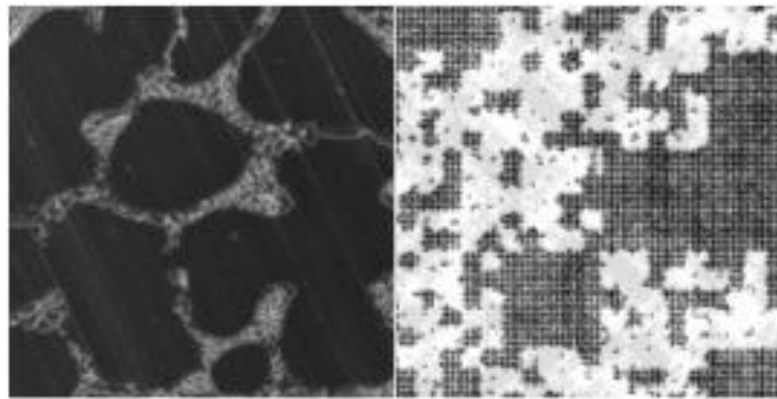


Fig. 2. The Example of the second structure's complex description by fractal 1.1 and fractal 2 with the same weighted coefficient value α_{ij} for the whole structure.

The second variant solution of the second problem statement is made up of interconnecting fractals with different weighted coefficients α_{ij} for each structure's pixel. The second variant solution of the second problem

considerably improved the values of identification criteria (table 4 and figures 3 and 4 respectively for the first and second natural structures.)

Table 4. The obtained values of the identification criteria.

Model fractals	Fractal 1.1	Fractal 1.2	Fractal 1.3	Fractal 1.4
Fractal 1.1	-	$Q_{j,l} = 71,3$	$Q_{j,l} = 62$	$Q_{j,l} = 59,4$
Fractal 1.2	$Q_{j,l} = 71,3$	-	$Q_{j,l} = 80,2$	$Q_{j,l} = 81,6$
Fractal 1.3	$Q_{j,l} = 62$	$Q_{j,l} = 80,2$	-	$Q_{j,l} = 71,9$
Fractal 1.4	$Q_{j,l} = 59,4$	$Q_{j,l} = 81,6$	$Q_{j,l} = 71,9$	-

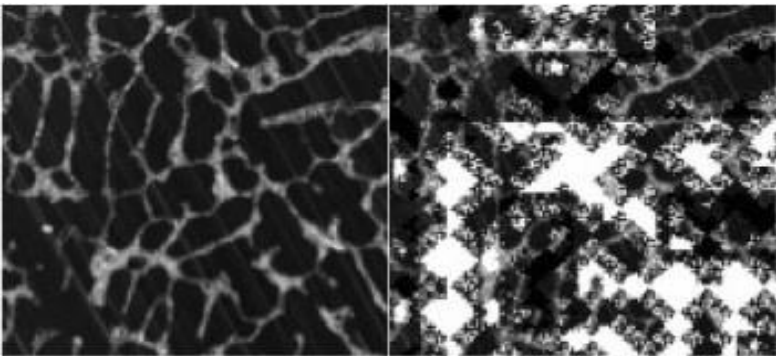


Fig. 3. The example of the first structure's complex description by fractal 1.1 and fractal 1.3 with different weighted coefficients α_{lj} for each structure's pixel.

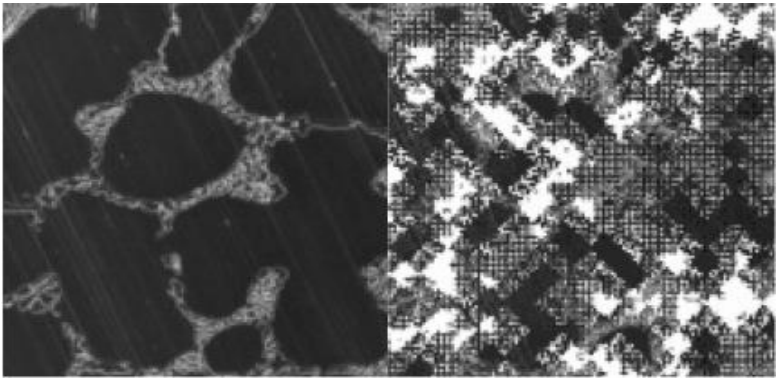


Fig. 4. The Example of the second structure's complex description by fractal 1.1 and fractal 2 with different weighted coefficients α_{lj} for each structure's pixel.

The best results were obtained in the solution of the third problem statement where the most appropriate model fractals were selected for each natural structure's fragment (Fig. 5).

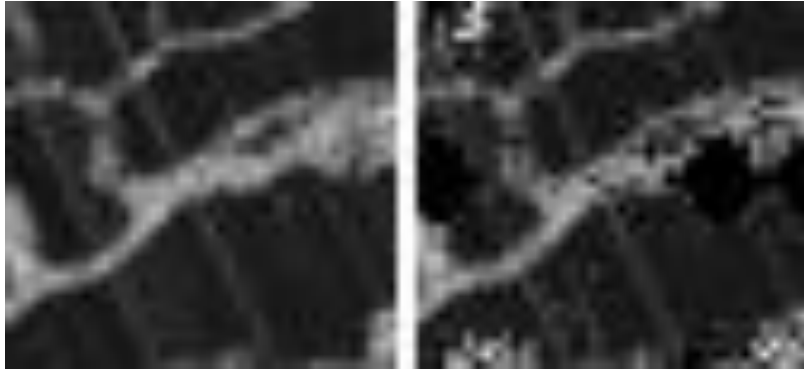


Fig. 5. The example of the first natural structure fragments' description by the most appropriate model fractals.

Conclusion

Different material description variants by the fractal complex are possible and depend on the application, required model structure accuracy, the initial information and computing resources. The most accurate model is obtained as the result of the individual structure fragments' description by model fractals.

References

- [1]. V.E. Ivanova, A.S.Balankin, I.Z. Bunin A.A. Oksogoev. Synergetics and Fractals in Materials. Moscow: Nauka, 1994. 383 p.
- [2]. P.V. Makarov, I.Y. Smolin, Y.P. Stefanov, others. Nonlinear mechanics of geomaterials and geomeia. Novosibirsk: Academic Publishing House "Geo", pp. 2007-235.
- [3]. L.B.Zuev, S.N. Starovatskaya, LP Myshlyaev. Task of controlling the structure of materials. Abstracts of the International Conference - "hierarchically organized system of animate and inanimate nature". IFPMSORAN-Tomsk, 2013, pp. 67-68.
- [4]. S.N. Starovatskaya, L.P. Myshlyaev, I.V. Tsiryapkina. For the task of identification material structures fractals. Proceedings of the IX-Russia scientific - practical conference - "Automation in education, science and industry", Novokuznetsk, 2013. pp. 400-403.

STRUCTURE AND PROPERTIES OF SURFACE ALLOY FORMED BY HIGH - INTENSITY ELECTRON BEAM TREATMENT OF THE FILM (Ti OR TiCu) / SUBSTRATE (AlSi)

Yu.F.Ivanov^{1,2}, E.A.Petrikova¹, A.V.Tkachenko²,

A.D.Teresov¹, A.A.Klopotov³

¹ Institute of High Current Electronics SB RAS, Tomsk, Russia.

² National Research Tomsk Polytechnic University, Tomsk, Russia.

³ Tomsk State University of Architecture and Building, Tomsk, Russia.

E-mail: yufi55@mail.ru

Abstract

Surface alloys of Al-Si-Ti and Al-Si-Ti-Cu systems have been formed under quenching from the molten state at cooling rates $\sim 10^6$ K/s. The studies of the structure and properties have been carried out and divisible increasing of mechanical (nano-and micro-hardness), physical (Young's modulus), tribological (wear resistance) properties have been realized.

Introduction

One way to improve the service characteristics of machine components and machinery is surface alloying, in which special surface properties are achieved by continuous or local formation of relatively thin surface doped layers. The properties of these layers meet the service requirements [1]. Effective method of the specified structural - phase modification of the surface layer is a pulsed electron-beam treatment, technology and equipment support are developed in Russia and in particular at the Institute of High Current Electronics (HCEI SB RAS). To date, at the HCEI SB RAS have been created experimental facility with electron source, allowing to carry out research at the different values of the energy density of the electron beam, the duration and the number of pulses [2-4]. The aim of the work is formation, analysis of the structure and properties of the surface alloys synthesized on the samples of eutectic silumin AK12M2MgN grade by pulsed electron beam treatment of the film / substrate system.

Material and research technique

Coatings composition Ti-Cu of thicknesses $\sim 0.5 \mu\text{m}$ and $1 \mu\text{m}$ have been synthesized by the vacuum arc technique on a silumin AK12M2MgN grade substrate by cathode (Ti-12%Cu) evaporation. Arc evaporator DI100 with enhanced cooling of the working cathode has been used during coating deposition, thus reducing the proportion of the droplet fraction in the coating and reduces the size of the microparticles. Prior to coatings deposition substrates were subjected to argon ions bombardment and during the last one the surface layer was cleared from the adsorbed gases and dielectric inclusions. Process parameters have been chosen thus that there is no significant heating and etching of the surface of specimens: an ion current density on the substrate was not more than 1.5 mA/cm^2 , the temperature during the ion bombardment did not exceed $\sim 348 \text{ K}$. Optimization of the deposition modes has been carried out such that the growth rate of the coatings was high, but the maximum sizes of the microparticles presented in the plasma flow did not exceed the thickness of the coating in diameter. According to this requirements the synthesis of Ti-Cu coating has been realized at an argon pressure of 0.2 Pa and arc current 60 A , thus the coating growth rate of $1.5 \mu\text{m}$ per hour. During deposition the samples were at a floating voltage (-15 V). The samples temperature during coating deposition did not exceed 393 K . The melting of the film / substrate system has been carried out by high-intensity pulsed electron beam submillisecond duration of exposure on the "SOLO" setup [5, 6]. Parameters of the electron beam: an electron energy $eU = 18 \text{ keV}$, beam energy density $E_s = (10 - 30) \text{ J/cm}^2$, pulse duration $\tau = 20, 50, 100, 200 \mu\text{s}$, the number of pulses $N = 3-30$.

The phase composition of the surface layers were examined by X-ray diffraction analysis (XRD 6000 diffractometer). The structure of the treated surface was analyzed by scanning electron microscopy (SEM-515 Philips microscope). The elemental composition of the material surface layer was

determined by X-ray microanalysis using EDAX ECON IV microanalyzer, which is attached to the scanning electron microscope SEM-515 «Philips».

The hardness of the surface layer of the film/substrate system at various stages of the electron- ion plasma exposure was measured at a load of 100, 200 и 500 mN (Vickers method, PMT-3 device) and at a load changing from 5 mN to 300 mN (Nano Hardness Tester NHT-S-AX-000X device). Friction coefficient and wear rate of the surface layer were measured on a tribometer (CSEM, Switzerland) in a disk – pin geometry at a room temperature and humidity. VK8 alloy ball with a 3 mm diameter has been used as a counter face, track diameter was (4-6) mm, rate of rotation – 2.5 cm/ s, load - (1-5) N, stop distance - (50 - 100) m, the number of revolutions - (3000-8000). Degree of a surface layer wear was determined after profilometry of formed track by a laser optical profilometer MicroMeasure 3D Station (Stil, France). The wear rate was calculated by the formula

$$V = \frac{2 * \pi * R * A}{F * L}, [mm^3 / (N \cdot m)],$$

where R - track radius [mm], A - cross-sectional area of the channel wear [mm²], F - the magnitude of the applied load [N], L - ball traversed distance [m].

Research results and discussion

As an integrating irradiation parameter it is convenient to choose the following characteristic: $W_S = (E_S * N / \tau)$, which takes into account the power density of the electron beam and background heating of the material at a multi-pulse treatment. Based on this irradiation parameter experimentally has been established that the TiCu film in a film / substrate (silumin) system does not melt at $W_S \sim 0.5 * 10^6$ (W/cm²*s)*pulse and less. In this case, the coating is remained, multiple cracking is fixed. The alloy Al-Si-Cu (a weight ratio of elements 88-10-2, respectively) is a material separating the coating fragments, as has been shown by X-ray microanalysis. At $W_S = \sim 1 * 10^6$ (W/cm²*s)*pulse is observed the formation of islet type structure (islets of coatings containing a

large number of micropores separated by interlayers which basic element is aluminum) (Fig. 1a, b). At $W_s = (3-6) \cdot 10^6$ (W/cm²*s)*pulse the film (TiCu) / substrate (silumin) system melts (Fig. 1, c, d). The cellular crystallization structure is formed on the surface, the average sizes of cells increase from 150 nm to 600nm at changing the W_s parameter in the specified interval.

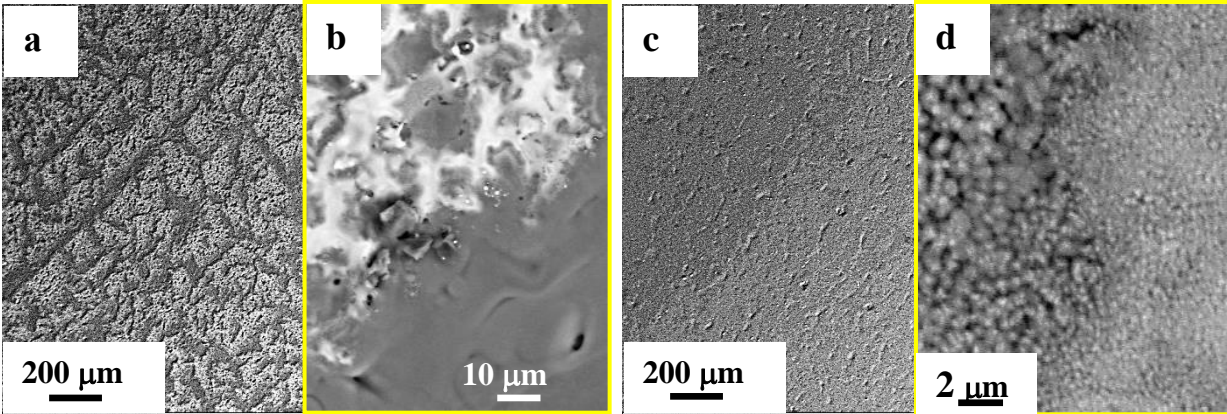


Fig. 1. Surface structure of a film (TiCu)/substrate (AlSi) system after electron beam irradiation at 15 J/cm² and variations of the duration and number of pulses: a, b - 50 μs, 3 pulses., c, d - 100 μs, 20 pulses. Scanning electron microscopy.

Changing the elemental composition of the alloy surface layer formed by electron beam irradiation of the film / substrate system revealed by X-ray microanalysis (Fig. 2) is shown in the Fig. 3. It can be assumed that the decrease of the titanium concentration in the alloy surface layer is due to its diffusion into the volume of material.

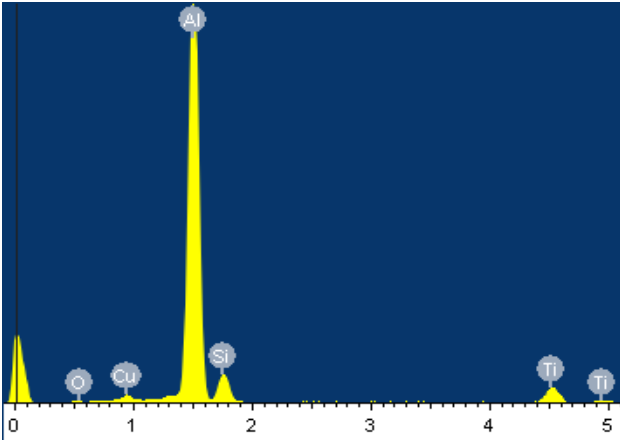


Fig. 2. The structure of irradiation surface (a).

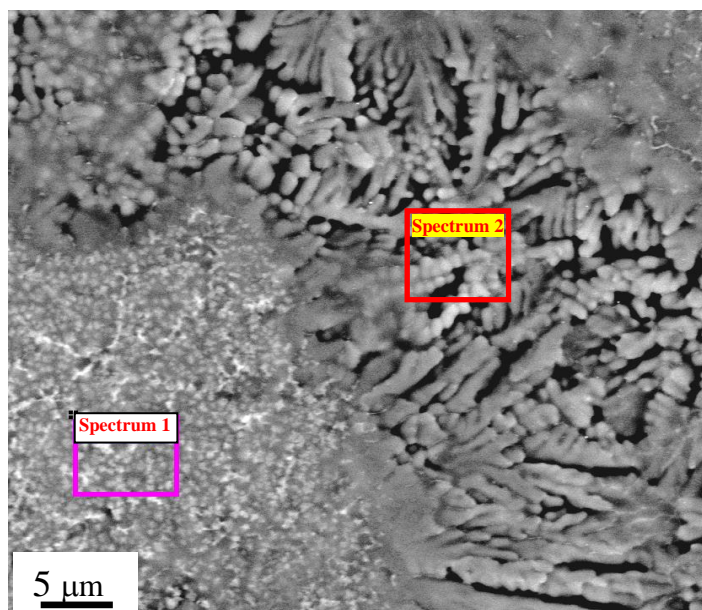


Fig. 2. The energy spectrum (b) and the results (Table I) of X-ray microanalysis of the film (TiCu) / substrate (AlSi) system, irradiated by an electron beam. (15 J/cm², 100 μs, 20 pulses., 0.3 s⁻¹).

Table 1. Fig2 b)

spectrum	Al, wt. %	Si, wt. %	Ti, wt. %	Cu, wt. %
spectrum1	74,13	13,18	9,27	3,42
spectrum2	89,11	7,66	0,2	3,03

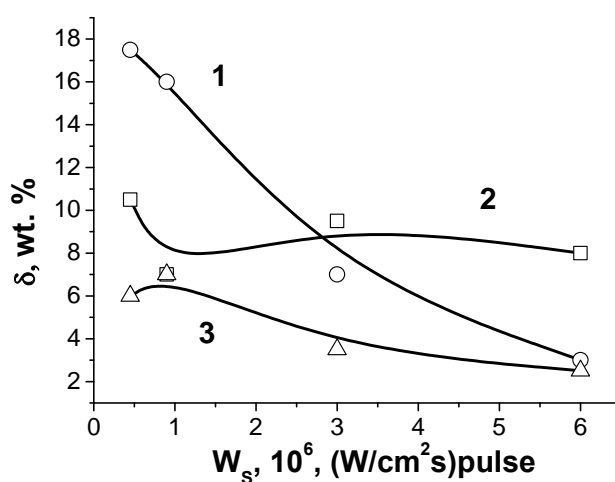


Fig. 3. Dependence of δ elements concentration of the surface alloy formed by electron beam irradiation of the film (TiCu) / substrate (AlCu) system on the irradiation parameters W_s ; 1 – Ti, 2 – Si, 3 – Cu (Al residual).

Analysis of the literature shows that in the Al-Si-Ti-Cu system under equilibrium conditions a number of phases can be formed [7]. Structural characteristics of the phases formed in ternary systems Al–Cu–Si, Al–Cu–Ti, Al–Ti– Si and Cu–Si–Ti are shown in Table 1. The example of the diagrams analysis for the system Al-Cu-Ti is shown in Fig. 3.

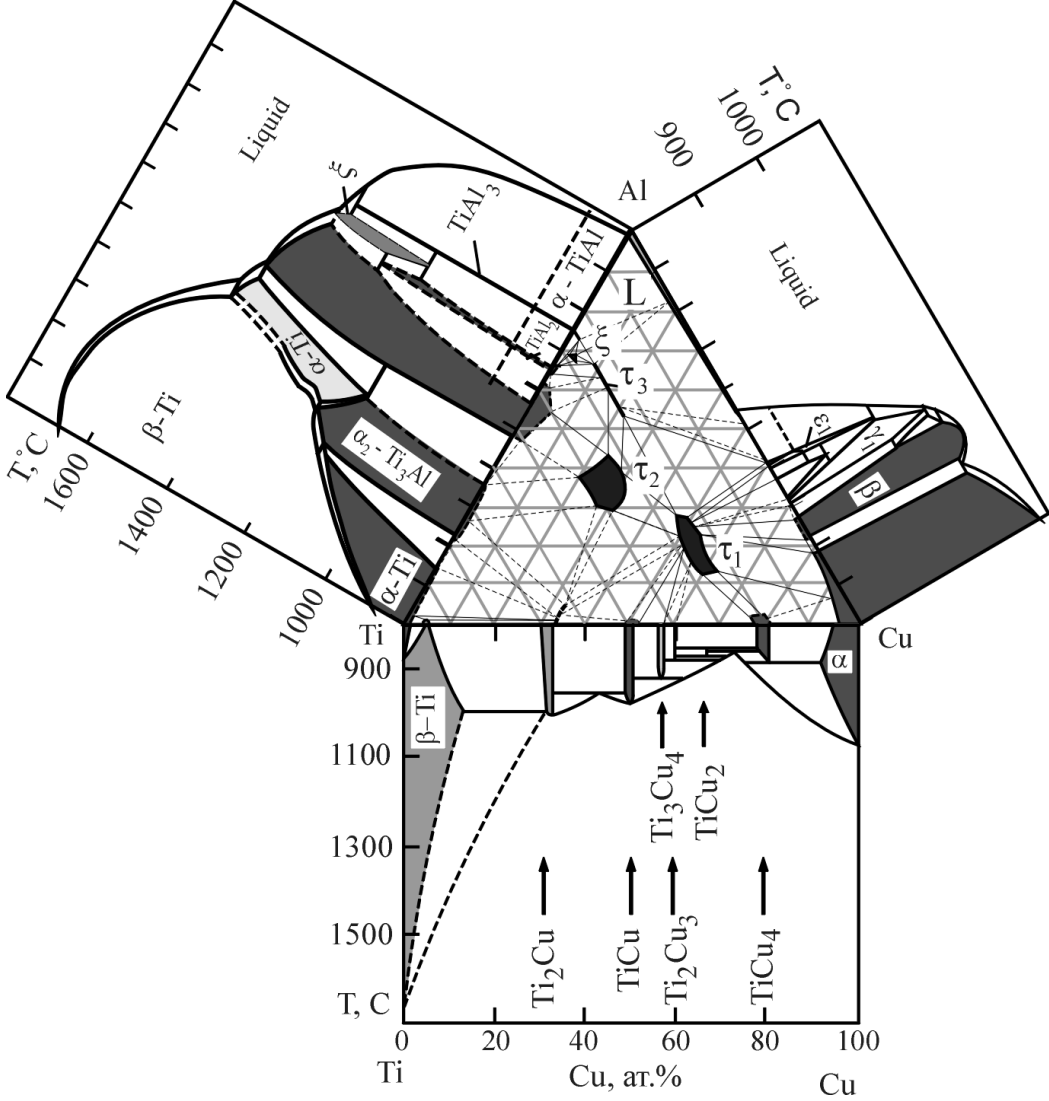


Fig. 4. Binary diagrams of the Al-Cu, Cu-Ti, Al-Ti systems [7] and the isothermal cross-section of the ternary Al-Cu-Ti system at 800°C [8, 11]. Gray and dark colors show single-phase areas.

The phase composition of the film (TiCu) / substrate (silumin) treated by high-intensity pulsed electron beam has been studied by X-ray diffraction, Bragg–Brentano geometry. The investigations revealed the formation of a multiphase structure in the surface layer (layer thickness of $\sim 10 \mu\text{m}$), qualitative and quantitative composition this structure depends on the elemental composition of the system and the mode of electron-beam treatment. Notably, in the system (TiCu) / (AlSi) was revealed a solid solution based on aluminum, silicon and titanium aluminide Al_3Ti , whose volume fraction is maximum ($\sim 18\%$) upon irradiation at 15 J/cm^2 , $100 \mu\text{s}$, 20 pulses, 0.3 Hz. Obviously, the relatively small amount of phases revealed in this work by X-ray analysis, is caused by small time of thermal influence for the film/substrate system at irradiating a pulsed electron beam.

Hardness, wear resistance and friction coefficient of the coating / substrate system have been studied before and after electron beam irradiation. It has been shown that the formation of surface alloys is accompanied by a multiple increase in hardness and wear resistance of silumin.

For (TiCu)/AlSi system multiple (in ~ 5 times) increasing in hardness is obtained after electron beam irradiation at 15 J/cm^2 , $100 \mu\text{s}$, 20 pulses (Fig. 5). Wear resistance increases in ~ 26 times, coefficient of friction decreases in $\sim 1,4$ times after an electron beam irradiation at 15 J/cm^2 , $100 \mu\text{s}$, 10 pulses (Fig. 6).

Studies of strength and frictional properties of the surface alloys, synthesized by electron beam treatment of the coating (TiCu) / substrate (AlSi) system, revealed the formation of multilayer structure, notably, thin surface layer with enhanced hardness (hardness of the treated sample increases ~ 5 times with respect to initial silumin), interlayer, which hardness is closed to initial sample and interlayer, which hardness increases the hardness of initial sample ~ 2 times (Fig. 5).

Table 2. Structural phases characteristics formed in ternary systems Al–Cu–Si, Al–Cu–Ti, Al–Ti– Si and Cu–Si–Ti.

Phase	Composition	Pearson's symbol	Space group	Structure type	Proto type	Source
Al – Si – Ti						
τ_1	$(\text{Ti}_{1-x}\text{Al}_x)_8(\text{Al}_y\text{Si}_{1-y})_{16}$	<i>tI24</i>	<i>I4₁/amd</i>		Zr ₃ Al ₄ Si ₅	[8, 9]
τ_1	Ti ₇ Al ₅ Si ₁₂	<i>tI24</i>	<i>I4₁/amd</i>			[9]
τ_2	$(\text{Ti}(\text{Al}_x\text{Si}_{1-x}))_2$ $0.15 \leq x \leq 0.3$	<i>oC12</i>	<i>Cmcm</i>	C49	ZrSi ₂	[8]
τ_2	Ti ₂ AlSi ₃	<i>oC12</i>	<i>Cmcm</i>	C49	ZrSi ₂	[9]
τ_3	Undetermined	<i>oC12</i>	<i>Cmcm</i>	C49	ZrSi ₂	[10]
	Ti(Al _{0,85} Si _{0,15}) ₃	<i>tI8</i>	<i>I4/mmm</i>	<u><i>D0₂₂</i></u>	TiAl ₃	[*]
Al – Cu – Si						
β	$\text{Cu}_{1-x-y}\text{Al}_x\text{Si}_y$ 70,6 – 82 at.% Cu	<i>cI2</i>	<i>Im $\bar{3}m$</i>			[11, 12]
γ	$\text{Cu}_{1-x-y}\text{Al}_x\text{Si}_y$ $0,31 \leq x \leq 0,402$	<i>cI52</i>				[13]
Al – Cu – Ti						
τ_1	TiCu ₂ Al	<i>cF16</i>	<i>Fm $\bar{3}m$</i>	L2 ₁	MnCu ₂ Al	[14]
τ_2	TiCuAl	<i>hP12</i>	<i>P6₃/mmc</i>	C14	MgZn ₂	[15]
τ_3	Ti ₂ CuAl ₅	<i>cP4</i>	<i>Pm $\bar{3}m$</i>	L1 ₂	Cu ₃ Au	[15]
	Ti ₂₅ Cu ₄ Al ₇₁	<i>tI16</i>	<i>I4/mmm</i>	<u><i>D0₂₃</i></u>	ZrAl ₃	[14]
ξ	Undetermined				Ti ₂ Al ₅	[14]
Cu – Si – Ti						
τ_1	TiCuSi	<i>oP12</i>	<i>Pnma</i>	<u><i>C37</i></u>	Co ₂ Si	[16]
τ_2	Ti ₁ (Cu _x Si _{1-x}) ₂	<i>oC12</i>	<i>Cmcm</i>	C49	ZrSi ₂	[16]
τ_3	TiCuSi ₂	Undetermined				[16]

Conclusion

The coating (TiCu) / substrate (AlSi) system has been formed. Nanostructured multiphase surface light alloys of Al-Si-Ti-Cu system have been synthesized by melting coating / substrate system with submillisecond high-intensity pulsed electron beam. Have been revealed the modes of electron beam which ensured manyfold increase strength and frictional characteristics of the silumin surface layer.

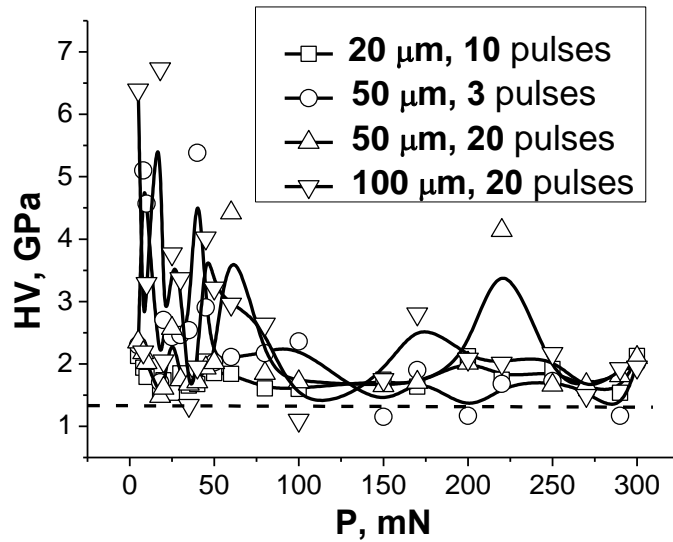


Fig. 5. Hardness of the surface layer of TiCu / AlSi system subjected by pulsed electron beam treatment at 15 J/cm² depending on the indenter load (P), the dotted line contains the original microhardness of the silumin.

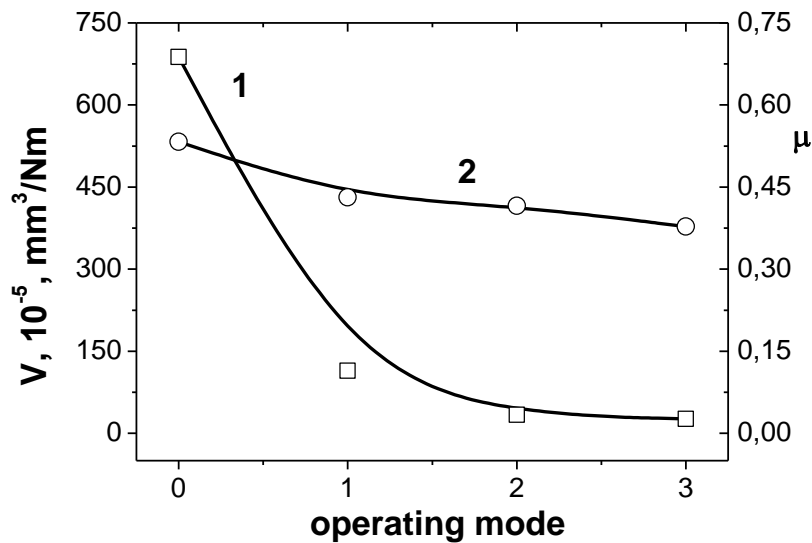


Fig. 6. Depending wear rate (curve 1) and friction coefficient (curve 2) on the operating modes of silumin; 0 – initial sample; 1 – sample with TiCu coating (1 μm thickness); 2 – coating – silumin substrate system after high-intensity electron beam treatment (15 J/cm², 50 μs, 10 pulses, 0.3 s⁻¹); 3 – coating – silumin substrate system after high-intensity electron beam treatment (15 J/cm², 100 μs, 10 pulses, 0.3 s⁻¹).

Acknowledgments

The work was partially supported by RFBR (projects Nos. 13-08-00416 and 13-04-98084).

References

- [1]. K.K. Kadyrganov, F.F. Komarov, A.D. Pogrebnyak et al. Ion-beam and ion-plasma modification of materials: Monography. MSU, 2005. 640 p.
- [2]. D.S. Nazarov, G.E. Ozur, D.I. Proskyrovsky. Generation of low-energy electron beams in a gun with a plasma anode . Russian Physics Journal. 1994. №3. pp. 100-114.
- [3]. V.N. Devyatkov, N.N. Koval, P.M. Schanin, V.P. Grigoryev, T.B. Koval. Generation and propagation of high-current low-energy electron beams. Laser and Particle Beams. 2003. V. 21. pp. 243-248.
- [4]. V. Rotshtein, Yu.F. Ivanov, A. Markov. Surface treatment of materials with low-energy, high-current electron beams. Chapter 6 in Book “Materials surface processing by directed energy techniques”. pp. 205-240. Ed. by Y. Pauleau: Elsevier. 2006. 763 p.
- [5]. Yu.F. Ivanov, N.N. Koval. Low-energy electron beams submillisekund duration: Generation and some aspects of the application in the field of material science – Chapter 13 in Book « Structure and properties of advanced metallic materials ». pp. 345-382 / Ed. by A.I. Potekaev. Tomsk: NTL, 2007. 580 p.
- [6]. N.N. Koval, Yu.F. Ivanov. Nanostructuring of the surface ceramic -metal and ceramic materials with pulsed electron beam treatment. Russian Physics Journal. 2008. №5. pp. 60-76.
- [7]. Diagrams of binary metal systems / Ed. by N.P. Lyakishev. M.: Mechanical engineering. 1996-2000. V. 1-3.
- [8]. A. Raman, K. Schubert. On the Constitution of Some Alloy Series Related to $TiAl_3$. II. Investigation on Some Systems $T-Al-Si$ and $T^4... T^6$. Z. Metallkd. 1965. 56. pp. 44-52.
- [9]. C. Brukl, H. Nowotny, O. Schob, F. Benesovsky. The Crystal Structure of $TiSi$, $Ti(Al,Si)_2$ and $Mo(Al,Si)_2$. Monatsh. Chem. 1961. V. 92. pp. 781-788.
- [10]. K. Schubert, K. Frank, R. Gohle and et. al. Structural Data on Metallic Phases VII. Naturwissenschaften. 1963. V. 50. p. 41 .

- [11]. J.L. Murray. The Aluminium-Copper System. *Int. Met. Rev.* 1985. V. 30. pp. 211-233.
- [12]. X.J. Liu, I. Ohnuma, R. Kainuma, K. Ishida. Phase Equilibria in the Cu-Rich Portion of the Al-Cu Binary System. *J. Alloys Comp.* 1998. V. 264. pp. 201-208.
- [13]. T.B. Massalski. *Binary Alloys Phase Diagrams*. ASM International, Materials Park, 2002.
- [14]. A. Raman, K. Schubert. On the Crystal Structure of some Alloy Phases Related to TiAl₃. III. Investigations in Several T-Ni-Al and T-Cu-Al Alloy Systems. *Z. Metallkd.* 1965. V. 56. pp. 99-104.
- [15]. P.I. Krypyakevich, V.Y. Markiv, A.A. Troyan. Crystal Structures of the Ternary Compounds TiCuAl and TiNiAl. *Dop. Akad. Nauk Ukr. RSR, A, Fiz.-Mat. Tekh. Nauki.* 1964. №7. pp. 922-924.
- [16]. J.J. Nickl, H. Sprenger. About New Compounds in the Titanium-Copper-Silicon Ternary System. *Z. Metallkd.* 1969. V. 60. pp. 136-139.

BIPHASE FILTRATION MODEL OF PLASTIC DEFORMATION

V.D. Sarychev, S.A. Nevskii, E.V. Cheremushkina, V.E. Gromov

Siberian State Industrial University, Department of Physics, 654007,

Novokuznetsk, Kirov str, 42.

Abstract

The filtration model of plastic flow based on the ideas of deformed material as a two-phase heterogeneous medium is suggested. Within this approach the wave displacement is regarded as a shock transition in this medium. One of the phases which is an excited one is responsible for system restructuring, and another one is normal and unrelated to structural transformations. The plasticity wave is the result of these two phases interaction. The equations of a filtration

model are obtained, that include the laws of pulse and mass conservation as well as filtration ratio between the phases.

Keywords: plastic deformation, the plasticity wave, filtration model, heterogeneous medium

Introduction

One of the problematic issues in the physics of strength and plasticity is the explanation of the observed inhomogeneities of plastic flow of materials as well as its stages during the experiment [1, 2]. To date, methods of modern physical materials science such as scanning and transmission electron microscopy and double-exposure speckle-interferometry have shown that the process of plastic deformation is of wave nature [3 – 5]. It is proved by the stress distribution at the boundary “surface layer – substrate” in the “staggered” order (the “checkerboard” effect) [3, 4] and non-uniform distribution of displacement fields and deformations [5]. These facts indicate that there are zones in the material not involved into the plastic deformation. The characteristic scales of inhomogeneities according to [5] can be from $\sim 1 \mu\text{m}$ to $\sim 1 \text{mm}$. Stages of plastic deformation are due to the changing nature of deformation localization, increase of the number of equidistant localization sites at the stages of linear and parabolic hardening, and at the stage of pre-fracture the collapse of plasticity wave occurs.

Studies of the dislocation substructures [6, 7] at various stages of plastic deformation showed that the transition from one stage to another is accompanied by a transformation of one type substructure to another and during the transition process two types of substructures can exist simultaneously. The combination of these experimental facts leads to the conclusion that the cause of the observed regularities of plastic flow is the collective nature of the changes of the internal structure [8 – 12]. To describe plastic deformation the ideas of mechanics of heterogeneous media can be applied [13]. Such approach was used in [14] for the study of phase transformations, plastic deformation and other structural

transformations of the solid. The peculiarity of this approach is the split of the entire ensemble of the structural elements of the medium (atoms, defects, etc.) into two subsystems: the excited one, responsible for the system restructuring and the normal one which is unexcited and not related to structural transformations. After splitting the resulting heterogeneous mixture is represented as a set of several continua-phases, each of which is described by the conservation laws and defining equations.

Problem statement

The proposed model in this paper provides an explanation of non-uniform distribution of displacements under uniaxial deformation [5] using the laws of momentum and mass conservation. As it is known [15], plastic deformation of polycrystals occurs due to the micro-and macroshifts that are presented in this model as a current of fast-moving phase in between the weakly deformable and inactive blocks, which can be seen as a current of two-phase heterogeneous mixture. The first component will be the microshifts, the second one – macroshifts. We will provide the conservation laws for each component. They will be:

$$\frac{\partial \rho_1}{\partial t} + \text{div} \rho_1 \vec{w} = I_{21} \dots\dots\dots (1)$$

$$\rho_1 \frac{d_1 \vec{w}}{dt} = \text{div} \tilde{\sigma}_1 + p_{21} - I_{21} \vec{w}; \frac{d_1}{dt} = \frac{\partial}{\partial t} + \vec{w} \cdot \vec{\nabla} (2)$$

$$\frac{\partial \rho_2}{\partial t} + \text{div} \rho_2 \vec{u} = I_{12} (3)$$

$$\rho_2 \frac{d_2 \vec{u}}{dt} = \text{div} \tilde{\sigma}_2 + p_{12} - I_{12} \vec{u} \frac{\partial \rho_2}{\partial t} + \text{div} \rho_2 \vec{u} = I_{12} (4)$$

where $\rho_1 = \alpha \rho_e$, $\rho_2 = (1 - \alpha) \rho_s$, $\tilde{\sigma}_1 = \alpha \tilde{\sigma}$, $\tilde{\sigma}_2 = (1 - \alpha) \tilde{\sigma}$, ρ_e and ρ_s – the true densities of phases, α - the volume fraction of the first phase, $\tilde{\sigma}$ – the voltage of the whole mixture, $\vec{p}_{21} = -\vec{p}_{12}$, $I_{21} = -I_{12}$ – the exchange intensity of momentum and mass, respectively, between the phases, w and u – velocities of the first and

the second phase, respectively. The intensity of pulse exchange between the phases can be represented as $\vec{p}_{21} = \vec{R}_{21} + I_{21}\vec{u}_{21}$, where R_{21} – interphase force associated with the friction forces, the clutch phases, and $I_{21}\vec{u}_{21}$ – with phase transformations.

We assume that the intensity of mass transfer is small compared to the intensity of the momentum exchange and the mixture components interact according to Rakhmatulin's scheme [16].

$$\text{Consequently, } \vec{p}_{21} = \vec{R}_{21}, \vec{R}_{21} = -p\nabla\alpha + \vec{F}_{21},$$

where force $F_{21} = \frac{1}{K}\alpha\rho_e(1-\alpha)(\vec{u} - \vec{w})$ is associated with high-speed non-equilibrium phases, where K – constant. With regard to all of the above facts the system (1) – (4) takes the form:

$$\rho_1 \frac{d_1 w}{dt} = \alpha \operatorname{div} \tilde{\sigma} + \alpha \rho_e (1 - \alpha) (\vec{u} - \vec{w}) / K; \quad (5)$$

$$\frac{d_1 \rho_1}{dt} + \rho_1 \operatorname{div} \vec{w} = 0; \quad (6)$$

$$\rho_2 \frac{d_2 u}{dt} = (1 - \alpha) \operatorname{div} \tilde{\sigma} - \alpha \rho_e (1 - \alpha) (\vec{u} - \vec{w}) / K; \quad (7)$$

$$\frac{d_2 \rho_2}{dt} + \rho_2 \operatorname{div} \vec{u} = 0, \quad (8)$$

In (5) assume that the inertial member $\rho_1 \frac{d_1 w}{dt} \approx 0$ then adding (5) with equation (7) leads to the following relation:

$$\alpha \operatorname{div} \tilde{\sigma} = -\alpha(1 - \alpha) \rho_e (\vec{u} - \vec{w}) / K \quad (9)$$

Equation (9) is a consequence of the law of momentum conservation for the first phase and is analogous to Darcy's law in the filtration theory [13]. Sense of the constant $1/K$ is that it is a factor of resistance to movement of the first phase from the second.

System (5) – (8) must be closed by the equation of state. Since the second phase is a weakly deformable blocks, then $\rho_s = \text{const}$. For the first phase, we

assume that $\rho_e = F(P)$. Now let us consider the problem in the one-dimensional setting. As it is known the voltage in a heterogeneous mixture depends on the pressure $\tilde{\sigma} = -P$. As it is known the voltage in a heterogeneous mixture depends on the pressure. Then (5) – (8) with regard to (9) and equations of state will be as follows:

$$\frac{\partial u}{\partial t} + u \frac{\partial u}{\partial x} = -\frac{1}{(1-\alpha)\rho_s} \frac{\partial P}{\partial x}; \quad (10)$$

$$\frac{\partial \alpha}{\partial t} + u \frac{\partial \alpha}{\partial x} = (1-\alpha) \frac{\partial u}{\partial x}; \quad (11)$$

$$\frac{\partial \rho_1}{\partial t} + \frac{\partial \rho_1 w}{\partial x} = 0 \quad (12)$$

We seek a solution in the form

$\alpha(x - u_0 t)$, $u(x - u_0 t)$, $w(x - u_0 t)$, $\rho_1(x - u_0 t)$, $P(x - u_0 t)$ therefore

$$u'(u - u_0) = -\frac{1}{(1-\alpha)\rho_s} P'; \quad (13)$$

$$\alpha'(u - u_0) = (1-\alpha)u' \quad (14)$$

$$-u_0 \rho_1' + (\rho_1 w)' = 0 \quad (15)$$

First integrals of the equations (13) – (15) are:

$$\alpha = 1 - \frac{C_1}{u - u_0} \quad (16)$$

$$P = (C_2 - C_1 \rho_s u) \quad (17)$$

$$\alpha \rho_e \left(u - u_0 - \frac{KP'}{B(1-\alpha)\rho_e} \right) = C_3 \quad (18)$$

Transforming (18) with (16), (17) and $\bar{u} = u - u_0$ we get an equation containing the rate of the second phase:

$$\frac{d\bar{u}}{d\eta} = \frac{C_3 - (\bar{u} - C_1)\rho_e}{\bar{u} - C_1}, \quad (19)$$

where $d\eta = \frac{d\xi}{K\rho_s}$. Consider the case $\rho_e = AP$ [17], then

$$\frac{d\bar{u}}{d\eta} = \frac{(\bar{u} - \bar{u}_1)(\bar{u} - \bar{u}_2)}{\bar{u} - C_1} \quad (20)$$

where \bar{u}_1, \bar{u}_2 – velocities of the second phase on the border focus localization.

Integration of this equation leads to:

$$\left(\frac{C_1 - \bar{u}_2}{\bar{u}_1 - \bar{u}_2} \right) \ln(\bar{u} - \bar{u}_2) - \left(\frac{C_1 - \bar{u}_1}{\bar{u}_2 - \bar{u}_1} \right) \ln(\bar{u} - \bar{u}_1) = d\eta + C \quad (21)$$

To determine the constants involved (20) and (21) we can write the boundary conditions:

$$\bar{u}(0) = \bar{u}_1, \bar{u}(L) = \bar{u}_2, \bar{u}'(0) = 0, \bar{u}'(L) = 0, \alpha(0) = \alpha_1, \alpha(L) = \alpha_2 \quad (22)$$

Then, by (22) the first integrals will take the form:

$$\begin{aligned} (1 - \alpha_1)\bar{u}_1 &= C_1 \\ P_1 &= C_2 - C_1\rho_s\bar{u}_1 \\ -\bar{u}_1^2 C_1\rho + (C_1^2\rho + C_2)\bar{u}_1 - C_3 - C_1C_2 &= 0 \\ (1 - \alpha_2)\bar{u}_2 &= C_1 \\ P_2 &= C_2 - C_1\rho_s\bar{u}_2 \\ -\bar{u}_2^2 C_1\rho + (C_1^2\rho + C_2)\bar{u}_2 - C_3 - C_1C_2 &= 0 \end{aligned} \quad (23)$$

Returning in (21) and (23) to the variable u , we construct the speed plotted for the second phase of the case $u_1 > u_2$ и $\alpha_1 < \alpha_2$ from the coordinates at various time points (Figure 1). The analysis of this dependence shows that it has a kind of "shock transition." Consequently, there are the areas of the deformable material, which are not involved in the plastic deformation, which is confirmed by experimental facts [5]. Speed containment chamber is defined as:

$$u_0 = \frac{(\alpha_1 - 1)u_1 + (1 - \alpha_2)u_2}{\alpha_1 - \alpha_2}. \text{ If } u_1 = 0 \text{ and } u_2 = u_*, \text{ where } u_* - \text{velocity of the}$$

traverse beam, the values of the marginal rate of localization focus on the order exceeds the rate of the traverse beam of the testing machine, which also corresponds to the experiment. The case $u_1 < u_2$ and $\alpha_1 > \alpha_2$ also allows the

existence of "shock transition". Note that these relationships were obtained in [18] for fixed and dynamic structures and in [19], for a shock wave in an ideal gas.

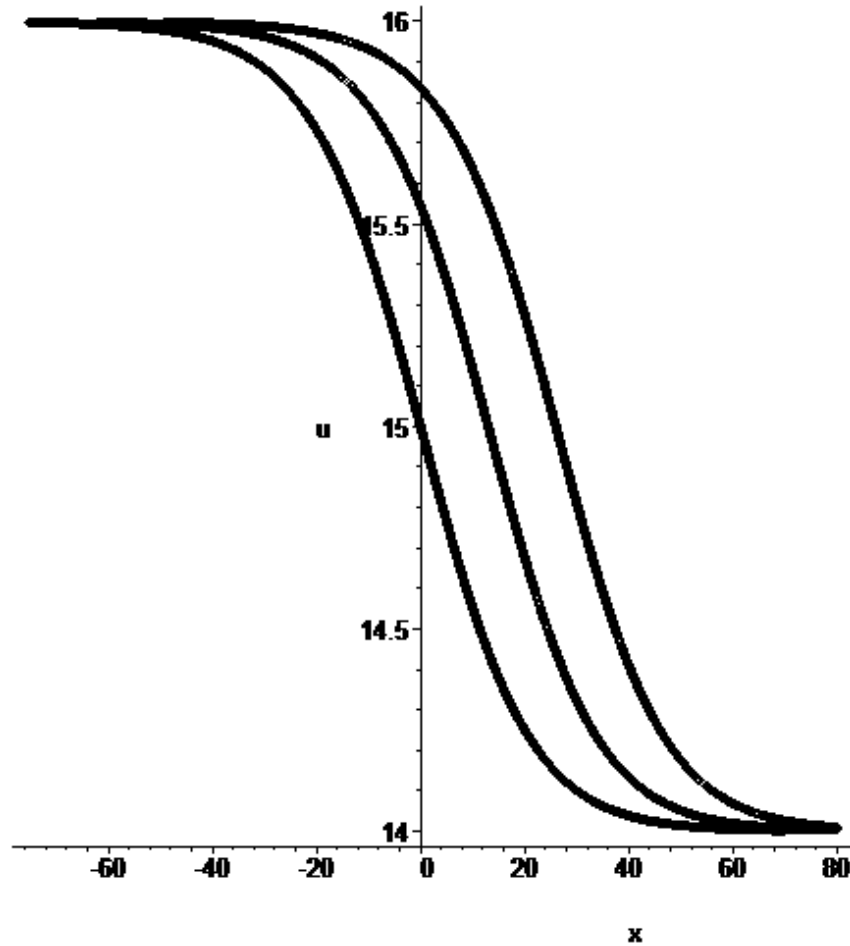


Fig.1. The velocity of the second phase from the coordinates at various points of time:

$$1 - t = 0, 2 - t = 1, 3 - t = 2.$$

We define the width of the "shock transition" with the formula, which has the following form: $l = \frac{u_1 - u_2}{\max\left(\frac{du}{dx}\right)}$. The evaluation of the magnitude shows that

it has the value of $\sim 10 \mu\text{m}$, which coincides with the characteristic length scales of heterogeneity observed in the experiment. Note also that the path of dislocations in the materials are of the same order of magnitude [20].

Conclusions

1. The system of equations of filtration plasticity model is built. A solution is obtained in the form of "shock transition." Its width was defined, which coincides with the characteristic values of the scale of the inhomogeneity of deformation.

2. It is shown that the maximum speed of the focus on the localization of the order exceeds the rate of crosshead of the testing machine, which corresponds to the experimental data.

References

- [1]. V.E. Panin, V.E. Egorushkin, T.F. Elsukova. Physical mesomechanics of grain boundary sliding in a deformed polycrystalline. Physical mesomechanics. 2011. V. 14. № 6. P. 15 – 22.
- [2]. P.V. Yasniy, P.O. Marushak., S.V. Panin and others. The vicissitudes of deformation of the material and the kinetics of growth of fatigue cracks in steel 25X1M1Φ at low loading frequencies. Physical mesomechanics. 2012. V. 15. № 6. P. 15 – 22.
- [3]. V.E. Panin, A.V. Panin. The effect of the surface layer in a deformable solid. Physical mesomechanics. 2005. V. 8. № 5. P. 7 – 15.
- [4]. V.E. Panin. Surface layers as a synergistic activator of plastic flow of the body. MiTOM. 2005. № 7. P. 62 – 68.
- [5]. L.B. Zuev, V.I. Danilov, S.A. Barannikova. Physics of macrolocalization of plastic flow. Novosibirsk: Nauka, 2008. 328 p.
- [6]. E.V. Kozlov, L.I. Trishkina, N.A. Popova and others. The place of dislocation physics in multi-level approach to plastic deformation. Physical mesomechanics. 2011. V. 14. № 3. P. 95 – 110.
- [7]. N.A. Koneva, E.V. Kozlov. The physical nature of the stages of plastic deformation. Izvestia vuzov. Physics. 1990. № 2. P. 89 – 106.
- [8]. G.A. Maligin. Self-organization processes of dislocation and crystal plasticity. UFN. 1999. V. 181. P. 1129 – 1156.

- [9]. S.P. Kiselev. The dislocation structure of shear bands in monocrystals // PMTF. 2006. № 6. P. 102 – 113.
- [10]. J. Pontes, D. Walgraef, E.C. Aifantis. On dislocation patterning: Multiple slip effects in the rate equation approach. International Journal of Plasticity. 2006. V. 22. № 8. P. 1486 – 1505.
- [11]. P.P. Kaminskii, Yu.A. Khon. Kinetic theory of low-temperature microscopic crack nucleation in crystals. Theoretical and Applied Fracture Mechanics. 2009. V. 51. P. 161 – 166.
- [12]. L.B. Zuev, Ju.A. Hong, S.A. Barannikova. The dispersion of self-sustained waves of localized plastic flow. The magazine of technical physics. 2010. V. 80. № 7. P. 53 – 59.
- [13]. R.I. Nigmatulin. The basics of mechanics of heterogeneous media. Moscow: Nauka, 1978. 336 p.
- [14]. E.C. Aifantis. On the Mechanics of Phase Transformations // Phase Transformation. London, 1986. P. 233 – 289.
- [15]. V.V. Rybin. Large plastic deformation and fracture and the destruction of metals. Moscow, Metallurgy, 1986. 224p.
- [16]. Kh.A. Rakhmatulin. The fundamentals of gas dynamics of interpenetrating motions of compressible media. PMM. 1956. V. 20. № 2. P.184 – 195.
- [17]. V.D. Sarychev, V.A. Petrunin. Filtration model of plastic deformation. Izvestia vuzov. Ferrous metallurgy. 1993. № 2. P. 29 – 33.
- [18]. V.G. Makaryan, N.E. Molevich, D.P. Porfiriev. Classification of gas-dynamic structures described by a nonlinear equation of acoustics of relaxing environment. Vestnik of SamSU. The natural science series. 2009. № 6. P. 92 – 104.
- [19]. B.L. Rozhdestvenskiy, N.N. Yanenko. System of quasi-linear equations and their applications to gas dynamics. Moscow: Nauka, 1968. 686 p.
- [20]. J. Hirth, I. Lothe. Theory of dislocations. M.: Atomizdat, 1972. 600 p.

THE METHODOLOGY OF DETERMINING ACOUSTICAL STRUCTURAL NOISE OF STEEL

V.V. Muraviev, O.V. Muravieva, A.V. Baiteryakov, A.I. Dedov

Kalashnikov Izhevsk State Technical University, Russia.

E-mail: pmkk@istu.ru, email1990@yandex.ru, superdedov@mail.ru

Abstract

This study represents the method used to determine the grain size of steel grade 45 to become the mean amplitude of the acoustic structural noise; describes the method of measurement and the processing algorithm of the signal received by the defectoscope; and displaying coincidence of theoretical and experimental research.

Keywords: acoustic, structural noise, structurescopy, dispersion of ultrasound waves, grain size.

Introduction

The majority of objects in nondestructive testing are polycrystalline firm bodies. Each grain of these bodies is a monocrystal which is possessed by elastic anisotropy which causes the dispersion of acoustic waves in a polycrystalline firm body due to reflection, refractions and transformations of acoustic waves on borders of metal grains.

During the manufacturing of the product (molding, processing by pressure, thermal processing, etc.) and during the product's life cycle, the structure of metal can essentially change because of the occurrence of discontinuities, the anisotropy caused by the structure of the metal, and damages to the structure [1-4].

Any structural damages can serve as an indicator of irreversible variations which have been developed in the material. Therefore the definition of a product's current material structural condition is one of many actual directions of structurescopy in nondestructive testing [5-8].

The majority of methods in an assessment of a metal structure are based upon the measurement of the speed of propagation or the attenuations of ultrasonic waves. Used methods have a number of restrictions in application, caused by insufficient sensitivity, and the influence of impeding factors on the results of the control [5-11].

This article represents the method used to determine the grain size of steel grade C45E to become the mean amplitude of acoustic structural noise.

Used approaches

Pattern noise is related to the scattering of the ultrasonic waves on the structural inhomogeneities, grains of the material. In a separate crystal elastic moduli (and, therefore, the wave propagation velocity) vary depending on the crystallographic direction.

Since the crystalline lattice of grains in polycrystalline body are randomly oriented relatively to each other that is why the grain boundaries is a partial reflection, refraction and transformation of ultrasonic waves.

Acoustic wave propagating in such an ambient generates scattered waves that propagate in any direction "do not support the" main stream of the wave (Fig. 1 a).

The attenuation coefficient of δ_d of ultrasonic waves caused by the scattering depends on the relationship between the wavelength λ and the average grain size D_g (Fig. 1 b). When $\lambda \ll D_g$ attenuation is minimal. Particularly large scattering at $\lambda \approx (3 \div 4) D_g$. For the most construction materials condition is performed $D_g \ll \lambda$ ($D_g = 20 \div 100$ microns, $\lambda = 0,5 \div 6$ mm in the frequency range from 1 MHz to 5 MHz).

Scattering in this area is called Rayleigh and occurs on particles with sizes smaller than the wavelength. Thus this ratio δ_d is proportional to the third degree of the grain diameter D_g^3 and the fourth degree of the frequency f^4 . The scattering coefficient δ_d of ultrasonic waves significantly depends on the elastic anisotropy of the material. Thus, due to the anisotropy ultrasound strongly

attenuated in copper, iron, austenitic steel. Elastic anisotropy is low in tungsten, aluminum. Technically pure iron and carbon steel considered to be the materials in respect to the amount of elastic anisotropy. Such materials as concrete, granite, iron being the materials with heterogeneous particles are characterized by a large scattering.

Along with scattering attenuation is caused thanks to absorption of ultrasonic wave energy by transition to thermal energy (absorption coefficient δ_a).

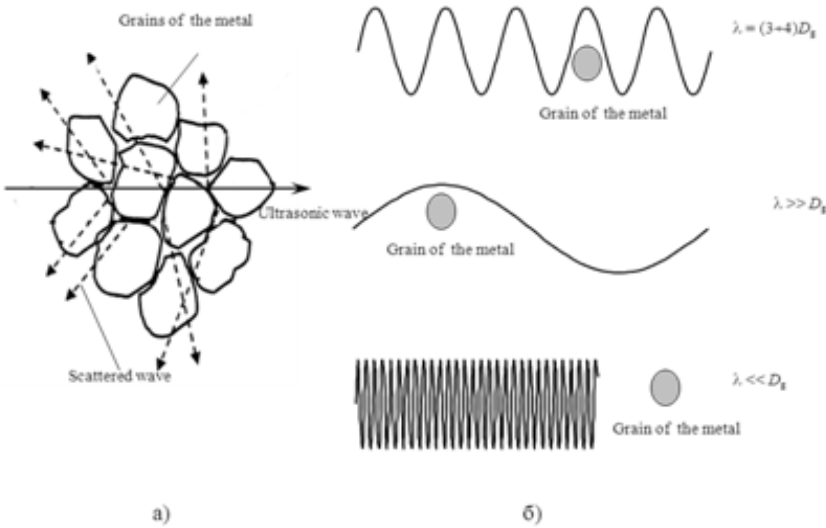


Fig. 1. Mechanism of ultrasonic wave scattering at the grain boundaries (a); Vector waves of different frequencies interaction with inhomogeneities of the medium (b).

In particular, for medium-carbon steel attenuation of longitudinal waves δ_l , due to absorption δ_a and scattering δ_d may be calculated by the simplified formula:

$$\delta_l = \delta_d + \delta_a = 0,12f + 20f^4 D_g^3 \tag{1}$$

where f - frequency [MHz], D_g - the average grain diameter [mm].

As an example, at Fig. 2 the curve of dependence of the attenuation coefficient from the longitudinal wave of frequency for the different numbers of grains G is shown. The growth rate and increase in grain size leads to a significant increase in attenuation, particularly at high frequencies, which leads to a significant reduction in the amplitude of the wave.

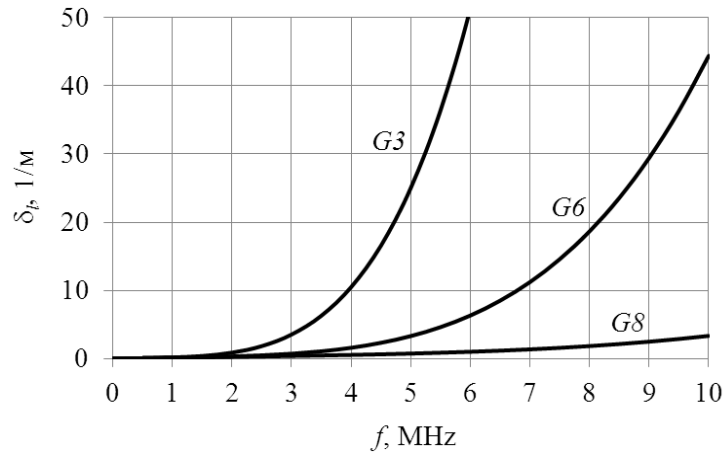


Fig. 2. The attenuation coefficient dependence of the longitudinal wave δ_l from frequency f for the different numbers of grains G .

The pulses are generated as a result of the inverse scattering of ultrasound on the inhomogeneous structure from the structure noise, which has the form of separate closely located peaks in the structurescopy's display. Depending on the random phase relationship of individual scattering pulses they can strengthen or weaken each other (Fig. 3).

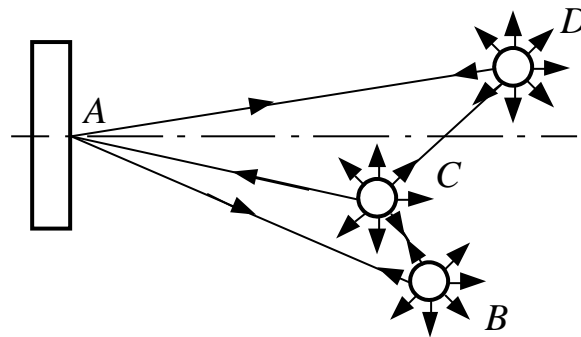


Fig. 3. Single and double scattering of waves at the grain boundaries/

Using the formula [12], we can calculate the average level of structural noises U_{sn} in the near (the formula (2)) and the far surface (the formula (3)) for the combined areas of the transmitter:

$$U_{sn} = U_0 \frac{\lambda}{2} \sqrt{\frac{\delta_d C \tau}{\pi S}} e^{-2\delta r} \quad (2)$$

and

$$U_{sn} = U_0 \frac{1}{2r} \sqrt{\frac{\delta_d C \pi S}{2\pi}} e^{-2\delta r}, \quad (3)$$

whereas U_0 - the amplitude of the transmitted signal, λ - the length of the ultrasonic waves, δ_d - ultrasound scattering coefficient, C - the speed of the ultrasonic waves in the medium, τ - duration of the ultrasonic pulse, S - area of the transducer, δ - the damping coefficient, r - distance from the transducer to the scattering region.

Presented formulae (1) - (3) allow us to investigate the influence of grain size (D_g) and piezoelectric transducer parameters (f , S , τ) to the level of structural noise. In particular, fig. 4 illustrates the effect of the average grain diameter D_g to the level of structural noise U_{sn}/U_0 of longitudinal waves for different operating frequency f . The results of calculations performed for the far zone transducer used in the experiments with the area $S=50 \text{ mm}^2$ at frequencies $f_1=2,5 \text{ МГц}$, $f_2=5 \text{ МГц}$ and $f_3=10 \text{ MHz}$. The presence of extremes, depending on the grain size $U_{sn}/U_0 D_g$ is owing to two major trends.

On the one hand, the level of noise is proportional to the ratio of structural

scattering: $U_{sn} \sim \sqrt{\delta_d} \sim \sqrt{D_g^3}$; exponential decay law: $U_{sn} \sim e^{-2\delta r} = e^{-(0,12f+20D_g^3f^4)r}$

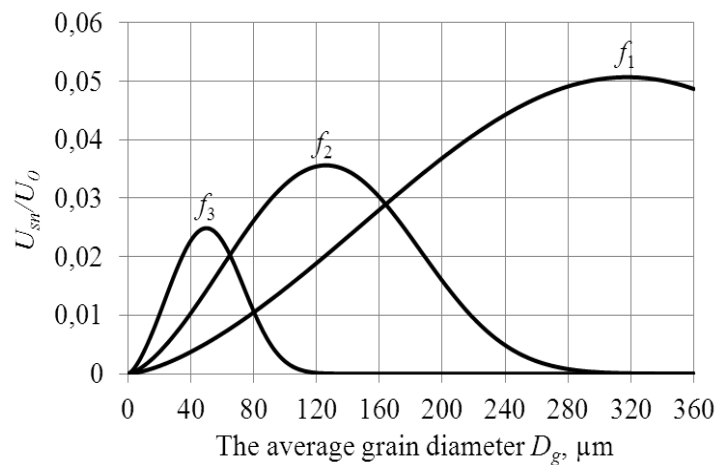


Fig. 4. The level of structural noise U_{sn}/U_0 depending on the diameter of the grain.

The use of different frequencies under the same area piezoelectric transducer changes the location and extreme steepness of curves. The resulting curves allow to optimize the transducer parameters to implement methodology for assessing the structure (grain size determination) with maximum sensitivity depending on the range of grain sizes investigated.

Measurement procedure

Amplitude of structural acoustic noises is generally much less than the level of back wall echo, so registration of structural noise requires using of high factors of strengthening. Wherewith the using of combined transducers is unreasonable because of the powerful hum of the probe pulse, the duration of which at high factor of strengthening blocks the entire area of structural noise appearing by creating a dead zone.

It is proposed to use of double-crystal transducer with short dead zones with separate transmitting and receiving function, structurally united in one case (Fig. 5). Electrical voltage submitted from the generator of probe pulses on radiating piezoelectric-crystal plate of transducer leads to the excitation of longitudinal wave in a transmission prism with a small angle ($0-7^\circ$).

The longitudinal waves is refracted on the division of two ambients: transmitting prism and the control object.

The longitudinal wave, reflected from the back wall surface and scattered by inhomogeneities of the medium, is refracted at the interface reception prism - the object of control and converted into an electrical signal with help of the receiving piezoelectric transducer. Note that in the contact area of the transmitting prism and a control object arises Rayleigh wave which is reradiated into the receiving prism [13]. In practice of ultrasonic control pulse occurrence of a Rayleigh wave on border zone control is undesirable because it limits the sensitivity and dead zone of control.

Thanks to the fact that the signal level of structural noises, as well as any echoes significantly influences on the quality of acoustic contact (particularly in the case of rough surfaces, instability couplant layer) therefore by development of a procedure is important the selection of the reference signal. Typically, as reference in a ultrasonic control one uses back wall impulses or reflections from artificial reflectors. However, control of real objects, especially during operation, the ultrasonic wave reflected from the opposite surface of the article

may vary considerably or even absent (At availability of corrosion, pitting, or lack of flatness).

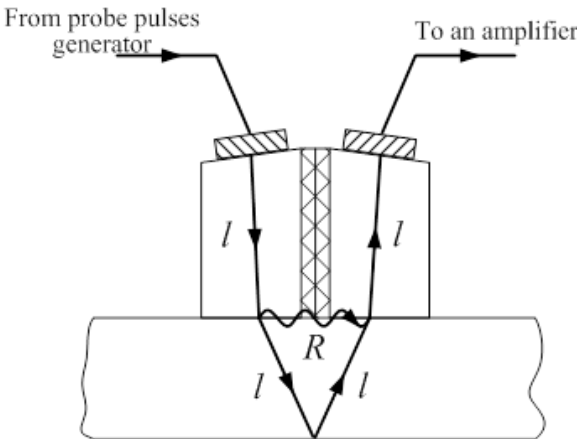


Fig. 5. Scheme of formation of Rayleigh waves: l - longitudinal wave, R - Rayleigh wave.

It is proposed to use as a reference the Rayleigh wave signal thanks to its re-emission in the reception prism. Unlike the back wall echo of Rayleigh wave is most stable with change of the contact or the surface roughness and not depends on condition of the back wall surface.

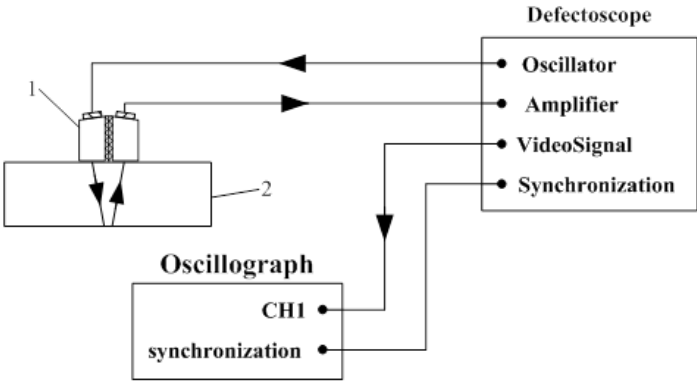


Fig. 6. Scheme of Control: 1 - double-crystal transducer.

The block diagram of the apparatus that implements the method of measurement is shown in Fig. 6. Electric pulse generator of ultrasonic defectoscope excites radiating plate of piezoelectric transducer. Ultrasonic pulses, scattered by irregularities structure are recorded by receiving piezoelectric plates and amplified by high frequency amplifier of defectoscope to 80-90 dB. For saving and further processing of the electrical signal to the

output «VideoSignal» of defectoscope connected digital oscilloscope, synchronized with the defectoscope through the synchronization line.

The investigated sample

Registration results of the probe pulse, the back wall echo and Rayleigh waves are shown in Fig. 7. Type of the amplified signals of structural noise in the control zone between the pulse Rayleigh waves and back wall echo shows the structural noise in the sample (Fig. 7).

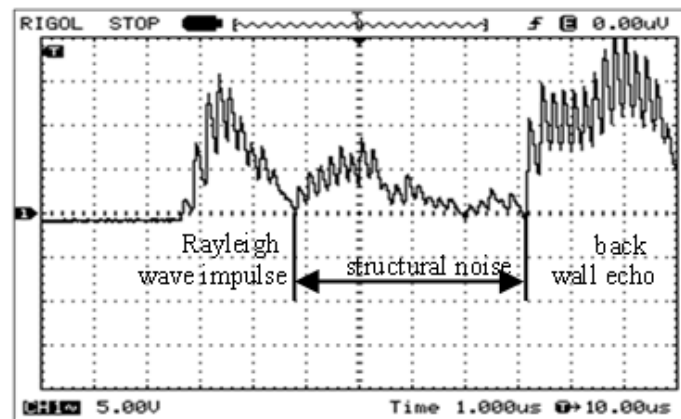


Fig. 7. The Oscillogram of pulses on the oscilloscope screen: the zone of structural noise.

Given to the level of structural noise is the result of waves interference repeatedly disseminated from grains of a material, in a methodology is estimated the integrated characteristic of structural noise defined as result of structural noise integration structural noise on all working zone. Integration is realized by MathCad programm after interpolation of the digitized signal.

To test the developed methodology of structural noises researching prepared samples from round hire bar of constructional steel C45E in the form of disks with a diameter d and height h with different thermal treatments, implementing different structures with different number of grain. The main characteristics of the samples are shown in Table. 1.

For an assessment of the structural changes made metallographic examination of the prepared samples. Pictures of flat grinding microstructures of samples surface after etching in 4 percent of HNO_3 aqueous solution for separation of grain boundaries obtained by microscope Altami c MET 1M

shown in Fig. 8. The results of the metallographic evaluation grain sizes shown in Table 1. The average grain size D_g of the scale and number of G evaluated.

Table 1. Characteristics of samples for research.

№ of the sample	sample sizes		Type of thermal processing	Temperature of heating under quenching, °C	Number of grain G / average diameter of grain D_g , a μm	Structure
	$d, \text{m m}$	$h \text{mm}$				
1	54,7	19,9	Original condition (normalization)	850	5/ 62	perlite + ferrite
2	54,7	19,9	water quenching	780	8/ 22	martensite
3	54,7	19,9	oil quenching	850	7/ 31	martensite + troostite
4	54,7	19,9	quenching+ tempering	850+600	6/ 44	sorbite
5	48,3	18,7	Original condition (normalization)	850	5/ 62	ferrite + perlite
6	48,3	16,0	Superheating for annealing	1050	3/ 125	coarse - grained ferrit + perlite

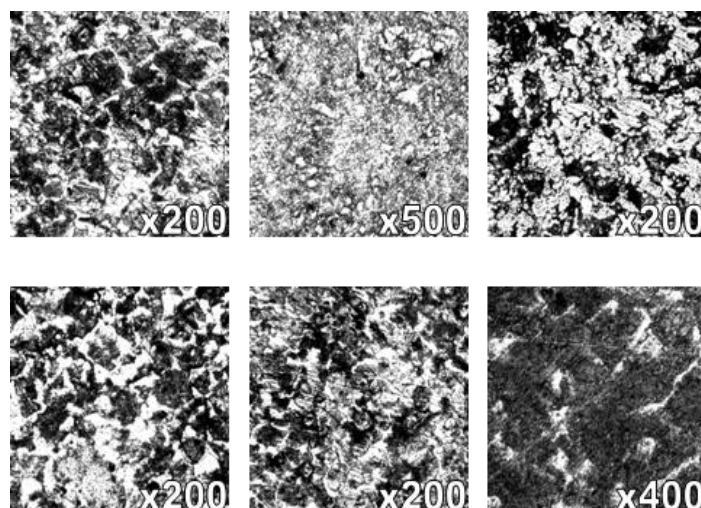


Fig.8. Metallography of samples: a) the sample number 1; b) the sample number 2; c) the sample number 3; d) the sample number 4; e) the sample number 5; f) sample number 6.

Results and discussion

The results of determination of the integrated and averaged over the level of integration of structural noise, amplitude of Rayleigh wave and the amplitude of the base echo for the samples are presented in Table. 2. Measurements were carried out in four areas of the samples and averaged afterwards. Random measurement error in one position of transducer does not exceed 15%.

Table 2. Results of measurements.

№ of the sample	Average value of amplitude of structural noise on three measurements at signal depression 10 dB, Volte				The average amplitude of structural noise U_{sn} , V	The average amplitude of base echo U_{bp} at signal depression 10 dB, Volte	The average amplitude of Rayleigh wave impulse at signal depression 10 dB U_R , V
	Pos. №1	Pos. №2	Pos. №3	Pos. №4			
1	2,51	2,61	2,80	3,17	2,77	122,67	12,67
2	0,21	0,26	0,47	0,48	0,34	120,67	11,25
3	1,22	1,30	1,46	1,72	1,42	120,00	11,10
4	1,45	2,44	2,34	2,15	2,09	124,00	11,80
5	2,66	2,90	2,76	3,21	2,88	130,67	10,80
6	8,33	9,16	9,05	8,72	8,82	135,33	12,10

Fig. 9 a and 9 b are charts of the ratio structural noise U_{sn} - U_{bp} base echo and structured noise U_{sn} - Rayleigh wave for the studied samples. Intervals for deviations of the experimental points correspond to the horizontal deviation of the grain diameter value D_g . Intervals of vertical deviations corresponding to deviations of structural noise level in various areas of the samples. The presence direct relationship of structural noise level from the grain size suggests the possibility of using the developed method for assessing the structure of the metal. In this case, variations in the level of structural noise indicates of structural differences in regions of the sample.

Analysis of the results of theoretical and experimental (metallographic and acoustic) research shows that the amplitude of the ultrasonic waves reflected from the structural elements is directly proportional to the size of grains in the heat-treated samples of investigated steel C45E. It was found out that there is the

monosemantic ratio between the heat-treated samples and averaged amplitude of structural noises. This dependence is in satisfactory agreement with theoretical predictions.

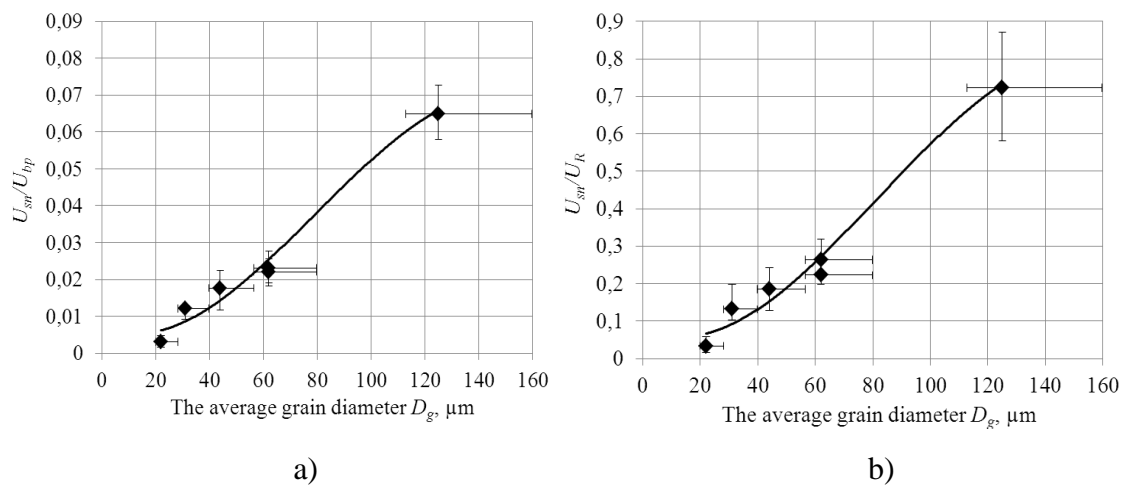


Fig. 9. Graphic relations: a) structure-borne noise - back wall echo;
b) structural noise – impulse of Rayleigh wave.

Conclusions

In the development of ultrasonic structurescopy is offered a new approach to the evaluation of the metal structure on the value of the integral level of structural acoustic noise.

Methodology of the acoustic noise assessing of structural metal products proved from position of selection of the frequency range, the control zone, the reference signal (impulse Rayleigh waves), the signal processing algorithm.

We found out the Influence of structure of samples of the steel C45E subject to various thermal processing, on a level of structural noise.

The developed algorithm of the structurescopy with help of the structural noise may be automated and used in a manufacture for the quality control and for the current condition control of the part being in process.

References

- [1] V.V. Muraviev. Prospective Method for Material and Product Unbroken Inspection and Engineering Diagnosis. Journal of petrochemical universities. Jun. 1998. V. 11. № 2. P.54-58.

- [2]. L.B. Zuev, O.V. Sosnin, D.Z. Chiracadze, V.E. Gromov, V.V. Muraviev. Acoustic control of steel sample durability and restoration of their resource. Applied mechanics and technical physics. 1998. V. 39. № 4. pp. 180 – 183.
- [3]. V.V. Muraviev, O.V. Korabeinikova, A.V. Platunov. Effect of stress-deformed and structural state in wires on basic regularities of Pohhammer rod wave spreading. Izvestiya vuzov. Ferrous metallurgy. 2009. № 6. pp. 44-48.
- [4]. V.V. Muraviev, O.V. Muravieva, A.V. Platunov et al. Investigation of acoustic – stress characteristics of rod wave in thermally treated steelwires by electromagnetic – acoustic method. Defectoscopy. 2012. №8. pp. 3-15.
- [5]. G.A. Budenkov, V.V. Muraviev, O.V. Korabeinikova. Investigation on stress – deformed state of rims of rolled steel wagon wheels by acoustic tensometry method. Fundamental methods of modern materials science. 2009. V. 6. № 3. pp. 111- 117.
- [6]. V.V. Muraviev, O.V. Muravieva, E.N. Kokorina. Quality control of heat treatment of rods from 60C2A steel by electromagnetic – acoustic method. Defectoscopy. 2013. № 1. pp. 20-32.
- [7]. V.V. Muraviev, O.V. Muravieva, E.N. Kokorina. Acoustic structure – scopy and defectoscopy of rods from 60C2A steel in production of springs with nanosize structure. Izvestiya vuzov. Ferrous metallurgy. 2013. № 4. pp. 66-70.
- [8]. V.V. Muraviev, O.V. Muravieva, E.N. Kokorina et al. Optimization of systems of magnetization of electro – acoustic transducers of body waves for non – destructive control of rod rolled products. Gauges and systems. 2013. №2. pp. 2-9.
- [9]. V.V. Muraviev, O.V. Muravieva, V. A. Strizhak et al. Evaluation of residual stresses in rims of wagon wheels by electromagnetic – acoustic method. Defectoscopy, 2011. № 8. pp. 16-28.
- [10]. V.V. Muraviev, L.V. Volkova, E.N. Balobanov. Control of residual stresses in electro – contact hardening of locomotive wheel tires. Technology of machinebuilding. 2011. № 9. pp. 42-45.

- [11]. V.V. Muraviev, L.V. Volkova, E.N. Balobanov. Control of residual stresses in locomotive wheel tires by method of acoustoelasticity. Defectoscopy. 2013. № 7. pp. 22-28.
- [12]. V.V. Muraviev, L.V. Volkova. Evaluation of tirev tightness value of locomotive wheels by method of acoustoelasticity. Defectoscopy. 2013. № 9. pp. 40-46.
- [13]. V.V. Muraviev, O.V. Muravieva, A.V. Baiteryakov et al Procedure of determination of acoustic structural noises of metal. Intellectual systems in manufacturing. 2013. № 1. pp. 143-148.

SURFACE HARDENING OF STEELS WITH BORON

A.M. Guriev^{1,2}, S.G. Ivanov¹, M.A. Guriev¹, Mei Shunqi², Gong Wenbang²

¹Altay State Technical University after Polzunov, Russia.

² Wuhan Textile Univerity, China.

Modern materials require a high surface hardness, abrasion resistance and other characteristics. Diffusion coatings based on boron often have a set of required properties. In this work the influence of the mixture composition and process parameters on the microstructure and technological properties of boride layers on alloy steels. The study was selected steel 5XHB, 5XHBM (L6, AISI / ASTM).

The structure of the diffusion coating was examined using an optical microscope «Axio Observer Z1m», scanning electron microscope JEOL JSM-7000F. Phase analysis was performed on X-ray DRON-6.

The surface structure of the studied steels are mainly formed of three elements such as iron, boron and carbon. Iron is a major component, and boron - main alloying element on the surface, the carbon is present in an amount

introduced into the steel. View borated steel microstructure and integrated boriding titanation 5XHB steel are presented in Figures 1 and 2.

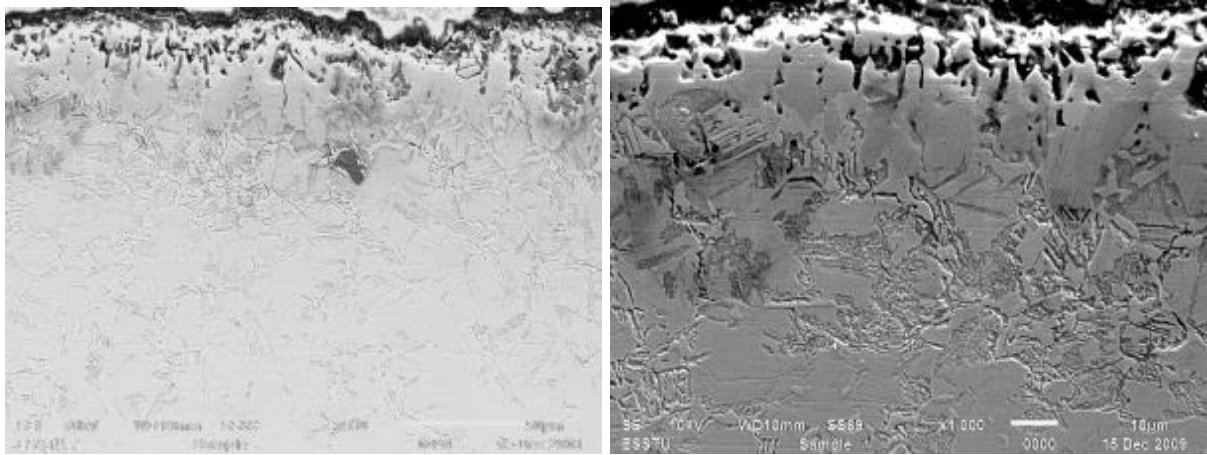


Fig. 1. Microstructure of boride layer on steel 5XHB.

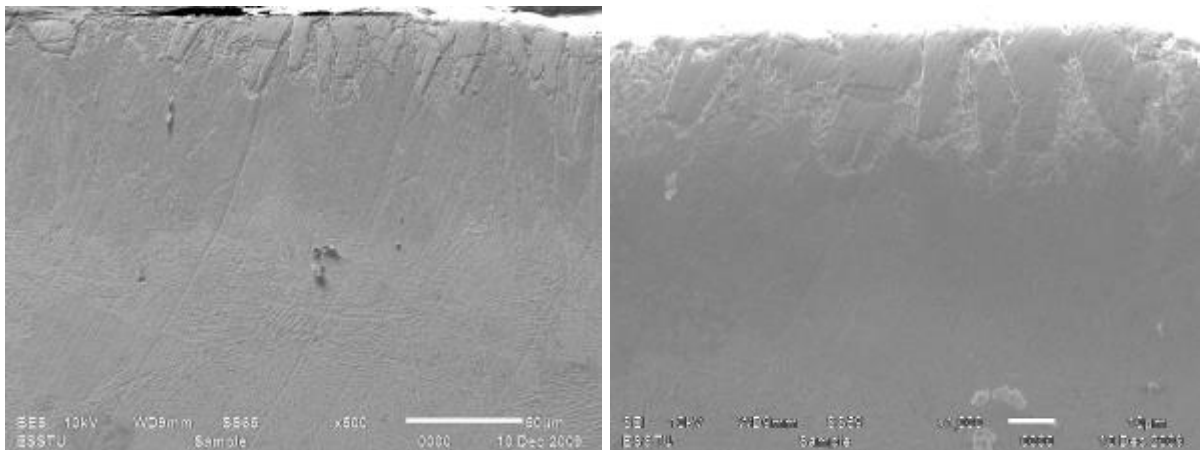


Fig. 2. Microstructure of the diffusion layer on steel 5XHB after complex boronizing and titanation.

Equilibrium in the system Fe - B in the diffusion process leads to the formation of three stable borides: FeB, Fe₂B and Fe₃B. Furthermore, it may be metastable boride Fe₂₃B₆, which has a cubic structure. It should be noted that unlike a solid solution of carbon in iron content of boron in iron phases is extremely limited due to the low solubility of boron in iron.

In addition to binary phase FeB, Fe₂B, Fe₃B, Fe₃C, there was a small amount of ternary phases: Fe₃(C, B) and Fe₂₃(C, B)₆, and of course a ferrite.

Fe_3C phase Fe_{23}C_6 isomorphic Fe_3B and Fe_{23}B_6 . Therefore it is easy to obtain the corresponding ternary phase symmetry, namely, $\text{Fe}_3(\text{C}, \text{B})$ and $\text{Fe}_{23}(\text{C}, \text{B})_6$.

Expected presence of boron carbide in the surface layer is hardened in this study was not found. This is due to the presence of small amounts of carbon in the surface layers of the steel as a result of decarburisation at saturation with boron.

Phase composition was diagnosed with the diffraction pattern obtained in two ways: 1) X-ray diffraction analysis, and 2) electron diffraction.

Borated cementite $\text{Fe}_3(\text{C}, \text{B})$, and normal cementite Fe_3C well characterized morphologically. Prior to boron penetration into the lattice can be clearly visible laminar structure of cementite (Fig. 3 a). After penetration of boron and education instead of borated cementite perfect layers formed fragmentary structure (Fig. 3 b).

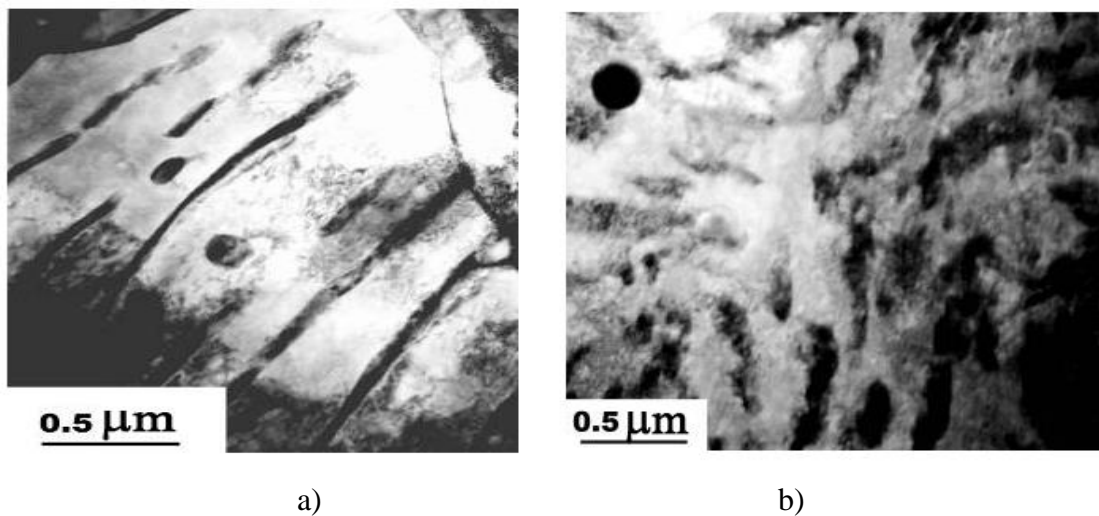


Fig. 3. Conventional microstructure (a) and borated (b) of cementite of steel 5XHB.

Cementite plates at boriding fragmented forms and fragments of plates which can be seen clearly in Fig. 3 b. Availability borated cementite in all studied in steels also confirmed X-ray analysis.

As the distance from the surface concentration of boron is reduced, and the density of crystal defects increases. This is due to the distance from the equilibrium structures as the distance from the surface of the borated.

While the integrated saturation boron and titanium diffusion layer is exposed minor changes (Fig. 2) - two-layer structure is formed, the upper part of which consists of columnar crystals boride containing titanium, and the lower (dark) portion is a mixed carbide and boride of iron and titanium. Furthermore, this zone is present up to 22% titanium, and about 0.47% carbon. Such concentration titanium and carbon, may be the result of the mutual diffusion of carbon from the metal and the depth of diffusion of carbon from the metal surface. Mechanical properties of this area has the effect of increasing the amount of microhardness boride needles 17-22% and a transition zone of about 25-35%, which in turn affects the strength of the hardened steel so. The remainder of the chemical composition and microstructure of the transition zone does not differ from borated.

Results of laboratory

Tests close working conditions stamps steels shown in Figure 4. As a standard of comparison selected Y8 (W 108 AISI/ASTM) steel having hardness of 55-57 HRC.

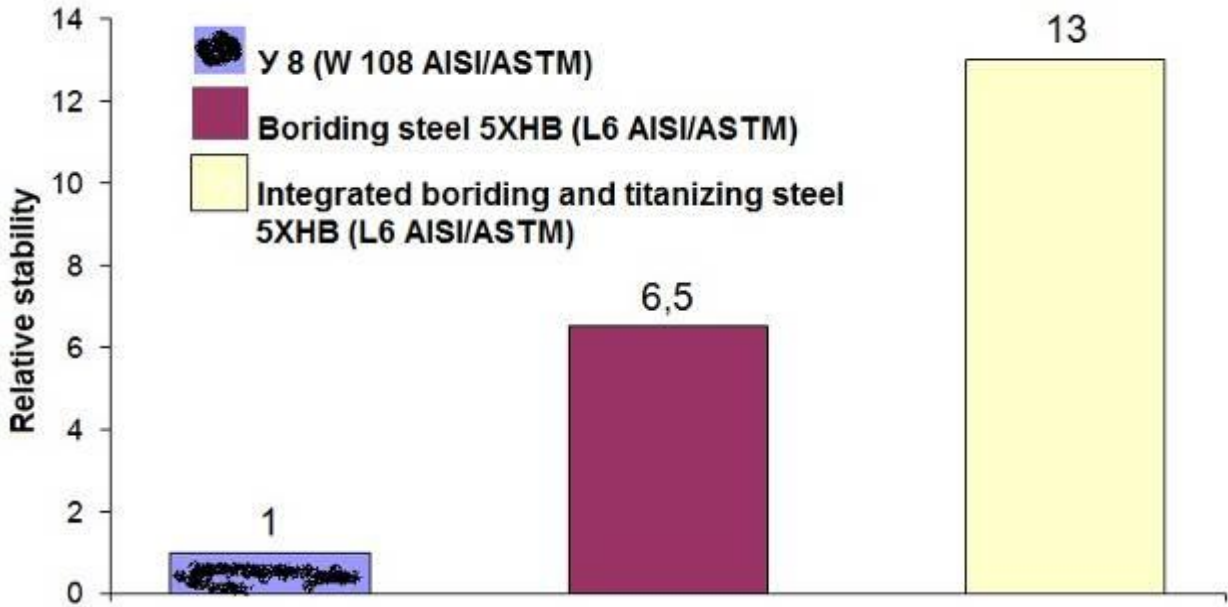


Fig. 4. Relative stability the borated and integrated borated and Titanizing steel 5XHB.

References

- [1]. A.M. Guriev, S.G. Ivanov. The mechanism of diffusion of boron, chromium and titanium, while multicomponent saturation surface iron alloys. *Fundamental problems of modern materials*. 2011. V. 8. № 3. pp. 92-96.
- [2]. A.M. Guriev, S.G. Ivanov, A. D. Greshilov, S.A. Zemlyakov. The mechanism of formation of boride needles in complex diffusion saturation of boron and chromium from saturating plasters. *Metalworking: technology, equipment, tools*. 2011. № 3. pp. 34-40.
- [3]. M.A. Guriev, D.S. Filchakov, I.A. Garmaeva, S.G. Ivanov, A.M. Guriev, Okolovich G.A. Technology applying multicomponent hardening coatings on steel parts. *Polzunovskii Herald*. 2012. № 1-1. pp. 73-78.
- [4]. S.G. Ivanov. Development of saturating mixture and technology diffusion saturation of boron and chromium heavy duty machine parts and tools. A thesis for the degree of candidate of technical sciences. Altai State Technical University after I.I. Polzunov. Barnaul, 2007. 175 p.
- [5]. A.M. Guriev, A. D. Greshilov, E.A. Kosheleva, S.G. Ivanov, M.A. Guriev, A.G. Ivanov, A.A. Dolgorov. Multicomponent diffusion surface hardening of machine parts and tools from mixtures based on boron carbide. *Metalworking: technology, equipment, tools*. 2010. № 2. pp. 19-23.
- [6]. A.M. Guriev, B.D. Lygdenov, S.G. Ivanov, O.A. Vlasova, E.A. Kosheleva, M.A. Guriev, S.A. Zemlyakov. A new way of diffusion Thermocyclic surface hardening iron alloys. *Polzunovskii miscellany*. 2008. № 3. pp. 10-16.
- [7]. A.M. Guriev, S.G. Ivanov, I.A. Garmaeva. Diffusion coatings of steels and alloys. Barnaul, 2013. 221 p.
- [8]. S.G. Ivanov, I.A. Garmaeva, M.A. Guriev, A.M. Guriev. Features a multi-component alloy steels saturation. *Modern engineering. Science and education*. 2013. № 3. pp. 1155-1160.

PHASE COMPOSITION OF GRADIENT STRUCTURES ON CARBON STEELS AFTER BORONIZING

B.D. Lygdenov^{1,2}, A.M. Guriev^{1,3}, V.A. Butukhanov²,

Mei Shunqi¹, Zhou Qinhu¹

¹ Wuhan Textile University, China.

² East Siberia State University of Technology and Management, Russia.

³ Altay State Technical University after Polzunov, Russia.

Introduction

Regularities and mechanisms of boronizing on the ferritic-pearlitic steel with 0.1 % carbon studied and described previously [1 - 4]. Structure of diffusion layer was investigated in each layer with the help of thin foils. Foil was cut at different distances from the surface of the sample. Structure of boronized layer on ferritic-pearlitic steel has a more complicated structure than expected in the previously described studies. The transition zone is carbon-boride. Phase composition within the entire carbon-boride zone is not change, however, in the layers of the mechanism of its formation in different areas varies. Carbon-boride zone can be divided into four layers (zones): 1 - layer formed the bulk diffusion of boron; 2 - layer where deposits of boron diffusion in volume and boron diffusion along the borders are approximately equal; 3 - layer where the diffusion of boron occurs mostly of newly created borders; 4 - layer where the diffusion of boron occurs practically only on the old boundaries (the grain boundaries).

It is shown that the process of boronizing is being implemented by seven mechanisms: 1. Reaction diffusion on interphase boundaries. 2. Diffusion across new grain boundaries. 3. Diffusion across old grain boundaries. 4. Diffusion together with migration borders. 5. Diffusion across sub boundaries. 6. Diffusion across dislocations. 7. Diffusion in a volume of the material without defects.

The main mechanism for each layer is symbolized in the table 1 with letter A. Secondary mechanisms which influence is significantly marked with the letter B, the mechanisms that act but have little effect on the process marked C.

Table 1. Diffusion mechanisms in the process of boronizing of steel.

Number of layer	The distance from the surface of the sample	Types of diffusions						
		Reaction on interphase boundaries	Across new borders	Across old borders	Together with migratory borders	Across sub borders	Across the dislocations	In the volume of material
1	Surface	A	-	-	C	-	-	C
2	125 μm	-	B	C	B	-	C	B
3	225 μm	-	A	C	B	C	C	B
4	350 μm	-	A	C	B	C	C	A
5	500 μm	-	A	C	B	C	C	B
6	2,5 mm	-	-	A	C	-	C	-
Centre of the sample	6,5 mm	-	-	-	-	-	-	C

The first layer is formed by the reaction diffusion. The diffusion of new borders gives the main contribution in the 2, 3 and 4 layers. In the 4 layer significant contribution gives volumetric diffusion. In 5 and 6 layers together the migration of existing borders makes their contributions to the core.

It is established that new grain boundaries and subgrains of boronizing are perform a triple role. First, they serve as the main channel saturation atoms of boron and carbon main underlying layers. Secondly, large part of carbonborides is localized there. Thirdly, a considerable part of the atoms of boron and carbon of not yet formed carbon-borides is concentrated there. It is established that the diffusion along the grain boundaries is the main mechanism of carbon-borides except the outer layer where the decisive factor is the reaction diffusion [5 - 7].

The general regularities and peculiarities of processes of structure formation to boronizing of steel with 0.45 % carbon are given in this paper.

Material and methods of research

The experimental investigations of the structure and phase composition of boronized layer on the surface of steel with 0.45 % carbon. (Fig. 1 - 3).

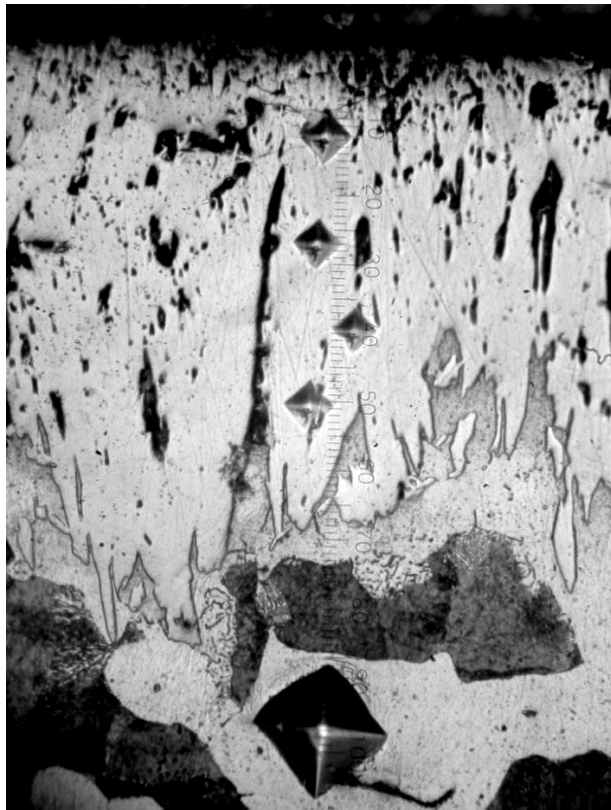


Fig. 1. Structure of boronized steel with 0,45 % carbon (x 400).

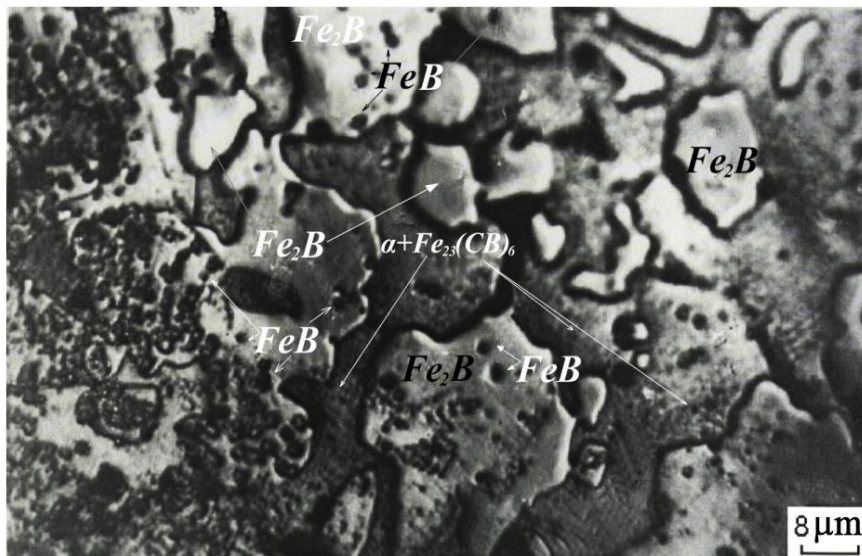


Fig. 2. Microstructure of boronized layer steel with 0.45 % carbon. Present phases are marked. Phase where identified using the method of diffraction microscopy. An incision was made along the surface at a depth of 40 microns.

The surface structure of the investigated steel is actually formed by three chemical elements: iron, boron and carbon. Iron is the main element, boron is the main alloying element on the surface and the carbon is in the number entered in steel.

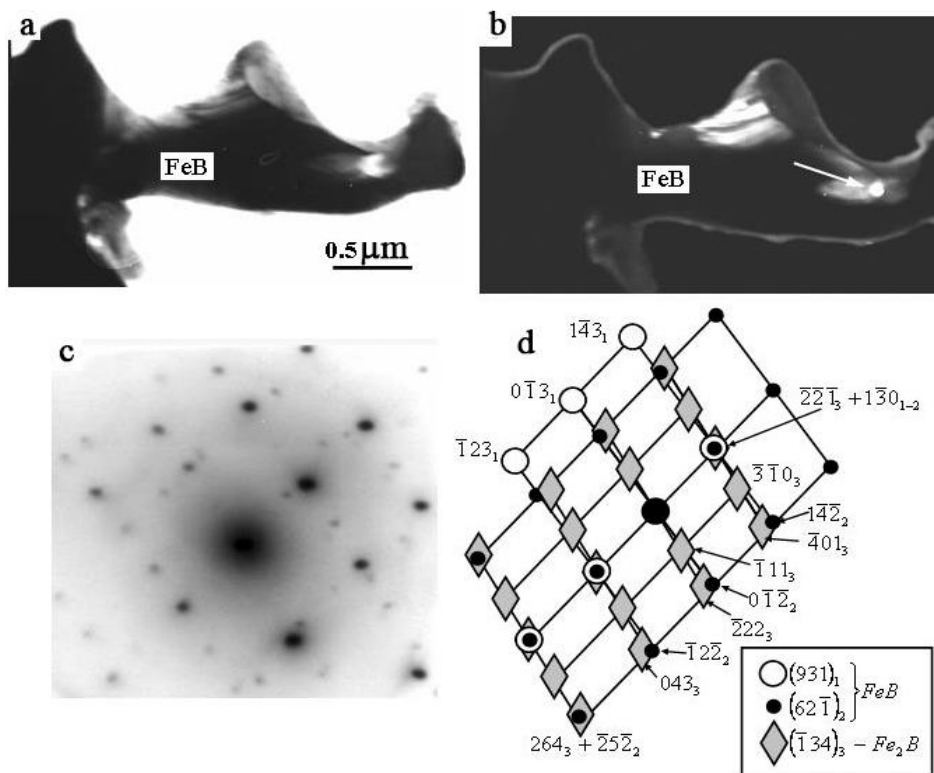


Fig. 3. Thin structure of boronized steel with 0.45 % carbon.

The investigations revealed the following:

1. There are ferrite grains with varying alloy components.
2. There is the plate perlite in the form of grains on boundaries of ferrite grain. Perlite is an alternation of parallel plates of ferrite and iron carbide.
3. Carbon-cementite (boric cementite) $Fe_3(C,B)$ in which a part of the carbon is replaced by boron. There is boronized cementite mainly in the transition zone.
4. Carbon-boride $Fe_{23}(C,B)_6$ is located in the body of the ferrite grain on dislocations.
5. Boron carbide B_4C presents only on the surface of the diffusion layer.
6. Boride of iron Fe_2B has a form like needles (see Fig. 1).
7. Boride of iron FeB presents in the layer in the form of particles of round shape.

In layer II there is an α -phase with defect (dislocation) structure in addition to borides FeB and Fe_2B . A scalar density of dislocations [8] in this layer constitutes the value $\sim 2.8 \cdot 10^{14} \text{ m}^{-2}$ (Table 2). View dislocation structure steel with 0.45 % of carbon presented in Fig. 4.

Table 2. Quantitative parameters of the structure.

Diffusion layer		Steel with 0,45 % carbon	
		$\rho \cdot 10^{-14}, \text{M}^{-2}$	χ, CM^{-1}
Boride zone	I	Layer without dislocations	
	II	No measurements	
The transition layer	III	2,8	No measurements
Base metal	IV	Diffusion layer is missing	

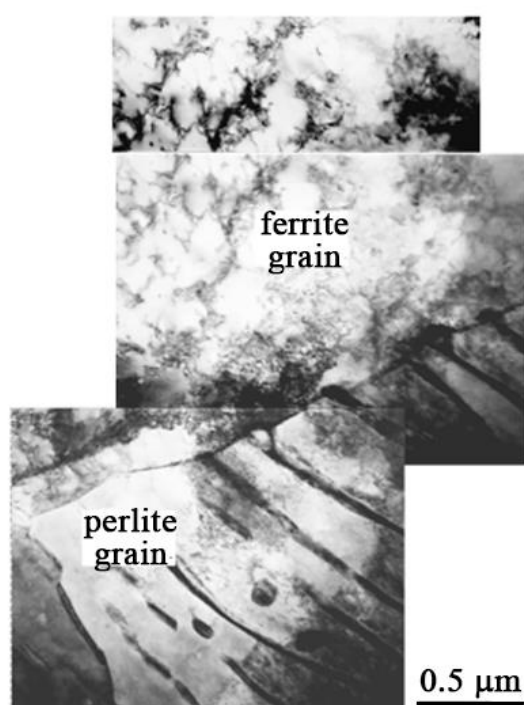


Fig. 4. Dislocation structure of boronized steel with 0,45 % carbon at a distance of 1.4 mm from the surface - joint of two grains: ferrite and perlite.

Conclusion

1. Authors investigated the patterns of diffusion layers after the saturation of steel with 0.45 % carbon in a situation when formation of big quantities of carbides and intermetallic compounds was possible.

2. A detailed study of the thin structure of boronized layer on steel with 0,45 % of carbon, phase composition and density of defects found that 4 main layers formed. The first layer consists almost entirely of boride of iron FeB.

Small amounts are present borides. There are Fe_2B borides in small amounts and in some cases - Fe_8B . In the second layer borides does not occupy the entire volume. Along with them there are α -phase, carbon-borides $\text{Fe}_3(\text{C},\text{B})$ and $\text{Fe}_{23}(\text{C},\text{B})_6$. The third layer contains the remains of borides iron. Boron in this layer situated mainly in carbon-borides. The fourth layer retains the original structure.

References

- [1] A.M. Guryev, E.V. Kozlov, L.N. Ignatenko, N.A. Popova. Physical basis of thermocyclic boronizing of steels. Barnaul: Altstu, 2000. 216 p.
- [2] A.M. Guryev, E.V. Kozlov, N.A. Popova and others. Change of phase composition and mechanism of formation of the structure of the transition zone after thermocyclic carbon-boronizing on ferritic-perlitic steel. Russian Physics Journal. 2000. V. 43. №. 11. pp. 60-67.
- [3] A.M. Guryev, E.V. Kozlov, N.A. Popova and others. Change of phase composition and mechanism of formation of the structure of the transition zone after thermocyclic boronizing on ferritic-perlitic steel. Russian Physics Journal. 2001. №. 2. pp. 58-63.
- [4] A.M. Guryev, E.V. Kozlov, A.M. Kirienko, N.A. Popova. Phase composition transformation and transition zone structure formation mechanism in the process of termocyclic ferrite-perlite steel borating. Book of Abstracts 7th international symposium on advanced materials (ISAM-2001). Islamabad, Pakistan. 2001. P. 122.
- [5] A.M. Guryev, B.D. Lygdenov, O.A. Guryeva and others. Features of formation of structure of diffusion layer cast steel after chemical-heat treatment. Fundamental problems in materials science. 2005. №. 1. P. 39-41.
- [6] Lygdenov B.D., A.M. Guryev, I.A. Garmaeva and others. Features of formation of structure of diffusion and development of the technologies of hardening of cast tool steels in accordance with the dendritic segregation. Fundamental problems in materials science. 2006. №.3. pp. 84-86.

- [7] A.M. Guryev, O.A. Vlasova, B.D. Lygdenov and others. Increase of durability of tool steels in the process of termocyclic boronizing. XVII Petersburg readings on problems of durability. Saint-Petersburg. 2007. V. 1. pp.196-198.
- [8] P. Khirsh, A. Howi, R. Nikolson and others. Electron microscopy of thin crystals. M.: Mir. 1968. 574 p.
- [9] G.V. Samsonov, I.M. Vinnitskiy Refractory compounds. M.: Mir. 1976. 500p.

FORMATION FINE STRUCTURE OF THE SUPERIOR QUALITY RAILS

**V.E. Gromov¹, K.V. Volkov², Yu.F. Ivanov³, K.V. Morozov¹,
S.V. Konovalov¹, K.V. Alsaraeva¹, O.A. Semina¹**

¹ Siberian State Industrial University, Kirov str., 42, Novokuznetsk, Russia, 654007, e-mail: gromov@physics.sibsiu.ru.

² EVRAZ Consolidated West Siberian Metallurgical Plant, av. Kosmicheskoe, 16, Novokuznetsk, Russia, 654043, e-mail: volkov_kv@nkmk.ru.

³ High Current Electronics Institute of the Siberian Branch of the RAS, av. Akademicheskii, 2/3, Tomsk, 634055, Russia, e-mail: yufi@mail2000.ru.

Introduction

The researches of structure, phase composition and dislocation substructure formed in rails section as a result of thermo mechanical effects are very important for understanding of the physical nature of transformations as they allow to form the operational parameters of products purposefully. The purpose of the present paper is the analysis of structure-phase states and of defects substructure formed in the bulk-hardened rail steel.

Material and methods of research

Samples of a rail steel of the category "B" (heat-strengthened rails of the superior quality) were used as a research material in accordance with Russian standard GOST 51685-200. Rails have been subjected to traditional heat treatment after rolling: a bulk oil hardening with the following high tempering. The structure-phase state of steel was investigated by the transmission electron microscopy (TEM) methods of thin foils in the layers located at the distance of 2 mm and 10 mm from a rail head surface on the central axis and on round corner.

Results of research and discussion

According to morphological character the following structural components of rail steel have been defined: lamellar pearlite (the relative content of 0.68), grains of ferrite-carbide mixture (0.28) and grains of structurally free ferrite. The lamellar pearlite of rail steel is structurally and morphologically imperfect. Structural imperfections of ferrite plates of pearlite colonies are related with the availability of dislocation substructure in them.

It has been defined that the dislocations in ferrite plates can be distributed chaotically (Fig. 1 a) or can form a net substructure (Fig. 1 b). The scalar density of chaotically distributed dislocations is $\sim 1.0 \times 10^{10} \text{ cm}^{-2}$. The net dislocation substructure in a pearlite colony, as a rule, is formed in ferrite bridges, the scalar density of dispositions in this structure reaches $\sim 5.0 \times 10^{10} \text{ cm}^{-2}$. The cementite plates are also of defect character. When analysing pearlite by the dark-field method the block structure of cementite plates is revealed (Fig. 1 c, d). The block dimensions vary within the limits of 15-25 nm.

The dispersity of pearlite was estimated by the interlamellar distance – the total width of two nearby located plates: ferrite and cementite. The estimates done by this way have shown that the interlamellar distance of pearlite colonies varies within the limits of 80 – 100 nm.

The grains of ferrite-carbide mixture can be divided into three sub-groups by the form and mutual location. The grains, in which cementite particles have a form of short plates, refer to the first sub-group. This structure can be referred to

the structure formed at bainite mechanism, namely to the upper bainite by the morphological character. The grains in which cementite particles of the round form are distributed chaotically in the volume of grains, are referred to the second sub-group. It is possible to suggest that these grains are formed by diffusion mechanism and are the globular pearlite. The cementite particles of the round (globular) form are distributed in parallel lines, the grains of which are referred to the third sub-group. The structure of these grains was formed evidently by shear mechanism and is packet martensite.

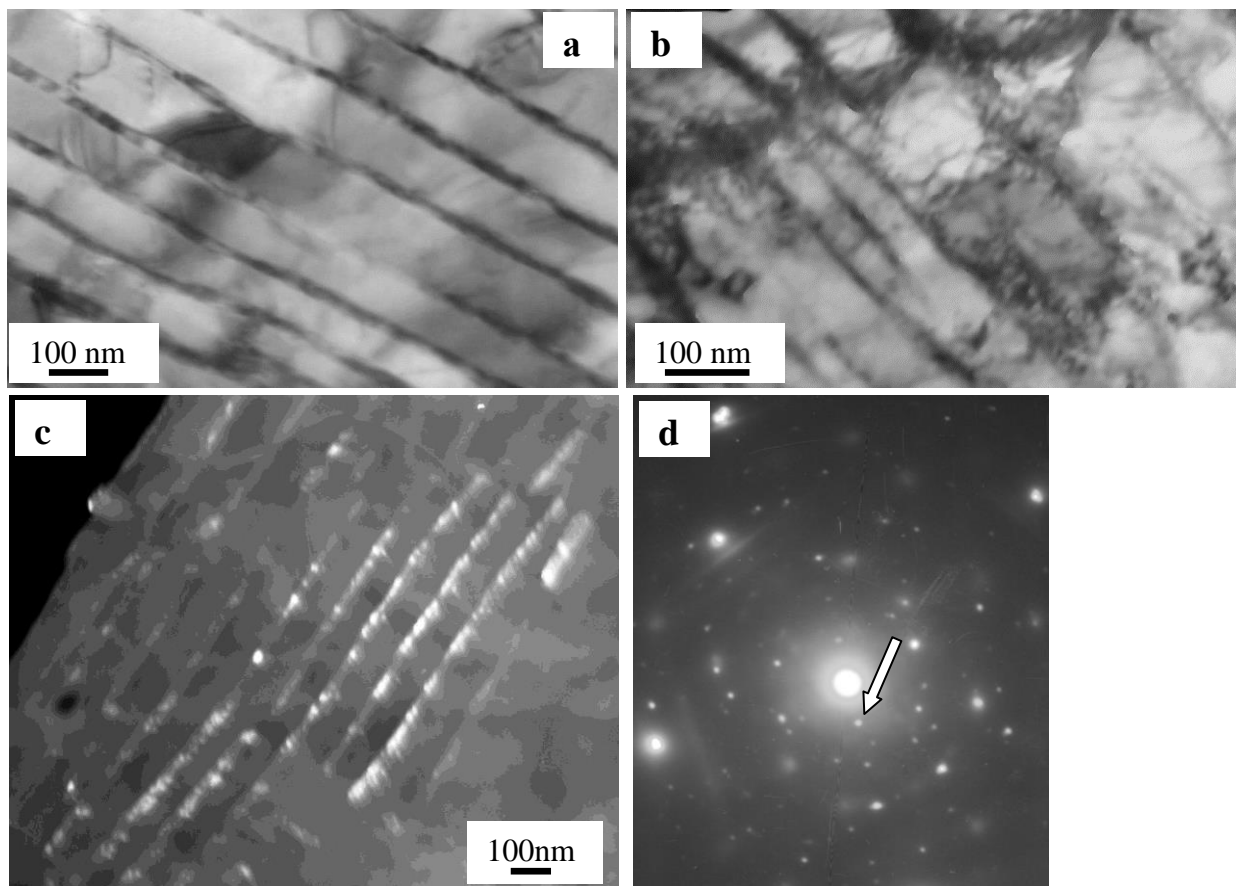


Fig. 1. Defect substructure of plates of ferrite (a, b) and cementite (c, d) of pearlite colonies; a, b – light fields; c – dark field obtained in reflex $[101] \text{Fe}_3\text{C}$; d – micro electron-diffraction pattern, arrowhead shows the reflex where the dark field obtained.

In the volume of grains of the first and third sub-groups the net dislocation substructure is present, predominantly the dislocation scalar density of which is $5-6 \times 10^{10} \text{ cm}^{-2}$. In the grains of the second sub-group the net, cell-net dislocation substructures and also the chaotically distributed dislocations are

observed. The carbide phase particles are often present within the limits of cells and in the cells' volume. In the first case the particle dimensions are 30-50 nm; in the second – 10-15 nm.

As a result of fulfilled researches it was established that the stress concentrators in steel are interfaces of cementite plates of pearlite grains, interfaces of pearlite and ferrite grains. In this case, the contour begins from the interface of the plates and/or grains. Often the sources of stress fields are the second phase particles distributed along the interfaces and in the volume of grains.

It is experimentally shown that the amplitude of the internal stress fields is inversely proportional to the width of the bend extinction contour h . The evaluations done in this work show that the average width of bend extinction contours revealed in pearlite grains, i.e. of contours being formed from the interface of cementite and ferrite plates is 80 nm, and in the grains of ferrite-carbide mixture, i.e. generated by the globular particles is 25 nm. Consequently, the particle/matrix interfaces are the most significant stress concentrators and can be referred to the typical areas of cracks forming.

Conclusion

The thermo mechanical processing of rails is accompanied by forming of multiphase, morphologically different structure generated by diffusion and shear mechanism of $\gamma \leftrightarrow \alpha$ - transformation of solid solution on the iron basis. The quantitative analysis is done and general parameters are revealed which characterize the gradient character of the structure, the phase composition and the defect substructure of steel. It is established that the preferred areas of micro-cracks nucleation in steel are the boundaries of globular particles matrix.

References

[1]. V.I. Voroshishev, Composition and manufacture technology of rails of heightened efficiency, Novokuznetsk polygraphic combinat, Novokuznetsk, 2008.

- [2]. K.V. Volkov, V.E. Gromov, Yu.F. Ivanov, V.A. Grishunin, Increasing of fatigue life of rail steel by the electron-beam treatment, Inter-Kuzbass, Novokuznetsk, 2013.
- [3]. R.O. Olivares, C.I. Garcia, A. DeArdo et al, Advanced metallurgical alloy design and thermo mechanical processing for rails steels for North American heavy use, *Wear*. 271 (2011) 364-373.
- [4]. Ren Anchao, Ji Yu, Zhou Gui-feng et al, Hot Deformation Behavior of V-Microalloyes Steel, *Journal of iron and steel research, international*. 17 (8) (2010) 55-60.
- [5]. E.A. Shur, Rail damages, Intext, Moscow, 2012.
- [6]. P.B. Hirsch, E.A. Howi, R.B. Nikolson et al, Electron microscopy of thin crystals, Krieger Publishing Co, Melbourne, 1977.
- [7]. V.E. Gromov, E.V. Kozlov, V.I. Bazaykin et al, Physics and mechanics of drawing and bulk forging, Nedra, Moscow, 1997.

**THE INFLUENCE OF ACID AND HYDROGEN-CHARGING MEDIA
ON THE MECHANICAL PROPERTIES OF AMORPHOUS AND
NANOCRYSTALLINE ALLOYS**

V.A. Feodorov, T.N. Plushnikova, S.A. Sidorov, A.V. Yakovlev

Abstract

This paper investigates the influence of corrosive media (NaCl+H₂S, 20 % H₂SO₄ solution and HNO₃) the amount of mechanical stress relief in samples of amorphous alloys based on cobalt and nanocrystalline iron-based alloy, which occurs depending on the σ - ε by passing electrical current pulses. Established the dependence of the strain relief in the material density of the pulsed electric current. The regularities of changes in plasticity and ductility temperature begin to drop, depending on the temperature of preliminary annealing.

This paper investigates the influence of corrosive media (NaCE+H₂S, 20 % H₂SO₄ solution and HNO₃) the amount of mechanical stress relief in samples of amorphous alloys based on cobalt and nanocrystalline iron-based alloy, which occurs depending on the σ - ε by passing electrical current pulses. Established the dependence of the strain relief in the material density of the pulsed electric current. The regularities of changes in plasticity and ductility temperature begin to drop, depending on the temperature of preliminary annealing.

Introduction

Expanding the range of application of amorphous and nanocrystalline alloys sets targets for studying the structure and properties of these materials after various influences. These may be both stationary and nonstationary thermal field pulse and a static electric and magnetic fields, as well as various environments leading to oxidation and corrosion. With its high corrosion resistance, metallic glasses show a significant sensitivity to hydrogen and corrosive environments, resulting in embrittlement of these materials [1].

Aim is to study the deformation of amorphous and nanocrystalline alloys subjected to external influences (corrosion and hydrogen-charging protection, pulsed electric current, heat).

Results and discussion

The following alloys were chosen for testing: amorphous cobalt-based metal alloys (AMAG-172–186) and nanocrystalline Fe-based alloy (AMAG–200) obtained by melt spinning. Sample dimensions: $\sim 3.5 \times 0.02 \times 40$ mm. The uniaxial stretching experiments were performed on the electromechanical machine for static testing Instron-5565. The current density (j), passing through the samples ranged from $1 \cdot 10^8$ to $5 \cdot 10^9$ A/m². Pulses with a duration of $\tau \sim 5$ ms were used. Corrosive medium were 20 % solution of sulfuric and nitric acids (exposure time - 40 minutes), and the solution NACE (50 g/l) + H₂S (100 mg/l) and NACE (50 g/l) + H₂S (400 mg/l) exposure time – 24 hours.

Deformation of amorphous metal alloys together with simultaneous passing of an electric current pulse on load charts is accompanied by a phenomenon

similar to an electroplastic effect, which is well-studied for crystal structures [2–3]. At the time when the current pulse passes, in diagrams σ - ε there is a short (~ 1.1 s) mechanical stress relief $\Delta\sigma$ with further complete reduction of variation σ - ε [4]. Moreover, the transmission of pulse electric current causes an abrupt short-term increase of the sample temperature.

The investigation dealt with the influence of a 40-minute exposure to 20 % solutions of sulfuric and nitric acids on the values of mechanical stress reliefs caused by passing pulse current. It was discovered that after keeping the samples in a sulfuric acid solution the value of stress relief falls by $\Delta\sigma \approx 20$ % as compared with the value of reliefs of the samples at the initial stage (Fig. 1 a, b).

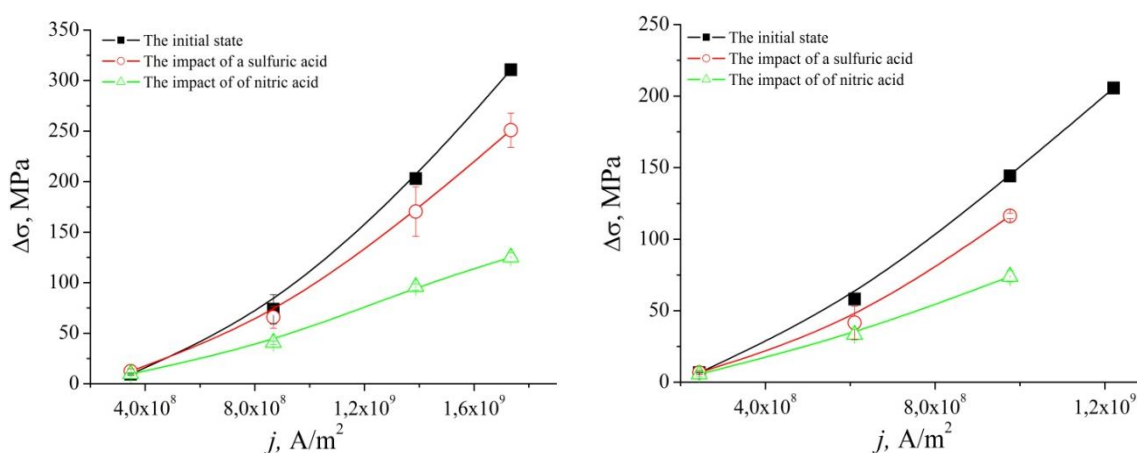


Fig. 1. Dependence of the mechanical stress drop value on current density in the alloy: after exposure to a 20 % solution of sulfuric and nitric acids: a) AMAG-172; b) AMAG-180).

Keeping them in a nitric acid solution reduces the value of stress relief by 50 % as compared with the value of stress relief at the initial state. Effects of an acidic medium on nanocrystalline Fe-based alloy do not affect the value of mechanical stress drops.

Decrease in the value of stress relief result from surface phenomena. The exposure to an acid environment leads to amorphous material on the surface appearance sulfate formations thickness up to 3 micron. Moreover, the oxide surface revealed formation, as evidenced by the study of the elemental composition. Formed on the surface of the kraft tape, metallic cross section of

the sample decreases, which leads to an increase in resistance and decrease the current acting on the sample. This accordingly causes less heating of the sample, thereby reducing the amount of discharge of the mechanical stress induced by passing a pulsed current.

Keeping a nanocrystalline iron-based alloy in solutions of sulfuric acid leads to the formation of pitting corrosion. The typical size of pitting holes is 300 – 350 nm \approx 40 nm deep.

Of interest to study the behavior of hydrogenated samples, while the deformation and current action. Metal cobalt is capable of absorbing large amounts of hydrogen [5] without forming compounds of constant composition. Therefore, hydrogen, apparently, does not evaporate but remains in the surface layer of the material, causing its embrittlement, which is observed experimentally. In this connection, we have conducted experiments on uniaxial tension and hydrogenated nanocrystalline metallic alloys based on Co and Fe, subjected to pulsed currents influence. Depending recession stress on the current density obtained during the experiments are shown in Fig. 2.

Experimentally found that when exposed to a solution of NACE + 400 mg/l H₂S an increase in mechanical stress (\approx 10 %) in the alloy samples AMAG-200 with respect to the samples AMAG-200 is not subjected to hydrating (Fig. 2c). Furthermore, the mechanical stress values declines at AMAG-200 caused by the pulsed current of hydrogenated samples not dependent on the concentration of hydrogen-charging environment.

In the Co-based alloys dependence of mechanical stress relief on the density of electric current supplied to the hydrogen-saturated and no hydrogenated samples practically coincide.

Effect of increasing the mechanical stress on the discharge of the nanocrystalline alloy explained by interaction of hydrogen-containing medium with an alloy that results in the formation of oxide films on the surface, as evidenced by an increase in the brittleness of the samples.

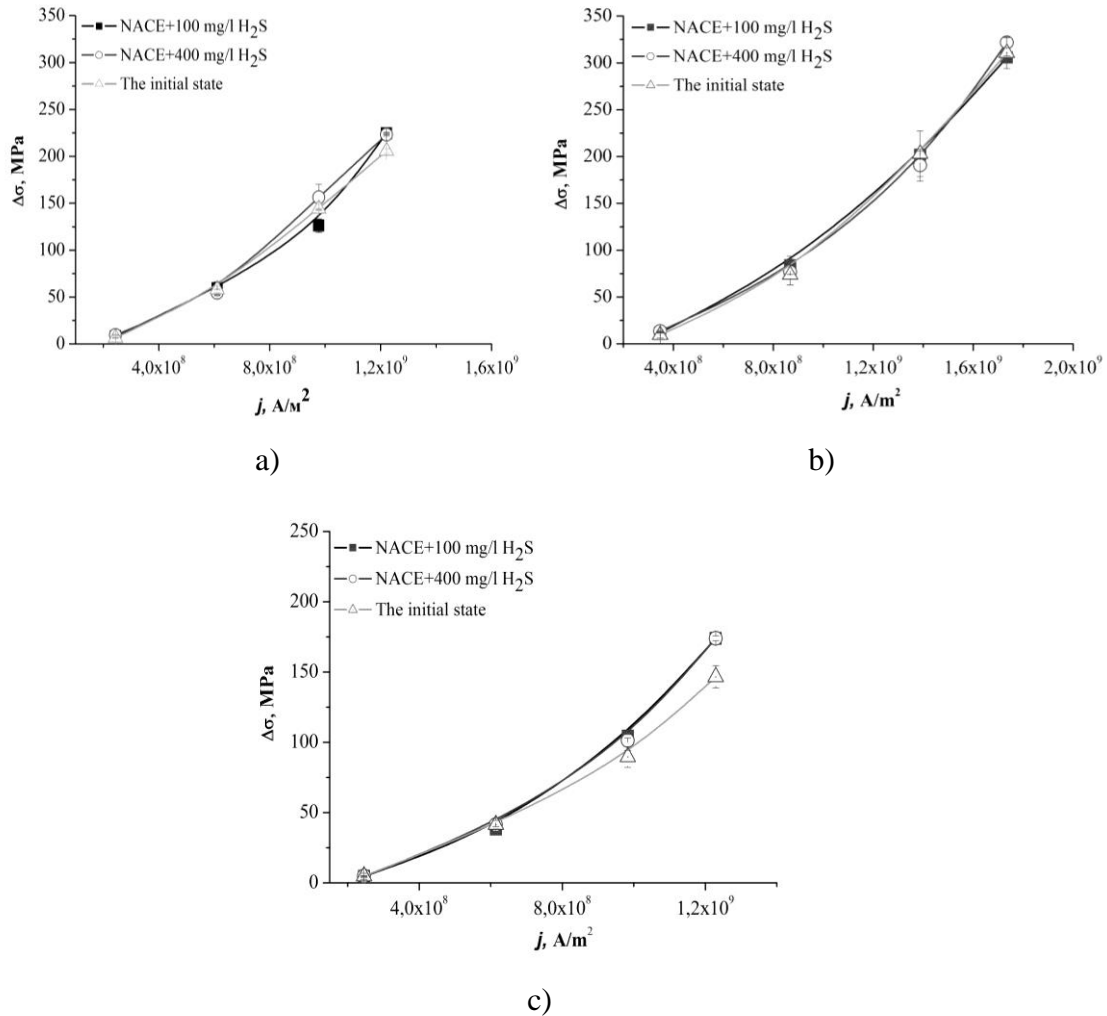


Fig. 2. Dependence recession stress the current density acting on the samples:
a) AMAG-172; b) AMAG -180; c) AMAG -200.

In the second part of the paper studied the effect of hydrogen-containing medium on the plasticity of the materials studied after isochronal annealing. Metallic glass ribbon was annealed in an oven to isochronous at specified temperatures with a dwell time of 10 minutes in the bulk of the stabilizing plates. Bending method investigated the variation of plasticity MS depending on the annealing temperature. Measure of the plasticity of evaluated expression $\varepsilon = h/(D-h)$: where $h = 20$ micron – belt thickness, D – distance between the parallel plates, in which the curved sample destroyed.

Possible degradation of the material due to changes in the material properties under the influence of hydrogen on the surface layer material. Study the elemental composition of a scanning electron microscope Quanta 3D, control

samples alloy AMAG–180 hydrogenated and showed that there is selection of elements sulfur, oxygen and carbon. Sulphur, in connection with entering into iron, which is found in all the amorphous strip forms a sulfide (black) film on the surface of metallic glasses. It was established that the ductility of the metallic glass subject to the action of the hydrogen medium is lower than the ductility of the samples annealed at the same temperature. The temperature began to fall plasticity reduced by ~ 50 K. Ductility falls an average of 20 % up to a certain temperature, then an increase in ductility to values corresponding to values of ductility of the annealed samples.

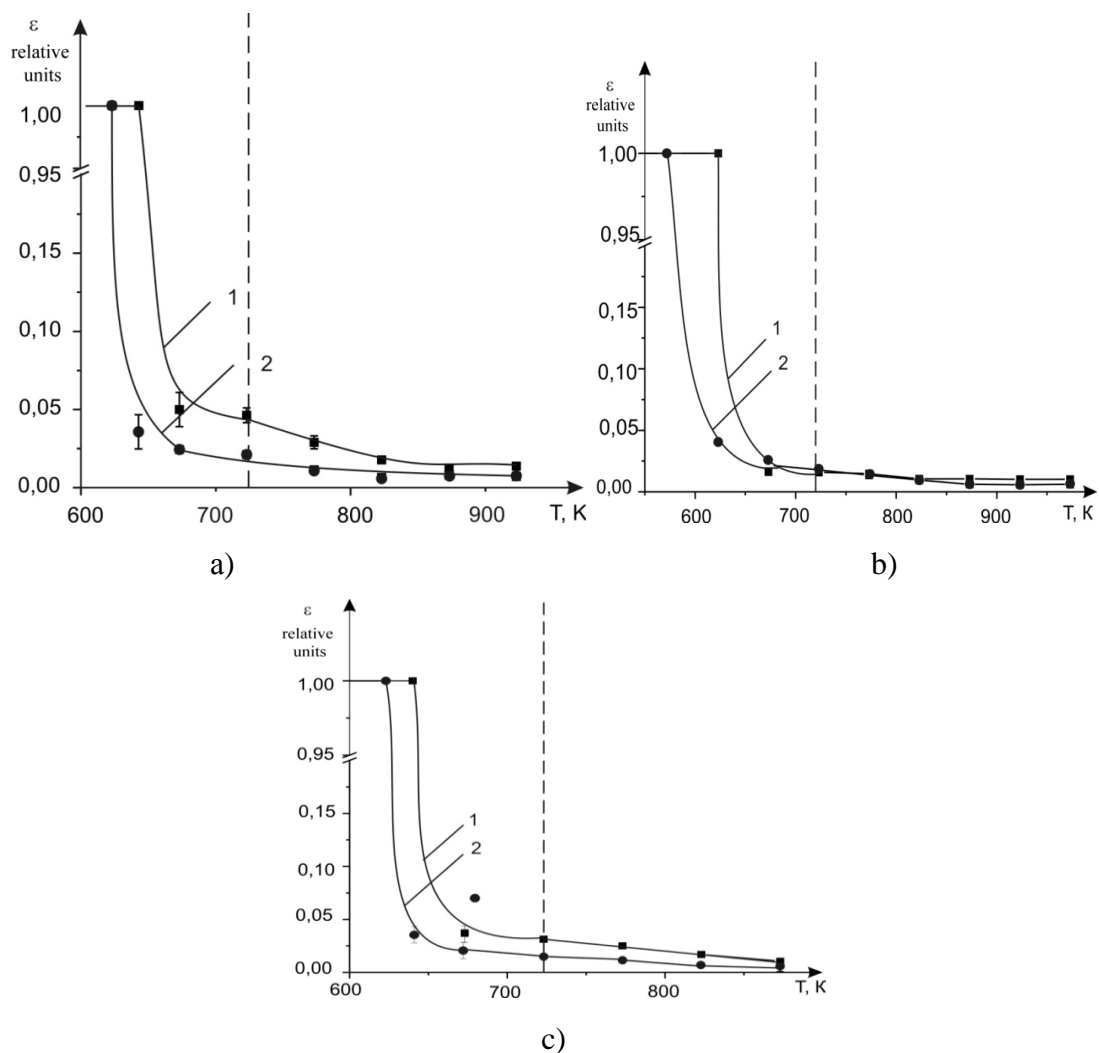


Fig. 3. Dependence on temperature ductility annealing (10 min) alloy: a) AMAG–172; b) AMAG–183; c) AMAG–186, 1 – no corrosion protection; 2 – corrosive environment NACE + H₂S (400 mg/l).

It is known that annealing of metallic glasses free volume decreases due to the existence of which there is hydrogenation. That this may be related to an increase in the ductility of the amorphous metal alloy after annealing at temperatures above 950 C. At higher temperatures starting from a temperature $T = 773$ K, the change in ductility is not a hydrogen-charging is dependent on the concentration of the medium. Such behavior plasticity in hydrogenation and annealing observed for other alloys. The dependences obtained for alloys AMAG – 172, AMAG – 183, AMAG -186 are shown in Fig.3.

It is seen that increasing the cobalt content also increases the ductility. Found that hydrogen-containing media affects plasticity AMAG MS-183 in a certain range of annealing temperatures (575 – 725 K). In the alloy AMAG-186 hydrogen-environment influence on the plasticity of metallic glass can be seen in a wider range of temperatures (625 - 825 K).

Conclusions

Exposure under acid conditions forms sulfate compounds on the surface of amorphous alloys, resulting in a marked reduction of the metal section of the sample, which leads to increasing resistance of the material, reducing the strength of the current and consequently to less heating of the sample, thus decreasing the value of the mechanical load drop.

Thus the change in the value of the mechanical load relief caused by pulse current in these alloys after their exposure to aggressive media happens only due to the change of the value of heating of the alloys.

Influence hydrogenous medium on annealed samples metallic glass based on cobalt leads to a reduction of plasticity, the temperature began to decrease incidence of plasticity due to hydrogen penetration depth of the material due to the existence of free volume. Upon annealing, the free volume is reduced, thereby reducing the hydrogenation, it is the reason for the increase of plasticity to the values corresponding to the annealed samples not exposed to hydriding.

Acknowledgments

This work was supported by grants from RFBR (№ 12-01-00638)

References

- [1]. A.M. Glezer, I.E. Permyakov, V.E. Gromov, V.V. Kovalenko. Mechanics of Amorphous Alloys. Novokuznetsk: SibGIU, 2006. 416 p.
- [2]. V.I. Spitsyn, O.A. Troitski. Electroplastic Deformation of Metals. M.: Nauka. 1985. 160 p.
- [3]. I.L. Bataronov. Electroplastic Mechanisms. Soros Educational Journal. 1999. № 10. pp. 93–99.
- [4]. V.A. Feodorov, T.N. Plushnikova, S.A. Sidorov, A.V. Yakovlev. The effect of pulsed electric current on the dependence mechanical stress – deformation in amorphous and nanocrystalline metallic alloys. Izvestiya VUZ. Chernaya Metallurgiya. 2013. № 4. pp. 62–64
- [5]. K.A. Bolshakov. Chemistry and Cobalt Technology. M. MITHT. 1981. 85 p.

INFLUENCE OF Zr^+ ION – BEAM SURFACE TREATMENT OF 30CrMnSiNi2 STEEL ON ITS STRUCTURE AND MECHANICAL PROPERTIES

S. Panin^{1,2}, I. Vlasov^{1,2}, V. Sergeev^{1,2}, V. Naidfeld²,
M. Kalashnikov², O. Bogdanov¹, B. Ovechkin¹

¹Department of Material Science in Mechanical Engineering, Institute of High Technology Physics, Tomsk Polytechnic University, 634050, Tomsk, Russia.

²Laboratory of Mechanics of Polymer Composite Materials, Institute of Strength Physics and Materials Sciences SB RAS, 634021, Tomsk, Russia.

Abstract

The structure of modified surface layer of the high-strength 30CrMnSiNi2 steel was investigated by optical, scanning electron and transmission electron microscopy as well as X-ray diffraction methods. The tests on static and cyclic tension were performed for 30CrMnSiNi2 steel specimens in as supplied state

and after subsurface layer modification by Zr^+ ion beam treatment. Differences of the specimen deformation behavior and changes of their mechanical properties are analyzed. The reason for fatigue life increase of the samples after the treatment is discussed.

Keywords: fatigue life, nanostructuring, strain, fracture.

Introduction

Aircraft industry is one of the most advanced areas where the problems of fatigue fracture prevent the long term effective and safe operation of the machine parts. During the exploitation most of the components experience variable cyclic loads which might lead to fatigue fracture. The service life time of machine parts and structure elements, many respects depends on their ability to resist nucleation and propagation of fatigue cracks which calls for development of new methods to increase fatigue durability.

One of the most effective and widespread methods of the surface modification that allows increasing the strength characteristics of metal surface layers, resistance to fatigue fracture and increase of corrosion resistance is ion beam treatment. The use of advanced engineering solutions makes it possible to realize modification of the subsurface layers accompanied by the formation of new phases at the depth of up to several micrometers on the basis of this method. A similar approach with the use of zirconium ion beam was previously used by the authors for the treatment of heat-resistant 12Cr1MoV steel [1, 2]. It is known that zirconium being the carbide-forming element contributes to the formation of intermetallic compounds with iron in steels. Thus, the modification of subsurface layer with the use of Zr^+ ion beam irradiation can be accompanied by the nucleation of high strength fine dispersed phases there. At the same time, this treatment is conducted at high temperatures that must be accompanied by local heating of the subsurface layer up to the temperature of 700°C which, in turn, can lead to high-temperature tempering (softening). However 12Cr1MoV steel is resistant to the high temperatures to occur during this treatment, and the

latter must not exert noticeable effect onto change of the strength properties [1]. Moreover, heating is mostly developed in the subsurface layers of a specimen under the treatment. As a result the modification of subsurface layer of heat-resistant 12Cr1MoV steel by the irradiation of Zr^+ ion beam gave rise to increasing ultimate strength by 15 % while for fatigue life time by 2-3 times.

Unfortunately, the similar even short-term high temperature impact is not appropriate for other classes of structural steels. In particular, high alloyed 30CrMnSiNi2 steel gains high strength during the process of preliminary quenching and tempering. Therefore the additional formation of intermetallic/carbide phases in its surface layer must not bring a noticeable effect onto increase of the strength properties while heating up to the high temperatures can give rise to noticeable softening (tempering). Nevertheless, investigations aimed to increasing the fatigue durability of 30CrMnSiNi2 steel as well as the necessity to reveal structural changes to take place in modified subsurface layer during Zr^+ ion beam treatment stimulates the interest to carrying out the current investigation. The importance of surface phenomenon processes for initiation and development of plastic deformation and fracture processes were multiply shown and discussed within concept of physical mesomechanics [3, 4].

Furthermore, the special regime of irradiation, which combines the rotation of specimens relative to the ion source, has been realized that allows reducing the temperature of the specimen to localize possible structural changes within relatively thin subsurface layer. It is assumed that it will allow to preserve the initial structure in the core of the specimens under treatment, and respectively, to minimize lowering of their mechanical properties. The authors realize that it will be impossible to avoid the softening of the subsurface layer completely. Therefore the third series of specimens was prepared which were undergone furnace tempering at the temperature of 700 °C. On the other hand, formation of the softened subsurface layer in high-strength steel must low the danger of the microcrack appearance that gives rise to nucleation of the main crack and the

subsequent fatigue fracture. The purpose of this paper is to study the modified subsurface layer structure of high-strength 30CrMnSiNi2 steel realized by Zr+ ion beam treatment and its effect on the fatigue life time.

Experimental material and procedure

Flat specimens in the shape of rectangular plates were cut out from the ingot bar of 30CrMnSiNi2 steel by electric spark cutting for the treatment and tests. The size of the specimens for the fatigue tests was 65×8×1 mm. A central hole with a diameter of 2 mm was drilled in the specimens as the stress concentrator at distance 45 mm from one of its edges. For the static tensile tests the coupons of the same shape and sizes were used. The specimens were subjected to quenching and subsequent normalization according to the standard regime described in [5]. After that, the specimens were divided into 3 groups. The specimens without the treatment composed the first group; the second one consisted of the specimens subjected to the subsurface layer modification, while the specimens from the third group were heated (high-tempering) in the argon atmosphere up to 700 °C and exposed under that temperature during 19 minutes.

The ion beam modification of the specimen subsurface layer was conducted with the aid of the high-current vacuum-arc source of metallic ions based on UVN -0.2 “Qvant” installation equipped with oilless cryogenic vacuum system [6]. The process of the specimens treatment was carried out in the chamber when a vacuum level reached the value of 5×10^{-3} Pa by the continuous flow of zirconium ions with the energy of ~2.5 keV and the ion current density of ~3 mA/cm². The duration of the treatment by the ion beam was ~4 minutes with the total time of the specimen exposure in the chamber of 19 minutes. The substrate holder with the specimens was mounted onto the stage and connected directly in the circuit of ion acceleration instead of the common used extraction of the selected ion beam from an implanter. In this case the acceleration of ions occurs in the dynamic self-organizing boundary layer which is the dual electrical one to be formed around the specimen surface experiencing the negative

potential. During the treatment the surface layer of the specimen is expected to be heated up to the temperatures of 700 °C.

For the sake of comparison the third group of the studied specimens were heated up to the temperature of 700 °C for the time corresponding to one of the ion-beam treatment. By doing so the authors attempted to distinguish the contribution from the ion-beam treatment and the thermal action.

The coupons were tested under high cyclic fatigue with the cycle asymmetry ratio $R_a=0.1$ (peak load – 270 MPa, minimum one – 27 MPa). The tests were carried out with the help of the servohydraulic testing machine Biss UTM 150. For the analysis of the crack propagation under loading photographs of the surface were taken with the aid of the digital photcamera Canon D550. Scanning electron microscopes JSM – 7500FA and Quanta 200 3dD were employed for structural studies. Optical microscopy was conducted by Carl Zeiss Axiovert 25 and Carl Zeiss Stemi 2000-C. The tests for static tension were carried out at the electromechanical testing machine Instron 5582. The structural – phase composition was determined with the help of the X - ray diffractometer Shimadzu XRD- 600.

Structural study of the modified subsurface layer

Scanning electron microscopy

It was found that during the ion-beam treatment highly dispersed particles with the size of ~100nm (Fig. 1, a) were formed on the surface of the irradiated specimens. With the help of the X-ray spectral microanalysis, the phase composition of specimens in the initial state (Fig. 1, b) and after the modification (Fig. 1, c) was determined. One can see that besides the elements being characteristic for the initial chemical composition, some additional peaks occur which testify for the presence of zirconium in the specimen after the treatment. At the depth of 6-8 μm the chemical composition does not differ from one of the untreated specimens.

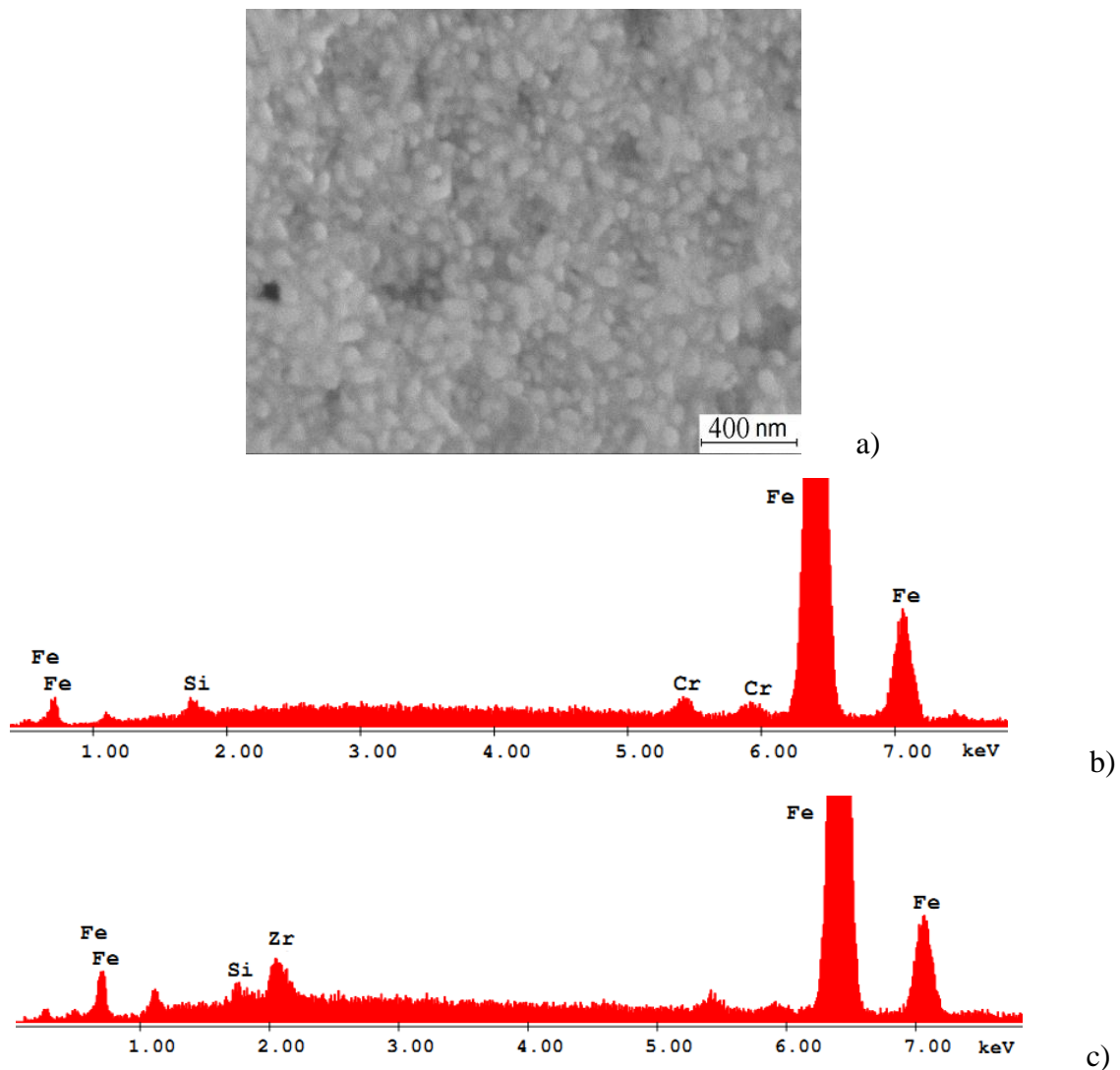


Fig. 1. a) SEM -micrograph of the specimen surface after the treatment; data of X-ray spectral microanalysis of the specimen surface b) in the as-supplied state.c).SEM -micrograph of the specimen surface after the irradiation.

Transmission electron microscopy

In Fig. 2 a the fine structure of the irradiated specimen over its cross section is presented. It is evident that near the surface the ferrite-cemented structure has formed as a result of heating that is characteristic for sorbite (at the depth of not more than 100 μm). In the underlayers of the specimen the initial martensite structure is remained.

X-ray diffraction

With the help of inclined X-ray beam technique that makes it possible to study thin subsurface layers, the presence of the α -Fe phase is revealed in the irradiated specimen, with the lattice parameter $a=2.8687 \text{ \AA}$ and the size of

coherent scattering regions (CSR)=58 nm. The specimens, not subjected to the irradiation, are characterized by the presence of the α -Fe phase with the lattice parameter $a=2.8722 \text{ \AA}$ and the size of CSR=26 nm. Additionally, intermetallic compound phases such as Zr_3Fe , FeZr_2 , and so ZrC (Fig. 2 b) are revealed.

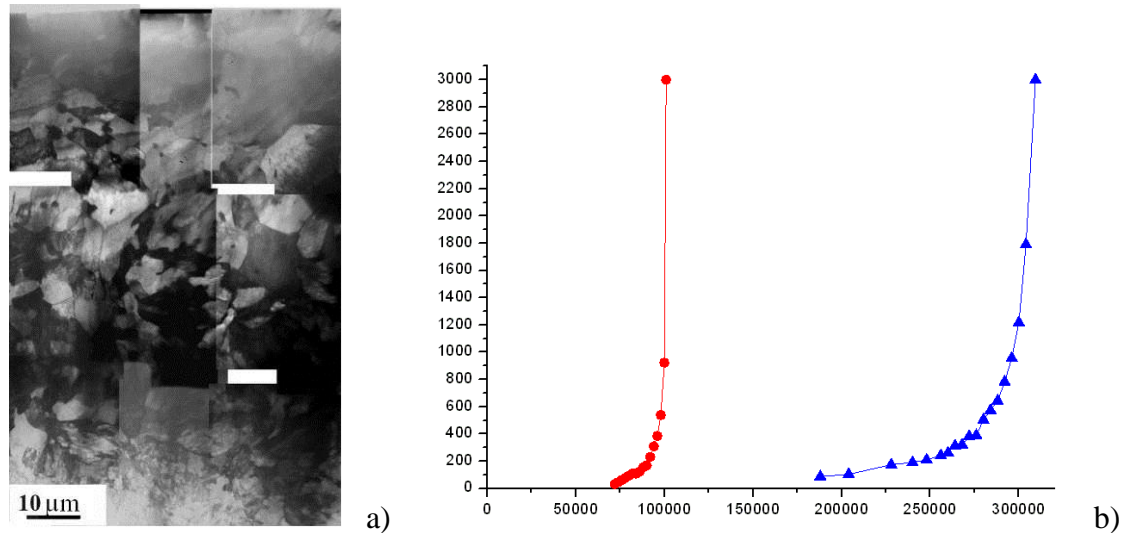


Fig. 2. a) TEM image of the subsurface layer cross section of the specimen after the irradiation; b) the crack growth diagram as the function of the number of cycles; 1) the specimen without the treatment; 2) after the irradiation.

Microhardness of 30CrMnSiNi2 steel specimens was measured with the use of PMT-3 microhardness meter at load applied onto Vickers pyramid of 1 N. The measurements were conducted on the top face for all types of specimens. The lateral face (cross section) was additionally analyzed for the treated specimen (see Table 1).

Table 1. Values of microhardness.

Type of specimens	Hardness, [GPa]	Change of hardness relative to initial specimen, [%]
As-supplied state	4.6 ± 0.08	0
Heated up to 700°C	3.2 ± 0.1	- 30.4
After the treatment (flat surface)	2.2 ± 0.06	- 52.1
After the treatment (cross section, core)	5 ± 0.22	+ 8

It is seen that microhardness of the specimen is changed after the irradiation by zirconium ion beam as the function of the distance from the specimen surface (Fig. 3 a). All the points besides the first, the third and the last ones, were calculated being averaged over 3 indentations, while the first, the third and the last points were based on averaging over 20 measurements. Microhardness in the first point was measured on the flat surface of the specimen. Minimum hardness during the measurements over the cross section was registered close to the surface (at the depth of 18 μm). Microhardness began to grow to the depth of 150-180 μm while after it was lowered and remained constant. Most probably during the surface layer recrystallization and the formation of ferrite grains the carbon could migrate towards deeper layers that also can give rise to local strengthening at the depth of 150-180 μm . The softened zone is extended from the surface to the depth not exceeding 100 μm . Another possible explanation is related to decay of residual austenite during the treatment that might give rise to increasing of the microhardness.

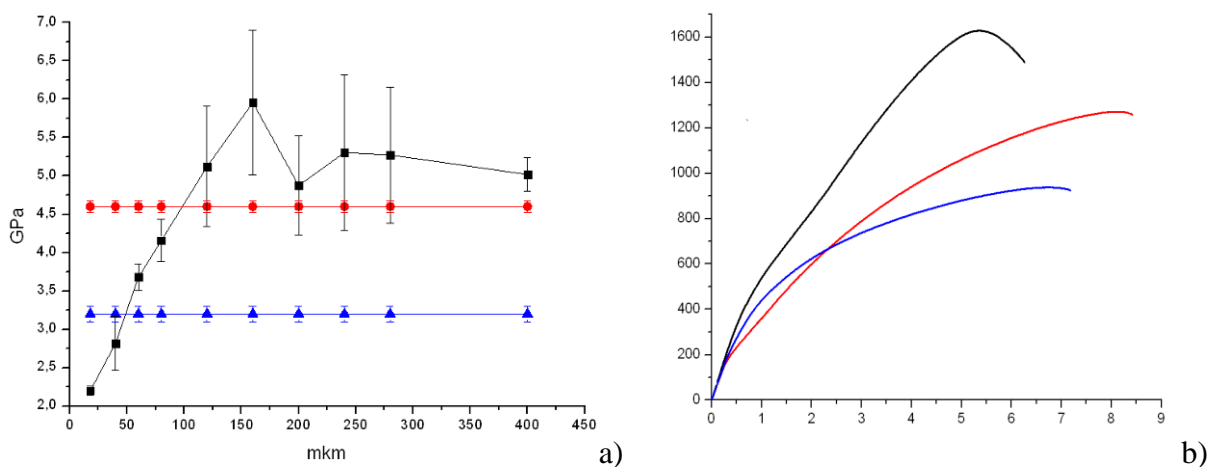


Fig. 3. Graph on microhardness through the specimen cross section as function of the distance from the surface of 30CrMnSiNi2 steel (a) and loading diagrams at specimen tension with central hole (b): 1) in as-supplied state; 2) after the treatment; 3) after the heating up to 700 °C.

Metallography.

With the help of 2 % solution of nitric acid the specimens of all three groups were etched (Fig. 4). It is evident that for the untreated specimen the martensite structure is characteristic of the standard thermal treatment (Fig. 4 a).

It is seen that in the surface layer of the specimen after the ion beam treatment, the grain structure with the average size of structural elements of 2-5 μm is revealed (Fig. 4 b d). At the same time the structure of sorbite is observed in the specimen after heating up to 700°C which is usually formed at heating above 650°C with further gradual cooling (Fig. 4 c). The microstructure through the cross section of the irradiated specimen was also analyzed (Fig. 4 d). It was found that at the depth of more than 35 μm the specimen had a structure similar to one of the sample heated to 700 C.

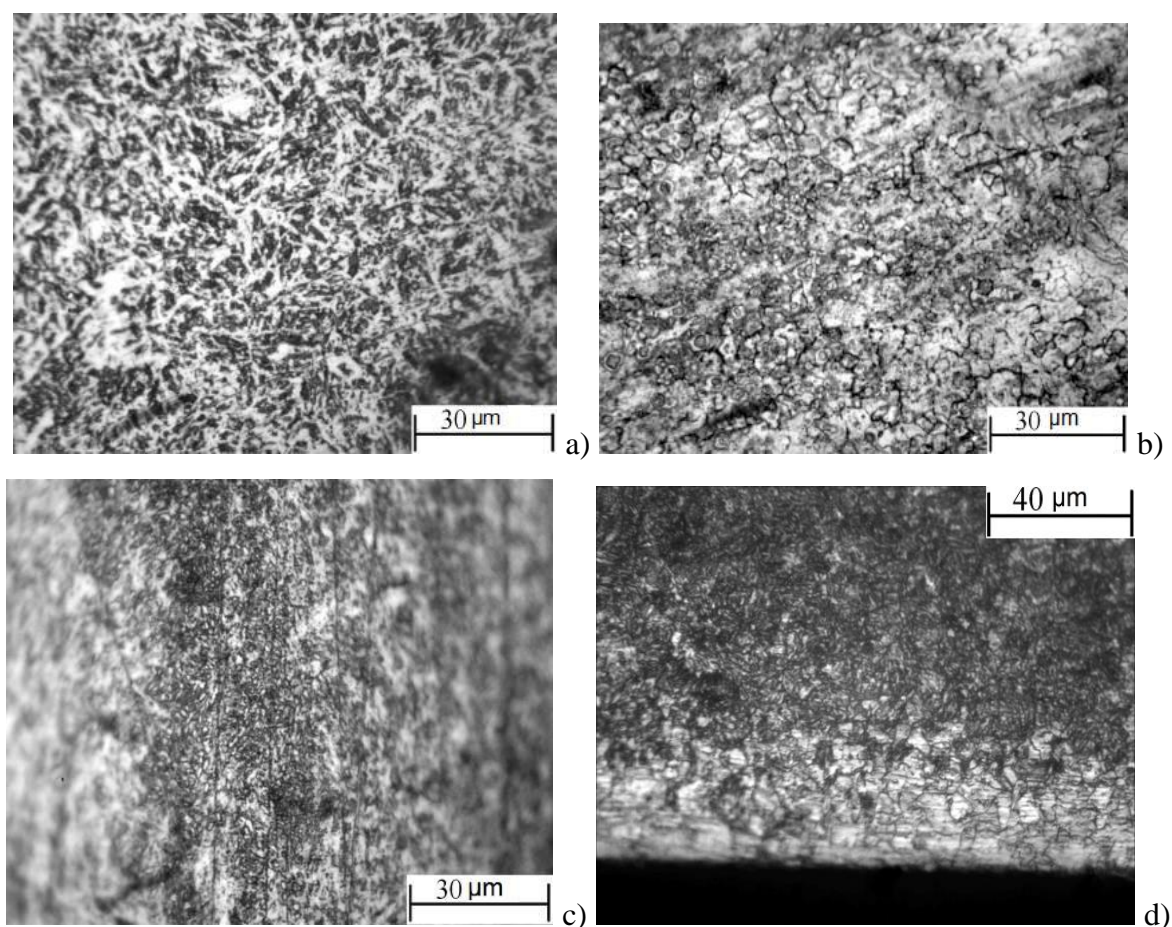


Fig. 4. a) Optical micrographs of the fractured specimen surface after etching: a) without treatment; b) after surface modification by ion beam irradiation (surface); c) after tempering at 700 °C; d) after the surface modification (cross section).

Additionally, by the optical micrographs of the cross section the characteristic depth of the layer with ferrite grains to form during the irradiation was estimated. It is shown that the average depth where ferrite grains become

distinguishable makes $35 \pm 4 \mu\text{m}$ (Fig. 4 d). It was practically impossible to detect the boundary at transition from the sorbite structure to the martensite one with the help of the optical microscopy because of the smooth temperature gradient occurrence within deeper layers. As a consequence, the transition from sorbite structure to the martensite one possesses more uniform pattern. The depth of distinguishable boundary between the heat-affected zone and the core material can be estimated as being equal to $\sim 90 \mu\text{m}$.

Testing results

Testings for cyclic tension

During the fatigue tests the average number of cycles prior the failure were determined. For the specimens without the treatment this value made $N_f = 110\,000 \pm 31\,000$ cycles while for the specimens after the irradiation it is equal to $N_f = 330\,000 \pm 40\,000$. The specimen after tempering failed after $138\,000 \pm 36\,000$ cycles. Thus, the surface modification by the Zr^+ ion beam irradiation of 30CrMnSiNi2 steel specimens ensures increasing the fatigue life-time by 3 times.

The dependence graph of the fatigue crack length vs the number of loading cycles was built being based on analysis of the surface image captured during the tests (Fig. 2 b). It is evident that the crack nucleates substantially later and develops slower in the specimen after the ion beam treatment. For the specimens without the treatment the rate of the crack growth is $L = 0.103 \mu\text{m}/\text{cycle}$ while after the treatment $L = 0.025 \mu\text{m}/\text{cycle}$. Thus, the surface modification of the specimens by the Zr^+ ion beam contributes to the delay of the fatigue crack nucleation by ~ 3 times, as well as increases the time of its propagation by ~ 4 times.

Static tension

The tests on the static tension of the specimens with the central holes were carried out to have the same shape as the specimens used under cyclic tension (Fig. 3 b). It was shown that the specimens without the treatment had the

ultimate strength of $\sigma_U=1630$ MPa, relative elongation $\varepsilon=6$ %; the specimens subjected to the ion beam modification had the ultimate strength $\sigma_U=1270$ MPa, relative elongation $\varepsilon=8$ %; the specimens after annealing at 700 °C had the ultimate strength $\sigma_U=935$ MPa, and the relative elongation $\varepsilon=7$ %. Thus, as a result of the ion beam treatment of the 30CrMnSiNi2 steel specimens the ultimate strength was lowered by 22 %, relative elongation increased by 25%; while in the specimens after annealing at 700°C ultimate strength was lowered by 42 %, relative elongation increased by 17 %.

Summary

The characterization of the subsurface layer structure modified by the Zr^+ ion beam irradiation was carried out. It was shown that the highly dispersed particles were formed on the surface with the characteristic size of ~ 100 nm. In the subsurface layer as a result of the high-temperature thermal affect martensite structure was converted into the ferrite-pearlite one. According to the data of microanalysis zirconium does not penetrate deeper than $6 \mu\text{m}$. It was shown that the nanohardness of the specimens was reduced noticeably after the ion beam treatment. The ion modification of the near-surface layer of the 30CrMnSiNi2 steel specimens under the static tension tests showed the ultimate strength reduction by 358 MPa (22 %) and increasing of elongation at failure by $\Delta\varepsilon=2$ % (25 %). During the fatigue tests it was shown that the specimens were 3 times larger in number of cycles prior to failure in contrast with the untreated specimens after the treatment. In doing so the modified subsurface layer contributed to the delay of origination and propagation of the fatigue crack in ~ 4 times. The main reason for the revealed changes was the certain softening of the subsurface layer while the hardened specimens were extremely sensitive to the nucleation of microscopic cracks that was completed by the fast appearance and the growth of the main fatigue crack.

Acknowledgements

The investigations were carried out under partial financial support of Energy, Mech. Eng. And Control processes Dept. of RAS № 12.3, SB RAS project № III.23.1.3, as well as RFBR projects № 13-08-90402_Ukr_f_a. Authors appreciate help of Research-Analytical Center of TPU and Center for shared use of equipment “Nanotech” of ISPMS SB RAS.

References

- [1]. S.V. Panin, I.V. Vlasov, V.P. Sergeev et al. Increasing the fatigue life of 12Cr1MoV steel by surface nanostructuring a Zr^+ ion beam. Part 1: Structure, properties and nature of fracture, Physical mesomechanics. V. 15, № 6. (2012) 93-106.
- [2]. S.V. Panin, S.K. Yussif, V.P. Sergeev et al. Multiple cracking as a way of increasing the resistance to fracture of surface-hardened materials, Advanced materials, V. 1. № 13. Spec.iss. (2011) 177-186.
- [3]. A.V. Panin, A.R. Shugurov. Effect of local curvature of internal and external interfaces on mass transfer responsible for thin film degradation. Physical Mesomechanics. V. 16. № 4. pp. 348-354.
- [4]. V.E. Panin, V.E. Egorushkin. Curvature solitons as generalized structural wave carriers of plastic deformation and fracture. V. 16. № 4. pp. 267-286.
- [5]. A.S. Zubchenko, M.M. Koloskov, Yu.V. Kashirsky et al. Reference book of steel types, second ed. Mashinostroenie, Moscow. 2003.
- [6]. V.E. Panin, V.P. Sergeev, A.V. Panin. Nanostructuring of surface layers of structural materials and deposition of nanostructured coatings, Izdatelstvo TPU, Tomsk. 2008.

MOLECULAR DYNAMICS RESEARCH OF STRUCTURE OF TRIPLE JUNCTIONS OF TILT BOUNDARIES AND MIXED TYPE GRAIN BOUNDARIES IN NICKEL

G. Poletaev, D. Dmitrienko, A. Soskov, V. Mikrukov, M. Starostenkov

Altai State Technical University, Barnaul, Lenin st. 46, Russia, 656038

E-mail: genphys@mail.ru, gmpoletaev@mail.ru

Abstract.

The atomic structure and the diffusion permeability of triple junctions of high-angle tilt boundaries and mixed-type grain boundaries in nickel have been investigated using the molecular dynamics method. It has been shown that equilibrium triple junction has not structural features, which able single it out as a special defect among its constituent grain boundaries. The diffusion permeability of triple junctions does not exceed the permeability of the boundaries. The effective diffusion radius of the considered triple junctions and the width of the grain boundaries are determined.

Keywords: molecular dynamics, triple junction, atomic structure, grain boundary, tilt boundary, mixed-type grain boundary, width of boundary.

Introduction

The triple junction of grains is a linear defect, along which three variously oriented grains or three grain boundary surfaces are conjugated. Despite the fact that the triple junctions are the main defects of polycrystals along the grain boundaries, researchers started to be interested in them comparatively recently. In some articles, the difference in the properties of triple junctions and their constituent grain boundaries is indicated. It is considered that the diffusion along triple junctions is more intensive than along the grain boundaries [1-3]. However, in the comparatively recent studies [4, 5] performed using the computer simulation, the conclusion is made that the diffusion permeabilities of the grain boundaries and the triple junctions can have the same order of magnitude. The question relative to the effective width of the grain boundaries

and the radius of the triple junctions, the knowledge of which would give the notion on the permeability of the “diffusion channels” in polycrystals, also remains open. For the grain boundaries, the width is usually accepted to be equal to 5 Å [3, 4], and there is substantially fewer data on the triple junctions. This study is devoted to the investigation of the atomic structure and the diffusion permeability of triple junctions of high-angle tilt boundaries {111} and {100} and mixed-type grain boundaries in nickel using the method of molecular dynamics.

Description of the Model

A triple junction of tilt boundaries was formed in a center of the computational block by means of conjugation of three grains misoriented relative to each other using the rotation around the axis parallel to the line of the triple junction. We considered two misorientation axes: {111} and {100}. When constructing the computational block, we initially formed three parallelepiped-shaped crystals. Then they were rotated for the angle around axis {111} or {100} specified for each grain. The next stage was cutting the segment of each grain according to the specified angles between the grain boundaries in the junction. In this study, the angles between the boundaries in the joint were specified to be equal to 120°. After cutting the segments, the conjugation of the grains was performed, during which the atoms situating at a distance shorter than 0.5 Å from the neighboring atom were removed. The final stage was cutting the final cylinder-shaped computational block. The number of the atoms in the computational block was about 40000 (Fig. 1). The periodic boundary conditions were specified at the cylinder ends (the infinite repetition of the cylindrical computational block along axis Z was specified). The rigid conditions were specified at the side cylinder surface, and the atoms near the side surface were not allowed to move during the computer experiment (in Fig. 1, the rigidly fastened atoms are shown dark-gray).

In this study, we considered two triple junctions of the tilt boundaries: with the misorientation of the grains by angles 15° , 15° , and 30° relative to axis $\{111\}$ and by angles 18° , 18° , and 36° relative to axis $\{100\}$ (at the construction of the triple junction of $\{111\}$ tilt boundaries in the model three crystal grains were rotated around the axes $\{111\}$ on angles 0° , 15° , 30° ; at the construction of the junction of $\{100\}$ tilt boundaries - on angles 0° , 18° , 36°). When constructing the triple junction of the mixed-type boundaries, we formed three variously oriented crystals so that the $\{111\}$ plane of the first crystal, the $\{100\}$ plane of the second crystal, and the $\{110\}$ plane of the third crystal corresponded to the XY plane. Then, to create a less ordered structure of the conjugated grain boundaries, the grains were additionally rotated by angles 5° , 15° , and 35° , correspondingly, relative to axis Z , after which, similarly to the formation of the junctions of the tilt boundaries, the segments 120° each were cut from them and conjugated. In this case, the boundary conditions on all the surfaces of the obtained cylinder were specified rigid.

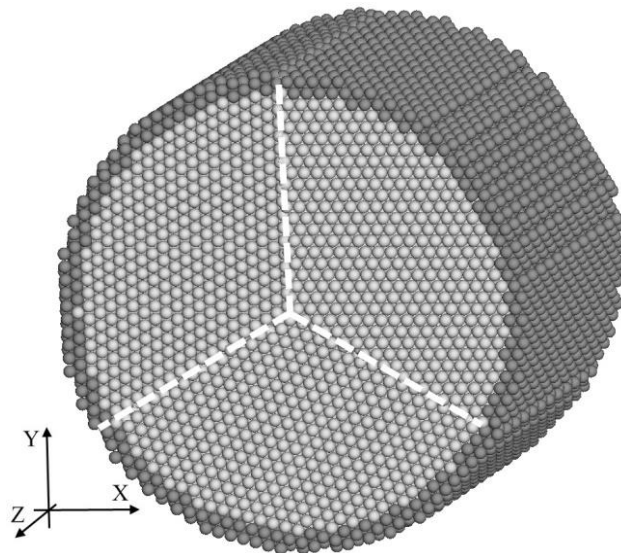


Fig. 1. Computational block containing the triple junction of the $\{111\}$ tilt boundaries. The atoms that are shown dark-gray remained immobile during the computer experiment (the rigid boundary conditions). The periodic boundary conditions were specified at the cylinder ends.

The grain boundaries are denoted by the bright dashed lines.

To present the structure of the computational block into the equilibrium state (in these conditions), the block was held for 100 ps at a constant temperature of 1500 K. After then the computational block was cooled to 0 K. Thus obtained computational blocks were starting when simulating the self-diffusion. The integration step over time in the molecular dynamics method was varied from 5 to 10 fs. The interaction of the nickel atoms with each other was described by the Cleri-Rosato tight binding potential [6]. The action radius of the potentials was limited by five coordination spheres.

Results and Discussions

Visualization of the structure of the triple junctions was carried out by estimating of the free volume distribution in the computational block. Fig. 2 shows the distribution of the free volume in the computational block (on the left) containing the triple junction of the 111 tilt boundaries with misorientation angles 15° , 15° and 30° (Fig. 2 a) and the triple junction of the mixed-type boundaries (Fig. 2 b) (the darker atoms have more free volume near himself). In all cases (including the junction of the mixed-type boundaries) was not observed any structural features that distinguish the triple junction as a specific defect. In other words, the equilibrium triple junctions of any configuration (formed by tilt or mixed-type boundaries) did not contain any excess defects compared with the grain boundaries forming the junctions, and were, in fact, a continuation of these boundaries.

In order to investigate the self-diffusion near the triple junctions, we performed the simulation of the process 300 ps long at various temperatures. The temperature during the process was held constant. Upon finishing the computer experiment, the computational blocks were cooled to 0 K in order to avoid the influence of the thermal atomic vibrations on the computations of the diffusion characteristics. The character of displacements of the atoms during the self-diffusion was investigated using the visualizer of the atomic displacement [7]. These displacements were depicted by the segments connecting the initial

and final locations of the atoms. Insignificant displacements were not imaged in this case. Fig. 2 (on the right) shows the patterns of the atomic displacements near the triple junctions of the $\{111\}$ tilt boundaries and the mixed-type boundaries during the computer experiment for 300 ps at a temperature of 1500 K. For the triple junction of the $\{100\}$ tilt boundaries, we obtained the pattern similar to that one observed for the $\{111\}$ boundaries.

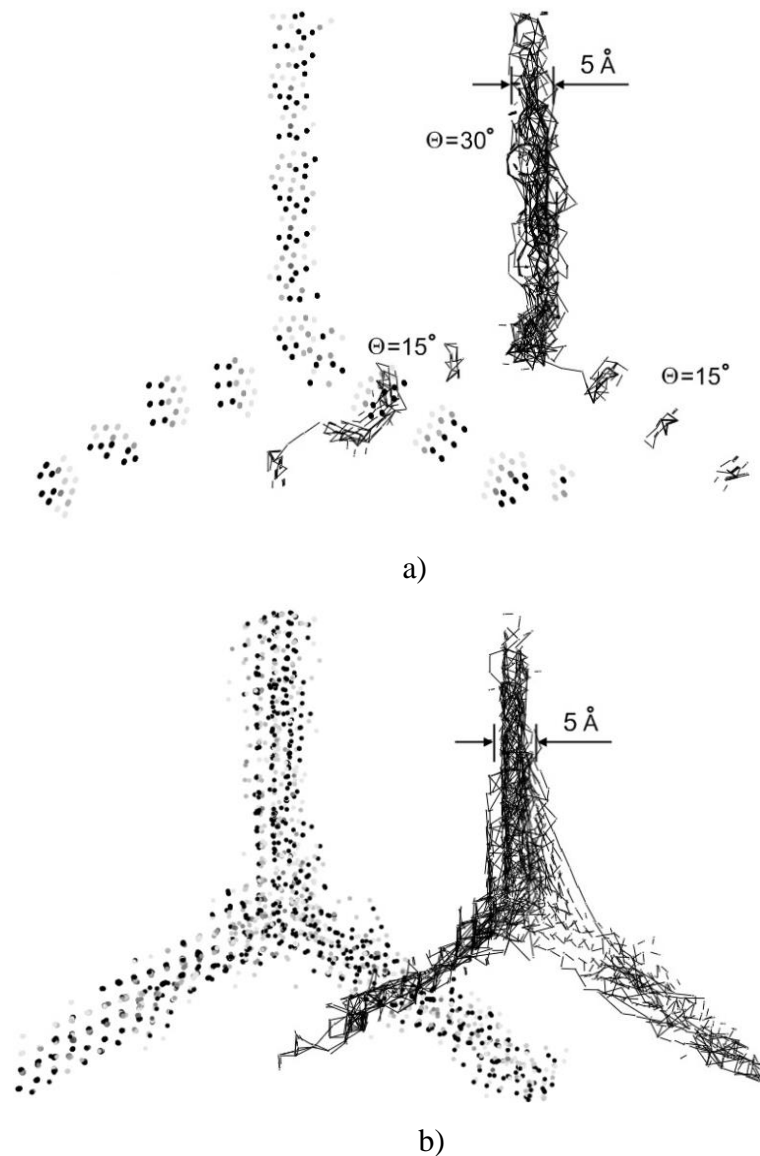


Fig. 2. Distribution of the free volume (on the left) and atomic displacements in the process of self-diffusion (on the right) near the triple junction of the $\{111\}$ tilt boundaries with misorientation angles $15^\circ, 15^\circ$ and 30° (a) and the triple junction of the mixed-type boundaries (b).

Despite a relatively high temperature, the diffusion atomic displacements in all cases occurred in comparatively narrow channels along the grain boundaries having the visual diffusion width of about 5 Å according to the acquired patterns. This agrees with the convenient width of the grain boundaries [3, 4]. For the {111} grain boundaries with the misorientation angle of 15° (Fig. 2a), despite the fact that such boundaries are often referred to high-angle boundaries, the “pipe” diffusion (the diffusion along the grain boundary dislocations), which is characteristic of the low-angle tilt boundaries [8], is clearly followed.

When comparing the intensity of atomic displacements along the grain boundaries and the triple junctions, no specific prevalence of the diffusion along the junctions was observed. According to the acquired patterns, the comparable intensities were of approximately the same order of magnitude. The diffusion radius of the triple junctions can be evaluated visually using the acquired patterns of the atomic displacements. It is seen from Fig. 2a that the radius for the junction formed by the {111} tilt boundaries is small and does not exceed 3 Å. The radius for the junction formed by the mixed-type boundaries (Fig. 2b) is larger and equals approximately 5 Å.

Summary

Thus, as shown by the molecular dynamics simulation, equilibrium triple junction (non-containing of additional defects) has not structural features, which able single it out as a special defect among grain boundaries forming this junction. The diffusion intensity along the equilibrium triple junctions has the same order as the diffusion intensity along the grain boundaries. The diffusion radius, i.e., the effective radius of the diffusion channel, oscillates in limits of 3–5 Å depending on the type of the grain boundaries forming the junction, and the junction radius becomes smaller with its formation by the tilt boundaries. The effective diffusion width of the considered boundaries was 5 Å. Moreover, the diffusion intensity in the boundary region is distributed nonuniformly and higher in the channel center as a rule.

It should be noted that the conclusions made in this article are referred to the equilibrium triple junctions. It is known that similarly to the grain boundaries themselves, the junctions of the boundaries in actual metals can serve the accumulation place of the different defects (disclinations, dislocations, point defects and others) as a result of the recrystallization, grain boundary sliding, the capture of the lattice dislocations, the deformations, etc. In this case the triple junctions already can have the structural energy features which differ their properties from the properties of the grain boundaries forming these joints.

Acknowledgements

The reported study was partially supported by RFBR, research projects No. 12-08-98046-r_sibir_a, No. 12-02-98000-r_sibir_a, No. 13-02-00301_a.

References

- [1]. G. Palumbo, K.T. Aust. *Scripta Metallurgica et Materialia*. V. 24 (1990), p. 1771.
- [2]. S.G. Protasova, V.G. Sursaeva, L.S. Shvindlerman. *Physics of the Solid State*. V. 45 (2003), p. 1471.
- [3]. Yu.R. Kolobov, A.G. Lipnitskii, I.V. Nelasov, G.P. Grabovetskaya. *Russian Physics Journal*. V. 51 (2008), p. 385.
- [4]. T. Frolov, Y. Mishin. *Physical Review B*. V. 79 (2009). p. 174110.
- [5]. A.G. Lipnitskii, I.V. Nelasov, Yu.R. Kolobov. *Defect and Diffusion Forum*. V. 309-310 (2011). p. 45.
- [6]. F. Cleri, V. Rosato. *Physical Review B*. V. 48 (1993). p. 22.
- [7]. G.M. Poletaev, M.D. Starostenkov. *Physics of the Solid State*, V. 51 (2009). p. 727.
- [8]. M.D. Starostenkov, D.V. Sinyaev, R.Yu. Rakitin, G.M. Poletaev. *Diffusion and Defect Data Pt.B. Solid State Phenomena*. V. 139 (2008). p. 89.

PROPERTIES OF CAST AND ROLLED STEEL AFTER NANOPOWDER INOCULATION

E. V. Protopopov, Yu. A. Seleznev, A. N. Cherepanov, V. Ya. Chinokalov,

D. V. Foigt, L. A. Ganzer

Siberian State Industrial University,

Institute of Theoretical and Applied Mechanics, Siberian Branch, Russian

Academy of Sciences

OAO EVRAZ ZSMK

Abstract

The modification of metal by nanopowder is studied as a means of improving the quality of continuous-cast bar, complex components, and rebar. The introduction of $\text{TiC}_x\text{N}_y\text{-Fe}$ nanopowder in the tundish of the continuous-casting machine reduces the liquation of the elements over the ingot cross section and the content of nonmetallic inclusions and also increases the structural and chemical uniformity. The use of nanopowder inoculators changes the structure of complex components (angle bar) and rebar, as well as the shape, size, and distribution of the nonmetallic inclusions, and also reduces the grain size and improves the mechanical properties.

A promising means of introducing the structure and properties of cast metal is to introduce nanopowder in the melt prior to casting [1—3].

Earlier research on the modification of metal in the mold and tundish of a continuous bar-casting machine at OAO EVRAZ ZSMK showed that the process is highly efficient and that microadditions of refractory nanopowders in the liquid steel boost the quality of the continuous-cast billet [4]. Nevertheless, the results require refinement and scientific confirmation, and the quality of the final product obtained by rolling the modified billet must be studied.

In converter shop 2 at OAO EVRAZ ZSMK, we consider a trial run in the continuous casting of 150 x 150 mm Cr3cn steel billet, with modification of the metal by titanium-carbonitride nanopowder (particle size 0.015—0.040 μm). The nanopowder is produced by self-propagating high-temperature synthesis of

carbon steel— $\text{TiC}_x\text{N}_y - \text{Fe}$ in a plating matrix, granulated, and converted to powder strip. In metal treatment, the powder strip is introduced in the intake bath of one of the tundishes by a push-rod system, and the metal cast through the second tundish is used for comparison.

In casting the experimental melts, the liquidus temperature of the steel is 1515°C , the metal temperature in the tundish is $1557\text{—}1565^\circ\text{C}$, the rate of ingot extrusion is $2.1\text{—}2.3$ m/min, the supply rate of the powder strip is 3.75 m/min, with flow rates of 980 g/min for the nanopowder and 490 g/min for the strip base. The ingots contain $0.046\text{—}0.068\%$ nanopowder and $0.023\text{—}0.034\%$ of the strip base. Experimental and comparison bar billets are rolled on the 450 mill to obtain hot-rolled and fast-cooled 7.5×6.0 angle bar and hot-rolled and heat-treated rebar no. 32.

Chemical analysis of metal samples from the tundish and samples from zones in transverse templates confirms that the liquation of chemical elements over the cross section is markedly less in billet with nanopowder inoculation. The density of the continuous-cast billet is increased to $70\text{—}80$ kg/m^3 (by $0.85\text{—}1.00\%$) on average after nanopowder inoculation. This is evidently due to breakdown of the dendrites.

Table 1 presents data on the macrostructure of the experimental and comparison billet. In fact, after modification by $\text{TiC}_x\text{N}_y - \text{Fe}$, the cross-sectional area of the ingot occupied by dense-metal crust is 26.9% , on average; the area occupied by dendritic crystals is reduced by 29.6% ; and the length of the first-order dendrite axes is reduced by 31.7% .

Mean values over the sample are given: positive and negative values correspond to increase and decrease in the parameter, respectively.

The increase in the cross-sectional area of the ingot occupied by equiaxial crystals is 86% , on average. Note also the reduced development of internal defects. We see in Table 1 that the central porosity (CP) and axial chemical inhomogeneity (ACI) are improved, while the development of liquation bands and cracks (LBC_{tot}) remains stable.

Table 1. Macrostructure of experimental/comparison billet.

Macrostructure scores (OST 4-1-235—91 standard)			Change, %			
			in area of zones over ingot cross section			in length of first-order dendritic axis
CP	AC I	LBC _{tot}	crust	dendrites	equiaxial crystals	
$\frac{0.9}{1.1}$	$\frac{1.05}{1.3}$	$\frac{1.1}{1.1}$	$\frac{+26.9}{-}$	$\frac{-29.6}{-}$	$\frac{+86.0}{-}$	
					$\frac{-31.7}{-}$	

Analysis of metallographic data shows that sulfide, silicate, and oxide inclusions predominate in the modified billet². The sulfides lie along the boundaries of the cast grain in the form of chains and are rounded particles (12.5-25.0 μm). Silicates are present in the form of disoriented globules (2.5—12.8 μm). The globular oxide inclusions (2.56—12.80 μm) are predominantly grouped at the grain junctions. In the comparison billet, oxide inclusions predominate, followed by silicates and then sulfides. Their distribution over the cross section is also different; the globular silicates and oxides (measuring 2.5—12.8 μm) mainly appear as rows along the grain boundaries. The sulfides lie along the grain boundaries in the form of rows (length up to 71.68 μm) and are grouped at the grain boundaries.

Overall, the nonmetallic inclusions in the modified billet are small and globular, which facilitates their ascent and removal from the metal; the inclusions are disoriented within the metal.

Next, we investigate the influence of nanopowder inoculation on the ratio of structural components (pearlite and ferrite) in complex components (7.5 x 6.0 angle bar) and rebar no. 32 after hot rolling and heat treatment (Table 2).

As is evident, the pearlite content is greatest in the fast-cooled angle bar and the heat-treated rebar rolled from modified billet. In the hot-rolled state, the modified angle bar and rebar has an elevated ferrite content (59 – 67%), and the

² We thank E.O. Kazyrskii, E.V. Shitik, E.A. Ivanov and N.V. Myskova for their assistance in rolling the cast billet.

mean ferrite grain size tends to decrease, as seen in the figure. Note that these structural changes benefit the mechanical properties.

Table 2. Structural change of rolled steel for experimental comparison billet.

State	Structural component, %		Ferrite grain, μm
	pearlite	ferrite	
Complex component			
After hot rolling	<u>38.5</u>	<u>64.5</u>	<u>15.91</u>
	<u>42.0</u>	<u>58.0</u>	<u>15.40</u>
After fast cooling	<u>40.7</u>	<u>59.3</u>	<u>15.69</u>
	<u>47.6</u>	<u>52.4</u>	<u>16.21</u>
Rebar			
After hot rolling	<u>34.9</u>	<u>65.1</u>	<u>19.59</u>
	<u>36.2</u>	<u>63.8</u>	<u>18.66</u>
After heat treatment	<u>36.8</u>	<u>63.2</u>	<u>15.39</u>
	<u>36.2</u>	<u>63.8</u>	<u>18.66</u>

Mean values for the samples are given.

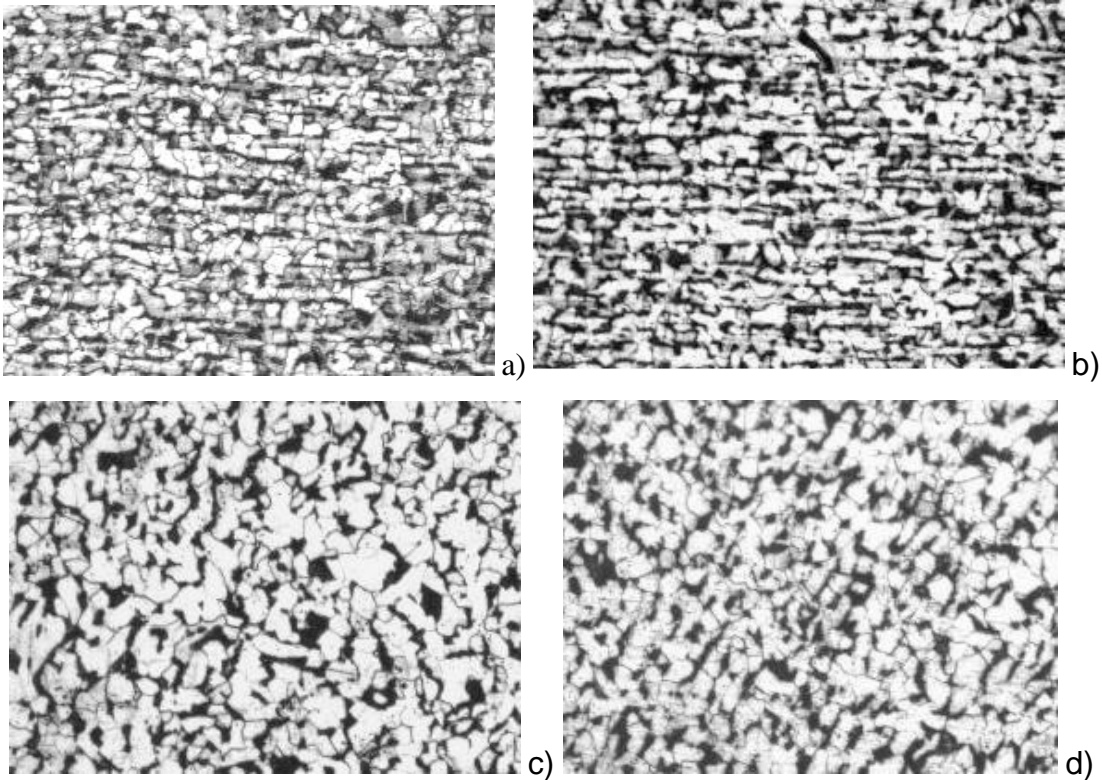


Fig. 1. Structure of hot-rolled 7.5×6.0 angle bar (a, b) and rebar no. 32 (c, d) without nanopowder inoculation (a, c) and after modification by $\text{TiC}_x\text{N}_y\text{-Fe}$ (b, d). $\times 200$.

Comparison of the mechanical tests data for cast and rolled steel (Table 3) confirms that the strength and plasticity are better after nanopowder inoculation. The strength σ_B of the cast metal is increased by 1.7% (0.7—2.7%), and the relative elongation δ by 24.8% (23.4—26.2%). In the rolled product, the improvement in the mechanical properties due to nanopowder inoculation is somewhat less than in the cast metal, evidently on account of reheating of the metal. At the same time, the plasticity is markedly improved. In particular, for 7.5 x 6.0 angle bar, δ is increased by 4.8% (3.5—5.7%) in the hot-rolled state and by 3.5% (2.2— 4.7%) in the heat-treated state. For rebar no. 32, the corresponding figures are 5.0% (2.8—7.1%) and 5.4% (2.5—7.9%).

Table 3. Mechanical properties of cast and rolled steel after nanopowder inoculation.

State	Change, %		
	σ_B	σ_y	δ
After modification by TiC_xN_y-Fe	1.7	ND	24.8
Complex component			
After hot rolling	0.3	0.5	4.8
After fast cooling	0	0.6	3.5
Rebar			
After hot rolling	0.3	1.0	5.0
After heat treatment	0.2	0.8	5.4

Mean values for all the experimental billet and samples are given: ND, no data.

Conclusions

The introduction of $TiC_xN_y - Fe$ nanopowder in the tundish of a continuous bar-casting machine improves the continuous-cast billet produced. The liquation of the elements over the ingot cross section and the content of nonmetallic inclusions are reduced, while the structural and chemical uniformity is increased. The use of nanopowder inoculators changes the structure of complex components (angle bar) and rebar, as well as the shape, size, and distribution of the nonmetallic inclusions, and also reduces the grain size and improves the mechanical properties.

References

- [1]. H. Gleiter. Acta Mater. 2000, V. 48. pp. 1—29.
- [2]. H. Mughrabi, H.W. Hoppel, M. Kautz. Scripta Mater. 2004. V. 51. pp. 807—812.
- [3]. V.A. Efimov, A.S. El'darkhanov. Tekhnologii sovremennoi metallurgii (Current Metallurgical Technology). Moscow: Novye Tekhnologii, 2004.
- [4]. V.P. Komshukov, A.N. Cherepanov, E.V. Protopopov et al. Izv. Vyssh. Uchebn. Zaved. Chern. Metall. 2008. № 8. pp. 10—11. № 10. pp. 21—24. 2010. № 8. pp. 57—63.

INFLUENCE OF HIGH-TEMPERATURE ANNEALING ON THE FORMATION OF NANOPARTICLES OF THE γ' -PHASE BASED ON THE Ni-Al SUPERALLOY

N.A. Koneva¹, N.A. Popova¹, E.L. Nikonenko¹,
M.V. Fedorischeva², E.V. Kozlov¹

¹Tomsk State University of Architecture and Building, Tomsk, Russia.

E-mail: koneva@tsuab.ru

²Institute of Strength Physics and Materials Science, SB RAS, Tomsk, Russia.

Abstract

The morphology of the γ' - phase of the Ni-Al superalloys doped by refractory elements after high temperature annealing was studied by SEM and TEM.

The success of modern engineering is substantially caused by producing and application of the metallic materials having necessary operational properties. The level of requirements for these materials is constantly increasing due to the new problems that arise at the development of new technologies, particularly for their use in extreme conditions such as high rates, high

temperatures, etc. One of perspective directions of search for new materials is producing alloys containing intermetallide phases. Superalloys on the basis of $(\gamma+\gamma')$ phases where γ is a disorder solid solution with the fcc structure and the γ' is an ordered phase with the $L1_2$ structure are such an example [1-3]. Now superalloys are produced on the basis of the Ni-Al alloy [4] doped by various refractory elements [2, 3, 5] where the γ' - phase is the basic one. For this reason, the phase is responsible for the formation of properties of a superalloy in many respects. As the γ' -phase morphology can influence in a certain way, on the mechanical properties of superalloys, the study of various superalloys using methods of research into structure and morphology of the γ' -phase in detail is obviously important.

Experimental

Superalloys on the basis of Ni-Al alloyed by refractory elements were the object of the study. The alloy composition was chosen so that the ratio of Ni and Al in the sum with the other elements replacing the sites of the Al in the $L1_2$ superstructure was 0.77/0.23. The composition corresponded to the boundary of the two-phase area [4]. Injection of the refractory metals about 9 at.% increased the volume fraction of the γ -phase up to ~ 0.08 in an alloy. The alloy was produced use the directed crystallisation method and then it was annealed at $T = 1150^\circ\text{C}$ for one hour. The main methods of research of the alloy structure were TEM and SEM.

The samples were cut from the ingot in the form of plates of different thickness using an electric spark machine in a soft mode. The plates were cut in a plane perpendicular to the direction of the crystal growth $\langle 001 \rangle$. The preparation of the foils for TEM included electropolishing of the plates in a supersaturated solution of chromic anhydride in the phosphoric acid. Electrolytic etching of the sample surface was carried out in the foam of the electrolyte at a voltage of 50 V for SEM examination. Research of the sample surface after etching was carried out by SEM using TESLA BS-301 device at 50-10000

magnifications. The structure of thin foils of the alloy was studied using the EM-125 electron microscope at an accelerating voltage of 125 kV and 25 000 magnifications.

The average size of structural elements and the fine-structure parameters were measured using the secant method [6, 7]. The obtained data were processed statistically. The phase analysis was carried out using the bright and dark fields and also regime of microdiffraction using TEM images [6, 8]. Application of SEM and TEM allowed to study the structure of the alloy at different scale levels.

Results and discussion

Fig. 1 shows a generalized schematic picture of the superalloy structure based on the results of the studies. It is clearly seen in SEM images that there are two different morphological components in the alloy: one component has particles of smaller size (25-90 μm), and the size of the second component is significant larger (150-500 μm). Thus, the second component consists of two phases. Identification of the present phases was carried out by TEM. Smaller particles observed by SEM are the γ' -phase. The particles are elongated along the direction of the $\langle 001 \rangle$ type and have a rounded form. The particle size varies from 25 to 90 μm . We denote them as γ'_{I} particles of γ' -phases of the first level.

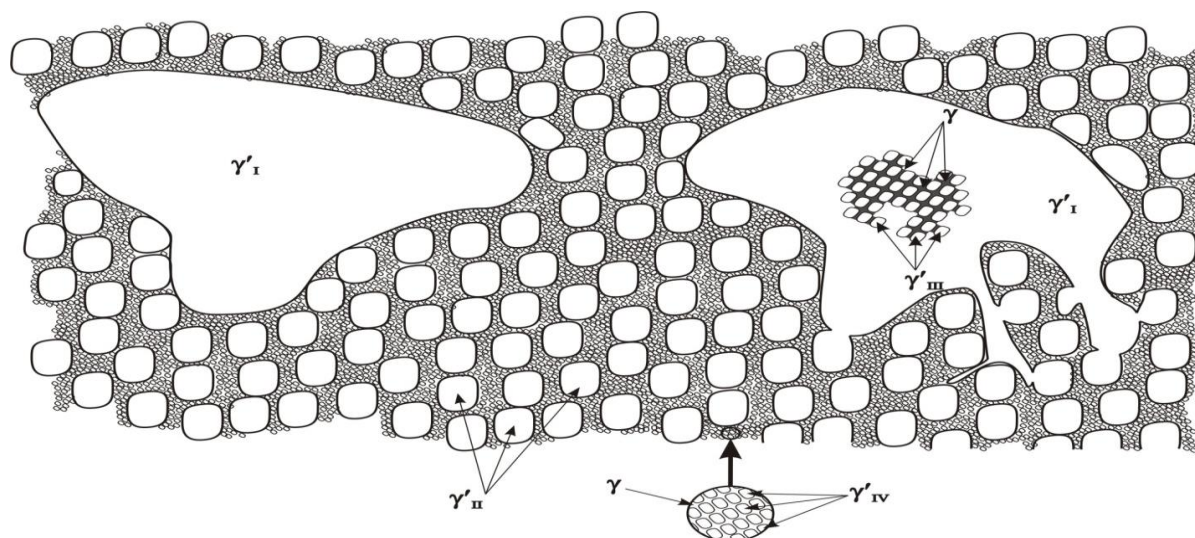


Fig. 1. Schematic images of the morphology of the phases observed in superalloys.

The second morphological component has a smaller particle size (Fig. 2 a). As mentioned above, it is a mixture of two phases: γ and γ' as clearly seen at high magnification (Fig. 2 b-d). There are particles of the γ' phase of the quasicubic form in this mixture. Their size is in limits from 2.5 to 10 μm . We denote these smaller particles as γ' -phase of the second level - γ'_{II} . The particles of γ'_{II} are located marked in two directions of $\langle 001 \rangle$ type.

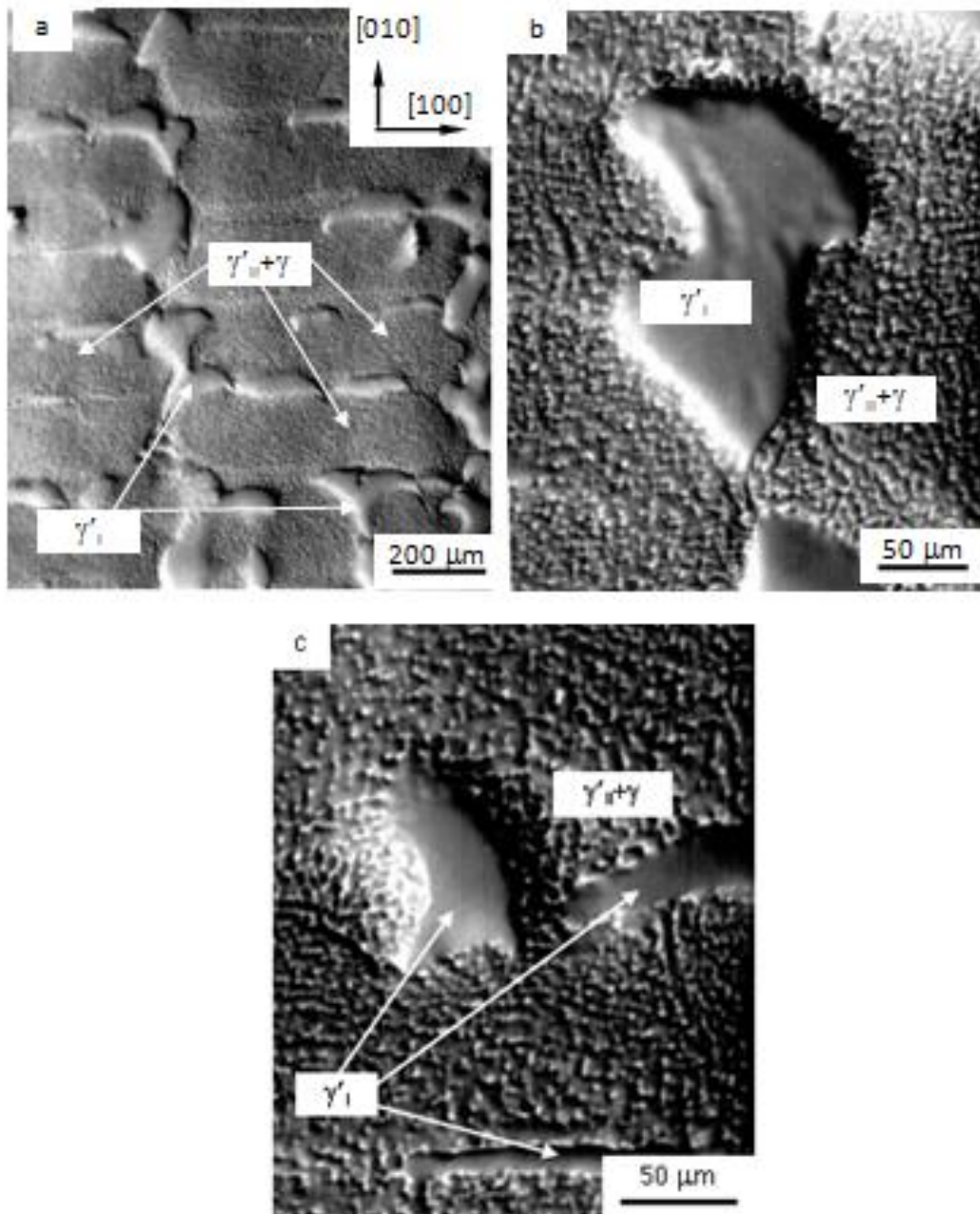


Fig.2. SEM image of the structure of a superalloy. Phases are indicated by arrows

Another component of a mixture is γ -phase - a disorder solid solution with the fcc structure. Thus, the SEM supports that there are two scale levels of the γ' -phase in the structure of the alloy. The first level is large particles (25-90 μm) of the γ'_{I} -phase and the second level – by the smaller particles (2.5-10 μm) of the γ'_{II} - phase being in ($\gamma'_{\text{II}} + \gamma$). The phase particles of γ'_{II} exhibit coagulation along certain directions (Fig.1g), ie there is the so-called "raft" structure [3].

The obtained data make it possible to present phase transformation processes of the γ'_{I} phase in a two-phase mixture ($\gamma + \gamma'_{\text{II}}$) during annealing of a superalloy. Under anneal, one can observe moving of the interphase morphological boundaries $\gamma'_{\text{I}} / (\gamma + \gamma'_{\text{II}})$. These results suggest that annealing effect on the superalloy structure, ie "refining" of γ'_{I} . is observed. The volume fraction of γ'_{I} particles decreases and the volume fraction of mixture of ($\gamma + \gamma'_{\text{II}}$) increases.

The researches carried by TEM not only confirmed the above conclusion but also described in detail the "refining " picture of the γ' - phase by identification of the observed phases in microdiffraction pictures. Application of the method in this work made it possible to study the morphology and the structure as the γ' - phases of the first level, and also the structure of two the phase mixture ($\gamma'_{\text{II}} + \gamma$) in details. The fine structure of the γ'_{I} - phase was studied using the microdiffraction analysis and the dark-field images (Fig. 3). The study of the particles of the γ'_{I} -phase, which looked like single-phase in the SEM images showed the a complex structure of these areas. The particles of the γ'_{I} - phase have the form of both homogeneous and heterogeneous particles (Fig. 1). At high magnification it is seen that there are two types of the particles of the γ'_{I} - phase: one-phase (γ'_{I}), the two-phase ($\gamma + \gamma'$) (Fig. 1). The two phase regions are the result of recrystallization [5] during the annealing of a superalloy. The volume fraction of these areas is relatively small, their examples are shown in Fig. 3. These areas consist of quasicubic nanoscale particles of the γ' -phase 90-

130 nm in size and the layers of the γ -phase about 10 nm in width. Let us designate these particles as γ'_{III} - particles of the γ - phases of the third scale level. The bright-field images show the particles of γ'_{III} separated by the layers of γ -phase (Fig. 3). Let us notice that there are dislocations in these layers (Fig. 3 a) In Fig. 3 b it is seen that there are particles in some areas of the images. The other areas contain dislocations which are formed owing to misfit of the parametres of the crystalline lattices of the γ - and γ' - phases at the transformation of the particles γ' in $((\gamma'_{II} + \gamma))$.

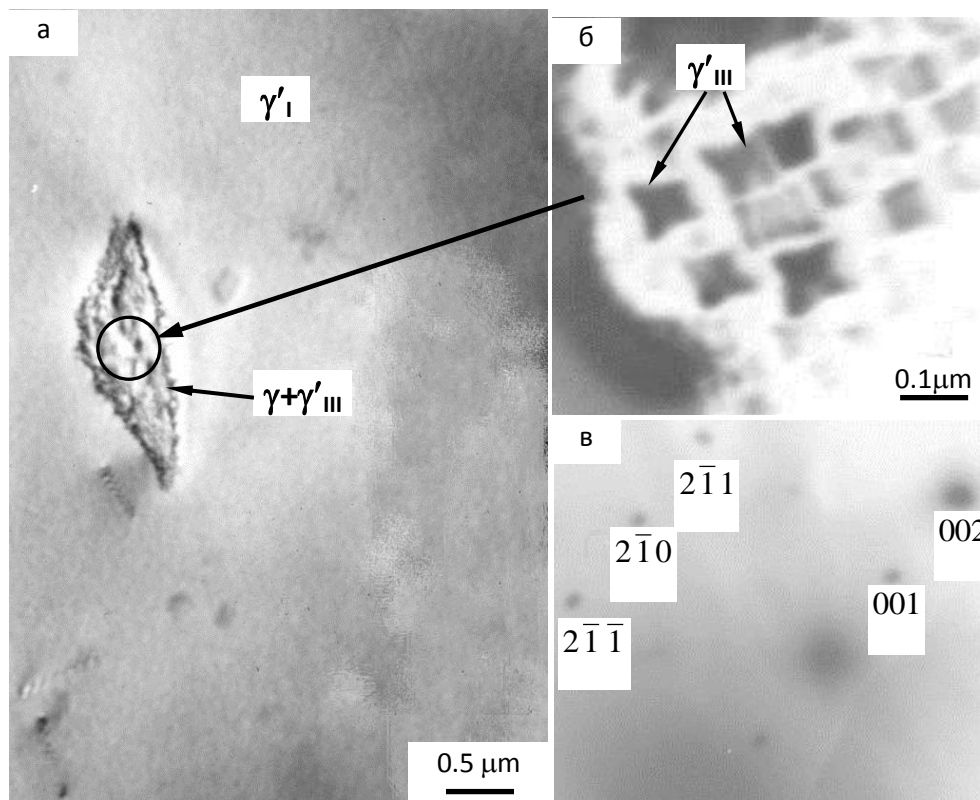


Fig. 3. Complex structure of the particles of the γ'_I - phase of the first level: a – a bright-field image, inside the particle of γ'_I is a two-phase mixture $\gamma'_{III} + \gamma$; b – a dark-field image in superstructure reflections [001], the arrows indicate the particle of γ'_{III} , c – a microdiffraction pattern having the superstructure reflections 001, $2\bar{1}\bar{1}$, $2\bar{1}0$, $2\bar{1}1$.

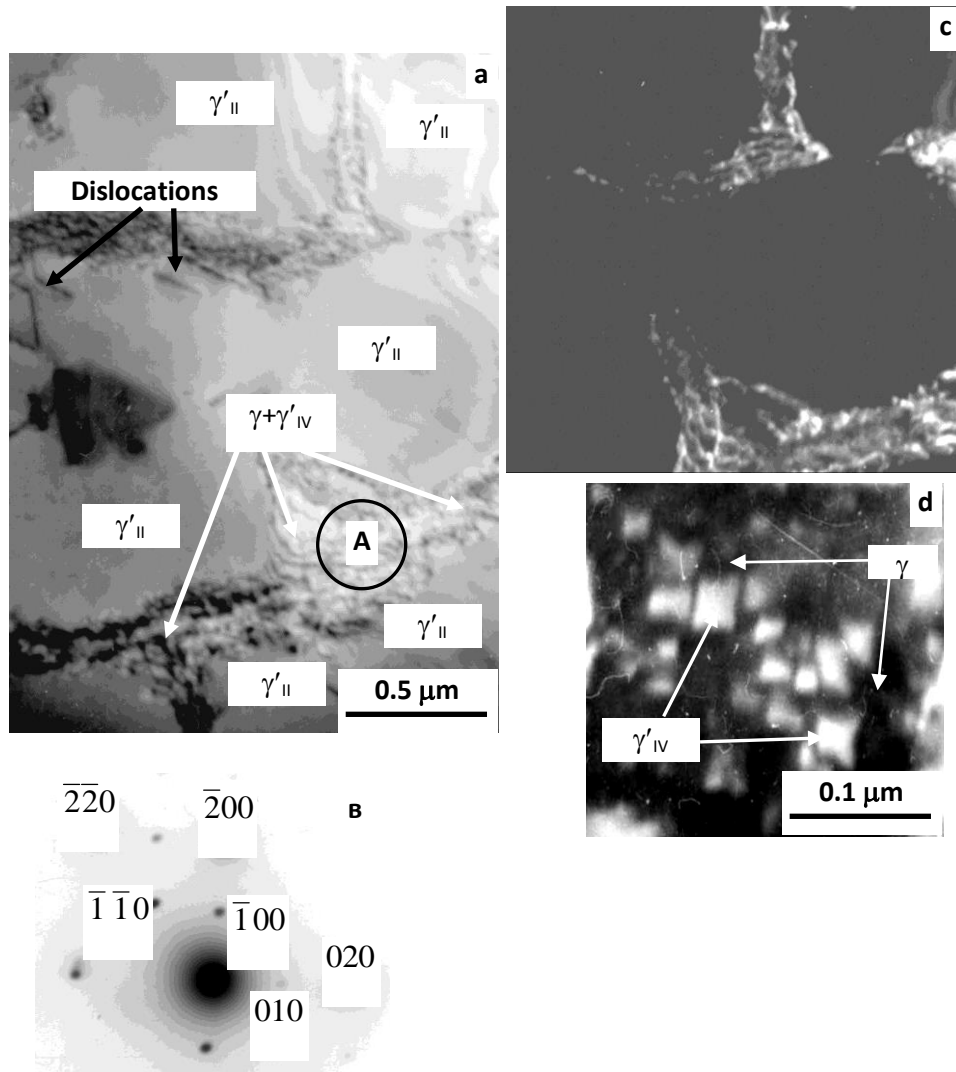


Fig. 4. The image of the structure of the alloy obtained by TEM: a – a bright-field image of the particles of the γ'_{II} , two-phase mixture $\gamma + \gamma'_{IV}$ is shown by white arrows, the dislocations are shown by black arrows; b – a microdiffraction pattern corresponding to the part of a foil and containing superstructural reflexes $\bar{1}\bar{1}0$, $\bar{1}00$, 010 ; c – in the basic reflex 020 ; d - the dark-field image of area A in the superstructural reflex 010 , the phases in two-phase mixture $\gamma + \gamma'_{IV}$ are shown by white arrows.

The fine structure of the quasicubic particles of the γ'_{II} -phase and γ -phase layers between them in the mixture of $(\gamma'_{II} + \gamma)$ is well shown on the images obtained by SEM (Fig. 4). In the diffraction patterns corresponding to the

mixture ($\gamma'_{II} + \gamma$) there are superstructural reflexes of the γ' -phases. On boundaries of the γ' - и γ -phases there are dislocations. A detailed study by TEM of the two-phase mixture ($\gamma'_{II} + \gamma$) showed that the interlayer of the γ -phase in this mixture also has a complex structure (Fig. 4).

They contain nanometer quasicubic particles of the γ' - phases which are not found in the SEM images. Their identification using the bright-field and dark-field (in superstructure reflections [010]) images are shown in Fig. 4 a,d. The nanometric particles of the γ' -phase, whose size is 30-80 nm, are classified here as the γ'_{IV} -particle of the γ' -phase of the fourth level. In the table the classification of the found particles by size and phase composition is given

Conclusion

Structural studies which we carried out in this work allowed us to study the morphology of the γ' -phase of the alloyed Ni-Al superalloy. The particles of the γ' -phase are classified according to their size. This analysis allows to present the structure of the superalloy in detail. We can see the γ' -phase of four scale levels. There are particles of γ'_I , γ'_{II} , γ'_{III} и γ'_{IV} . The space between the particles of the γ' -phase of different size is occupied by the γ -phase.

Table 1. Classification of scale levels and dimensions of the structural components of γ'_I - phase and morphological components of $\gamma + \gamma'$ phases.

Structural level	Structure elements	Size, μm
Level of dendrite	Areas ($\gamma + \gamma'_{II}$)	150 – 500
	Particles γ'_I	25 – 90
Mezolevel	Particles γ'_{II}	2.5 – 10
	Areas ($\gamma + \gamma'_{III}$)	0.45 – 1.0
	Interlayer ($\gamma + \gamma'_{IV}$)	0.25 – 0.70
Microlevel	Areas of quasi decomposition	0.45 – 4.5
	Particles γ'_{III}	0.09 – 0.13
Nanolevel	Particles γ'_{IV}	0.03 – 0.08

The general scheme of the phase morphology in the investigated superalloy is follows: there are large particles of γ'_I , some of them contain a decomposition region ($\gamma + \gamma'_{III}$); there is a two-phase mixture of ($\gamma + \gamma'_{II}$) between the large particles of the γ'_I . The interlayers between the particles of γ'_{II} are often filled with a mixture of the two-phase ($\gamma + \gamma'_{IV}$). The investigated alloy tends to decompose into γ - and γ' -phases in different parts of the material under annealing. The decomposition looks like ($\gamma'_{III} + \gamma$) inside the γ'_I phase and ($\gamma'_{IV} + \gamma$) in the two-phase field of ($\gamma'_{II} + \gamma$). At the decomposition that the refining of the areas of the γ' -phase occurs up to particles of the nano-sized scale. This can, undoubtedly, contribute to hardening of the superalloy.

References

- [1]. N.S. Stoloff, R.G. Davies. Prog. Mater. Sci. 1966. V. 13. P. 3.
- [2]. Superalloys II / ed. Sims CH.T. M. et al : Metallurgy, 1995. 384 p.
- [3]. R.E. Shalin, I.L. Svetlov, E.B. Kachanov and others. Nickel-base superalloy single crystals. M.: Engineering, 1997. 336 p.
- [4]. E.V. Kozlov, E.V. Konovalov, E.L. Nikonenko etc. Math. RAS. Ser. physical. 2004. V. 68. № 5. p. 632.
- [5]. Diagrams of binary metallic systems. / Ed. Lyakisheva N.P. V. 1. 1995; V. 2. 1997; V. 3 (in two parts), 1999-2000.
- [6]. P. Hirsch, A. Howie, R. Nicholson and others. Electron microscopy of thin crystals. New York: Wiley, 1968. 574 p.
- [7]. K.S. Chernyavskii. Stereology in metal. Moscow: Metallurgy, 1977. 280 p.
- [8]. K. Andrews, D. Dyson, C. Keown. Electron diffraction and their interpretation. New York: Wiley, 1971. 255 p.

ION – INDUCED PLASTIC DEFORMATION IN SOLIDS

V.A. Stepanov, E.I. Isaev

Obninsk Institute of Nuclear Power Engineering, National Research Nuclear University MEPhI (Obninsk branch), Studgorodok 1, Obninsk, Kaluga region, 249040, Russia.

E-mail: stepanov@iate.obninsk.ru

Abstract

In materials subjected to radiation, plastic deformation arises in nanometer-sized regions. This deformation resulting from the formation and evolution of 2D defects causes structuring on a nanometer level. Experimental data are presented for the structure of metallic and dielectric materials in which plastic deformation is initiated by ion irradiation. In metallic alloys states with a characteristic cluster nanostructure appear, which propagate over a large depth (the long-range action effect). The experimental evidence of the long-range action effect in diamond is presented.

Introduction

The long-range action effect results from material–radiation interaction. Its name is derived from the fact that the structure and properties of irradiated materials change over a depth far exceeding the penetration depth of the radiation or over a distance far exceeding the size of energy liberation regions. The long-range action effect may show up in metals and insulators exposed to different external influences, such as laser and ion beams, low-temperature plasma, and pulsed electromagnetic and even optical radiations.

Experimentally, this effect has been comprehensively studied for materials interacting with ion beams. In this case, it shows up in the formation of a radiationally modified zone at a depth that may several orders of magnitude exceed the ion range [1–5]. Such a deep-seated zone represents a structurally modified layer with elevated microhardness that contains an anomalously high concentration of structural defects (such as dislocation loops, voids, and stacking

faults) and sometimes new crystalline phases. The effect is observed in both polycrystals and single crystals [6]. Along with structural modifications, the long-range action effect may cause superdeep mass transfer, which takes place, as a rule, at high current densities and low electron energies [7, 8].

Since forces related to elastic deformation are the only long-range forces in a material, the effect is theoretically explained by considering the influence of the elastic component of the action on different statistical processes in solids. The influence of elastic stresses on the formation of defects and diffusion into the material is touched upon in [3, 9–11]. Gaining insight into the key role of collective processes in the phenomenon of long-range action has led researchers to suppose that cooperative effects in mass transfer, nonequilibrium phase transitions, and wave mechanisms behind the propagation of long-range action may govern the long-range action effect [12–16].

Unfortunately, most available models describe processes that occur directly in the zone of action and cannot “travel” long distances. This is because the elastic long-range component of any process disappears because of inevitable structural changes in the material. The formation of point defects, dislocations, and new phases favors, as a rule, the elastic stress relaxation and suppresses the long-range action. In this work, the authors suggest an approach according to which the radiation-induced super-deep modification of the structure is the result of “special” plastic deformation in the material. Here, the long-range action is due to radiation-induced elastic stresses the relaxation of which occurs not through a plastic flow but keeps another path.

Radiation – induced plastic deformation

Under radiation exposure (ion, laser, or reactor actions), the density of the material may considerably change in small areas in the volume. This is due to an excess concentration of structural defects or the liberation of a large amount of energy as a result of the slowdown and/or absorption of radiation flux particles. Under such conditions, high mechanical stresses arise and plastic deformation

develops in limited areas of the materials. Deformation due to ion- and laser-beam irradiation results from the dilatation of a thin ion-implanted layer and from the thermal expansion of the skin layer, respectively. For example, ion implantation causes the expansion of the material at a depth equal to ion projected range h , which, in turn, generates biaxial compression stresses. We will show that these stresses are high enough to result in plastic deformation. According to [17], the increase in the ion concentration in a h -thick implanted layer per unit time is I/h , where I is the ion flux intensity. The diffusion-related decrease in concentration n of implanted ions is $D \frac{n}{h^2}$ (D is the diffusion coefficient), so that the stationary concentration is given by

$$n = Ih / D, \quad (1)$$

Implanted ions cause the expansion

$$\Delta V / V = nb^3 = Ihb^3 / D_c \quad (2)$$

(b is the interatomic distance), which causes the biaxial compression stress

$$\sigma / E \sim Ihb^3 / 3D_c \quad (3)$$

(E is Young's modulus). For $D_c \approx 10^{-13} - 10^{-12}$ cm²/s (the diffusion coefficient of ions implanted into a metal at a temperature of about 800 K), flux density $I \approx 10^{14}$ cm⁻²s⁻¹, ion projected range $h \approx 10$ nm, and $b = 0.25$ nm, the deformation stress equals $(10^{-3} - 10^{-2})E$. Such stresses exceed the yield stress of different materials. Stresses arising under the pulsed laser irradiation are estimated at the same level. The expansion of the skin layer is estimated from the balance between the energy absorbed by the layer and the energy lost by the layer due to heat conduction [18].

Irradiation by neutrons with energies corresponding to the fast-neutron fission spectrum or by ions with energies above 10 keV generates cascades of atom-atom collisions. Depending on the energy of the primary knocked-on atom, as well as on the temperature and type of material, the cascades represent either a set of small regions with point defects or a compact region in which the

energy is spent on ionization and atomic displacement. Calculations [19] show that dense cascades with an energy of the primary knocked-on atom up to 0.1 MeV may occupy a region $d \sim 6-7$ nm in size. Four development stages of atom–atom collision cascades are distinguished [20]. At the first stage lasting about 10^{-13} s, ions slow down because of atom–atom collisions. At the second stage (the stage of microscopic nonequilibrium), the energy is distributed among atoms and is roughly equal to 1–2 eV per atom. The third stage (the thermalization stage or the stage of a “thermal peak”) is followed by the stage of acoustic relaxation. At the last stage, pressures up to 10^{11} Pa ($\sim E_{casc}/d^3$) arise at the boundary of the cascade region for 10^{-10} – 10^{-9} s and the material plastically deforms within areas about 10 nm across.

Thus, different radiation exposures lead to plastic deformations in the material. Such a deformation is, as a rule, constrained deformation and is observed on a scale smaller than the minimal possible distance between dislocations in metals (~ 10 nm or about $40b$), which corresponds to the maximum possible linear density of dislocations in metals, $\sim 10^{12}$ cm $^{-2}$. For example, under ion irradiation, constrained plastic deformation is observed within ion projected range h (from 10 nm on according to the mass and energy of the ion) and in a h -thick thin layer after the implanted region. The thickness of the deforming layer turns out to be insufficient for the formation of dislocations. In this case, plastic deformation follows the dislocation-free mechanism. Here, the deformation is due to the formation and evolution of 2D defects (shear planes, stacking faults, twin boundaries, etc.), rather than linear ones (dislocations). Because of the insignificant elastic interaction and activationless formation mechanism, the linear density of 2D defects may exceed 10^7 cm $^{-1}$. In addition, the dislocation-free strain hardening of metals is notable for an at least one order of magnitude higher strain hardening modulus. If hardening is related to twinning, the degree of hardening is estimated under the assumption that a twin arises from unbounded expansion of a stacking fault under stress [17]

$$\tau = \partial U_{\partial y} / \partial b = (2 \div 55) \cdot 10^{-3} G, \quad (4)$$

where G is the shear modulus. In [17], the reader can find different mechanisms of plastic deformation: the formation of polysynthetic twins and “farms,” twinning of twins, etc. A high volume dilatation may arise, for example, at the site of stacking fault intersection.

Nanostructuring and long – range action effect

The dislocation-free plastic flow is accompanied by the nanostructuring of the material. This can be demonstrated by phenomenologically considering the plastic flow in terms of the Ornstein–Zernicke general approach. This approach was first used to analyze the stability of uniform plastic deformation in [17, 21]. It was shown that the macroscopic structural stability under deformation is lost when the scales of fluctuations and plastic flow grow. Although the structural stability under deformation has been studied as applied to the dislocation plastic flow, the approach used in [17, 21] seems to be applicable to the analysis of plastic deformation following any microscopic (including dislocation-free) mechanism.

When the plastic strain deviates from its mean value δ , a change in the free energy density or the work of plastic deformation in a unit volume is given by

$$f = \sigma \delta + \frac{d\sigma}{d\delta} \frac{\delta^2}{2} = \sigma \delta + S \frac{\delta^2}{2}, \quad (5)$$

where σ is the stress and $S = d\sigma / d\delta$ is the strain hardening modulus. The total change in the free energy in the volume is expressed as

$$\Delta F = \frac{1}{2} \int_V [S\delta^2 + \beta(\nabla \delta)^2] dV. \quad (6)$$

Here, the second term describes the interaction of strain fluctuations. It reflects a decrease in the energy density stored in the volume as a result of elastic relief upon constrained strain δ . This term is negative ($\beta < 0$), and its value depends on the type of structural defect that is responsible for elastic relief

at a given point upon deformation. Coefficient β is expressed as $|\beta| \sim El^2$, where l is a constant on the order of interatomic distance b , so that

$$\Delta F = \frac{1}{2} \int_V [S\delta^2 - El^2(\nabla\delta)^2] dV \quad (7)$$

The first and second terms in the integrand stand for the energy of plastic deformation and the elastic relaxation upon deformation, respectively; hence, ΔF must be positive. Therefore, representing the strain as a superposition of plane waves, $\delta(r) = \frac{1}{N} \sum_k \delta_k e^{ikr}$, we find that a minimum of the free energy is attained at

$$S - El^2k^2 = 0 \text{ and } \lambda = 2\pi l \sqrt{\frac{E}{S}}, \quad (8)$$

where λ is the scale (i.e., the characteristic length) of microstructure inhomogeneity under plastic deformation.

The above analysis is general and does not depend on the plastic deformation microscopic mechanism. However, since strain hardening modulus S and elastic relief characteristic length l depend on the type of structure defect (plasticity carrier), the scale of plastic strain fluctuations is determined by the microscopic mechanism of plastic deformation. If the plasticity is of dislocation character, for elementary metals we have $S \approx (10^{-4} \div 10^{-3})E$ and $\lambda \approx 10^2 \div 10^3 b$. In the case of the dislocation-free plastic flow with strain hardening modulus $S \geq 10^{-3}E$, microstructural inhomogeneities arise on scales $\lambda/2 < 40b$ (over several tens of nanometers) and the nanostructuring of the material takes place. Using a scanning tunnel microscope, we examined the nanocluster structure of Ni–41Cr–Mo alloy irradiated by 30 keV Ar⁺ ions with a dose of $1.5 \times 10^{18} \text{ cm}^{-2}$ at 870 K [21]. The ion flux intensity was $10^{14} \text{ cm}^{-2} \text{ s}^{-1}$. Fig. 1 shows the microstructure of the irradiated surface exhibiting clusters from 50 to 80 nm in size.

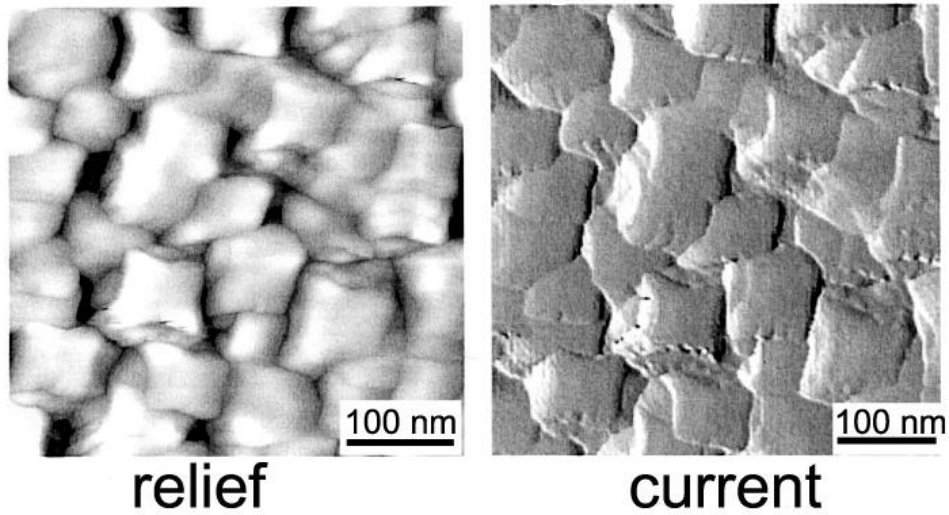


Fig. 1. Surface microstructure of the Ni-41Cr-Mo alloy subjected to ion irradiation (scanning tunnel microscope) [21].

Nanostructuring causes a considerable volume dilatation. This is associated with an extremely high concentration of defects arising from the plastic flow and stabilizing the resulting nanostructure. Among such defects are (see above) shear planes, twin boundaries, and stacking faults, the substructures of which are related to a large dilatation volume. The volume dilatation, in turn, causes the plastic deformation of the next layer (Fig. 2). The layer-by-layer deformation and nanostructuring (the domino effect) propagate over depth H far exceeding effective ion range h . Therein lies the long-range action effect. The implantation-related elastic energy and a change in the volume of the crystal in the implanted layer is compensated for by the work of plastic deformation over the region of long-range action,

$$\frac{K}{2} \left(\frac{\Delta V}{V} \right)^2 h \sim \frac{S}{2} \left(\frac{\Delta V}{V} \right)^2 H \quad (9)$$

where K is the modulus of dilatation. The value of H is roughly given by

$$H \sim h \frac{K}{S} \leq 10^3 h,$$

and can be estimated as several tens of micrometers at $h \approx 10$ nm.

This is confirmed by measuring the microhardness along the depth of ion-irradiated alloys [22].

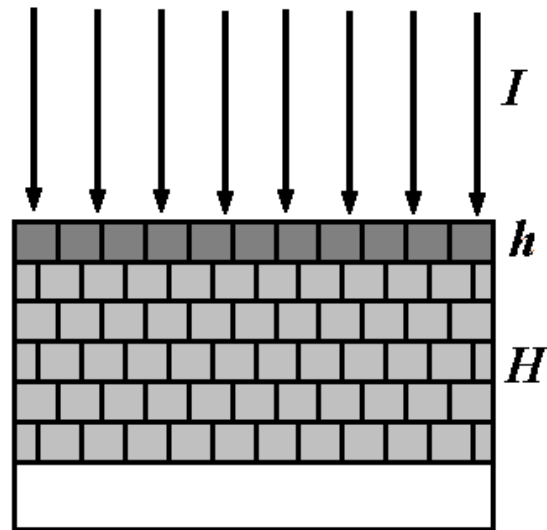


Fig. 2. Mechanism of nanostructuring under ion irradiation.

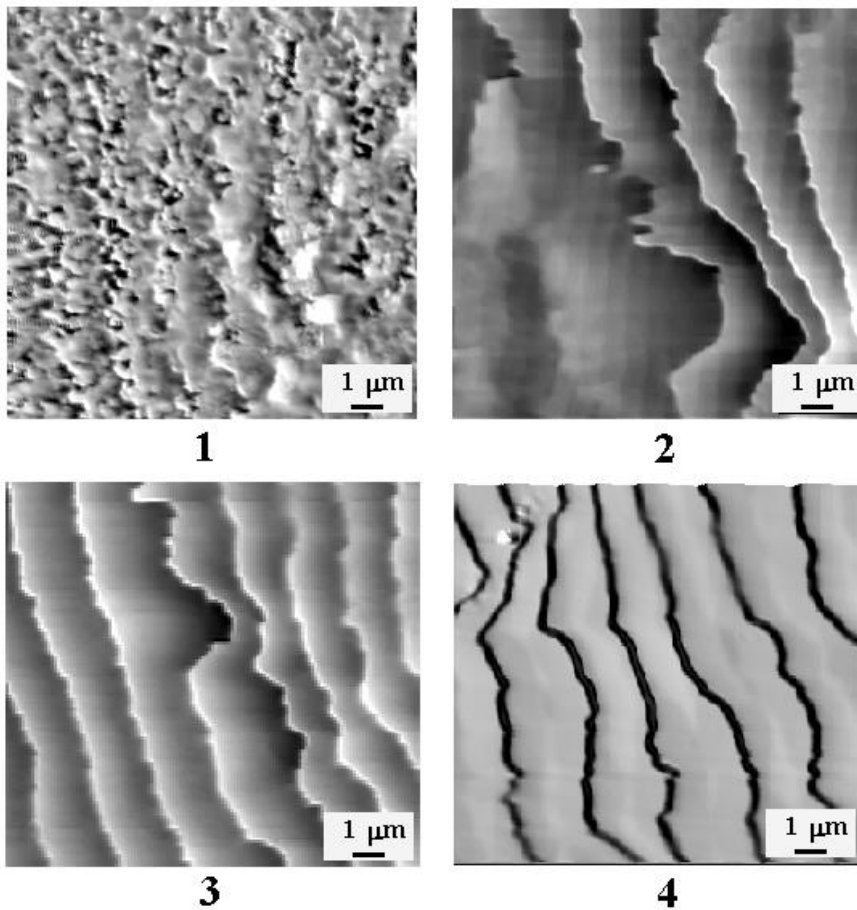


Fig. 3. Surface microstructure of the Ni-41Cr-Mo alloy subjected to ion irradiation with subsequent etching to a depth of (1) 509–600, (2) 150–180, (3) 250–290, and (4) 350–400 nm (scanning tunnel microscope) [21].

Fig. 3 shows the microstructure of the ion-irradiated Ni–41Cr–Mo alloy upon layer-by-layer etching to working depths. The surface microstructure of this alloy is shown in Fig. 1. A nanolayered structure is seen at depths far exceeding the ion projected range ($h \approx 10 \text{ nm}$). We studied the formation of nanocluster structural states in many metallic materials. There are experimental data on nanostructuring upon ion implantation into Zr and Ti metals; Fe–Ni–Cr, Ni–Cr, Cu–Ni, Fe–Cr, and V–Ti–Cr alloys; and Cu_2MnAl and Ni_2MnGa Geissler phases (intermetallics) [23–27]. Deep-seated nanostructures are attendant on radical changes in the properties (such as the microhardness and electronic properties) of the metal subsurface [23]. Anomalously high concentrations of 2D defects in nanoclusters severely change the shape of X-ray diffraction lines and cause them to shift [25–27].

Long – range action effect in diamond

During plastic deformation of materials vacancies appear. In the diamond lattice vacancies modify the initial (nitrogen) defects [28,29]. Nitrogen defects A (two nitrogen atoms) and B1 (four nitrogen atoms around vacancy) are associated with the IR absorption bands at 1282 and 1175 cm^{-1} . After plastic deformation A and B1 defects become in H2-H3 defects (complexes of two nitrogen atoms and vacancies) and H4 defect (four nitrogen atoms and two vacancies) which are not active in the IR spectrum. Therefore, plastic deformation leads to a decrease in intensity of the IR absorption bands of these defects. B2 (1366 cm^{-1}) is a plate defect in the {100} plane in the thickness of a few atomic layers of the linear dimensions from nanometers to micrometers. They consist of the interstitial carbon atoms with a low content of nitrogen. Plastic deformation destroys B2 defects (irreversible process).

Natural diamond single crystals of Ia(A,B1)-type (thickness 300 μm) were irradiated by 30 keV Ar^+ ions with a dose of 10^{17} cm^{-2} at 350 K. The ion flux intensity was $10^{15} \text{ cm}^{-2} \text{ s}^{-1}$. After this, the intensity of the IR bands A, B1 and B2 decreased by more than 15% (Fig. 4). This means that the defect transformation

occurred at a depth $H > 40 \mu\text{m}$. This value is more than 10^3 times as compared to ion projected range $h < 20 \text{ nm}$. Annealing of vacancies in irradiated single crystals at 800°C led to the content recovery of nitrogen defects A, to a partial recovery of defects B1, and B2 defect band intensity was not restored.

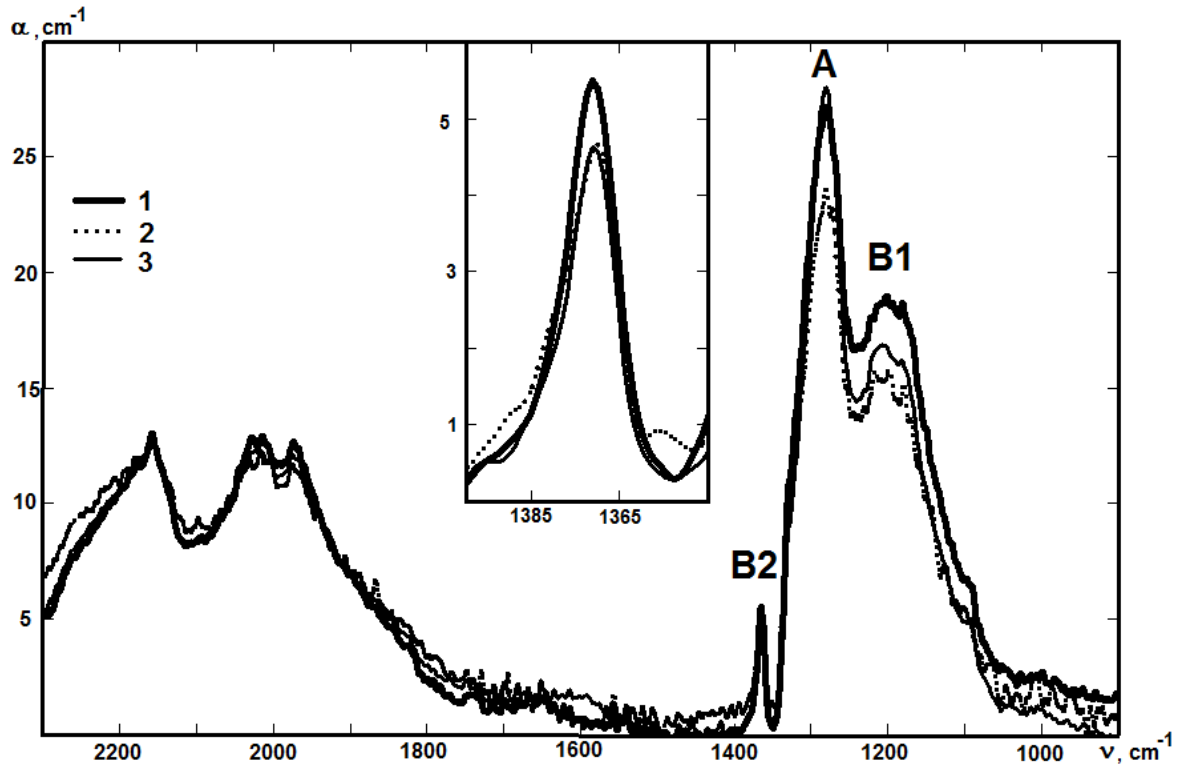


Fig. 4. IR absorption spectra of diamond: initial (1), after ion irradiation (2), after annealing at 800°C (3). The inset is absorption band B2.

Conclusions

Radiation induces plastic deformation in the volume of the material, which is constrained because the deforming region is small. The deformation is of a dislocation-free character and causes nanostructuring of the metal subsurface. The depth of the plastic deformation and nanostructuring over which the physical properties of materials change radically far exceeds the radiation penetration depth. Therein lies the long-range action effect, which is observed in different materials exposed to beam actions.

References

- [1]. M.I. Guseva. Poverkhnost. Fiz. Khim. Mekh. № 4. 27 (1982).
- [2]. V.N. Bykov, V.G. Malynkin, V.S. Khmelevskaya. Vopr. At. Nauki Tekh. Ser.: Fiz. Rad. Povrezhd. Rad. Materialoved. № 3. 45 (1989).
- [3]. Yu.V. Martynenko. Itogi Nauki Tekh. Ser.: PuchkiZaryazh. Chastits Tverd. Telo. № 7. 82 (1993).
- [4]. A.L. Pivovarov. Metallofiz. Noveishie Tekhnol. 16 (12). 3 (1994).
- [5]. V.P. Gol'tsev, V.V. Khodasevich, V.V. Uglov, Yu.S. Kovchur. Vestn Akad. Nauk BSSR. № 4. 21(1985).
- [6]. A.A. Taran, Z.B. Baturicheva, E.F. Chaikovskii. Poverkhnost'. № 2. 146 (1988).
- [7]. A.A. Badad-Zakhryapin, M. I. Lagutkin. Fiz. Met. Metalloved. № 52. 95 (1987).
- [8]. G.V. Kuznetsov. Metalloved. Term. Obrab. Met. № 11. 21 (1987).
- [9]. A.V. Fedorova, E.V. Vasil'eva, B.G. Vladimirov et al. Poverkhnost'. № 8. 123 (1983).
- [10]. D.J. Douquette, R. C. Krutenat. Philos. Mag. 24. № 14. 11 (1971).
- [11]. V.N. Chernikov, A. P. Zakharov. Poverkhnost: Fiz. Khim. Mekh. № 2. 79 (1984).
- [12]. I.B. Levinson, D.L. Maslov. Poverkhnost: Fiz. Khim. Mekh. № 4. 5 (1987).
- [13]. S.D. Zvonkov, B.S. Luk'yanchuk, V.A. Stepanov. Tr. Inst. Obshch. Fiz. Akad. Nauk SSSR. № 30. 83 (1991).
- [14]. Yu.N. Devyatko, V. N. Tronin. Dokl. Akad. Nauk SSSR. 269. 97 (1983) [Sov. Phys. Dokl. 28, 259 (1983)].
- [15]. S.A. Krivelevich. Vysokochist. Veshchestva. № 4. 109 (1995).
- [16]. D.I. Tetel'baum, V.A. Panteleev, A.Yu. Azov, M.V. Gutkin. Poverkhnost': Rentgen. Sinkhrotron. Neitron. Issled. № 5. 87 (2000).

- [17]. M.A. Shtremel'. Strength of Alloys: A Textbook for Institutes of Higher Education, Part 2: Deformation. MISiS, Moscow, 1997.
- [18]. Laser Techniques and Technology a Textbook for Institute of Technology, Book 6: Bases of Laser Thermostrengthening of Alloys. Ed. by A.G. Grigor'yants, A. N. Safonov. Vysshaya Shkola, Moscow, 1977.
- [19]. V.V. Kirsanov, A.L. Suvorov, Yu.V. Trushin. Processes of Radiation Defect Formation in Metals. Energoatomizdat, Moscow, 1985.
- [20]. V.A. Stepanov. Vopr. At. Nauki Tekh., Ser.: Materialoved. Nov. Mater. № 1 (66). 54 (2006).
- [21]. V.A. Stepanov, V.S. Khmelevskaya. Technical Physics, 2011. V. 56. № 9. pp. 1272–1276.
- [22]. V.S. Khmelevskaya, I.A. Antoshina, M.N. Kordo. Fiz. Met. Metalloved. № 6. 652 (2007).
- [23]. V.S. Khmelevskaya, S.P. Solov'ev, V.G. Malynkin. Itogi Nauki Tekh., Ser.: Puchki Zaryazh. Chastits Tverd. Telo. № 2. 151 (1990).
- [24]. V.S. Khmelevskaya, N.Yu. Bogdanov, M.N. Kordo. Fiz. Khim. Obrab. Mater. № 2. 14 (2008).
- [25]. V.S. Khmelevskaya, N.Yu. Bogdanov, M.N. Kordo. Pis'ma Zh. Tekh. Fiz. 34 (23), 33 (2008) [Tech. Phys. Lett. 34, 1011 (2008)].
- [26]. V.S. Khmelevskaya, N.Yu. Bogdanov, K.A. Gorchakov. Fiz. Khim. Obrab. Mater. № 5. 5 (2008).
- [27]. V.S. Khmelevskaya, M.N. Kordo. Vopr. At. Nauki Tekh., Ser.: Materialoved. Nov. Mater. № 72. 151 (2008).
- [28]. V.G. Vins, A.P. Eliseev, V.A. Sarin. Precious metals. Precious jewels (2009). №3 (183). pp.127-148.
- [29]. V.A. Nadoliny, O.P. Yurieva et.al. Dokl. Akad. Nauk(2004). V. 399. №4. pp. 532-536.

CARBON STEEL ULTRAFINE STRUCTURE FORMATION IN HIGH-SPEED DEFORMATION AT ELEVATED TEMPERATURES

N.V. Koptseva, J.J. Efimova, O.A. Nikitenko,

M.P. Baryshnikov, M.S. Zherebtsov

FSBEI HPE “Nosov Magnitogorsk State Technical University.

For the moment, various ways of obtaining bulk ultra-fine grained (UFG) metals and alloys are known, most of which are based on severe plastic deformation [1-3]. The main methods, owing to which major deformation with true powers equal to 10 governmental and more have been obtained without destroying the samples, are high pressure torsion (HPT) [4] and equal channel angular pressing (ECAP) [5]. There are some papers that describe obtaining UFG structures in a number of metals and alloys by using comprehensive forging [6], equal channel angular stretching [7], screw extrusion [8], etc. However, these methods of producing UFG structures are not applicable for large-lot production that hinders their practical use.

To date, there are developments aimed at improving methods of severe plastic deformations for their practical use [9, 10]. In recent years, great scientific and practical interest has been aroused in the high-speed deformation of metals [11-14] in connection with the development of a number of new technology areas, as well as in connection with the development and introduction of new promising technological methods of materials processing in manufacturing industry.

Plastic strain rate increase is known to lead to significant changes in the metallic material microstructure [15, 16]. Herewith metal structure and properties will be determined by such factors as pressure (or pulse) amount, strain rate (or the duration of the process) and the temperature. At the same time the influence of high strain on the material microstructure is insufficiently investigated.

At present physical modeling complexes Gleeble 3150, 3500, 3800 [17, 18] provide great opportunities for high-speed deformation modeling process at elevated temperatures. They are, virtually a high-velocity plastometer to implement an unlimited number of metal forming stages with constant or variable during processing temperature or strain rate. Their own easy-to-use software forms a very convenient interface to create programming support of mechanical testing and of a physical simulation, as well as for collecting and analyzing the obtained data.

The sample heating is carried out by direct passing an electric current that allows to heat the samples at a speed of up to 10,000 °C/s, and supports constant temperature with an accuracy of 1 °C. Due to the high thermal conductivity of copper hooks, which attach a sample in a complex Gleeble 3500 one can reach high cooling rates.

In reference with the information above, the purpose of the work was to study the possibilities of obtaining UFG state steel grade 20 by high-speed deformation (HSD), which was performed on the complex Gleeble 3500 using “compression-stretching” module. Samples of 10 mm in diameter and 100 mm long were deformed by compression at temperatures of 800, 900, 1000 and 1200 °C with a strain rate of 1000 mm/s and then cooled at 34 °C/s. Deformation degree at different temperatures was similar and was sized by compression of the specimen up to 25 mm, which was carried out by moving traverse to the appropriate distance. To identify qualitative and quantitative characteristics of the microstructure was used an optical microscope Meiji Techno using image computer analysis system Thixomet PRO [19], as well as scanning electron microscopy (SEM) using a scanning electron microscope JSM 6490 LV.

In the initial state the volume fraction of the main structural component of steel grade 20 – ferrite – was 76 %, and pearlite – 24 % (Fig. 1 a), the grain size was ranging from 10 to 30 microns, and the average interlamellar spacing in pearlite was 0.32 μm (Fig. 1 b).

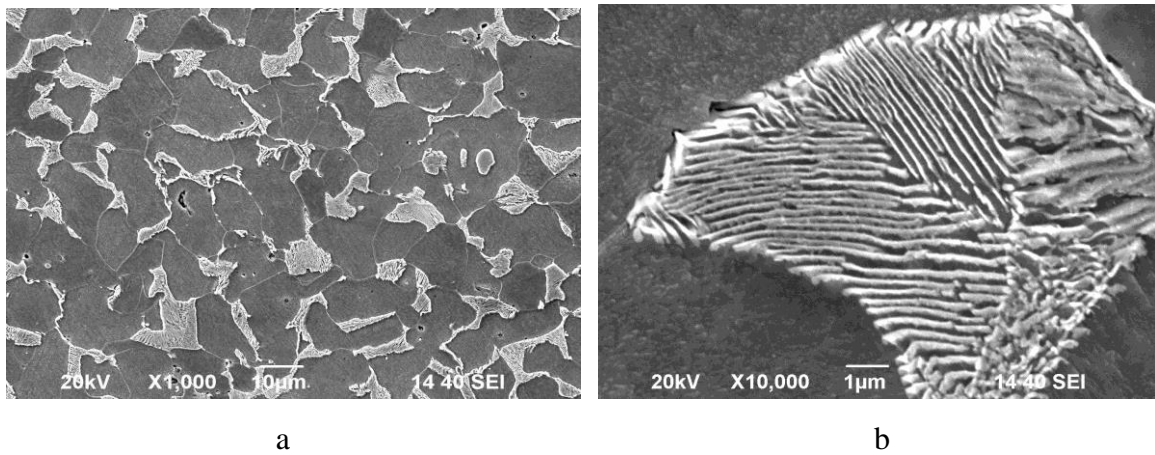


Fig. 1. The microstructure of steel grade 20 in the initial state.

The microstructure after HSD at different temperatures is shown in Fig. 2. It is characterized by the presence of parallel or mutually perpendicular deformational strips arranged in increments of 300-1000 nm, which are formed in the most favorably oriented grains and similar to band- structure frames that arise in traditional method deformation with degrees $\varepsilon \leq 3-4$. Simultaneously one can trace deformation bands partition and original "free" ferrite crystals (which lacked deformation bands) to smaller size regions (fragments), which have the form of equiaxial grains with thin rectilinear boundaries and equilibrium angles at triple junctions. It testifies to high angle boundaries formation, ferrite grains refining to the size of 300-400 nm (fragmenting) and genesis of UFG structure.

The smallest grain size and more relative amount of fragmented ferrite were observed in the sample deformed at 800 °C (Fig. 2 a). At this temperature, deformation occurred in steel 20 intercritical intervals Ac_1-Ac_3 , i.e. in the two-phase field austenite + ferrite, when simultaneously both austenitic and ferrite grains deformed. Thereby half dynamic recrystallization occurred, resulting in ferrite fragments assumed almost equiaxed form.

Recrystallized grains genesis is specified by temperature increase in the field of strain localization and is a mechanism of stress relaxation. Recrystallized grains are grouped in deformation bands and chains, which are located between the bands (Fig. 2 b). However, the recrystallization process has

obviously no time to be fully completed, a significant growth of recrystallized grains does not occur and therefore dispersed ultrafine ferrite grains remain fine - the average size is about 400 nm. Not crystallized parts, apparently, are elongated grain consisting of sub grains formed, apparently as a result of dynamic cell formation.

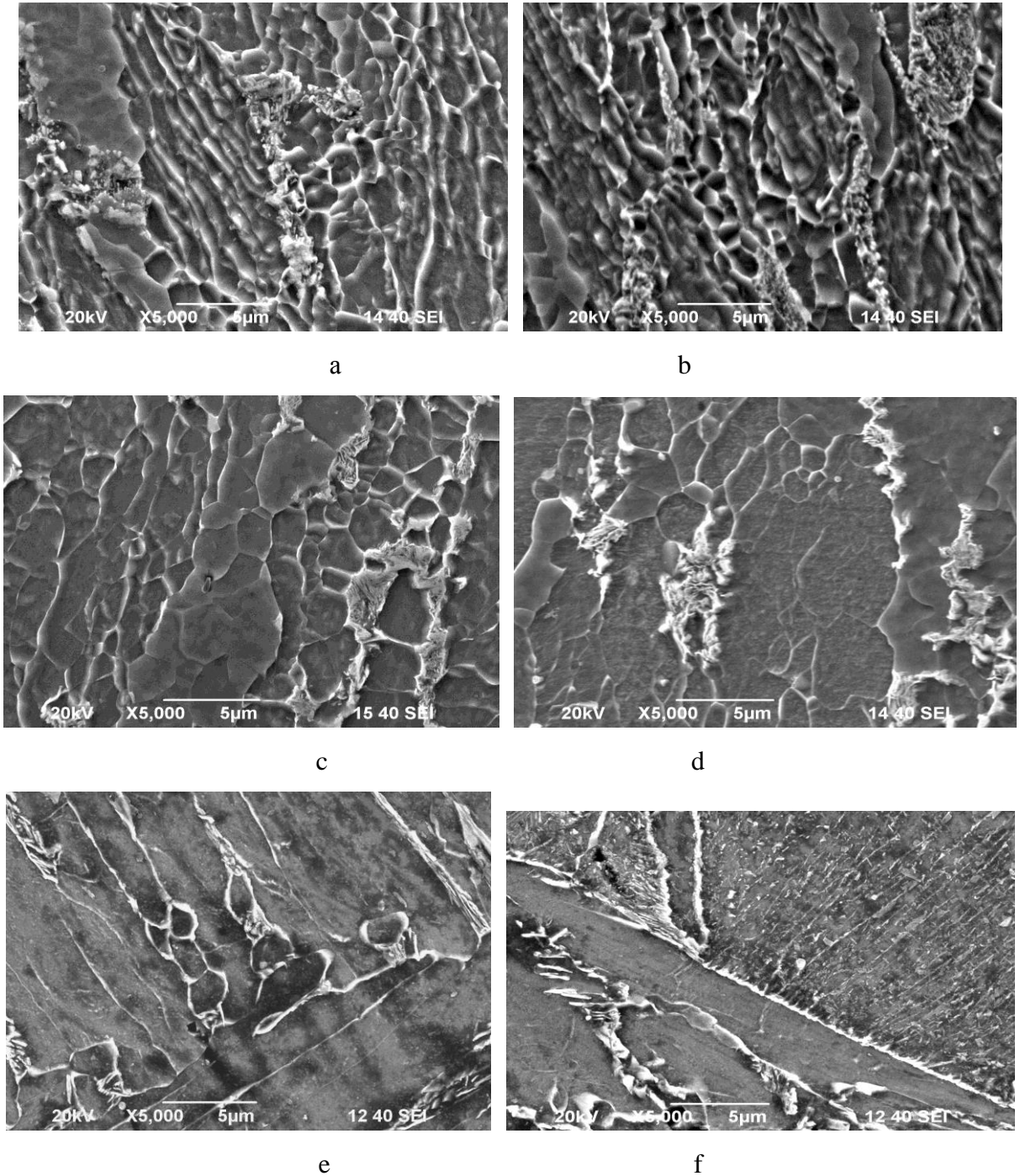


Fig. 2. Steel grade 20 microstructure after high-speed deformation at temperature 800 (a, b), 900 (c), 1000 (d) 1200 ° C (e, f).

The structure obtained by high-speed deformation at the temperature of 800 °C was largely similar to the structure, which was observed in steel 20 after ECAP at 400 °C (deformation bands and ultrafine grain size of 300-500 nm were formed in the microstructure [20, 21]), as well as in the dynamic channel-angular pressing of titanium at high temperatures [11].

Deformation at the temperature above A_{c3} (900, 1000 and 1200 °C) occurred in a single-phase austenite region and also provided the structure deformation refinement. Structure after HSD at 900 and 1000 °C was largely similar to the structure after deformation at 800 °C and differed only by larger grain size (Fig. 2 c, d). On cooling, which was carried out immediately after deformation, excurrent ferrite apparently inherited features of the deformed austenite dislocation structure and was recrystallized. Due to the higher deformation temperature dynamic recrystallization proceeded more completely, and recrystallized grain growth occurred, which led to an increase in the grain size up to 750-2500 nm. Pearlite regions in such a structure are also dispersed.

After deformation at 1200 °C the main characteristic structural element formed as a deformation result, are deformation bands of width 1-5 microns (Fig. 2 e). In the structure one can rarely find ultrafine ferrite grains, which denotes almost full dynamic recrystallization. After HSD at the temperature of 1200 °C, moreover, the structural components morphology changes: a needle-like structure of ferrite and low carbon bainite structure is often observed instead of a sheet-like ferrite-carbide mixture (Fig. 2 c).

Cementite phase at deformation temperature modes partially suffers coalescence in the austenite fragmentation region.

Comparison of steel 20 microhardness obtained after high-speed deformation at elevated temperatures and ECAP, is illustrated in Fig. 3.

Noticeable decrease in hardness is observed only after deformation at 1200 °C, and in comparison with ECAP hardness after HSD has been reduced. However, after HSD at a temperature 800-1000 °C hardness compared with

baseline has been increased by approximately 20 % due to ferrite grains refinement and ferrite fragmentation.

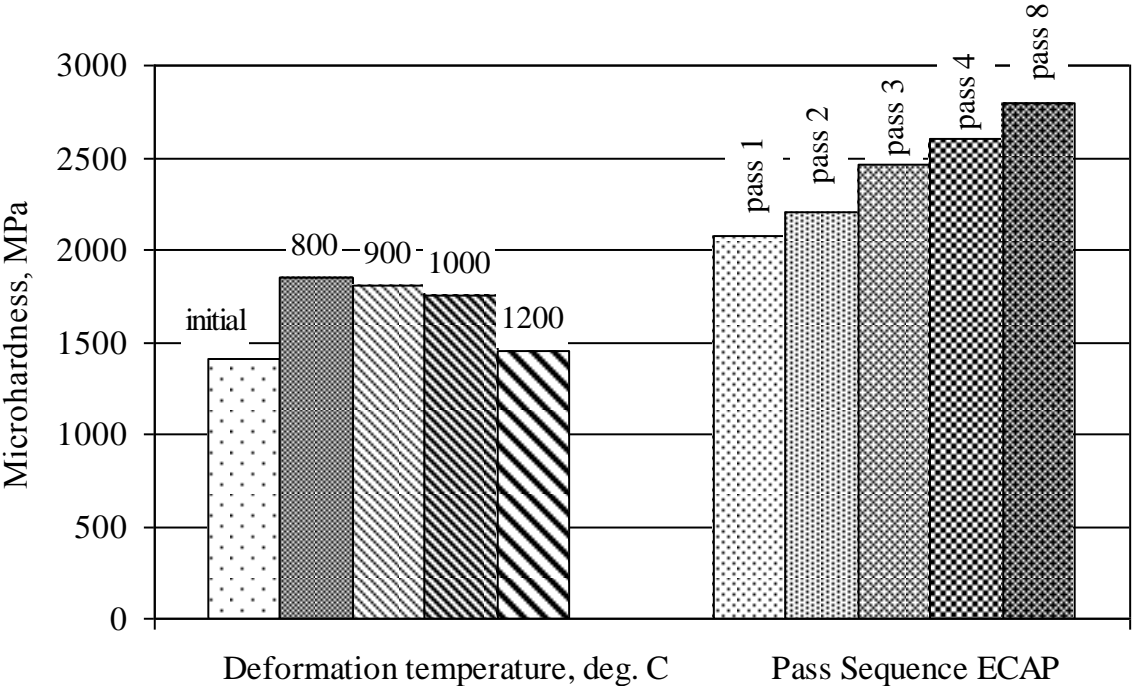


Fig. 3. Comparison of steel grade 20 microhardness after high-speed deformation at elevated temperatures and at 400 °C ECAP.

Conclusion

The research results obtained by using research complex Gleeble 3500, showed the principle ability to provide steel grade 20 structure strain grinding at high-speed deformation at temperatures of 800-1000 °C to a grain size of about 400 nm similarly to the size achieved in the process of large plastic deformation without metal heating or with slight one without exceeding recrystallization temperature.

Acknowledgments

The work was done as a part of a complex project for creating high-tech production with the participation of higher education institution (contract 02.G25.31.0040), as well as the University strategic development program in 2012-2016. (Competitive support of the Ministry of Education RF strategic development programs SEI HPE).

Reference

- [1]. R. Song, J.G. Speer, D.K. Matlock, D. Ponge, D. Raabe. Overview of processing, microstructure and mechanical properties of ultrafine grained bcc steels. *Materials Science and Engineering: A*. 2006. V. 441. № 1-2. pp. 1-17.
- [2]. R.Z. Valiev, I.V. Alexandrov. *Bulk nanostructured metal materials*. M.: ICC "Akademkniga ", 2007. 398 p.
- [3]. J. Zrník, S.V. Dobatkin, T. Kovarik, J. Dzukan. Ultrafine grain structure development in steels with different carbon content subjected to severe plastic deformation. *The Minerals, Metals and Materials Society - 3 -rd International Conference on Processing Materials for Properties in 2008, PMP III: Bangkok, 2009*. pp. 850-855.
- [4]. G.L. Kolmogorov. Technological features of nanostructure materials production by severe plastic torsion deformation. *News of higher educational institutions. Iron and steel*. 2008. № 9. pp. 18-20.
- [5]. T. He, Y. Xiong, F. Ren, Z. Guo, A.A. Volinsky. Microstructure of ultrafine-grained highcarbon steel prepared by equal channel angular pressing. *Materials Science and Engineering: A*. 2012. V. 535. pp. 306-310.
- [6]. O.Sh. Sitdikov. Microstructure Evolution of high-strength aluminum alloy during elevated temperature all-way forging with large deformation. *Deformation and fracture of materials*. 2011. № 11. pp. 15-26.
- [7]. M.V. Chukin, D.G. Emaleeva Heat treatment effect on the evolution of steel wire structure and properties in ECA broach process. *Vestnik of Nosov Magnitogorsk State Technical University*. 2008. № 2. pp. 70-71.
- [8] Y.E. Beigel'zimer, S.G. Synkov, D.V. Orlov. Screw Extrusion. *Metal-forming process*. 2006. № 4. pp. 17-22.
- [9]. R.Z. Valiev, G.I. Raab, A.V.Botkin, S.V. Dubinina. Ultrafine metals and alloys Obtaining by severe plastic deformation : new approaches in technology development. *News of higher educational institutions. Iron and steel*. 2012. № 8. pp. 44-47.

- [10]. M.V. Chukin, A.G. Korchunov, M.A. Polyakova, D.G. Emaleeva. Forming ultrafine-grain structure in steel wire by continuous deformation. *Steel in Translation*. 2010. V. 40. № 6. pp. 595-597.
- [11]. V.I. Zel'dovich, N. Frolova, A.E. Heifetz, I.V. Khomskaya, E.V. Shorohov, P.A. Nasonov. Improvement of the mechanical properties of titanium by dynamic channel- angular pressing. *Material science issues*. 2012. № 1 (69). pp. 29-37.
- [12]. Dun Yuechen, V.D. Sitdikov, I.V. Alexandrov, D.T. Wang. High deformation influence on the microstructure and crystallographic texture of the copper in different structural states. *Letters of materials*. 2013. V. 3. № 2 (10). pp. 169-172.
- [13]. M.P. Bondar, S.G. Psakhie, A.I. Dmitriev, A.J. Nikonov About deformation localization conditions and microstructure fragmentation in high-speed loading. *Physical Mesomechanics*. 2013. V. 16. № 2. pp. 5-13.
- [14]. A.N. Petrova, I.G. Brodova, I.G. Shirinkina, P.A. Nasonov, E.V. Shorohov. Features of ultrafine and nanocrystalline states of the aluminum-manganese alloy obtained by the severe exposure. *Letters of materials*. 2013. V. 3. № 2 (10). pp. 126-129.
- [15]. M.A. Meyers. *Dynamic Behavior of Materials*. John Wiley & Sons, New York, 1994. 393 p.
- [16]. A. Bhattacharyya, D. Rittel, G. Ravichandran. Effect of strain rate on deformation texture in OFHC copper. *Scripta Mater*. 2005. V. 52. pp. 657-661.
- [17]. A.I. Rudskoy, N.G. Kolbasnikov, O.G. Zotov, D.A. Ringinen, A.A. Nemtinov, V.V. Kuznetsov. Investigation of the structure and properties of TRIP-steels on complex GLEEBLE-3800. *Ferrous metals*. 2010. № 2. pp. 8-14.
- [18]. D.M. Chukin, A.S. Ishimov, M.S. Zherebtsov. Complex Gleeble3500 use for the analysis of phase transitions in eutectoid composition steel microalloyed by boron. *Handling solid and laminates: Hi. Sat scientific. tr. Ed. M.V. Chukin. Magnitogorsk: Magnitogorsk Publ. NMSTU, 2012. № 38. pp. 53-57.*

- [19]. N.V. Koptseva, M.V. Chukin, O.A. Nikitenko. Use of the Thixomet PRO software for quantitative analysis of the ultrafine-grain structure of low-and medium-carbon steels subjected to equal channel angular pressing. *Metal Science and Heat Treatment*. 2012. V. 54. № 7-8. pp. 387-392.
- [20]. N.V. Koptseva, Y.Y. Efimova, M.P. Baryshnikov, O.A. Nikitenko. Formation of the structure and mechanical properties of carbon structural steel in the process of nanostructuring by equal-channel angular pressing. *Deformation and fracture of materials*. 2011. № 7. pp. 11-17.
- [21]. N.V. Koptseva. Structure deformation refinement of carbon structural steel by equal-channel angular pressing for increasing the strength of hardware production. *Steel*. 2012. № 8. pp. 50-56.

NONUNIFORMITY OF 08Cr18Ni10Ti STEEL HOT DEFORMATION

M.V. Temlyantsev, M.V. Filippova, V.N. Peretyatko, S.V. Konovalov

Siberian State Industrial University, Kirov str., 42, Novokuznetsk, Russia,
654007. E-mail: gromov@physics.sibsiu.ru

Abstract

The study of deformation nonuniformity of 08Cr18Ni10Ti steel with 28% δ -ferrite content was carried out with the application of high temperature metallographic set-up.

It was determined that average value of ferrite deformation is larger than that of austenite and this difference is increased with a temperature rise. A slip along the interphase boundaries is increased with temperature rise. Ratio of hot microhardness of austenite and δ -ferrite is increased with a temperature rise as well.

In stainless austenite steels of 18-8 type the presence of the second phase is considered to be one of the reasons of low technological characteristics. The main factor reducing the plastic properties of metal is nonuniformity of deformation [1].

Study of nonuniformity of deformation on stretching of 08Cr18Ni10Ti steel in a temperature range of 700 – 1000⁰C was carried out in the present paper.³

Tests were done on samples after pretreatment which allowed to obtain a significant quantity of the second ferrite phase (up to 45%) in 08Cr18Ni10Ti austenite steel.

Nonuniformity of deformation was studied by fixed points and method of coordinate grids.

Preparation of samples for study consisted in the microsection preparation on one of the sample surfaces and marking its working zone with diamond pyramid of hardness tester PMA-3. Test sample was mounted in vacuum chamber of unit IMASH-20-75 “Ala-Too” to the grips of stretching unit with bars. A junction of platinum-platinum-rhodium thermocouple was welded to the side surface of the sample. The air evacuation from the chamber was done to the residual pressure of $5 \cdot 10^{-5}$ mmHg ($6.7 \cdot 10^{-3}$ Pa). Heating of the sample to the temperature 700 – 1000⁰C was done at the expense of heat action of the industrial frequency current passed through it.

Accuracy of temperature maintenance was $\pm 5^0$ C. Samples were stretched to deformation 20 -30% at the rate of deformation $3.2 \cdot 10^{-2} \text{C}^{-1}$ [2].

In the course of sample stretching a photographing of coordinate grid form change at different deformation degrees was made in the vacuum chamber of high temperature metallographic unit.

A relative deformation of microsections was determined in the direction of stretching

$$\varepsilon = 1 - l_0/l_0 \quad (1)$$

³ The work was done and financially supported by RFFI for 2014-2015 (stste contract № 14 – 08 -00686)

where l, l_0 – size between fixed points before and after deformation.

The three groups of microsections were analyzed:

- the first groups of microsections locating totally in austenite grain.
- the second group of microsections locating totally in δ -ferrite grain.
- the third group of microsections through which an interphase boundary located.

Deformation on microsections 1 and 2 characterizes a plastic deformation in austenite and δ -ferrite grains respectively. The third group of microsections was taken for interphase shift estimation.

Statistic processing of the results with determination of average deformation $\varepsilon_a, \varepsilon_f,$ and ε_{af} and root-mean-square deviation of S was done for microsections of each type.

Absolute error of microsection deformation determination at confidence coefficient 0.90 is equal in average 0.010. In experimental data processing the value m was determined according to the dependence

$$m_a = \frac{\varepsilon_a}{\varepsilon}, m_\phi = \frac{\varepsilon_\phi}{\varepsilon} \text{ and } m_{a\phi} = \frac{\varepsilon_{a\phi}}{\varepsilon}$$

where m – characterizes a contribution of separate microsections into sum deformation ε .

The results of investigation are given in Table 1.

Table 1. Nonuniformity of plastic deformation of steel 08Cr18Ni10Ti.

Temperature, °C	m_a	$m_{a\phi}$	m_ϕ	$m_\phi - m_a$	m_ϕ / m_a	$m_{a\phi} - \frac{m_a + m_\phi}{2}$
700	0,71	1,15	1,23	0,52	1,7	0,18
800	0,52	1,26	1,27	0,75	2,4	0,36
900	0,49	1,29	1,36	0,87	2,8	0,37
1000	0,27	1,35	1,52	1,25	5,6	0,46

In this table: m_a, m_f, m_{af} – relative fraction of deformation of austenite, boundary sections and ferrite in a sum deformation.

As is seen from Table 1, a relative austenite deformation is reduced by a factor of 2.6 with a temperature rise. Relative δ -ferrite deformation is increased by a factor of 1.23 and deformation along interphase boundaries – by a factor of 1.17. It may be also noted that at temperature of 700°C ferrite is deformed larger than austenite by a factor of 1.7, and already at temperature of 1000°C – by a factor of 5.6.

As it was noted above, the third group included the sections through a middle of which the interphase boundary located. The sum deformation of this section without a slip on the boundary will be equal to $(\epsilon_f + \epsilon_a)/2$. If a slip along the phase boundary contributed to microsection deformation, then $\epsilon_{af} > (\epsilon_f + \epsilon_a)$. In the last column of Table 1 a value of plastic deformation along the interphase boundary δ -ferrite – austenite. As is seen from Fig. 2, the intensity of shifts along the phase boundaries increases with a temperature rise.

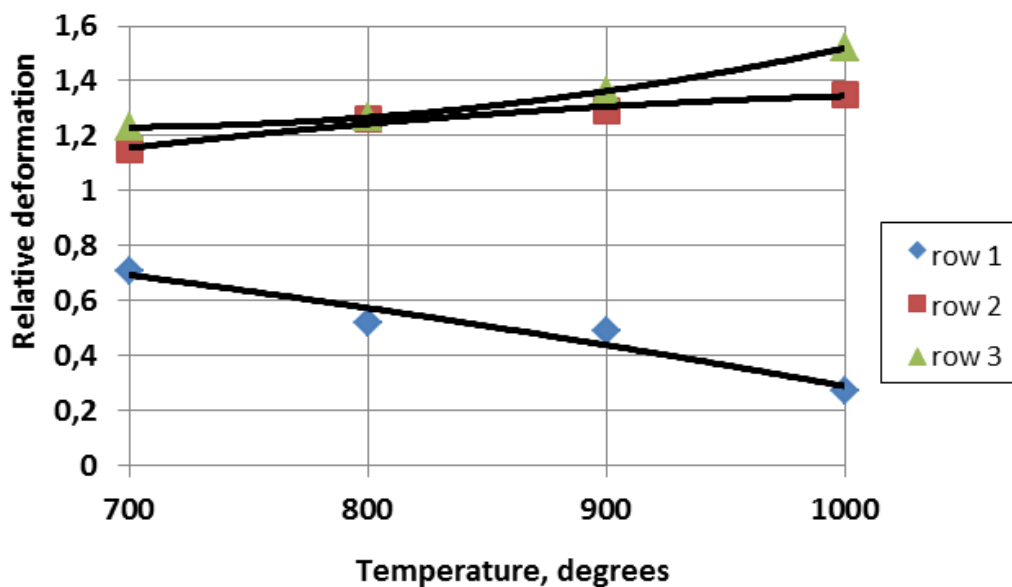


Fig1. Temperature dependence of relative deformation of: 1- austenite; 2- interphase boundaries; 3 – ferrite.

Resistance to deformation of δ -ferrite and austenite grains at temperatures $700 - 1000^{\circ}\text{C}$ was estimated from value of hot microhardness H_a/H_f , where H_a/H_f – microhardness of austenite and ferrite respectively.

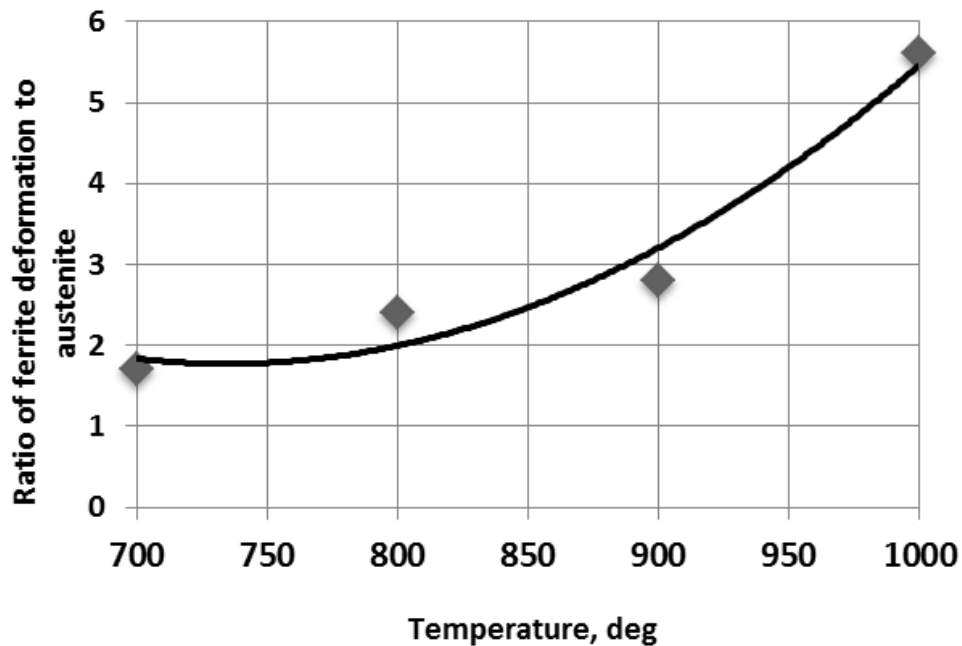


Fig. 2. Temperature dependence of ferrite relative deformation to austenite relative deformation.

The measurement of δ -ferrite and austenite hot microhardness was done on the unit IMASH – 9 – 66. The polished sample made of steel 08Cr18Ni10Ti was placed into a vacuum chamber, from which air was evacuated up to the pressure $6.7 \cdot 10^{-3}$ Pa. Heating of samples to temperatures 700 – 1000⁰C was done at the expense of heat action of electric current of industrial frequency passed through the sample.

Ten indentations were applied by indenter to the surface of sample heated to the test temperature in sites of δ -ferrite and austenite grain location. Load on the indenter was 0.1 N. The statistical processing results of experiment are given in Fig. 3. As is seen from the diagram, at high temperatures a microhardness of austenite grains is larger than δ -ferrite ones. With temperature rise the ratio of austenite and δ -ferrite microhardness increases.

A character of temperature dependence of ratio of δ -ferrite and austenite average deformations (Fig. 2) is analogous to the ratio change of their hot microhardness.

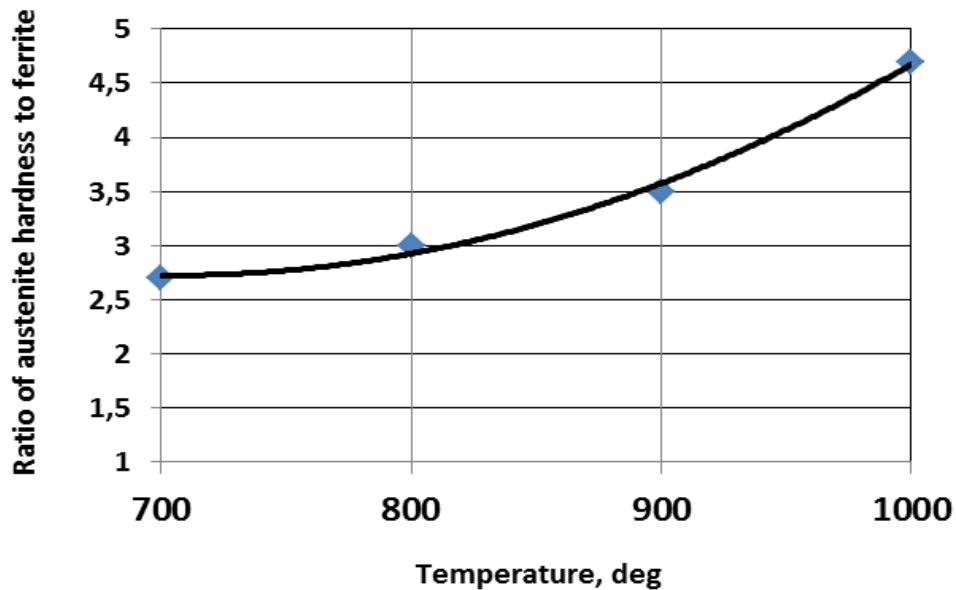


Fig. 3. Temperature dependence of austenite hardness ratio to ferrite hardness.

Thus, nonuniformity of hot deformation by phases of steel 08Cr18Ni10Ti is specified by the difference of deformation resistance of austenite and δ -ferrite phases.[4].

A slip along the high-angle boundaries is done at the expense of movement of grain boundary dislocation and their complexes in which, one of the dislocations is a sessile one. A temperature rise facilitates the displacement of grain boundary dislocations. In this case the annihilation of opposite sign dislocations and movement of grain boundary dislocations of identical sign to the source takes place and this causes a slip along δ -ferrite and austenite boundaries.

Conclusions

Hot deformation of steel 08Cr18Ni10Ti is nonuniform and is characterized by the fact that δ -ferrite is deformed larger than austenite. The ratio of δ -ferrite average deformation and austenite average deformation grows with temperature rise and total deformation of sample. Ratio of austenite and δ -ferrite hot microhardness is increased with temperature rise as well.

References

- [1]. L.P. Laricheva, V.N. Peretyatko, A.N. Rostovtsev, A.M. Levius. Nonuniformity of hot plastic deformation of stainless steels of austenite – ferrite structure. *Izvestiya vuzov. Chernaya metallurgiya*, 1987. № 4. pp. 79 – 83.
- [2]. M.G. Losinskii. Structure and properties of metals and alloys at high temperatures. M., Metallurgizdat. 1963. 536 p.
- [3]. V.K. Grigorovich. Hardness and microhardness of metals. M., Nauka. 1976. 230 p.
- [4]. Development of theory and practice of metallurgical technologies: monograph: in 3 volumes. / Edited by V.N. Peretyatko, E.V. Protopopov, I.F. Selyanin. Vol. 2: Plasticity failure of steel in the processes of heating and pressure working. / V.N. Peretyatko, M.V. Temlyantsev, M.V. Filippova. M.: Teplotechnik, 2010. 352 p.

STUDY OF ELECTROMAGNETIC STIRRING IN THE CONTINUOUS CASTING OF RAIL STEEL SEGREGATED PROCESSES TO DEVELOPMENT

S.V. Feiler, E.V. Protopopov, E.V. Polevoy, V.P. Dement'ev

Siberian state industrial university, 654007, Novokuznetsk, Russia.

Abstract

The article presents the results of a comparative analysis of the development of phase separation processes in the cross section of continuous casting, resulting in CCM traditional design and equipped with a system of electromagnetic stirring of the metal in the mold. The degree of phase separation on the bloom obtained with the use of systems for electromagnetic stirring is less than 2,6 times the carbon, 3,2 times manganese, 3,4 times silicon, 1,9 times phosphorus and sulfur of 2,7 times.

Keywords: continuous casting of steel, segregation, electromagnetic stirring, templet, quality metal

Most defects in continuous casting is due to the development of processes of segregation. Various elements of the solubility in the liquid and solid phases resulting in the enrichment layer solidification boundary segregating impurities. When there along the surface of the convective flows of the liquid crystal become part of the atoms of that layer is removed in the mother melt, increasing the concentration of impurities in the bulk of the metal melt. Of particular importance is the study of segregation of continuously rail steel because chemical heterogeneity that occurs during the solidification of the ingot results in anisotropy of mechanical properties.

Uneven distribution of chemical elements in a cross section of continuous casting influence on the stress- strain state of metal rolling process, which leads to a change in the probability of occurrence of defects depending on the process conditions for the realization of the process [1].

In recent decades, has accumulated considerable experience in the use of external influences on the dynamic solidified continuously cast ingots, for example, a widely used system of electromagnetic stirring of the metal in the mold. When this magnetic field is generated penetrating through the solidified shell of the ingot to initiate the eddy currents of molten steel under the influence of which the metal starts to rotate. It is known that electromagnetic stirring helps to improve the quality of the subsurface area and the center of continuously cast billets, affects the formation of the crystalline structure, the movement of non-metallic inclusions, chemical segregation and distribution of gas [2].

In accordance with the development strategy of "EVRAZ ZSMK" in 2012 reconstructed radial four-strands continuous casting machine (CCM) № 1, which allowed for obtaining high-quality continuous casting for the production of 100-m rails. During the reconstruction of increased cross-section billet caster with 300×330 to 300×360 mm and installed electromagnetic stirring of the metal in

the mold. To analyze the effectiveness of the systems of external dynamic effects on the solidifying ingot used to study the segregation of elements in the cross section of continuous casting before and after reconstruction of the CCM. The study was conducted using a sample cross section of continuous casting – of templet (Fig. 1), obtained by casting steel rail E76F smelted in a 100-ton electric arc furnace and treated on the unit "ladle - furnace" and degasser.

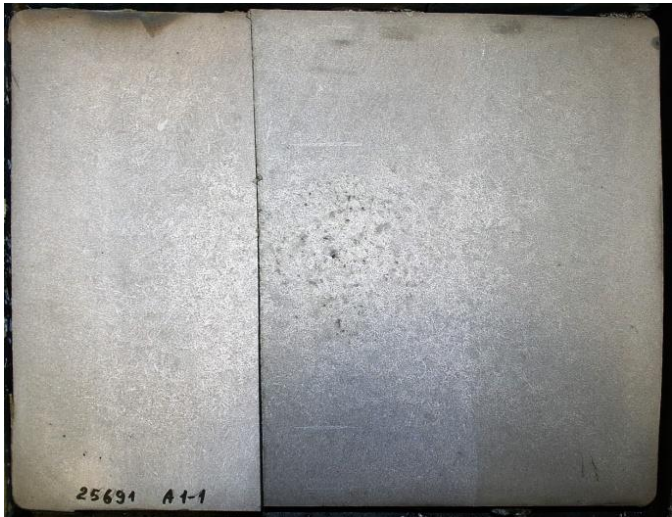


Fig. 1. Templet with the first bloom first strand from CCM after reconstruction.

After pretreatment of templates conducted their drilling in seventeen points, followed by sampling for chemical analysis in the circuit shown in Fig. 2. Chemical analysis is performed on the contents of C, Mn, Si, P, S, due to the fact that these elements have the greatest effect on the development of phase separation phenomena [2].

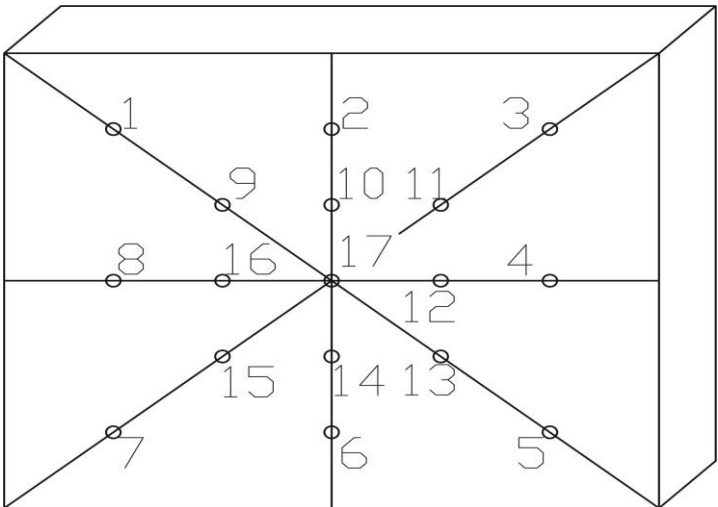


Fig. 2. Scheme of sampling for chemical analysis.

Calculation of values of the degree of segregation produced by the expression [3]

$$K = \frac{C_{\max} - C_{\min}}{C_{\text{ladle}}} \cdot 100\%,$$

where C_{\max} and C_{\min} – minimum and maximum content of the element in some of the templet, %; C_{ladle} – element content in ladle sample, %.

The results of calculating the degree of segregation of the elements shown in Fig. 3, which shows that the tendency to phase separation of the various elements contained in the steel is not the same, as follows: sulfur (50%), phosphorus (43,48 %), silicon (32,26 %), carbon (17,07 %), manganese (14,81 %). The degree of phase separation on the bloom obtained with the use of electro-magnetic stirring systems is less by a factor of 2,6 carbon, 3,2 manganese, 3,4 silicon, 1,9 phosphorus and sulfur of 2,7 times compared to the values obtained on the bloom with the CCM before reconstruction, which takes on particular importance in the implementation of production technologies 100-m rails.

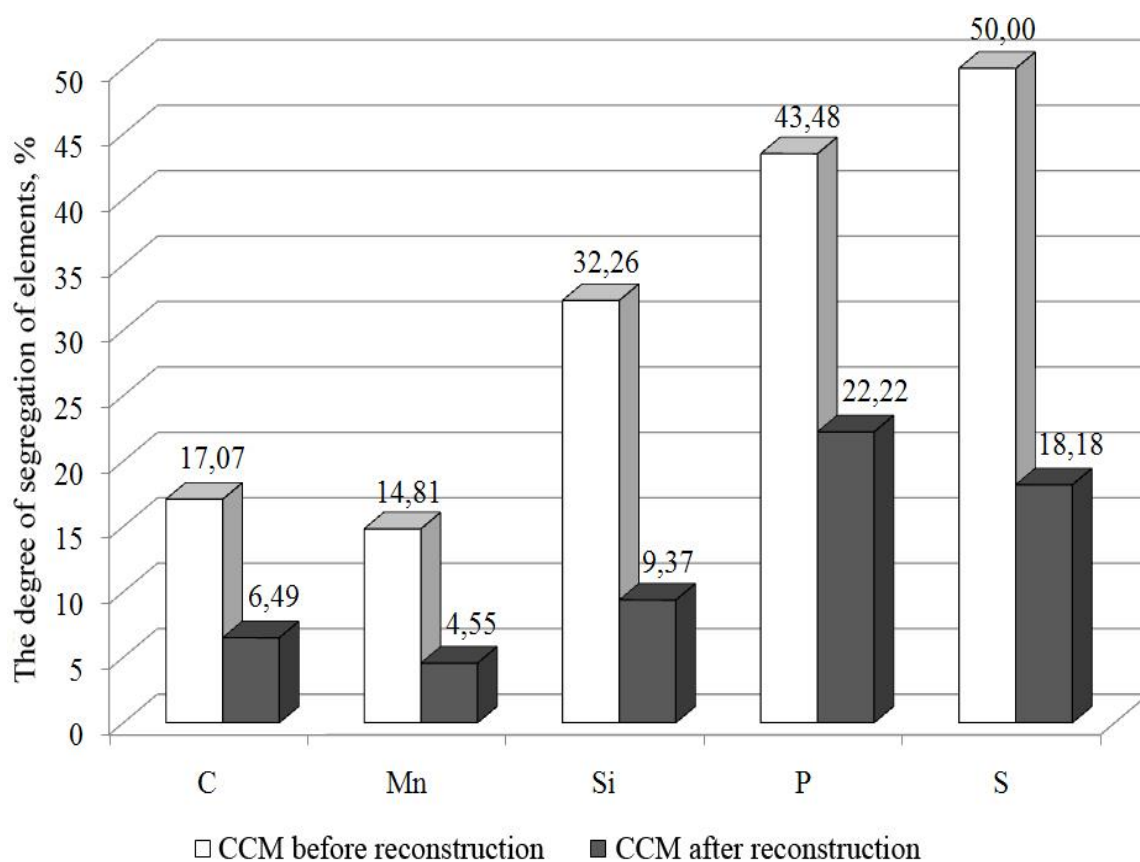


Fig. 3. Degree of segregation elements by loft of cast billets.

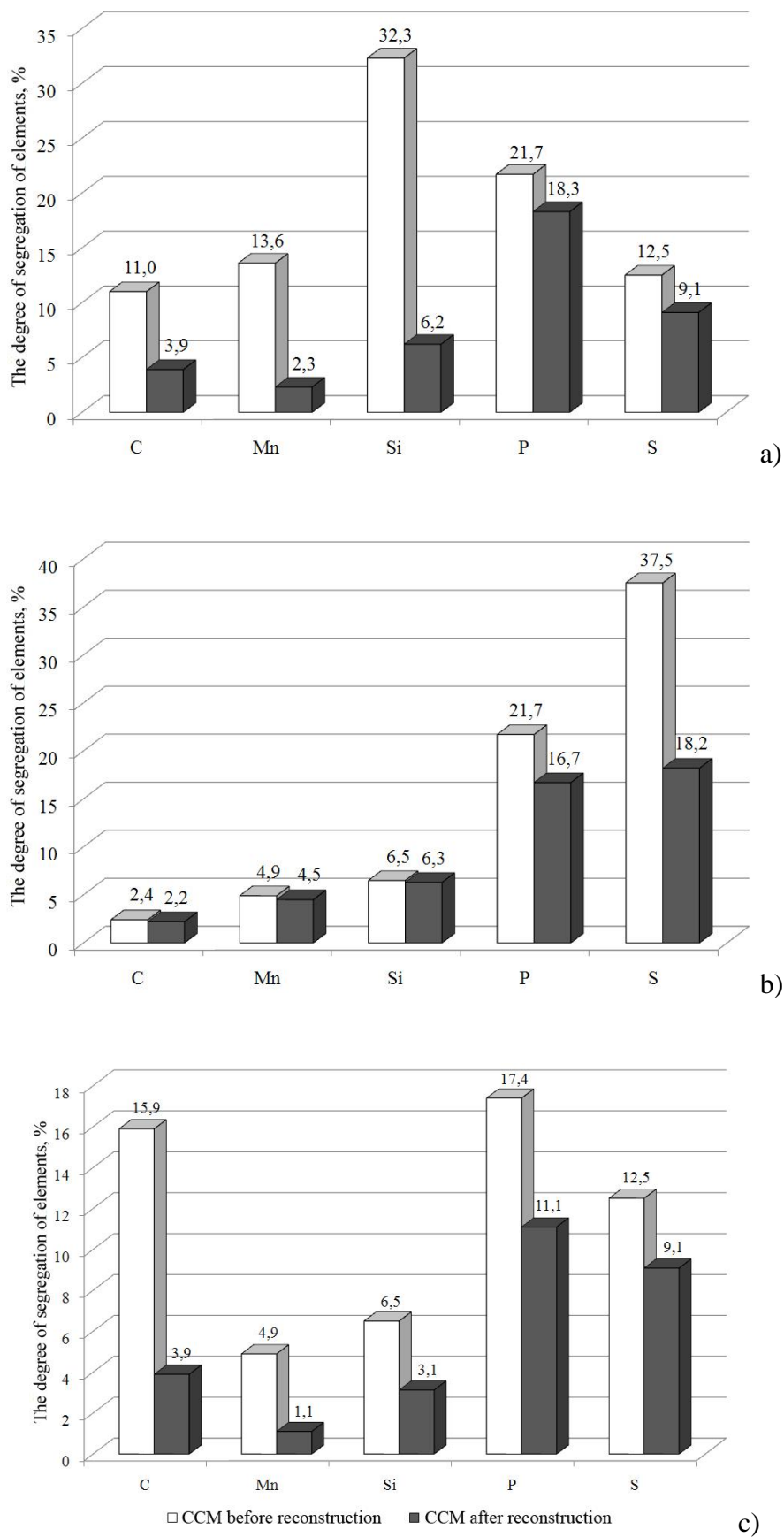


Fig. 4. Degree of segregation elements in the zones of cast billets: a – peripheral b – medium, c – the central.

Further assessment of the effectiveness of the use of external dynamic effects on the solidifying ingot casted performed when calculating the degree of segregation in some areas of the ingot by the expression [3]:

$$K_i = \frac{C_i - C_{ladle}}{C_{ladle}} \cdot 100\%,$$

where C_i – concentration of element i in the sample, %.

In this cross-section of the bloom conditionally divided into three zones – the central (Fig. 2, point 1-7), medium (Fig. 2, 9-16 points) and peripheral (Fig. 2, points 1-8). Calculation results are presented in Fig. 4.

Analysis of the results showed that when using a system of electromagnetic stirring in the peripheral zone of a decrease in the degree of segregation on all elements, with respect to carbon and phosphorus occurs predominantly zero segregation, Sulphur – positive, and of manganese and silicon – negative. In the middle and central zones and a decrease in the degree of segregation of elements, with respect to carbon, phosphorus and sulfur segregation is observed mainly positive, and of manganese and silicon – negative.

References

- [1]. V.A.Lutsenko, P.V. Borovik, N.N. Zablodsky, S.V. Kuberskiy. Simulation of transient hot-rolling process of continuously cast slabs subject of segregation. Proc. scientific. works. Production technology and data processing of materials in mechanical engineering, Lugansk, 2010. pp. 10-17.
- [2]. A.N. Smirnov, S.V.Kuberskiy, E.V. Stepan. Continuous casting: Tutorial. Donetsk: Donetsk National Technical University, 2011. 482 p.
- [3]. V.A. Kudrin. Theory and technology of steel. Moscow: Mir, AST, 2003. 552 p.

SURFACE ALLOYS SYNTHESIZED BY HIGH-INTENSITY PULSED ELECTRON BEAM TREATMENT OF FILM–SUBSTRATE SYSTEMS: STRUCTURE AND PROPERTIES

**Yu.F. Ivanov^{1,2}, E.A. Petrikova¹, A.D. Teresov¹,
O.V. Krysina¹, A.A. Klopotov³**

¹Institute of High Current Electronics SB RAS (IHCE SB RAS), Tomsk, Russia.

²National Research Tomsk Polytechnic University (TPU), Tomsk, Russia.

³Tomsk State University of Architecture and Building (TSUAB), Tomsk,
Russia.

Abstract

Nanostructured multiphase light surface alloys of Al–Ti–Cu systems were synthesized by high-intensity pulsed electron beam melting of film – substrate systems. Irradiation modes allowing a many-fold increase in the strength and tribological characteristics of the initial material were determined.

Keywords: film – substrate system, electron beam, surface alloys, phase composition, structure, properties.

Introduction

Surface irradiation of metals and alloys by high-intensity pulsed electron beams, as rule, results in nonequilibrium structural phase states with a nanostructured component. The physical basis for the process consists in superhigh-rate (up to 10^9 degree/s) heating of a surface layer to supercritical temperatures (melting, evaporation) and formation of limiting temperature gradients (10^7 – 10^8 degree/m) which provide cooling of the surface layer through heat removal into the material bulk with a rate of 10^4 – 10^6 degree/s [1]. The objective of the work was to clarify the physical mechanisms by which surface alloys are synthesized in a film – substrate system irradiated by a submillisecond high-intensity pulsed electron beam.

Material and research technique

In the study, Ti–Cu films of thickness 0.5 and 1 μm were synthesized on commercially pure A7 aluminum substrates by the plasma-assisted vacuum arc method through evaporation of sintered Ti–12%Cu cathodes. For the coating synthesis, a DI100 arc evaporator with enhanced cooling of the working cathode was used ensuring a decrease in droplet fraction in the coating and in microparticle size. Immediately before deposition, the specimens were exposed to argon ion bombardment for surface layer cleaning from adsorbed gases and dielectric inclusions. The parameters of the cleaning were chosen so that the specimen surface did not experience substantial heating and etching: the ion current density to the substrate was no more than 1.5 mA/cm^2 and the temperature in ion bombardment was no greater than $\sim 348 \text{ K}$. The deposition modes were optimized so that the coating growth rate was high and the maximum microparticle size (diameter) in the plasma flow was no greater than the coating thickness. So the Ti–Cu films were synthesized at an argon pressure of 0.2 Pa, arc discharge current of 60 A, and coating growth rate of $1.5 \mu\text{m/h}$. During the deposition, the specimens were at floating potential (-15 V) and their temperature was no greater than 393 K .

The film–substrate system was melted by a submillisecond high-intensity pulsed electron beam on the SOLO setup [2]. The electron beam parameters were the following: electron energy $eU = 18 \text{ keV}$, energy density $E_S = 10\text{--}30 \text{ Jh/cm}^2$, pulse duration $\tau = 20, 50, 100, \text{ and } 200 \mu\text{s}$, number of pulses $N = 3\text{--}30$, and pulse repetition frequency 0.3 Hz .

The phase composition of the surface alloys was examined by X-ray diffraction methods (irradiation surface, XRD 6000 diffractometer). The irradiation surface structure was analyzed by scanning electron microscopy (Philips SEM-515 microscope). The elemental composition of the surface layer was determined by X-ray microdiffraction analysis with an EDAX ECON IV microanalyzer, which is an attachment of the Philips SEM-515 scanning

electron microscope.

The surface layer hardness of the film – substrate system at different stages of electron-ion plasma exposure was determined at normal indenter loads of 100, 200, and 500 mN (PMT-3 microhardness tester) and at an indenter load of 5–300 mN (NHT-S-AX-000X Nano Hardness Tester). The friction coefficient and wear rate of the surface layer were measured with a pin-on-disk tribometer (CSEM, Switzerland) at room temperature and humidity. The counter body was a VK8 alloy ball of diameter 3 mm; the track diameter was 4–6 mm, the rotation rate was 2.5 cm/s; the load was 1–5 N; the distance was 50–100 m, and the number of revolutions was 3000–8000. The wear volume of the surface layer was determined after laser profilometry of the formed track with a MicroMeasure 3D Station profilometer (Stil, France). The wear rate was calculated by the formula

$$V = \frac{2 * \pi * R * A}{F * L} \text{ (mm}^3\text{/N}\cdot\text{m)},$$

where R is the track radius (mm), A is the wear groove cross-sectional area (mm²), F is the applied load (N), L is the distance traveled by the ball (m).

Results and discussion

Analysis of the available data on phase transformations in the Al–Ti–Cu system revealed the following main mechanisms. The state diagram of the Cu–Ti system revealed the following main mechanisms. The state diagram of the Cu–Ti system is complex and still under discussion. We take the state diagram from [3]. In the Cu–Ti system (Fig. 1), there are six compounds, of which two are melted congruently: γ -CuTi₂ (prototype MoSi₂, Pearson symbol *tI6*, space group *I4/mmm*) at a temperature of 1010 °C and δ -CuTi (CuTi, *tP4*, *P4nmm*) at a temperature of 984 °C. The other four compounds are β -Cu₄Ti (ZrAu₄, *oP20*, *Rppa*), α -Cu₄Ti (MoNi₄, *tI10*, *I4/t*), λ -Cu₂Ti (VAu₂, *oC12*, *Att2*), Θ -Cu₃Ti₂ (Cu₃Ti₂, *tP10*, *P4/mmn*), and ϵ -Cu₄Ti₃ (Cu₄Ti₃, *tI4*, *I4/ttt*) which are formed by peritectic reactions [3]. The λ and Θ compounds exist in narrow temperature ranges and decompose by eutectoid reactions. The ζ , ϵ , δ , and γ compounds have

narrow ranges of composition homogeneity. Moreover, some works revealed the existence of Cu_7Ti_3 which is melted congruently at 905 °C and decomposed into Cu_7Ti_2 and Cu_3Ti_2 by eutectoid reaction at 865 °C.

Aluminum with copper (Al–Cu system) form a diagram of the eutectic type on the side of aluminum (Fig. 1). In the Al–Cu system, 15 phases are found. Two phases of Cu and Al are solid solutions based on Cu and Al. Six phases: a β - phase (Cu_3Al -based solid solution), χ -, γ_1 -, ε_1 -, and η_1 -CuAl (Pearson symbol $oP16$, space group $Pban$) and θ -CuAl₂ (CuAl_2 , $tI12$, $I4/tst$) are formed with participation of liquid phase. The others are γ_2 -Cu₉Al₄ ($cP52$, $P\bar{4}3m$), α_2 (prototype Al_3Ti , $tI12$, $I4/mmm$), ε_2 -Cu_{1+x}Al (AsNi, $hP4$, $P6_3/mmc$), δ_1 -Cu_{100-x}Al_x ($38.1 \leq x \leq 40.7$) ($R3m$), ζ_1 ($hP4$, $P6_3/mmm$), ζ_2 -Cu_{11.5}Al₉ ($oI24-3.5$, $Imm2$), and η_2 -Al₁₀Cu₁₀ ($mC20$, $C2/m$) which are formed through solid state transformations [3].

Under thermodynamic equilibrium conditions, the Al–Ti system reveals a series of intermetallic compounds (Fig. 1): Ti_3Al (prototype Ni_3Sn , $hP8$, $P6_3/mmc$), TiAl (AuCu , $tP2$, $P4/mmm$), TiAl_2 (HfGa_2 , $tI24$, $I4_1/amd$), TiAl_3 (TiAl_3 , $tI8$, $P4/mmm$), and $\text{Ti}_9\text{Al}_{23}$ with a tetragonal structure [3].

The triple Al–Cu–Ti system features a series of peculiarities (Fig. 1). First, in this system, all alloy-forming elements are metals greatly differing in electronic structure (Table 1). The atomic sizes of two elements (Al and Ti) are close and that of the third element (Cu) is much smaller (Table 1).

Table 1. Electronic and crystal structure of alloy-forming elements in Al–Ti–Cu [3].

Metal	Electronic structure	R, nm	Pearson symbol	Space group	Structure type in <i>Strukturbericht</i>
Al	[Ne]3s ² 3p ¹	0.143	<u>cF4</u>	Fm3m	<u>A1</u>
Ti	[Ar] 3d ² 4s ²	0.1462	<u>hP2</u>	<u>P6₃/mmc</u>	<u>A3</u>
Cu	[Ar] 3d ¹⁰ 4s ¹	0.128	<u>cF4</u>	Fm3m	<u>A1</u>

Second, the homogeneity ranges of phases adjacent to the sides of the isothermal triangle at a temperature of 800 °C are small, whereas the homogeneity ranges of triple compounds inside the phase diagram are large (Fig. 1).

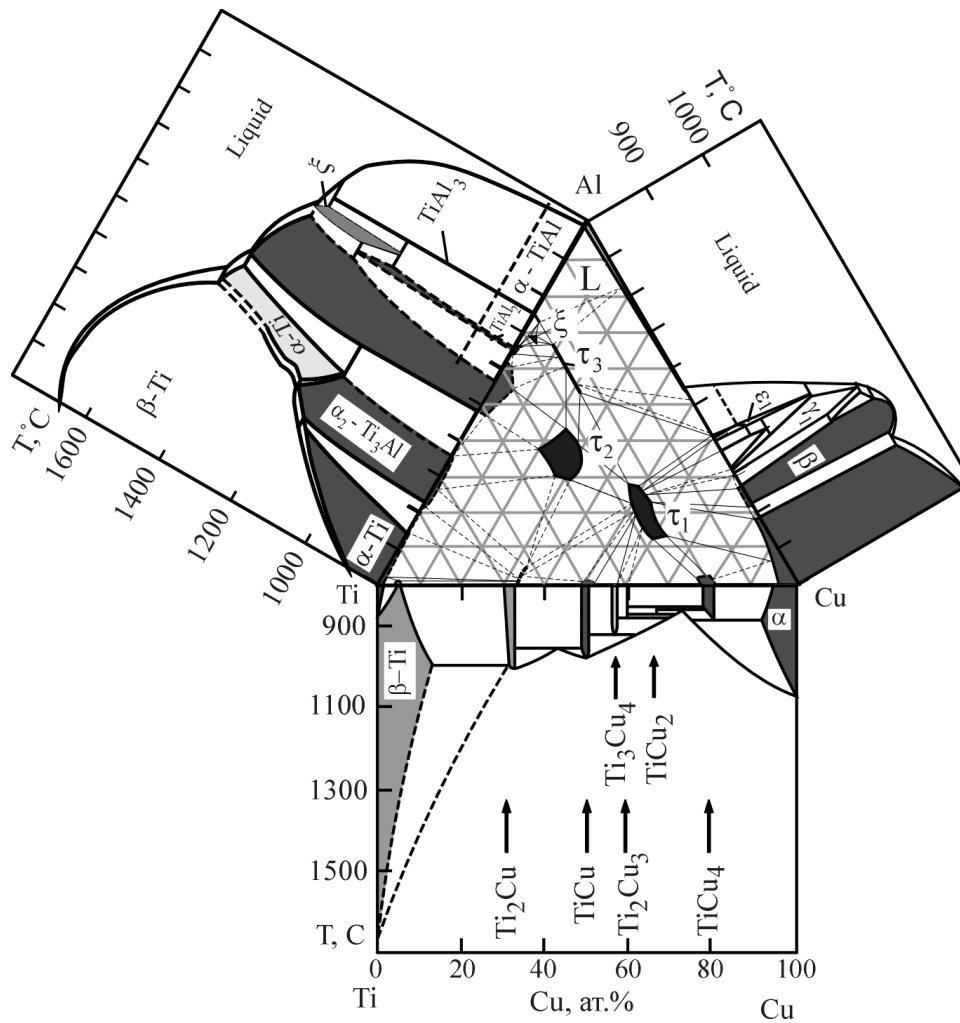


Fig. 1. Binary diagrams of Al–Cu, Cu–Ti, and Al–Ti [3] and isothermal cross-section of Al–Cu–Ti at 800 °C [4, 6]. Single-phase regions are in grey and dark colors.

Third, the triple compounds in the internal regions of the phase diagram possess close-packed structures with a wide spectrum of syngony: cubic, tetragonal, and hexagonal (Table 2).

Table 2. Structural characteristics of phases formed in Al–Ti–Cu.

Phase	Composition	Pearson symbol	Space group	Structure type	Prototype	Source
τ_1	TiCu ₂ Al	<i>cF16</i>	<i>Fm</i> $\bar{3}$ <i>m</i>	L2 ₁	MnCu ₂ Al	[4]
τ_2	TiCuAl	<i>hP12</i>	<i>P6</i> ₃ / <i>mmc</i>	C14	MgZn ₂	[5]
τ_3	Ti ₂ CuAl ₅	<i>cP4</i>	<i>Pm</i> $\bar{3}$ <i>m</i>	L1 ₂	Cu ₃ Au	[5]
τ_4	Ti ₂₅ Cu ₄ Al ₇₁	<i>tI16</i>	<i>I4/mmm</i>	<u>D0</u> ₂₃	ZrAl ₃	[4]
ξ	not determined				Ti ₂ Al ₅	[4]

Thus, in the Al–Cu–Ti system under thermodynamically equilibrium conditions, a great many double and triple phases are formed. The high-speed thermal treatment considerably constrains the phase formation due to high rates of heat removal into the integrally cold substrate volume.

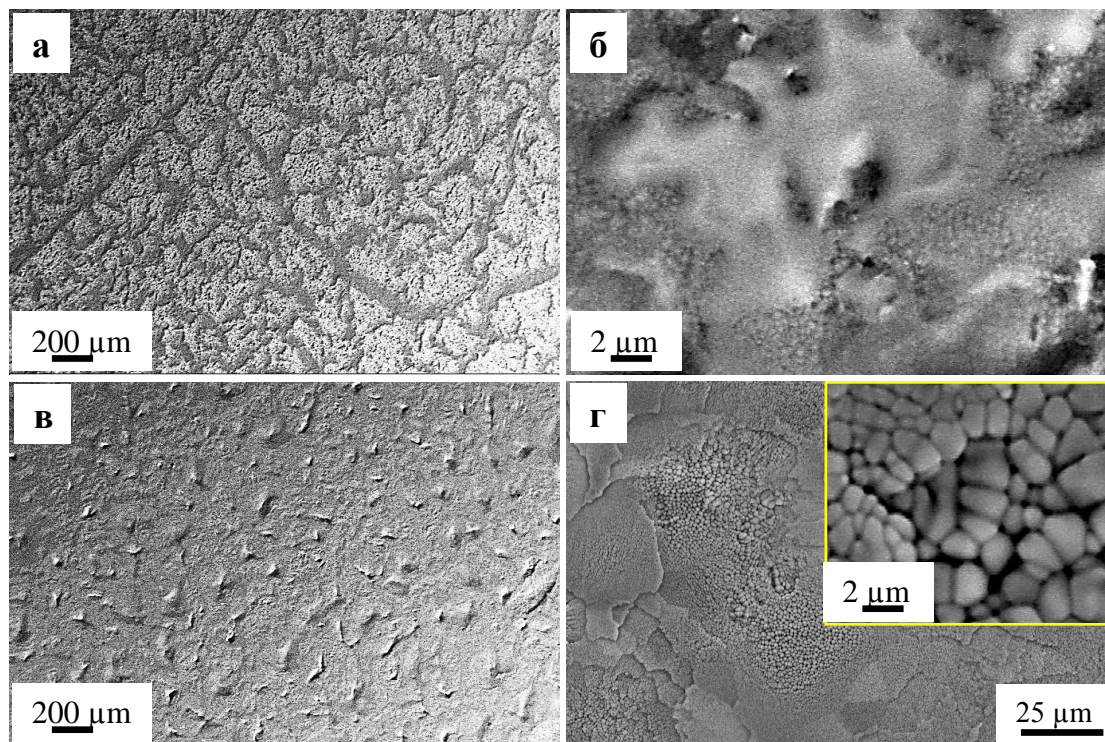


Fig. 2. Irradiation surface structure of the TiCu film – A7 substrate system for 15 J/cm², 50 μs, 3 pulses (a, b) and 15 J/cm², 20 μs, 20 pulses (c, d). Scanning electron microscopy.

The generalization parameter characterizing the mode of pulsed electron beam irradiation and level of alloy formation is taken to be the characteristic $W_s = (E_s * N / \tau)$ which accounts for both the electron beam power density and the background heating of a specimen in multipulse treatment. Experiments show that the TiCu film – Al substrate system is not melted at $W_s \leq \sim 0.5 * 10^6$ (W/cm²) *pulse. In this case, the coating is preserved being broken into fragments by multiple cracking. The material that separates the coating fragments is aluminum, as evidenced by X-ray microdiffraction analysis. In the range $(1-6) * 10^6$ (W/cm²) *pulse, an island structure is formed with coating islands separated by cellular crystallization sites of the film – substrate system (Fig. 2 a, b). At $W_s = 15 * 10^6$ (W/cm²) *pulse, the TiCu film – A7 substrate system

experiences stable melting (Fig. 2 c, d). On the surface, there arises a polycrystalline structure in which the grain size ranges from 5 to 40 μm (Fig. 2 d). In the grain volume, a cellular crystallization structure with a cell size of 0.4–2.0 μm is found (Fig. 2 d, inset).

X-ray diffraction analysis reveals the formation of surface alloys of composition Al–Ti–Cu in which the element concentration depends largely on irradiation parameters. In analyzing the data presented in Fig. 3, it can be pointed out that the concentration of alloying elements in the Al surface layer can vary over a wide range (from 52 to 2.5 wt%) depending on the electron beam energy. Thus, electron beam irradiation of the film – substrate system makes it possible to widely vary the elemental and phase compositions of the material surface layer.

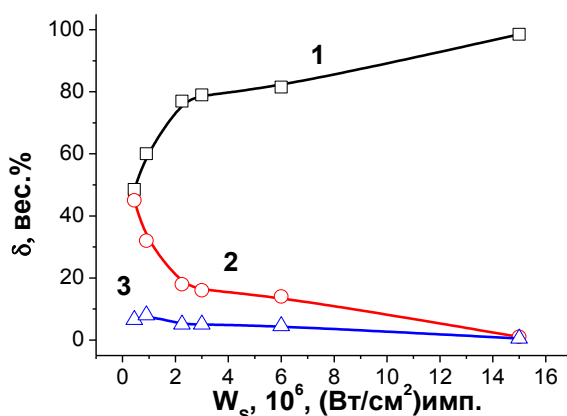
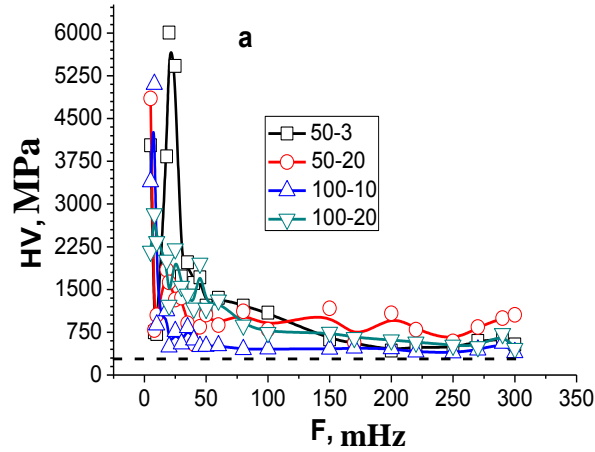
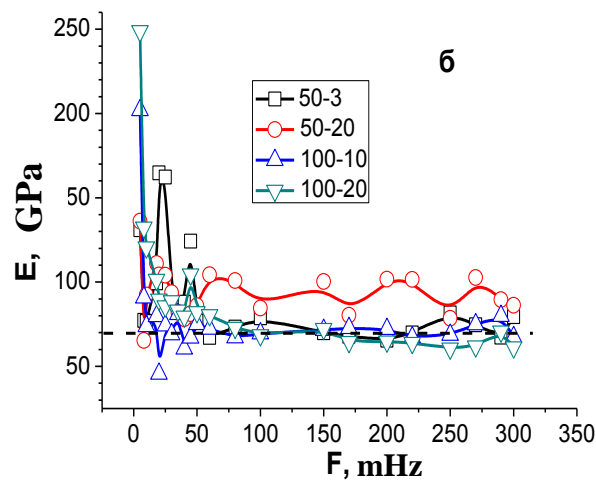


Fig. 3. Element concentration in the surface layer of the TiCu film – A7 substrate system vs. the parameters of pulsed electron beam irradiation; 1 – aluminum, 2 – titanium, 3 – copper.

The surface layer phase composition in the TiCu film – A7 substrate system was analyzed by X-ray diffraction methods in the Bragg–Brentano geometry. The analysis shows that in a surface layer $\sim 10 \mu\text{m}$ thick, there arises a multiphase structure whose qualitative and quantitative composition depends on the mode of electron beam treatment. It is found that the maximum total volume percentage of second phases (Al_3Ti , Ti_3Al , Ti_3Cu) is $\sim 40 \%$ and is attained on irradiation at 15 J/cm^2 , $100 \mu\text{s}$, 20 pulses, and 0.3 Hz, i.e., in the surface alloy of composition 79Al–16Ti–5Cu, wt% (Fig. 3).



a)



b)

Fig. 4. Hardness (a) and Young's modulus (b) vs. the indenter load F for surface alloys formed on pulsed electron beam irradiation of the TiCu film – A7 substrate system at an electron energy density of 15 J/cm^2 and pulse repetition frequency of 0.3 Hz ; the pulse duration and number of pulses are indicated in the diagrams.

The modified phase and elemental compositions of the defect substructure in the Al surface layer are bound to influence the physicochemical and tribological properties of the material. The properties of the Al surface alloy were examined by measuring the hardness, Young's modulus, and wear resistance of the coating – substrate system before and after electron beam irradiation. The results for the hardness of the surface layer and Young's modulus are presented in Fig. 4 a and b, respectively. It is clearly seen that the maximum hardness (5–6 GPa) and the maximum Young's modulus (200–250

GPa) are reached on the irradiation surface. Considering that the Young's modulus of Al_2O_3 varies in the range from 200 to 400 GPa and that of aluminum is no greater than 70 GPa, it can be said that at the stage of cooling, a thin oxide film was formed on the specimen surface. At an indenter load of 20–70 mN, a sublayer with a hardness of ~2 GPa and Young's modulus of ~110 GPa was revealed; these hardness and Young's modulus are respectively ~7 and ~1.8 times higher than those of the initial material. As the indenter load is further increased, the hardness and Young's modulus decrease and approach the characteristics of the initial material. It should, however, be noted that electron beam irradiation of the film–substrate system at 15 J/cm^2 , 0.3 Hz, 50 μs , and 20 pulses makes it possible to form an extended layer whose hardness is more than 3 times higher and Young modulus is 1.5 times higher than those of the initial aluminum. The increase in the strength properties of the surface layer involves an about 1.2-fold increase in wear resistance, which is detected in the film – substrate system exposed to electron beam irradiation at 15 J/cm^2 , 0.3 Hz, 100 μs , and 20 pulses.

Conclusion

Thus, light Al-based surface alloys with high hardness, Young's modulus, and wear resistance were synthesized by a submillisecond high-intensity pulsed electron beam. Structural examinations shows that the increase in the physicomechanical characteristics of aluminum is governed by the formation of a submicro-nanocrystalline multiphase state on melting and high-rate crystallization of the TiCu film – Al substrate system.

The work was partially supported by Russian Science Foundation, projects № 14-19-00240.

References

[1]. V. Rothstein, Yu.F. Ivanov, A. Markov. Surface treatment of materials with low-energy, high-current electron beams. Charter 6 in Book “Materials surface processing by directed energy techniques”. pp. 205–240.

- [2]. N.N. Koval, Yu.F. Ivanov. Surface nanostructuring of metal ceramic and ceramic materials by pulsed electron beam treatment. Russian physics journal, № 5. pp. 60–76 (2008).
- [3]. State diagram of double metal systems. Ed. by N.P. Lyakishev, Mashinostroenie, Moscow. V. 1–3. 1996–2000.
- [4]. A. Raman, K. Schubert. On the Crystal Structure of some Alloy Phases Related to TiAl₃ III. Investigations in Several T-Ni-Al and T-Cu-Al Alloy Systems. Z. Metallkd. 1965. V. 56. pp. 99–104.
- [5]. P.I. Krypyakevich, V.Y. Markiv, A.A. Troyan. Crystal Structures of the Ternary Compounds TiCuAl and TiNiAl. Dop. Akad. Nauk Ukr. RSR, A, Fiz.-Mat. Tekh. Nauki. 1964. № 7. pp. 922–924.
- [6]. J.L. Murray. The Aluminum-Copper System. Int. Met. Rev. 1985. V. 30. pp. 211-233.

**EVOLUTION OF STRUCTURAL CHANGES IN ZONES OF LOCAL
CATASTROPHIC DESTRUCTION OF PIPELINE SYSTEMS OF
PROCESSING OF OIL PRODUCTS**

**A.A. Evstigneev, A.A. Debelyak, V.I. Muravyev,
S.Z. Lonchakov, V.S. Pitcyk**

Komsomolsk-on-Amur State Technical University.

OOO « RN-Komsomolsk Refinery ».

OAO « Amurlitmash», Russia, Komsomolsk-on-Amur.

Abstract

Found that the most dangerous type of corrosion is pitting TSPN. Macrostructure studies and electronic fractography established presence on the inner surface of solid samples dense black deposits. Chemical analysis showed that deposits are the products of sulfide corrosion also revealed elevated mobile

hydrogen in the metal. Based on the volume and thickness measurement of the results of measurements of the coercive force, the mechanism of local catastrophic corrosion of TSPN. A method of non-destructive quality control of welding and subsequent heat TSPN, which will prevent accidents.

Keywords: corrosion, micro-and macro-structure, cavitation, thickness, coercive force, sulfide deposits

Introduction

Natural cataclysms (earthquakes, a tsunami) as well as technogenic catastrophes demand continuous improvement existing and development of the new constructional materials providing high reliability of products and in particular of the pipeline systems of processing of oil products (PSPOP) and their transportation.

Now to 40% of accidents on pipeline systems it is connected with corrosion destructions. In the general production cycle of processing of oil products cases of corrosion destruction of adapters of pipeline systems most often meet.

From all variety of local types of destruction of materials it is possible to draw a conclusion that in aggressive liquids of damage result especially quickly from double influence both a cavitation erosion, and corrosion. The erosion destroys a surface of metal and promotes removal from it a protective oxide film, creating thereby ideal conditions for corrosion. So far there is no consensus about mechanisms of local destruction of pipeline systems in the course of processing of oil products, and from here and a consensus on elimination of the reasons of this phenomenon. Therefore materials research justification and research of evolution of structural changes of local destruction and creation of uniform structure of the pipe preparations providing their reliability an actual task of the modern oil processing industry. This article is devoted to the analysis of regularities of evolution of structural changes of the local centers of destruction of the TSPN elements for the purpose of increase of their reliability and creation of high-corrosion-resistant uniform structure of pipe preparations.

At behavior of analytical estimates data from various foreign and domestic oil processing enterprises were used.

As samples cuttings from TSPN from various materials, in particular St3 were used, St20 and became brands 15X5H.

Smooth surface for metal graphic researches were made on the standard technology of consecutive grinding and polishing. For cutting of samples the desktop abrasive detachable machine of the Delta AbrasiMet brand (Germany) was used. Grinding and polishing of samples was made by means of the grinding and polishing machine of the EcoMet 250 brand (Germany) with a semi-automatic nozzle AutoMet 250 (Germany). For an exception of "blockages" used samples were filled in with epoxy or Wood's alloy in cylindrical capsules. Etching was carried out by the solution corresponding to a chemical composition of a material and its technology of processing (Table 1). The microstructure was defined on a metal graphic electronic microscope of the Micro-200 brand (Russia) in the range of increases from 100 to 1000 крат. The digitized images were processed further on the specialized Image.Pro.Plus.5.1 program.

Table 1. Chemical composition of reactants for etching smooth surface.

Material brand	Chemical composition of reactants
Steel 3	4 g of picric acid, 2 g of chloric copper, 100 ml of water (for tempered)
Steel 20	4 ml of HNO ₃ , 100мл izoamilovy alcohol (for crude)
Brand 15X5M steel	25 ml of hydrochloric acid, 50 ml. 10% of water solution of chloride anhydride

Thickness metrical was made on the portable ultrasonic feeler gage of the PANAMETRICS 26GM brand of the Olympus NDT company (USA). As the fixing device the D799 brand sensor made by the same company was used. Technical characteristics of the used sensor are given in Table 2. Thickness metrical was carried out by a method of continuous scanning.

Table 2 Technical characteristics of the sensor of the D799 brand.

Technical characteristics	Of Value
Frequency of a signal, MHz	5,0
Cable type	Tight
Connection of a cable with PEP, hail	90
Diameter of a contact surface	11
Measurement range (for steel), mm	1 ... 500
Range of temperatures, hail	-20 ... +150

Chemical composition of metal of samples investigated the spectral analysis on optical issue the analyzer of the Q4 TASMAN brand of BRUKER firm (Germany) for definition of alloying and impurity elements. The chemical composition of sulfides coverings was defined on a scanning electronic microscope of the Hitachi S3400N brand (Japan). On the X-ray fluorescent power dispersive analyzer of the NEXT CJ brand of the RIGAKU company (Japan) the complex analysis of a chemical composition of samples was carried out.

Measurements of coercive force were made digital semi-automatic coercimeter the KRM-Ts brands (Russia) who allows to predict mechanical and some physical properties of ferromagnetic materials, strength and plastic properties of details and designs [1]. Measurement of coercive force is based on magnetization of a ferromagnetic alloy therefore it gains residual magnetization. Then the degaussing due to change of the direction of polarity before achievement of residual magnetization of zero value is made. The difference between intensity of a magnetic field at magnetization and a degaussing gives numerical value of coercive force, i.e. at measurement of coercive force a tested sample at first magnetize practically before saturation in the magnetizing device. Then through a sample pass the direct current which magnetic field degausses a sample. Current increases until magnetization of a sample won't decrease to zero that is registered different indicators.

Results of researches and their discussion

In the chemical industry as showed the analysis of the reasons of failure of the equipment at the enterprises of one of the foreign companies, local types of corrosion make the main contribution to destruction of materials (Fig. 1) [2]. In Fig. 2 the histogram of influence of various factors on development of processes of corrosion received on the example of RVSK-1000 which is operating in the Southern federal district [3] is submitted.

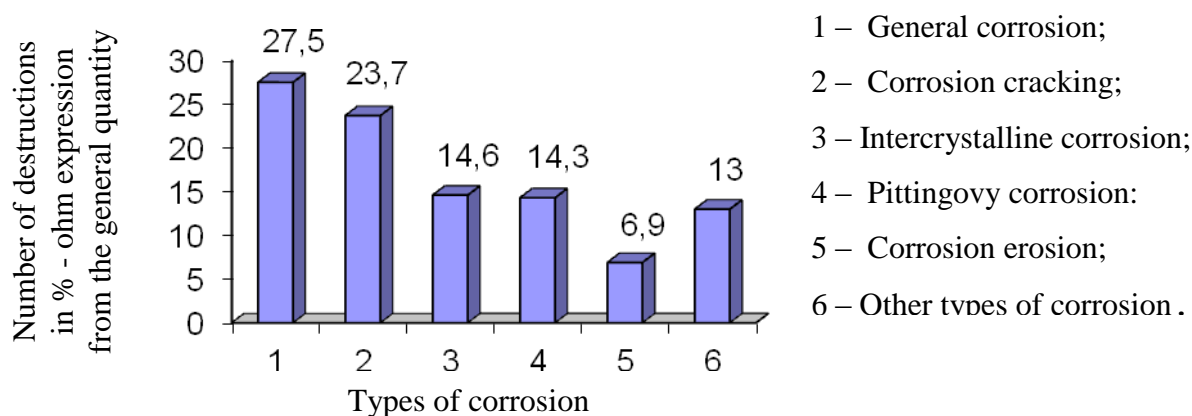


Fig. 1 Histogram of results of inspection of cases of failure of the equipment processing's of oil products on the example of one of the foreign company (685 cases).

Apparently from these Fig. 1 and 2 steel is exposed to all types of corrosion, but the general corrosion and pitting is more presented. Pitting (dot corrosion) – the most dangerous person of corrosion. Pitting development in the environment of oil products possibly only in the presence of electrolyte and mechanical impurity and depends on a chemical composition of fuel. From the provided analysis of defects and destructions it is visible that one of the major tasks is establishment of factors of corrosion on aggression degree to metal in the course of their operation that will allow to define the main directions of a solution of the problem of reduction of losses of metal from corrosion and in particular to avoid technogenic catastrophes.

The TSPN ELOU-AVT-2 operational resource analysis,-3 showed that pipeline systems in the same conditions maintain a 40-year resource, but separate elements reach limit admissible sizes less than in 5 years, and in certain

cases and several months. It as a rule, zones of inserts, radiuses of transitions, welded seams and sites [4, 5, 6] adjoining to them.

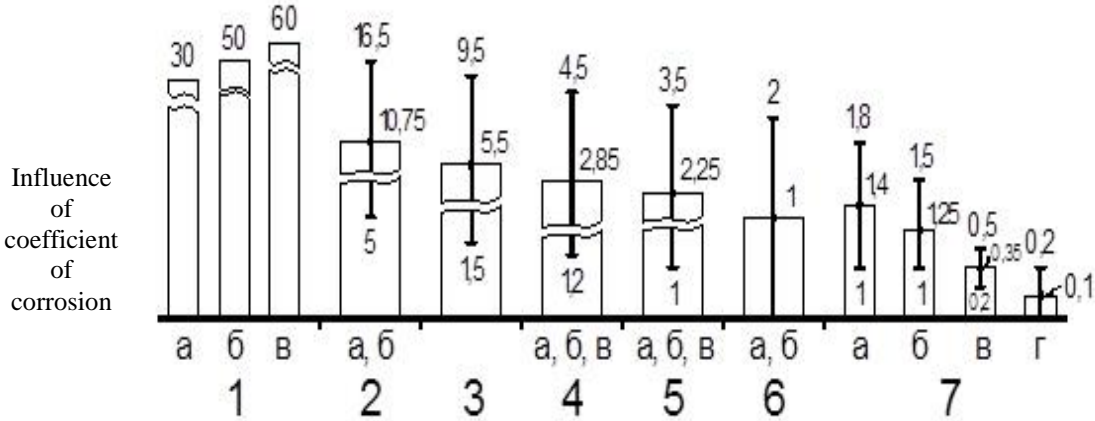


Fig. 2. Factors influencing development of corrosion processes in stationary tanks.

- 1 – Operational: and – tanks of task force; – tanks of the mixed form of operation; in – tanks of long storage;
- 2 – Corrodibility of fuel: and – a chemical composition of fuel; – presence of water and its chemical composition;
- 3 – Features of a design;
- 4 – Way of installation of the tank: and – buried and semi-buried; – land; in – buried and semi-buried a kazematny tic;
- 5 – Quality of a material of a design: and – structure and chemical properties of an alloy; – hire manufacturing techniques; in – quality of welding materials;
- 6 – Production: and – cavitation; – wandering points;
- 7 – Natural and – influence of ground waters; – atmosphere influence; in – soil influence; climate influence (humidity, temperature, pressure).

Corrosion destruction is characterized by locality on entrance and output branch pipes of passing of a head by-pass product and branch of an oven coil. Local uneven destruction is observed and in the sites struck with corrosion. Uneven corrosion destruction in the form of the spherical holes forming chains, extends in the direction of movement of working liquid. Spherical holes are various by the sizes and depth and can be both superficial, and through, the last are germs of formation of cracks (Table 3).

The general zone of the increased corrosion wear is uneven and on branch pipe circles, i.e. preservation of initial thickness of a branch pipe on the one hand and thinnings on the other hand, up to wall destruction.

Table 3. Corrosion destruction of an output branch pipe in various zones.

Section No.	Parameters of corrosion destruction	
	Diameter of a spherical hole (Δ), mm	Thickness of a wall (h), mm
1	0,65-17,6 / 5,2	3,6-6,4 / 4,15
2	1,6-12,8 / 5,9	2,4-6,4 / 4,45
3	1,6-15,2 / 6,1	1,2-4,8 / 3,0
4	1,2-15,2 / 6,3	1,45-4,0 / 2,5

Note: in numerator the interval of dispersion of value, in a denominator – arithmetic-mean is specified.

Results of an ultrasonic thickness metriya a method of continuous scanning (Fig. 3) on three sections of branch showed that in section I thickness remains almost identical in all points (at the level of 10 mm), and in places of turbulization of a stream on bend radius (sections II and III) intensive local corrosion wear. If for section I (out of a zone of turbulization of a stream) the settlement speed of corrosion for the 7-flight period of operation made about 0,3 mm/g, in a turbulization zone (sections II and III) – 1,7 mm/g. Volume nature of distribution of depth of defeats in pipe development, testifies to localization of defeats in a certain zone (Fig. 3, b).

As from these Fig. 3 it is visible that on an internal surface of studied samples there are black deposits, characteristic for metal sulfide. Thickness of a film is insignificant, it is well linked to the main metal and has no friability.

Proceeding from theoretical bases of corrosion [7] structural degradation in local zones can be referred to an active stage of corrosion destruction, and in a finishing catastrophic zone of corrosion destruction. Apparently from data (Fig. 4, a) the dark shade of a microstructure is result of etching of dot objects with higher chemical potential, tension representing concentrators nano - and micro large-scale level typical for diffusive process. Atomic oxygen and hydrogen, sulfur and ions of various low-molecular connections can be possible diffuzant. Skeletirovanny transformation of structure of a blanket allows to reveal limits of the section (Fig. 4, b). Quantitative assessment of extent of degradation of a

microstructure on density of borders of the grains, calculated in the Image. Pro. Plus program. 5.1 I allowed to establish depth of coverage of corrosion of equal 50-65 microns (Fig. 5) [4, 5, 6].

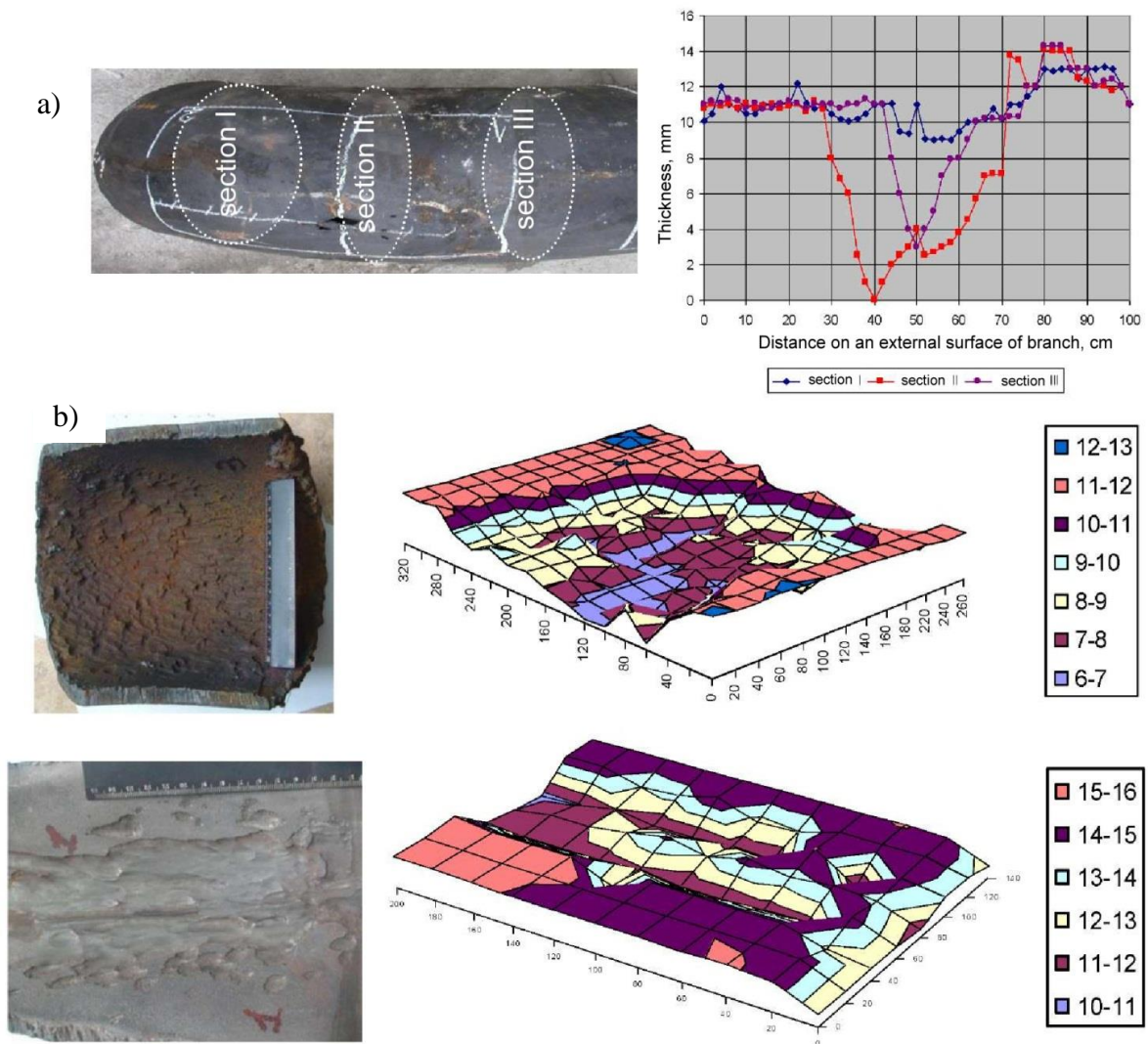


Fig. 3. Profilogramma of distribution of depth of defects: and – linear on depth and circles; – volume pipes in development.

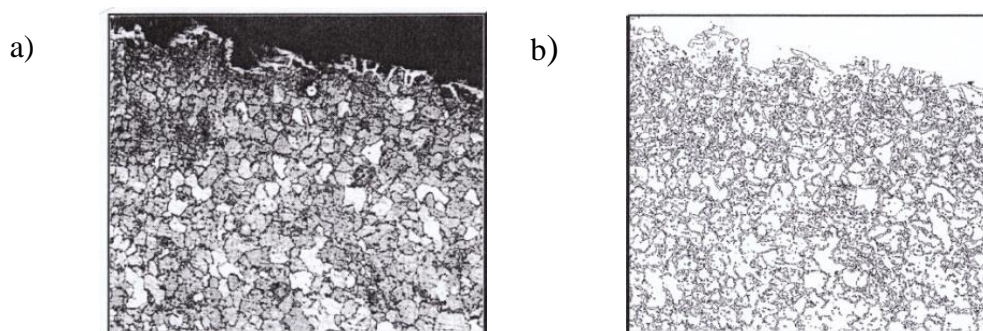


Fig. 4. Microstructure of a blanket of the pipeline from St20 and its "skeletirovanny" transformation, subject to corrosion process ($\times 400$):

a) – a microstructure, b) – its skeletirovanny transformation.

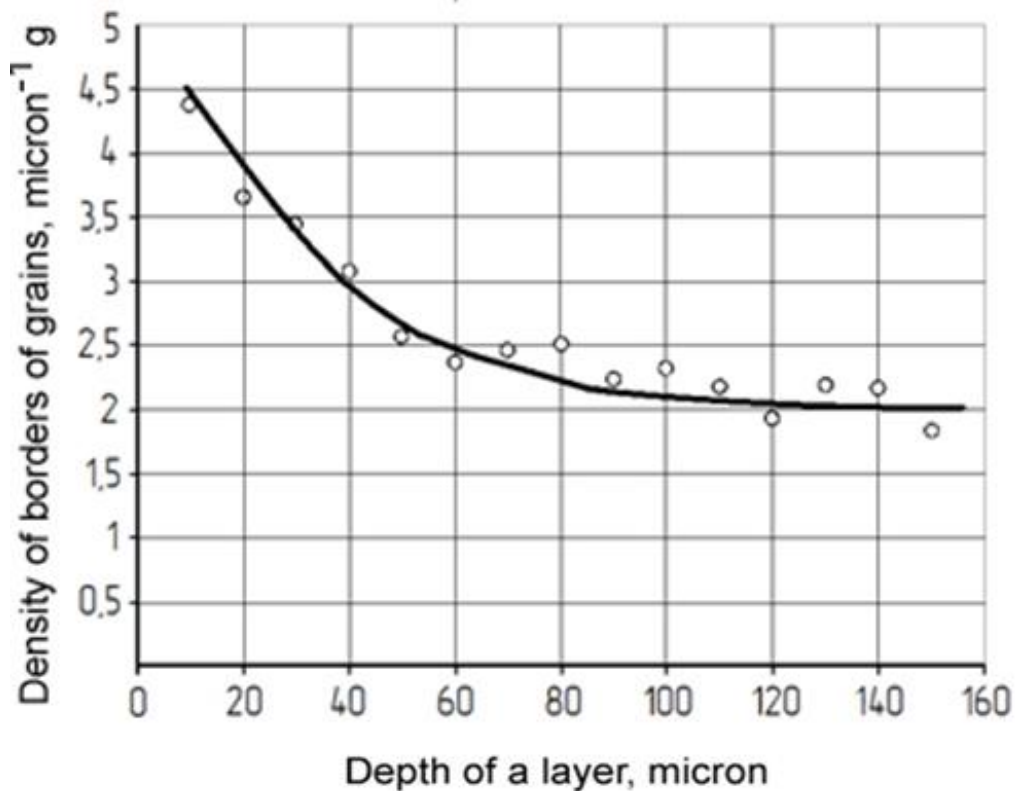


Fig. 5. Distribution of density of borders of grains on layer depth, subject to corrosion destruction.

Change of a chemical composition in a degradation zone is presented in tab. 4 on pipeline section. By results of the chemical X-ray diffraction analysis (Table 5) it is established that deposits represent products of sulphidic corrosion of metal (first of all gland), the remains of compounds of the sulfur, which most part went wrong owing to hydrolysis and oxidation by air oxygen in the course of storage of samples, coke and impurity insoluble in acids of mechanical pollution. From the considered data follows that the iron-sulphidic component is a direct product of corrosion reactions.

In damp hydrosulphuric environments conditions for a metal navodorazhivaniye are created. All became with ferritic, ferritno-perlitny, beynitny and martensitny structures can be exposed to the hydrogen embrittlement (HE). Especially actively it occurs in the presence, so-called, easily mobile (diffusive) hydrogen. Hydrogen reduces forces of a mutual attraction of atoms of iron in a crystal lattice, creates high pressures at a molyarization in micropores and microcracks that causes metal destruction.

Table 4. Change of a chemical composition in a degradation zone on pipeline section.

Steel	Alloying element	Chemical composition in % on zones		
		Internal surface coke deposits	On a surface after removal of coke deposits	Main metal
Steel 15X5M	C	-	-	0,102
	Si	0,615	0,28	0,319
	S	13,5	2,5	0,0098
	Cr	0,467	0,265	5,23
	Mo	-	-	0,445
	Mn	0,297	0,348	0,29
	Ni	0,479	0,279	0,358
	Cu	1,2	0,615	0,158
	Fe	80,7	95,7	92,69
Steel 20	C	2,32	1,19	0,26
	Si	0,71	0,35	0,25
	Cr	1,19	0,69	0,12
	Mn	0,74	0,87	0,39
	Ni	0,80	0,57	0,12
	Cu	1,87	0,92	0,22
	Fe	63,85	0,93	98,29
	S	3,84	1,233	0,033

Table 5. Results of the chemical analysis of deposits.

Indicators	Samples of an oven coil	Pipeline samples
The general sulfur in initial adjournment (% of masses)	2,19-2,39	2,5-3,9
The rest after calcinating (% of masses)	89,0	56,4
Iron (% of masses)	54,88	23,17
The rest after washing with acetone (% of masses)	-	66,4
The general sulfur in the rest washed out by acetone (% of masses)	-	5,96-5,99
Sulfide ion	be present	be present

Presence at structure of products of corrosion of sulphurous connections (Table 4, 5) testifies to participation of hydrogen sulfide in corrosion process, i.e. high-temperature hydrosulphuric corrosion. Research of the received samples of metal showed that along with signs of high-temperature hydrosulphuric corrosion, samples have the specific corrosion damages caused as by erosive impact of a stream of fuel oil on protective sulphidic films, and presence of other corrosion agents who are also breaking protective properties of sulphidic films.

It is known that under the influence of vacuum temperature of boiling of all fractions of fuel oil considerably decreases and in volume of a stream of fuel oil intensive steam formation with formation of vapor-liquid mix at which density and viscosity differ from fuel oil that conducts to increase in speed of a stream and finally to increase in corrosion wear begins. Thus, high speeds of movement of a vapor-liquid stream in zones of the constructive elements creating hydraulic conditions for development of local turbulent liquid streams and a turbulence, are caused by destruction of protective sulphidic films and cavitation and erosive damage of TSPN.

The monitoring organization as in the course of a choice and material justification for TSPN, and in use for the purpose of control of the factors making aggressive impact on metal is essential on prevention of emergencies. Measurements of values of coercive force of welded connections of control samples from St20 were made on perimeter of a seam (Fig. 6) and welded connections on technological pipelines of installation of the slowed-down coking along a pipeline axis. Both in the first and in the second case of instability it isn't revealed, values keep within standards of the admission.

Measurements of values of coercive force on a surface of pipe elements from a material 15X5M it was made on control samples and on pipe elements of technological pipelines mounted on installation of the slowed-down coking of JSC RN-Komsomolsk Refinery. The measurement direction – along a pipe axis. Apparently from these Fig. 7, 8 of instability it isn't revealed, values keeps

within standards of the admission in compliance with technical documentation on pipeline production.

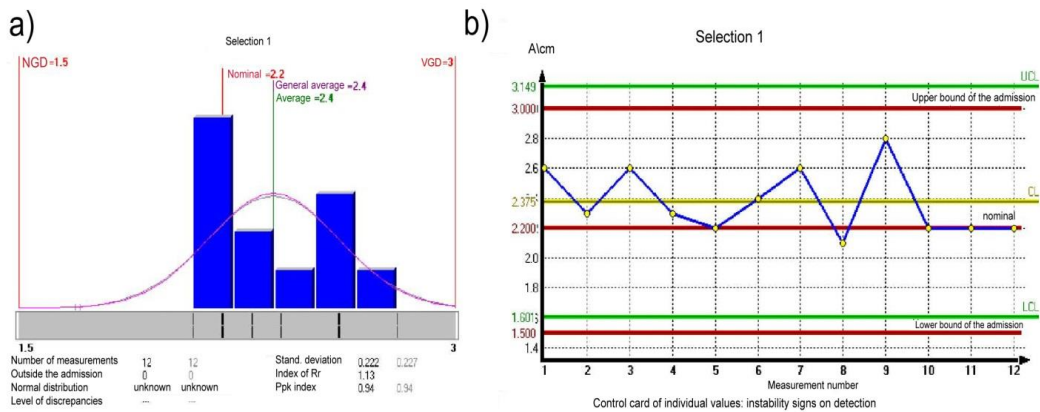


Fig. 6. The histogram (and) and the control card distributions of values of coercive force on a surface of a welded seam of samples from St20, a standard size $\varnothing 102 \times 4$, samples 1 – 4.

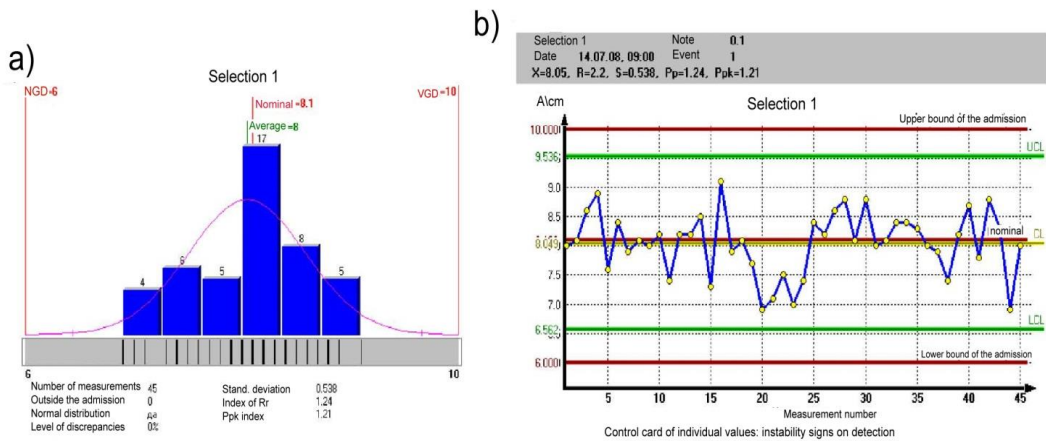


Fig. 7. The histogram (and) and the control card distributions of values of coercive force on a surface of the main metal of steel 15X5M $\varnothing 102 \times 12$.

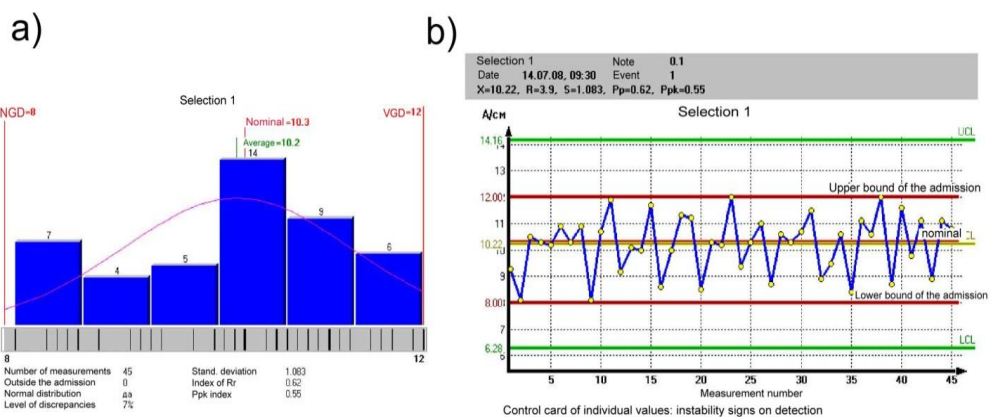


Fig. 8. Histogram (and) and control card distributions of values coercive force on a surface of the main metal of steel 15X5M $\varnothing 168 \times 102$.

Use of sensors of constant/continuous control of thickness of a wall of adapters and branch pipes of TSPN will allow to reveal zones of corrosion damage of critical size at early stages and to prevent emergencies.

Conclusions

1. From an analytical assessment of defects and destructions of TSPN follows that the most dangerous person of corrosion is pitingovy (dot corrosion). To which are more subject: zones of inserts, radiuses of transitions, welded seams and sites adjoining to them.

2. Local sites of corrosion destruction are characterized by uneven distribution along an axis of branch pipes of the extended holes with a diameter of 5-7 mm and from 0,1 to 2,0 mm in depth, forming the extended grooves. Profilogramma thickness of the wall received by a method of ultrasonic scanning from the outer side of a pipe showed volume nature of distribution of depth of defeats in development of a pipe and testify to localization of defeats in certain places of turbulization of a stream on bend radius.

3. Researches of a macrostructure and electronic fraktografiya established existence on an internal surface of a coil of dense continuous black deposits of products of the corrosion undergoing destruction by the whole conglomerates in local zones of catastrophic corrosion. Skeletirovanny transformation of a microstructure with the dark shade typical for diffusive and strengthened, a blanket allowed to estimate quantitatively extent of degradation of a microstructure on density of borders of grains and depth of coverage of corrosion of equal 50-65 microns.

4. Definition of a chemical composition by the masspektralny analysis and the x-ray elektronmikroskopichesky analysis of local micro sites of catastrophic destruction, it is established that deposits represent products of sulphidic corrosion of metal, and the content of sulfur in coke deposits makes more than 13%, in an oxidic film from 1,5 to 3,5%, besides the raised content of mobile hydrogen in metal is established.

5. The mechanism of local catastrophic corrosion destruction of TSPN Is installed. Turbulization of streams of vacuum gasoil and fuel oil, direct-flow gasoline, in zones of the constructive elements, caused by hydraulic conditions leads to cavitation erosive destruction because of low damping properties of a sulphidic film with coke deposits in the subsequent high-temperature hydrosulphuric embrittlement of TSPN metal.

6. The method of nondestructive control by a volume ultrasonic toshchino-metriya, and also a method of nondestructive quality control of welding and the subsequent heat treatment of TSPN on means of determination of coercive force which in combination with traditional control methods of mechanical properties, allow to define an intense and deformation state, the TSPN residual operational resource, and also to reveal cavitation and erosive destructions that allows to prevent emergencies Is offered.

References

- [1]. S.I. Lukyanov, A.V. Butin, A.A. Yevstigneyev, V.I. Muravyev, V.A. Kim Magnetic identification of a microstructure of material. Control and diagnostics. 2010. №10.
- [2]. Ya.M. Kolotyркиn. Metall and corrosion. M.: Metallurgy, 1985. 88 p.
- [3]. V. N. Zaychenko. New technologies of repair of steel tanks. M.: JSC Tsniiteneftkhim, 2002. 168 p.
- [4]. Ants V. I. influence of structural changes of metal of pipes on damages of pipeline systems of processing of oil products / Century. I. Muravyev, P. V. Bakhmatov, A.V. Frolov, A.A. Yevstigneyev, A.V. Butin. Chemical and oil and gas mechanical engineering. 2011. № 9. pp. 42-46.
- [5]. Ants V.I. Analiticheskaya assessment and development of methods of increase of corrosion resistance constructional staly TSPN / Century. I. Muravyev, A.A. Yevstigneyev, P. V. Bakhmatov, A.V. Butin. Scientific notes of "Komsomolsk-on-Amur state technical university". 2011. №. IV-1 (8). pp. 58-70.

[6]. V.A. Kim, V.I. Muravyev, S.I. Lukjyanov, A.V. Butin. Corrosion processes and resource of operation of technological pipelines of the ELOU-AVT-3/VA installation. Chemical and oil and gas mechanical engineering. 2012. № 11. pp. 35-38.

[7]. G.G. Uling, R.U. Revi. Corrosion and fight against it. Introduction in corrosion science and equipment: the lane with English under the editorship of A.M. Sukhotina. L. : Chemistry, 1989. 456 p.

RESEARCH OF DEFECTS CONCENTRATORS OF TENSION BY PARAMETERS OF ACOUSTIC ISSUE AT DEVELOPMENT OF DAMAGES

S.Z. Lonchakov, O.V. Bashkov, V.I. Muravyov, A.V. Frolov
FGBOU VPO "Komsomolsk-on-Amur state technical university",
Komsomolsk-on-Amur, Russia.

Introduction (relevance of a problem)

Reliability of engineering constructions and designs in big degree is defined by ability to resist to damageability at operational loadings. Existence of concentrators of tension can have catastrophic impact on durability of a metalwork.

Researches [1, 2] established possibility of forecasting of limit characteristics of a material on the example of samples from OT4 alloy by use of the analysis of akustiko-issue information at a stage of elastic deformation, namely dependence between mechanical characteristics of a material and the AE parameters is established.

Results of a theoretical and pilot study of influence of size of concentration of tension are given in the real work α on damageability of titanic alloys of OT4 and VT3-1.

Technique of carrying out researches

For an assessment of influence of concentration of tension on the AE parameters a series of experiments on samples with concentrators of tension of various radiuses on 10 samples on everyone was carried out. Samples from two titanic alloys of OT4 (α - a class) and VT3-1 ($\alpha + \beta$ - a class) were investigated. Concentrators of tension were carried out in the form of bores at the edges of working part of samples. Radiuses of concentrators made 0,5 mm, 2,0 mm, 5,5 mm, 12,0 mm. All experiments of this series were made at a speed of deformation of $V_2 = 71,1$ mm/h.

In the course of test registration of signals of AE by means of the 2nd fixed on the opposite ends of a sample of piezoelectric converters was made. The signal from an exit of each AE sensor amplified, filtered from low-frequency hindrances (with a frequency up to 20 kHz) and its amplitude was demodulated. Further the signal was exposed to analog-digital transformation with a frequency of sampling of 170 kHz and with a dynamic range of 70 dB and was processed on the personal computer [3]. For the analysis of AE of information the AE following parameters of signals were used: amplitude, duration, energy, energy density, form coefficient division of AE of signals on types of sources generating them by a special technique [2-4] also was carried out. For a filtration of AE of signals from the hindrances arising in a zone of captures of samples the location of AE of sources with use of the cross-correlation analysis was carried out.

Registration of signals of AE in the course of loading was accompanied by shooting of changes of a microstructure of a surface of the polished samples on video. The values of strength given in the description of results of experiments, paid off as the relation of the maximum loading at sample deformation, to the section area net (section in narrow part of a sample). For samples with a radius of concentrator of 0,5 mm the speed of the account of signals of AE smoothly increases with increase of extent of deformation. The total number of signals of

AE and the maximum speed of the account for samples from OT4 have big, than for samples from VT3-1, value.

In both materials with this radius of the concentrator the maximum jump of energy of AE at level $0,77\sigma_B$ is observed. Change of structure of a surface of the samples, connected, most likely, with an exit of groups of dislocations to a surface, doesn't coincide over time sharp emission of elastic energy of AE. For the material OT4 change of structure is observed at level $0,86 \sigma_B$. On the basis of told, it is possible to draw a conclusion that irreversible damages to a material come how they become visible by means of devices of visual control. It can be connected with that the radiation of a portion of energy of AE occurs at an exit of group of dislocations not only to a material surface, but also and to a crystal surface. Limitation of degree of increase in optical devices as can be connected with later moment of registration of occurring changes. Use of electronic scanning microscopes probably only after carrying out experiment. The inevitable unloading of a material brings to not to absolutely correct results as the return movement of dislocations at its unloading involves structure change in comparison with an intense material.

On samples with a radius of concentrator of 2,0 mm the smooth continuous growth of the total account of AE from time remains. But thus for the material VT3-1 the fluidity area that is characterized by existence of peak of speed of the account by the time of material destruction is more brightly expressed. Total energy of AE on the average decreases in comparison with samples with a radius of concentrator of 0,5 mm. The total account of AE of signals thus has bigger value. Visible changes of structure for the material OT4 are observed at level $0,97 \sigma_B$, for VT3-1 - at level $0,88 \sigma_B$.

Numerical values of the AE parameters, namely, the total account and total energy of AE, have still smaller sizes on samples with a radius of concentrator of 5,5 mm. Together with reduction of total number of signals the number of signals identified as signals from micro cracks decreases also. Visual changes of

structure of objects of researches it is observed for OT4 at level $0,95 \sigma_B$, for VT3-1 - at level $0,93 \sigma_B$.

Acoustic issue when loading samples with a radius of concentrator of 12,0 mm has big activity, than for the concentrator of 5,5 mm. Total energy radiated thus for samples from studied materials has the smallest value. All signals of AE are evenly distributed on all range of tension when loading material. The initial area of loading corresponding to level of tension about $(0,22 - 0,28)\sigma_B$, is accompanied by surge in activity of AE. It, most likely, is connected with that the increase in radius of the concentrator influences reduction of localization of the volume involved in deformation. In other words the number of defects involved in deformation increases. Thus in a heterogeneous material always there are defects of a crystal lattice which start proving at an early stage of deformation. The quantity of the defects getting to area of the concentrator of tension, decreases in proportion to reduction of radius of the concentrator.

It is known that at increase in concentration of tension the area of a material involved in deformation decreases. It is earlier established that the total account of AE of signals with some degree of probability can be described separate dependences on the operating tension. These theoretical assumptions are confirmed with a number of experimental data. In literature it is offered to classify all sources of AE as follows: 1) inactive, 2) active, 3) critically active, 4) the catastrophically active. As the source of AE can change the activity, and classification of sources of AE needs to be carried out with a binding to the operating tension. So, one source can be classified as inactive at low loadings and as active at high [5].

On the other hand, the assumption that at a material always there are defects of structure will be fair. These defects can be divided by their size into a number of groups. It is possible to include all dot and linear defects of a crystal lattice in the first group (dislocations, etc.). In the second – as increase in the extent of defects, a not entirely between grains. In the third – nonmetallic inclusions, cracks. The fourth group can characterize deficiency of structure of a

material from the point of view of the grain size (the grain is larger, the communications between them are less strong and the material as a whole is less strong). However the carried-out division of defects into groups is conditional. Dependence of total number of defects on their size and danger to a sample can be constituted in the form of exponential dependence that is confirmed with AE data.

Other option of classification of defects is based on their activity. In a certain volume of a material there is a certain number of defects of tension "working" or "radiating" at a certain level arising in volume. "Working" or "radiating" at this tension it is necessary to consider defect which radiates the impulse of the elastic energy registered at set sensitivity by measuring equipment during the movement, size or development changes.

The number of radiating defects has sedate dependence on the operating tension (Fig. 1) [5].

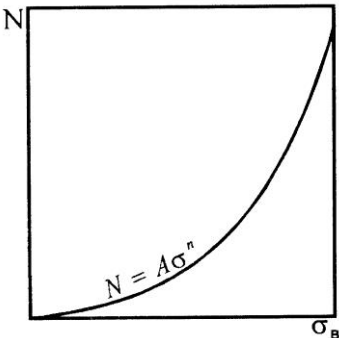


Fig. 1. Dependence of number of sources of AE on the operating in a material of tension.

$$N \sim A\sigma^n, \tag{1}$$

where: A - proportionality coefficient; σ - tension operating in a material; n - exponent.

The final number of radiating defects is connected with final value of possible tension in a material. In this case it is a question of tension operating in macrovolumes, in the area subjected to deformation at the appendix of external forces. Along with tension operating in macrovolumes, in a material there is also microtension which arise in all sites of separately taken grain or a crystal.

Thus the maximum tension in microareas can reach theoretical strength of the material which excess conducts to a rupture of molecular communications [6]. The increase in number of ruptures of molecular communications conducts to material destruction in that place where these communications were weakened by existence of defects. All calculations connected with determination of theoretical durability of materials, don't consider heterogeneity of materials.

Uniform distribution of tension on the area of cross section of a core takes place only when cross sections on length of a core are constant. Existence of sharp changes of the area of cross section owing to sharp transitions, openings, bores, cuts, etc. leads to uneven distribution of tension and to increase them in separate places of section. This phenomenon is called as concentration of tension [7]. The reasons causing concentration of tension (an opening, bore, scratch, etc.) are called as concentrators of tension. The defects connected with heterogeneity of structure of a material as can be concentrators of tension.

The increase in coefficient of concentration of tension conducts to increase in tension operating in a place of concentration (local tension).

$$\alpha = \frac{\sigma_{max}}{\sigma_n} \quad (2)$$

where α - coefficient of concentration of tension; σ_{max} - the greatest local tension; σ_n – rated voltage.

Rated voltage is defined as an average in the weakened section

$$\sigma_n = P/d \quad (3)$$

where P - effort in section; d - the area of the weakened section called by the area net.

The relation of the maximum effort at which there is a sample destruction, to the initial area of the weakened section it is possible to call nominal strength.

Theoretical coefficients of concentration depend on a form and the concentrator sizes. They have various values depending on a ratio of radius of a rounding off to section in the weakened place.

In Fig. 2 change schedules α are provided at various relations of radius of the concentrator to section in the weakened place of r/d .

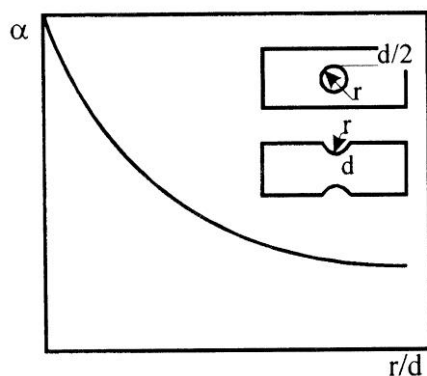


Fig. 2. Dependence of coefficient of concentration of tension from the concentrator size.

On the basis of expressions (1) and (2) the ratio showing is removed that at constant value of rated voltage ($\sigma_n = \text{const}$) the number of sources of AE is proportional to concentration of tension α : $N \sim \alpha^n$.

The statement will be fair that the volume of the material involved in deformation, is proportional to this relation $V \approx r/d$.

It is the most probable that this dependence isn't linear. The maximum tension in the weakened section is proportional to concentration of tension $\sigma_{max} \sim \alpha$ that follows from expression (2).

Dependence of volume of the material involved in deformation, on the maximum local tension has to have the distribution similar presented in Fig. 2.

At concentration coefficient $\alpha = 1$, i.e. at uniform distribution of tension on the areas of cross section, volume of a deformable material is infinite in the assumption of the unlimited size of a core or a plate with an identical area of section on all length. But even at the identical area of section on all length of beyond all bounds long product subjected to loading, exists so-called weak places. Concentration of defects in these areas exceeds average concentration on all volume of a material. It means that the volume of the real heterogeneous material involved in deformation, always конечен. As the maximum tension is final also. They depend on a form and the size of the concentrator of tension and a material.

Obviously, the total number of radiating defects of N at a certain concentration of tension can be calculated as work of number of defects – sources of impulses of AE for the single volume of $Ny\delta$ and volume of the material V involved in deformation at coefficient of concentration αn

$$N = N_{y\delta} V \tag{4}$$

It is established that depending on a form of the concentrator of tension and, as a result, from a type of a curve of change of the volume involved in deformation, nature of distribution of a curve of total number of radiating defects of N it can be various. It is connected with that the volume of the material involved in deformation, as a rule depends on properties of the material. For the accounting of sensitivity of a material to local tension into settlement formulas enter instead of theoretical coefficient effective coefficient of concentration of tension. It decides as the relation of an ultimate load of P_1 for a sample without concentrator to an ultimate load of P_2 of the same sample, but on the concentrator of tension $K = P_1/P_2$.

As a rule, the effective coefficient appears less theoretical, its size is in limits $1 \leq K \leq \alpha$.

Distribution of total number of signals can be presented in the form of dependence on the radius of the concentrator of tension. The schematic image of this distribution is submitted in Fig. 3.

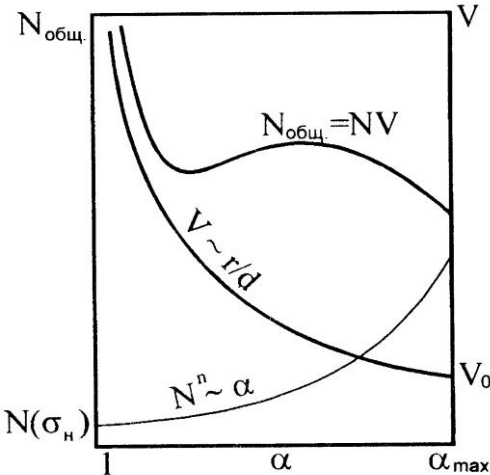


Fig. 3. Dependence of total number of sources of AE from sizes of concentration of tension.

A series of the made experiments allows to confirm justice of the offered model with some degree of probability. In Fig. 4 schedules of distribution of key parameters of AE depending on concentrator radius for two titanic alloys of OT4 and VT3-1 are submitted. All data of AE are provided not as average values for a series of tests from π is exemplary, and as results of AE at stretching of a concrete sample the AE parameters for which are closest to average values of key parameters of AE.

On histograms values of the AE parameters at the time of sample destruction are presented. For OT4 alloy the maximum total account of signals corresponds to the radius of the concentrator of 2 mm, minimum - to the radius of 5,5 mm.

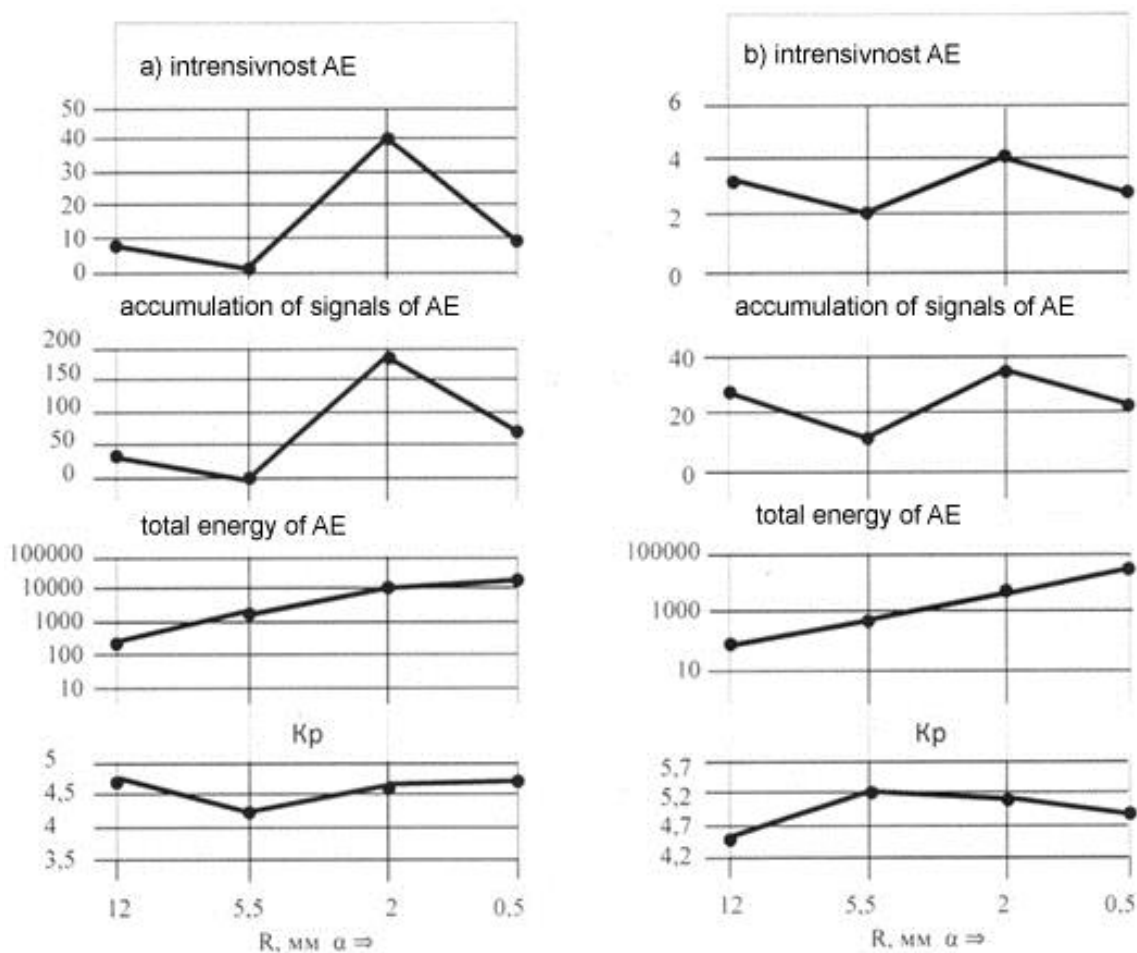


Fig. 4. The AE parameters at level $0,75\sigma_v$ depending on concentrator radius for a series of samples from an alloy: a) OT4; b) VT3-1.

Total energy thus evenly decreases with increase in radius of the concentrator. It is necessary to notice that the maximum value of the total account of signals and total energy of AE corresponds to a sample with an infinite radius of the concentrator (a flat sample).

Results of researches and their discussion

On a curve of the total account of signals it is possible to observe confirmation of the offered statement on nature of distribution of the total account of signals. For total energy a bit different picture of distribution is observed. It is connected with that total energy of signals of AE radiated by defects at their movement, doesn't submit to the sedate law of distribution. The type of distribution in this case isn't established. It is possible to claim only that the smallest value of total energy of AE corresponds to samples with a radius of concentrator more than 12,0 mm.

For VT3-1 alloy the minimum value of the total account of AE corresponds to the radius of 5,5 mm (similar to OT4 alloy), maximum corresponds to the radius of 2 mm.

To sample with a radius of concentrator of 0,5 mm there corresponds smaller, than for samples with a radius of concentrator of 2,0 mm, numerical value of the total account of AE. By analogy to the material OT4 it is possible to assume that at increase in radius of the concentrator signals of AE will grow. As well as in OT4 alloy total energy of AE for samples from VTZ-1 monotonously decreases with growth of radius of the concentrator. The minimum value of energy of AE, probably, corresponds to samples with a radius of concentrator more than 12,0 mm.

In the analysis of experimental data it is established that the dispersion of nominal breaking points for samples with concentrators of tension is quite great and can reach 30%.

And it increases with reduction of radius of the concentrator and has bigger value for the material VT3-1. Introduction β - stabilizers in an alloy of VT3-1

improves its strength properties, but thus plasticity of a material and a susceptibility to concentration of tension inevitably decreases. It probably is connected with that the defects, getting to concentrator area, are subject to action of big tension in size. Finding of some global defect in an area of coverage of the concentrator is less probable. But, if it nevertheless happens, existence of such defect catastrophically affects strength characteristics of a product.

The chart of distribution of key parameters of AE is given in Fig. 5 for samples with various concentrators of tension from OT4 and VT3-1 alloys depending on a nominal breaking point.

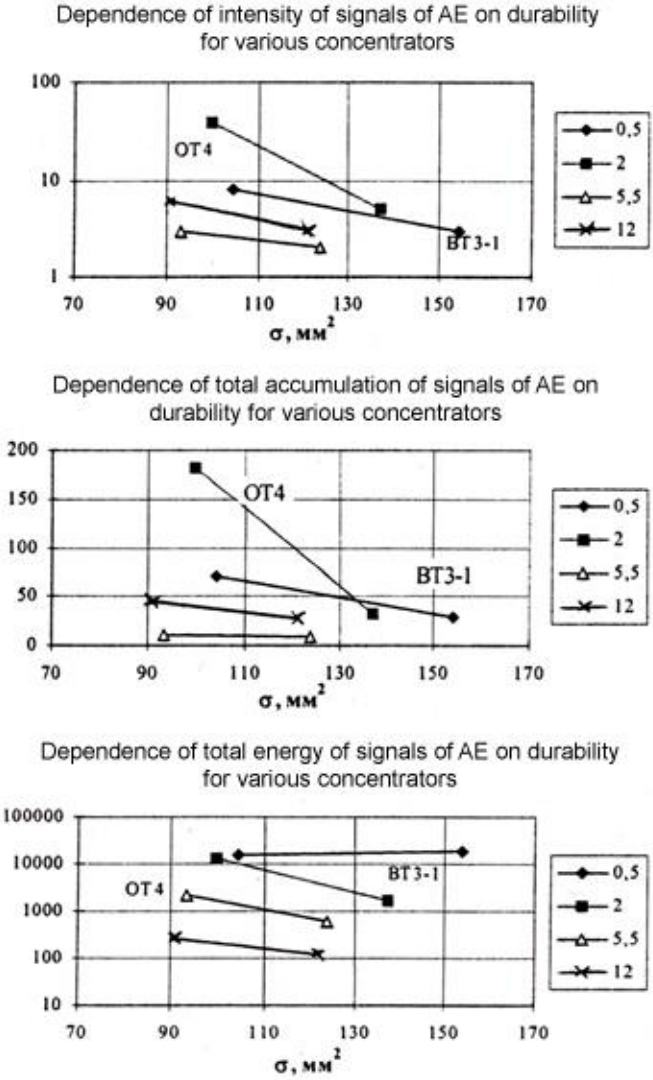


Fig. 5. Charts of distribution of key parameters of AE for samples with various concentrators of tension from OT4, VT3-1 alloys, depending on a nominal breaking point.

The established dependences open new possibilities of studying of physical properties of materials as can be postponed from macroscopic volumes of samples for microvolumes of concrete materials. Besides, the revealed results of researches can be used for development of techniques of diagnosing of designs from the point of view of definition of the least dangerous form of the concentrator of tension in designs where their existence is technologically necessary.

References

- [1]. N.A.Semashko, V.I. Muravyov, O.V. Bashkov, A.V. Frolov Forecasting of a limit condition of an alloy of OT-4 with use of a method of acoustic issue. Control. Diagnostics. 2001. № 6. pp. 30 – 31.
- [2]. N.A.Semashko, A.V. Frolov, V.I. Muravyov, M. M. Lyakhovitsky. Use of new parameters of acoustic issue for forecasting of limit mechanical characteristics of a titanic alloy of OT4. Control. Diagnostics. 2002. № 12. pp. 24 – 27.
- [3]. N.A.Semashko, V.I. Muravyov, A.V. Frolov etc. Acoustic issue in research practice of plastic deformation and destruction of materials. Materials science. 2004. № 7. Special release. pp. 36 – 40.
- [4]. N.A.Semashko, V.I. Muravyov, A.V. Frolov etc. Acoustic issue at the solution of some questions of aviation production. Aviation industry. 2004. № 2. pp. 85 – 89.
- [5]. V.I. Ivanov. Bulls Accusative. Classification of sources of acoustic issue. Diagnostics and forecasting of destruction of welded designs. 1985. № 1. pp. 67-74.
- [6]. P.G. Miklyaev, G.S. Neshpor, V.G. Kudryashov. Kinetika of destruction. M.: Metallurgy, 1979. 279 p.
- [7]. S.P. Fesik. Reference book on resistance of materials. Kiev: Budyvelnik, 1982. 280 p.

ELECTROTHERMIC TREATMENT OF WIRE

V.V. Rubanik^{1,2}, Y.V. Tsarenko, V.V. Rubanik, Jr^{1,2}

¹Institute of Technical Acoustics of National Academy of Sciences of Belarus,
Vitebsk, Belarus.

²Vitebsk State Technological University, Vitebsk, Belarus.

E-mail: ita@vitebsk.by

Stainless steel 12X18H10T has a large amount of carbides, which deprave its plastic and corrosion properties. Annealing is applied to cold-worked stainless steel at high temperatures (1000... 1100°C) to provide solution of carbides and transfer carbides into the solid solution. High speed heating is used for thermal treatment of stainless steel wire that improves the efficiency of the process and combines it with drawing [1].

Experimental studies of the kinetics of high-speed annealing of metals and alloys are mainly devoted to the degree of deformation, which is well above the critical [2, 3]. However, the degree of deformation that closed to the critical and supercritical is used during calibration wire and cable products in the drawing of metal shells. At the same time, the practicability of high-speed heating during recrystallization after drawing and upsetting with the critical degree of deformation is shown in [4].

The study was carried out on the samples of steel wire 12X18H10T (diameter of 1.0... 3.0 mm) pre- annealed in a hydrogen furnace by pass. The grain size of the wire was more than 20 μm after annealing. After deformation by drawing with different drafting high speed annealing was performed according to the following regimes: heating to a predetermined temperature, air cooling (I); heating to a predetermined temperature, water quenching (II). Heat treatment was carried by application of ultrasonic vibrations according to similar regimes upon heating.

The heating rate was 100°C, the displacement amplitude of ultrasonics - 6 μm . With the increasing of annealing temperatures from 900 to 1100°C a

significant increase in plastic properties of the steel are observed, moreover, after annealing with application of ultrasound σ is 10...30% more than after annealing without ultrasound. The most difference is observed in the mechanical properties of steel 12X18H10T (Fig. 1, a) after annealing at 900...1000°C.

With increasing degree of pre- deformation from 6 to 12% the dependence of mechanical properties of wire on the annealing temperature does not change (Fig. 1, b). However, recrystallization process is shifted to lower temperatures at further increase in ε , as evidenced by the increase in the plastic properties of the wire (δ) at low annealing temperatures. With increasing annealing temperatures the difference is decreased between the mechanical properties depending on the degree of deformation.

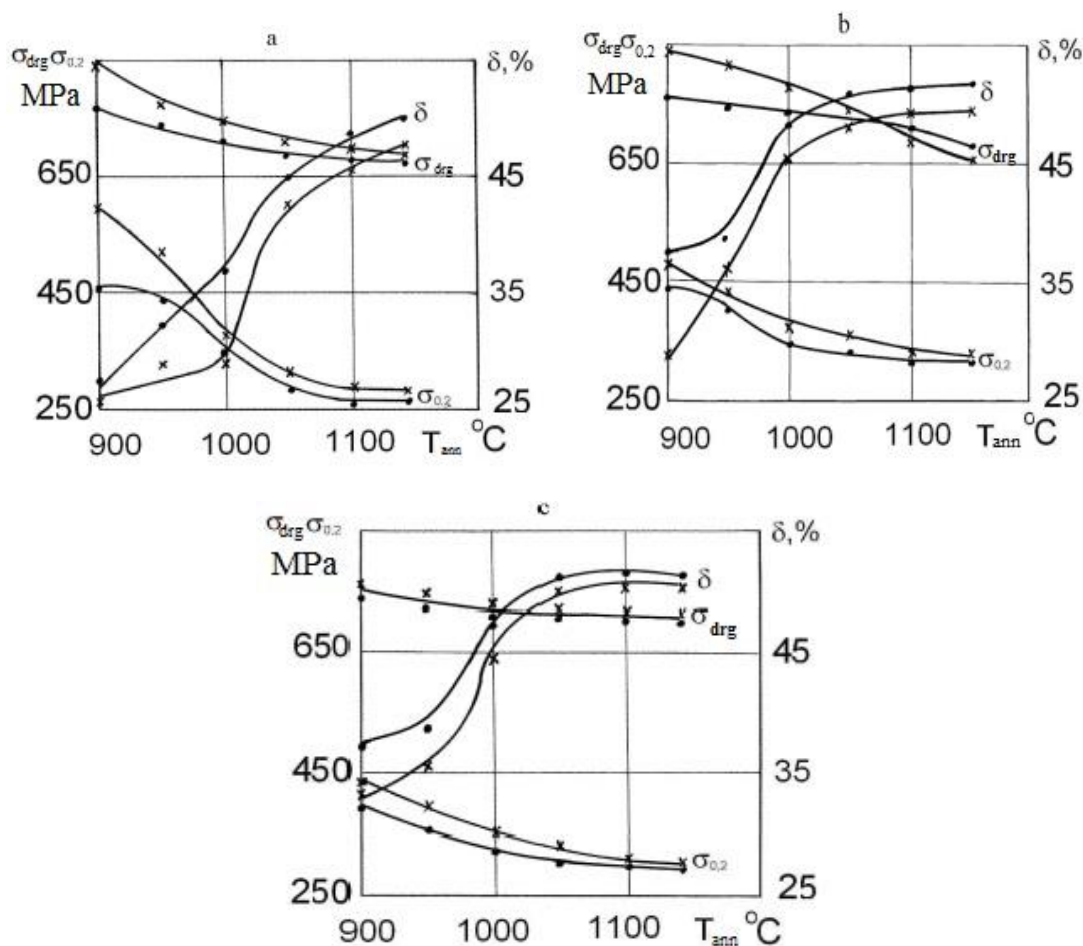


Fig. 1. The dependence of the mechanical properties of the steel wire 12X18H10T ($\varepsilon = 6\%$) on the temperature of heat treatment after drawing: a - $\varepsilon = 6\%$; b, c - $\varepsilon = 12\%$. Heating rate 100°C/s, air quenching - a, b; water quenching - c, x - without ultrasonic vibrations.

Tensile strength and yield strength of 12X18H10T wire are slightly changed after heat treatment with quenching according to the regime II (Fig. 1, c). High elongation values are observed, especially after small degrees of deformation.

The character of changes of mechanical properties of the wire shows that the ultrasonic vibrations accelerate the formation of the recrystallization structure during annealing. This phenomenon is due to activation of the grain boundaries under the influence of alternate stresses due to the separation of borders from impurity atoms that fixing its borders [5]. The speed of border migration under ultrasonic influence exceeds speed at creeping which is reduced when the irradiation time increases [5-7]. The influence of high speed heating and ultrasonic vibrations on the wire leads to a process of recrystallization and dislocational deformation of recrystallization grains and formation of additional vacancies. This explains a slight increase in σ_{drg} and $\sigma_{0.2}$ of the wire samples after water quenching compared to natural air cooling. However, high density of dislocations is not observed within the grain by application ultrasonic vibrations upon annealing [8], since the formed dislocations are easily shifted to the grain boundaries under the influence of vibrations. Ultrasonic vibrations accelerate the diffusion process in metals [9, 10], so when solubility of carbides in solid solution is apparently increased upon thermosonic annealing at high temperatures. This provides an increase in plastic properties of 12X18H10T wire after annealing with ultrasound at high temperatures [10-12].

After annealing with the use of ultrasonic vibrations the wire has finer grains of austenite and the variations in grain size are observed under normal conditions upon annealing (Fig. 2). The initial deformed wire ($\varepsilon = 12\%$) is characterized by elongated grain structure according to the drawing direction, the presence of secondary carbides are observed.

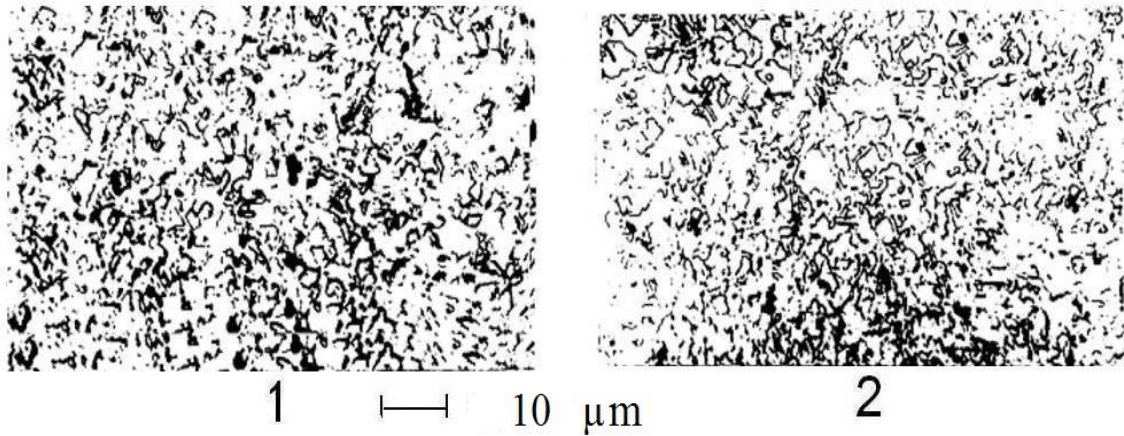


Fig. 2. The microstructure of 12X18H10T steel wire ($\varepsilon = 6\%$) after heat treatment at 900°C : 1 - without ultrasonic vibrations, 2 - with ultrasonic vibrations.

After electric resistance annealing of stainless steel wire in the air an oxide film is formed on its surface, which maintains lubrication upon future drawing. The wire undergoes non-oxidizing annealing in vacuum under the same heating conditions. The residual pressure in the chamber was $10^{-1} \dots 10^{-2}$ Torr, which eliminated surface oxidation of the metal.

The results of studies of the influence of heating rate on the plastic properties of the wire are shown in Fig. 3. The wire heating rate was adjusted by changing the speed of its motion at a constant heating base. The heating temperature was 1000°C , and the degree of pre-drafting - 6%. Increase in the heating rate from 10°C to 900°C results in an increase in elongation of steel wire 12X18H10T from 25% to 37%. The elongation is higher after annealing with the application of the ultrasonic vibrations. The most intensive growth of δ is observed after annealing at heating rates up to 400°C . Further increase of the heating rate has little effect on the plastic properties of the wire. The value of tensile strength with increasing heating rate is slightly increased only at 45...50 MPa [12 - 14].

The austenite grain size decreases by more than 2 times with increasing heating rate up to 900°C . The austenite grain size increased from $23\ \mu\text{m}$ to $70\ \mu\text{m}$ after annealing at 1000°C for 1 hour. As the grain coarsening of

12X18H10T steel is not observed upon drafting of 4.5%, then $\varepsilon = 6\%$ can be considered close to critical, since an abrupt change in the grain size occurs [4]. Two competing processes of coarsening initial grains at the expense of others and nucleation take place under recrystallization after small compression [4]. Since after small ε the number of defects is small in the structure, a slow initial grain growth occurs upon heating. Recovery and recrystallization occur simultaneously under rapid heating. High number of defects and inhomogeneity has been determined in the steel structure. Suppression of recrystallization by nucleation of new grains takes place. Therefore, a decrease in the austenite grain size is observed. After thermosonic annealing the grain size of wire is lower than that upon the common annealing conditions. Thus, this difference is 4...5 mm at a heating rate of 50°C and reduced to 1...2 mm at higher speed. This is apparently due to the formation of the additional amount of dislocations and vacancies in a steel structure under the ultrasonic influence, generation of elastic stress that promotes nucleation [10, 13]. Thus, the optimal annealing regime of 12X18H10T wire is the temperature range of $1100\text{...}1150^\circ\text{C}$ for small drafting by application resistance heating, and the temperature range is $1000\text{...}1100^\circ\text{C}$ for drafting of 12...30%.

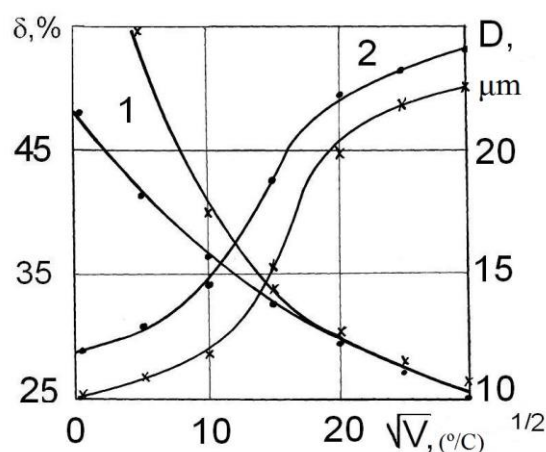


Fig. 3. The dependence of the average grain size (1) and elongation of the steel wire 12X18H10T (2) on the heating rate. x - without ultrasonic vibrations.

Hardening is associated with the development of the martensite transformation $\gamma \rightarrow \alpha'$ for 12X18H10T steel during plastic deformation. The martensite formation is defined by stress acting in the deformation region, by the degree of deformation and thermal deformation. Tensile stress intensifies transformation, and compression stresses lead to the opposite effect. The transformation practically slows down under warm plastic deformation. Intense hardening of austenite steel is determined by two processes under deformation: hardening of austenite and martensite transformation. The austenite has stability with temperature increase, in this connection, the transformation slows down and a decrease in hardening occurs.

The wire has an austenite single- phase structure in the initial state prior to drawing. The initial austenite grain size is equiaxed in structure and about the same size. Grain shattering and its elongation in the direction of drawing take place during drawing. Since etching of martensite is higher than austenite, dark grains indicate intense of $\gamma \rightarrow \alpha'$ transformation in the microstructure of 12X18H10T steel. Light areas are also observed in the steel structure where the martensite transformation is negligible. This is apparently due to the factor that the formation of martensite occurs mainly along sliding planes under deformation. Therefore, rapid martensite formation is observed in favorably oriented grains upon plastic deformation, and shift does not occur in unfavorably oriented grains [15-17]. In this case the martensite transformation is not observed in a steel structure.

Grains undergo elongation along drawing direction that is less visible after wire drawing with application of ultrasonic vibrations, and therefore, there is a small amount of martensite, which is probably due to thermal effects of ultrasonic vibrations. Local heating in the deformation zone leads to inhibition of $\gamma \rightarrow \alpha'$ transformation that is defined by the results of strength properties of 12X18H10T steel wire after drawing under normal conditions and with the application of ultrasound [18, 19]. The increase in strength σ_{drg} is observed for

small degrees of deformation. After drafting of 12%, the tensile strength of a pre-annealed steel increases from 700 MPa to 1020 MPa, i.e. more than 45 %. The values of σ_{drg} for the samples obtained by drawing the wire under normal conditions and with the application of ultrasonic vibrations almost coincide. Percentage elongation of the wire after drawing by the same route is decreased from 48% in the initial state to 7% after drawing under normal conditions, and to 9% after drawing with the application of ultrasonic vibrations [15].

The influence of high-speed electro-thermal treatment on drawing process and properties of NiTi shape memory alloy wire has also been studied.

Manufacturing of NiTi wire is a very complex process and includes long heat treating operations in a furnace, further drawing using expensive lubricants and reduction per pass.

One of the peculiarities of treatment of shape memory material is full or partial recovery process of the treated semi-finished product after annealing. The number of operations also increases. Manufacturing of items having shape memory effect is associated with the number of intermediate operations in modern industry. It is of interest to optimize the number of operations during manufacturing process. It is necessary to cancel completely the shape recovery effect, or at least reduce it as much as possible in these stages. The shape recovery for the finished product can be initiated choosing the heat treatment regime.

The main difficulty in drawing NiTi is to restore the geometry of a stretched wire after intermediate annealing to stress relief. Shortening of the wire and increasing its diameter appears to occur. This change depends on the degree of deformation of the wire during plastic deformation [20].

The results for cold drawing of the NiTi wire are shown in Figure 4. When the deformation is 7% the-100 percent recovery occurs after annealing.

The shape memory effect is completely cancelled when the deformation is 23% above.

Fig. 4 shows the mechanical properties of the nitinol wire alloy after electric resistance annealing in air at a heating rate of 50°C. Plastic deformation of the samples was carried out by drawing, reduction ratio was 20%. As can be seen from the graph, the most intensive weakening of the of Ti-Ni wire begins at 550°C, with a sharp decrease in σ_{drg} and $\sigma_{0,2}$.

Elongation is increased from 4% to 22%. Tensile strength σ_{drg} and yield strength $\sigma_{0,2}$ have higher values compared to furnace annealing. Elongation δ is 18 % after annealing in furnace and - 22% after electrothermic treatment.

With increasing the total draft ratio of the wire up to 30 % the dependence of the mechanical properties on the annealing temperature is not changed. However, increasing the degree of deformation, a shift of recrystallization processes occurs at lower temperatures, as the improvement of plastic properties of the Ti-Ni wire is observed at lower annealing temperatures [21].

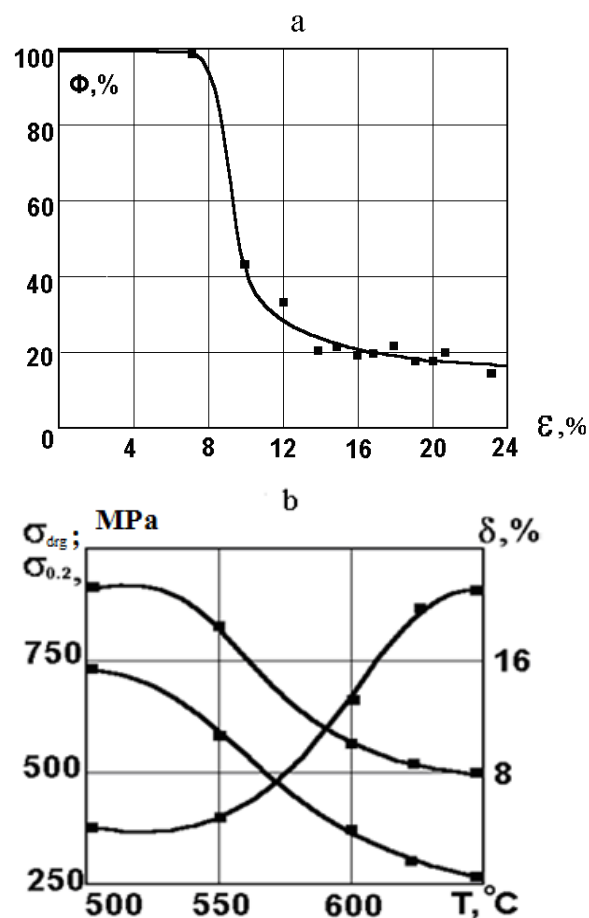


Fig. 4. The dependence of shape recovery on reduction after drawing (a) and mechanical properties (b) of the TiNi wire on the temperature of speed annealing.

The heating rate has no significant effect on the mechanical properties of the Ti-Ni wire. Increasing the heating rate from 50°C to 300°C leads only to an increase in the tensile strength of 50...60 MPa and elongation remains unchanged.

Drawing of the nitinol wire was carried out after heat treatment using resistance heating. For comparison, drawing was applied to the Ti-Ni wire annealed according to a common technology in a furnace. Speed drawing was 0.3 m/s, and engine oil +2% molybdenum disulphide was used as lubricant. The results are shown in Fig 5.

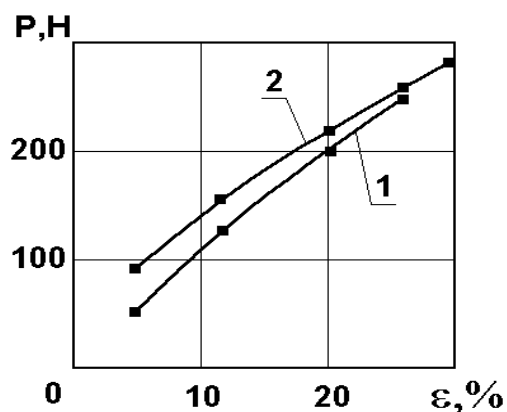


Fig. 5. The dependence of drawing force of the TiNi wire on reduction after : 1 - heat treatment in a furnace, 2 - resistance heating.

The graphs show that the drawing force of the Ti-Ni wire after the high speed annealing has higher values than after heat treatment in a furnace. This is particularly noticeable at low degrees of deformation and associated with a high strength heat-treated samples using resistance heating.

However, the degree of deformation of the wire annealed in the furnace reaches 25 % and a further increase in ϵ leads to constant breakages. Maximum degree of deformation is slightly higher for the TiNi wire after electrothermic treatment due to its high plasticity [21].

Conclusion

Thus, the process of drawing provides a fine-grained structure of the 12X18H10T stainless steel wire and nitinol using high resistance annealing

speed. Heat treatment time is reduced improving plastic properties of materials. Drawing at high draw ratio can possible by heat treatment application.

References

- [1]. I.I. Nedovizij, S.I. Petruhin, A.G. Komarov. Sovmeshhenie processov proizvodstva provoloki. M.: Metallurgija, 1979. 224 p.
- [2]. D.I. Romanov. Jeletrokontaktnyj nagrev metallov. M.: Mashinostroenie, 1981. 167 p.
- [3]. V.V. Klubovich, V.V. Rubanik, Ju.V. Carenko. Skorostnaja jeletrotermiicheskaja obrabotka kompozicionnogo materiala. Vesci AN Belarusi. Ser. fiz.-tjehn. navuk, 1997, № 1. pp. 51-54.
- [4]. M.N. Bodjako, S.A. Astapchik, G.B. Jaroshevich. Termokinetika rekristalizacii. Minsk: Nauka i tehnika, 1968, 252 p.
- [5]. V.N.Gridnev, Ju.Ja.Meshkov, S.P.Oshkaderov, N.F.Chernenko. Tehnologicheskie osnovy jeletrotermicheskoj obrabotki stali. Kiev: Navukova dumka, 1977. 204 p.
- [6]. V.I. Ivanov, K.A. Osipov. Vozvrat i rekristalizacija v metallah pri bystrom nepreryvnom nagreve. M.: Nauka, 1962. 186 p.
- [7]. O.V.Abramov, V.I.Dobatkin, V.F. Kazancev. Vozdejstvie moshhnogo ul'trazvuka na mezhfaznuju poverhnost' metallov. M.: Nauka, 1986. 277 p.
- [8]. V.I. Biront Primenenie ul'trazvuka pri termicheskoj obrabotke metallov. M.: Metallurgija, 1977. 166 p.
- [9].A.V. Kulemin. Ul'trazvuk i diffuzija v metallah. M.:Metallurgija, 1978.199p.
- [10]. C.E. Winsper, D.N. Sansome. Fundamentals "ultrasonic" of Wire Drawing. J. of the Inst. of Metals. 1969. V. 9, № 97. pp. 274-281.
- [11]. Sposob volochenija nagrevostojkogo kabelja: pat. № 2060852 Rossijskaja Federacija, MPK 6 B21C3/00 / V.V.Klubovich, V.V. Rubanik, Ju.V. Carenko. № 92015653/02; zajavl. 30.12.92; opubl. 27.05.96 // Otkrytija. Izobret. 1996. № 15. p. 166.
- [12]. O.V. Abramov, I.G.Horbenko, Sh. Shveгла. Ul'trazvukovaja obrabotka materialov. M.: Mashinostroenie, 1984. 280 p.

- [13]. S.S. Gorelik. Rekrystallizacija metallov i splavov. M.: Metallurgija, 1978. 568 p.
- [14]. V.V. Klubovich, V.V.Rubanick, Ju.V. Carenko. The prospects of the ultrasound vibrations use in the processes of the materials heat treatment // Ultrasonics Word Congress. Berlin, Germany, 1995. pp. 733-736.
- [15] V.V. Rubanik, Ju.V. Carenko, V.P. Bobrov. Martensitnoe prevrashhenie v stali posle deformacii s nalozheniem ul'trazvuka. Mezhdunarodnaja konferencija «Gradientnye strukturno-fazovye sostojanija v splavah i staljah», Novokuzneck, SibTU, 2006, pp. 64-67.
- [16]. V.V. Klubovich, V.V.Rubanick, Ju.V. Carenko. Jelektrotermicheskaja obrabotka stal'noj provoloki v ul'trazvukovom pole /Perspektivnye materialy i tehnologii /pod redakciej V.V. Klubovicha. – Vitebsk: Izd-vo UO «VGTU», 2008. Ch. 6. pp. 119-141.
- [17]. V.V. Klubovich, V.V.Rubanick, Ju.V. Carenko. Primenenie ul'trazvukovyh kolebanij pri volochenii i termoobrabotke kompozicionnyh materialov. Tendencii razvitija tehnologii mashinostroenija. Mater. mezhd. konf. Zelena Gura, Pol'sha, 1990. Part. 2. pp. 45-49.
- [18]. V.V. Rubanick, Ju.V. Carenko. Jelektrotermicheskaja obrabotka kompozicionnyh izdelij. Perspektivnye tehnologii i metody kontrolja. Vitebsk: Izd-vo UO «VGTU», 2009. Ch. 9. pp. 232 - 266.
- [19]. B.B. Klubovich, Ju.V. Carenko, V.G. Krauze Volochenie i otzhig stal'noj provoloki s nalozheniem ul'trazvukovyh kolebanij. Primenenie fizicheskikh i fiziko-himicheskikh metodov v tehnologicheskikh processah. Tematicheskij sbornik nauchnyh trudov. M.: Metallurgija, 1990. pp. 98-102.
- [20]. Lihachev V.A., Kuz'min S.L., Kamenceva Z.P., Jeffekt pamjati formy. Izd-vo Leningr. un-ta. Leningrad 1987. 238 p.
- [21]. V.V. Klubovich, V.V.Rubanick, Ju.V. Carenko, V.V. Rubanick ml. Volochenie i jelektrotermicheskaja obrabotka TiNi provoloki. Tehnologii, materialy, instrumenty. V. 5. № 4, 2000. pp. 80-84.

EFFECT OF ION-ARC VACUUM-BEAM TREATMENT BY Zr^+ ON A STRUCTURE AND FATIGUE DURABILITY OF 30CRMNSINI2 STEEL

I. Vlasov, S.Panin, V.Sergeev, O.Bogdanov, P.Maruschak, B.Ovechkin.

Abstract

The structure of modified surface layer of high-strength 30CrMnSiNi2 steel was investigated by optical, scanning electron and transmission electron microscopy as well as X-ray diffraction analysis. The tests on static and cyclic tension were carried out for 30CrMnSiNi2 steel specimens in as supplied state as well as after subsurface layer modification by Zr^+ ion beam irradiation. Differences of the specimen deformation behavior and changes of their mechanical properties are analyzed. The reason for fatigue life-time increase of the specimens after the treatment is discussed.

Keywords: fatigue life-time, ion-beam surface irradiation, strain, fracture.

Introduction

High-strength steels are high-tech metallurgical products whose increased physical and mechanical properties are achieved due to substantial alloying as well as multi-stage thermal treatments. According to the opinion of the VIAM director academician E.N.Kablov – modern structural steels do not possess problems with providing high level of strength, but their weak point is fatigue durability. This drawback is caused by two main reasons. First, extremely low ductility and the limited number of effective mechanisms of stress relaxation leads to reduced resistance to crack growth (in the first instance, fatigue ones). Secondly, for the same reason, any defect on the surface quickly becomes dangerous stress concentrator, whose relaxation is completed by microcrack formation and subsequent quasi-brittle fracture. These questions, in the light of the special role of surface layers as separate subsystems in a deformable solid – have been discussed in detail in the papers of academician V.E. Panin within the concept of physical mesomechanics of materials [1, 2].

Based on the physical laws the perspective direction of fatigue durability increase of high strength steels is a modification of the surface layer, above all, from the perspective of decreasing its hardness (perhaps plasticization) that while maintaining the strength properties of the material core may preserve the strength and bearing capacity of the structural material. Ion-beam effect for a long time was used as a finishing surface treatment and is widespread in the semiconductor and optical industry. Recently, in the laboratory of materials science and nanotechnologies of ISPMS SB RAS modes allowing modifying the structure of a subsurface layer at a depth of up to 100-150 microns by ion-beam of metals without losing strength properties of the core have been obtained. The formation of the modified surface layer is accompanied by a lowering of its hardness, but it can substantially increase the fatigue durability of specimens.

In previous work, the authors investigated the influence of ion-arc treatment by ion Zr^+ on structure, mechanical properties and fatigue durability changing of the heat-resistant 12CrMoV steel, [3]. As a result of ion treatment fatigue durability increase in 2-3 times, as well as increasing the tensile strength by 15% was revealed. In this regard improving durability of high-strength steels, in particular structural alloyed steel 30CrMnSiNi2 used for the manufacture of high-loaded responsible details is relevant. However, this steel has no refractoriness, so as a result of ion-beam treatment its mechanical properties can significantly degrade. In addition, the adding into a thin surface layer of ion Zr^+ as one more alloying element, should lead to complication of its structural-phase composition, and probably to the embrittlement. In doing so, a special regime that includes a rotation of specimens during the treatment (Fig. 1) that allows to replace specimens from the ion-beam impact zone thereby dosing the thermal influence.

Changing the character of mechanical properties caused by the proposed method of treatment is illustrated by the loading diagram presented in Fig. 1. 2. More detailed discussion is below. It can be assumed that a periodic ion-beam effect on specimens can also be accompanied by their ultra-fast hardening as the

major thermal influence only when interacting with electron beam ion Zr^+ . In this article the analysis of structure and evaluation of change in mechanical properties of steel specimens after treatment.

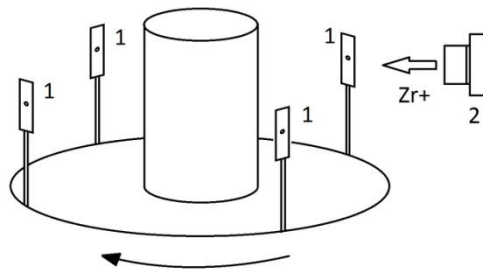


Fig. 1. Scheme of the specimens ion treatment: 1 – specimens; 2 – ion gun.

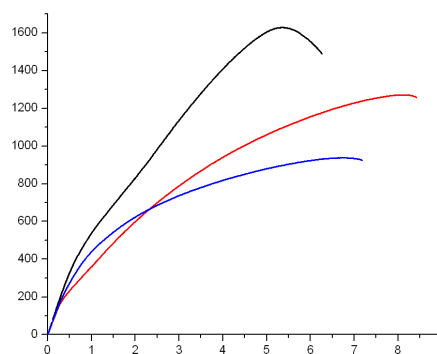


Fig. 2. Loading diagrams at specimen tension with a central hole: 1) in initial state; 2) after treatment; 3) after heating to 700°C.

Experimental material and procedure

Flat specimens in the form of rectangular plates were cut out from the ingot bar of $30CrMnSiNi2$ steel by electric spark cutting for the treatment and tests. The size of the specimens for the fatigue tests was $65 \times 8 \times 1$ mm. A central hole with a diameter of 2 mm was drilled in the specimens as the stress concentrator at distance 45 mm from one of its edges. The specimens were subjected to quenching and subsequent normalization according to the standard regime described in [4]. After that, the specimens were divided into 3 groups. The specimens without the treatment composed the first group; the second one consisted of the specimens subjected to the subsurface layer modification, while the specimens from the third group were heated (high-tempering) in the argon atmosphere up to 700 °C and exposed under that temperature during 19

minutes. By doing so the authors attempted to distinguish the contribution from the ion-beam treatment and the thermal action. A more detailed description of ion-beam treatment of specimens can be found in [3, 5, 6].

The coupons were tested under high cyclic fatigue with the cycle asymmetry ratio $R_a=0.1$ (peak load – 270 MPa, minimum one – 27 MPa). The tests were carried out with the help of the servohydraulic testing machine Biss UTM 150. Scanning electron microscopy was performed with the use of JSM-7500FA and Quanta 200 3D. The tests for static tension were carried out at the electromechanical testing machine Instron 5582. X-ray diffraction analysis was conducted with the help of x-ray diffractometer DRON-7. Microhardness of 30CrMnSiNi2 steel specimens was measured with the use of PMT-3 microhardness meter at load applied onto Vickers pyramid.

Structural study of a modified subsurface layer

Microhardness.

Microhardness of 30CrMnSiNi2 steel specimens was measured with the use of PMT-3 microhardness meter at load applied onto Vickers pyramid of 100 g. The measurements were conducted on the flat surface for all types of specimens (Fig. 3, a). The lateral face (cross section) was additionally analyzed for the treated specimen. Graph of microhardness distribution through the specimen cross section after treatment is shown in Fig. 3, a Minimum hardness during the measurements over the cross section was registered close to the surface. Microhardness began to grow to the depth of 150-180 μm while after it was lowered and remained constant (~ 5 GPa).

Most probably during the surface layer recrystallization and the formation of ferrite grains the carbon could migrate towards deeper layers that also can give rise to local strengthening at the depth of 150-180 μm . The softened zone is extended from the surface to the depth not exceeding 100 μm . Another possible explanation is related to decay of residual austenite during the treatment that might give rise to increasing of the microhardness.

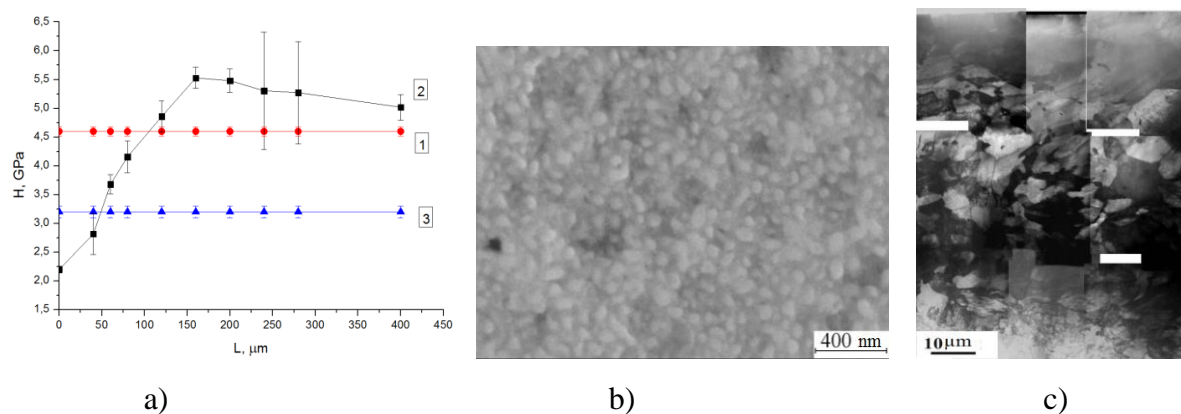


Fig. 3. a) Graph on microhardness through the specimen cross section as function of the distance from the surface of 30CrMnSiNi2 steel: 1) in initial state; 2) after treatment; 3) after heating to 700°C; b) SEM -micrograph of the specimen surface after the treatment; c) TEM image of the subsurface layer cross section of the specimen after the irradiation.

Scanning electron microscopy.

It was found that during the ion-beam treatment highly dispersed particles with the size of ~100 nm (Fig. 3, b). The presence of Zr at the depth not exceeding 6 μm was confirmed by the X-ray spectrum microanalysis.

Transmission electron microscopy.

In Fig. 3, c the fine structure of the specimen after treatment over its cross section is presented. It is evident that near the surface the ferrite-cemented structure has formed as a result of heating that is characteristic for sorbite (at the depth of not more than 100 μm). In the underlayers of the specimen the initial martensite structure is remained.

Testing results

Static tension

The results of tests on static tension are given in Fig. 2 and Table 1.

Table 1. Results on static tension tests.

Sample	σ_B , MPa	ε , %
In initial state	1630	6
After treatment	1270 (↓22%)	8 (↑25%)
After heating to 700°C	935 (↓42%)	7 (↑17%)

Testings for cyclic tension

During the fatigue tests the average number of cycles prior the fracture were determined. For the specimens without the treatment this value made N_p $110\,000 \pm 31\,000$ cycles while for the specimens after the irradiation it is equal to $330\,000 \pm 40\,000$. The specimen after tempering failed after $138\,000 \pm 36\,000$ cycles. Thus, the surface modification by the Zr^+ ion beam irradiation of 30CrMnSiNi2 steel specimens ensures increasing the fatigue life-time by 3 times.

Calculation of displacement vectors. Vector fields were built according to the images obtained during cyclic tensile tests. In figure 4 images of both type specimens at the pre-fracture stage are given. It is seen that in the specimen without treatment deformation is localized in the top of fatigue cracks being propagated from the stress concentrators (Fig. 4, a, b). The growth of cracks is accompanied by a plastic deformation which is manifested also by cross contraction of the specimen (Fig. 4, c).

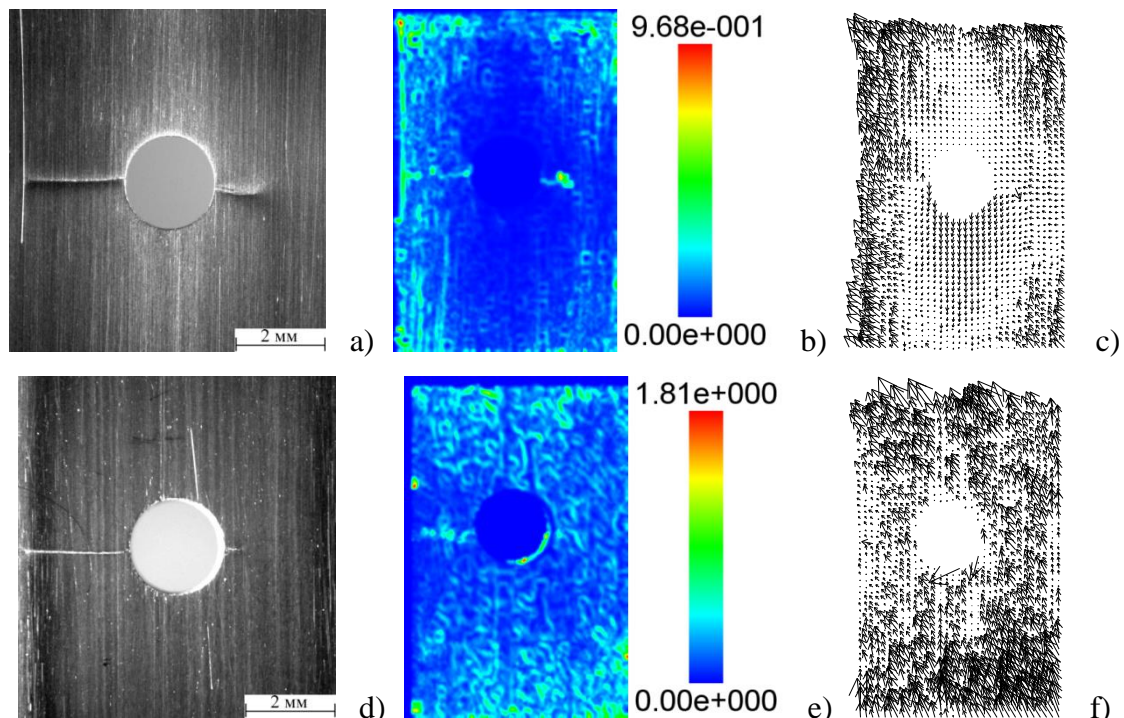


Fig. 4. Surface image, displacement vector fields and displacement vectors of specimens: a), b), c) – in the initial state (100×10^3 cycles); d), e), f) – after treatment with Zr^+ ions (384×10^3 cycles).

In general it can be said that the deformation behavior of the specimen with a couple of fatigue cracks is determined by their gradual disclosure and visco-elastic response of the surrounding material to reduce the cross-sectional area of the specimen in this area. A different picture is observed in the specimen after the treatment where near-surface layer is softened at a minimum thickness of 100 microns. Like the specimen without treatment a fatigue crack is growing from the stress concentrator (Fig. 4, d); but its growth is accompanied by intense deformations in the area around the hole, that can be the reason of dispersing the powerful stress concentrator due to the involvement of a large number of mesoconcentrators of lower power (Fig. 4, e). As a result, instead of disclosing cracks on the normal fracture mechanism for the case of specimen without treatment, there is quasi-homogeneous distribution of mesoscopic deformation (Fig. 4, f). This may be the cause of a fatigue crack growth damping and fatigue durability increase.

Discussion of results

The following interpretation of the results is proposed. Treatment of steel 30HGSN2A specimens by the ion beam Zr^+ brings to the formation of intermetallide compounds of Fe-Zr system as well as zirconium carbide in the subsurface layer to the depths up to 6 μm . It is assumed they are observed on the specimen surface (fig. 3, b). At the depth of 25-35 μm from the surface due to the cyclic high temperature effect the tempering takes place and ferrite are formed. Next, at a depth of less than 100 μm the structure of sorbite characteristic for the high-temperature tempering at the temperature above 650° C is formed. This structure is observed in samples heated to 700° c, which indirectly indicates that when exposed to material at a depth of 35-100 μm is similar to thermal impact. This structure is observed in specimens heated to 700° C that indirectly indicates that when the treatment at a depth of 35-100 μm the material is subjected to the similar thermal impact. At the same time at the surface of modified specimens the temperature is much higher which should lead to the formation of a grain structure. Deeper than 100 μm due to thermal

cycling under the ion-beam treatment a residual austenite becomes the bainite resulting in bainite-martensitic structure which leads to a slight increase of hardness compared to austenite-martensitic structure of the specimen after the standard thermal treatment. According to the authors, the effects are possible due to cyclic transient thermal influence occurring at the moment of the ion beam and the specimen surface interaction.

Thus, the realized ion-beam treatment differs to advantage from a simple heating to 700° C, above all, that the width of the heat affected zone is reduced to a minimum (near surface layer depth is not exceeding 100 µm). The core material, in general, maintains its strength. On the other hand there is a modified layer on the surface of the processed specimen, positively affects the resistance to origin and growth of fatigue cracks.

Analysis of the results shows that in the steel 30CrMnSiNi2 specimens were subjected to the treatment the reduction of the ultimate strength is going due to weakening a surface layer that at the same time accompanied with rising specific elongation to fracture. Analysis of deformation fields allows you to say that the presence of q modified surface layer provides efficient redistribution of load resulting in much later origin of the main crack and its slower propagation. This leads to an increase of fatigue durability of specimens after treatment.

Summary

The characterization of the subsurface layer structure modified by Zr⁺ ion beam irradiation was carried out. It was shown that the highly dispersed particles were formed on the surface with the characteristic size of ~100 nm. In the subsurface layer as a result of the high-temperature thermal affect martensite structure was converted into the ferrite-pearlite one. There are also structural changes to give rise to hardness increasing by 8 % at in the specimen core after treatment.

During the fatigue tests it was shown that the specimens were 3 times larger in number of cycles prior to failure in contrast with the untreated specimens after the treatment. The main reason for the revealed changes was the

certain softening of the subsurface layer while the hardened specimens were extremely sensitive to the nucleation of microscopic cracks that was completed by the rapid appearance and the growth of the main fatigue crack.

Acknowledgements

The research was performed with the partial financial support of the RFBR project No. 13-08-90402 Ukr_f_a, as well as SB RAS III.20.1.3 and grant of the President of the Russian Federation NSH-2817.2014.1 "School of academician V.E. Panin". Some of structural studies were carried out in the Center of shared use of high-tech equipment "Nanotech" at ISPMS SB RAS.

References

- [1]. V.E. Panin, V.E. Egorushkin, A.V. Panin. Nonlinear wave processes in a deformable solid as a hierarchically organized system. V. 15. № 3-4. pp. 133-146.
- [2]. V.E. Panin, V.E. Egorushkin. Curvature solitons as generalized structural wave carriers of plastic deformation and fracture. Physical Mesomechanics. V.16. № 4. pp. 267-286.
- [3]. S.V. Panin, I.V. Vlasov, V.P. Sergeev et.al. Improvement of fatigue durability of steel 12Cr1MoV by a surface nanostructuring with ion beam Zr+. Part 1. Structure, properties and fracture character. Phys. Mesomech. 2012. V.15. № 6. pp. 93-106.
- [4]. A.S.Zubchenko, M.M. Koloskov, Yu.V. Kashirsky et al. Reference book of steel types, second ed. M.: Mashinostroenie, Moscow. 2003. 784 p.
- [5]. S.V. Panin, S.K. Yussif, V.P. Sergeev et al. Multiple cracking as a way of increasing the resistance to fracture of surface-hardened materials, Advanced materials. V. 1, № 13. Spec.iss. (2011) 177-186.
- [6]. V.E. Panin, V.P. Sergeev, A.V. Panin. Nanostructuring of surface layers of structural materials and deposition of nanostructured coatings. Izdatelstvo TPU, Tomsk, 2008. 286 p.

THE DETERMINING OF METAL GRAIN SIZE BY ACOUSTICAL STRUCTURAL NOISE

V.V. Muraviev¹, A.J. Kotolomov, A.V. Baiteryakov¹, A.I. Dedov¹

¹ Kalashnikov Izhevsk State Technical University, Russia.

² Gazprom Transgaz Tchaikovsky, Tchaikovsky.

Abstract

This study demonstrates the method used to determine the grain size of steel grade C45 by becoming the mean amplitude of the acoustic structural noise. It describes the method of measurement and the algorithm of processing the signal received by the defectoscope, and displays coincidence of theoretical and experimental research.

Keywords: ultrasound, structural noise, dispersion of ultrasound, grain size.

Introduction

Most of the methods for assessing the structural condition of the metal are based on the measurement of ultrasonic wave velocity or attenuations of ultrasonic waves [1-3].

The use of the electromagnetic acoustic excitation-reception method for ultrasonic wave measurement, increases the applied facilities of the structurescopy [4-6]. A considerable part of the work is devoted to investigating the deflected mode of products and the thermal hardening of metals by the parameters of ultrasonic waves [7-11]. An investigations on the influence of grain size on the rate of propagation of acoustic waves in different metals and alloys are presented in [1, 12]. Of particular interest are studies on the effect of fatigue damage accumulation on acoustic wave characteristics [13-15].

This article presents the new method used to determine the grain size of steel grade by becoming the mean amplitude of acoustic structural noise.

Used approaches

Acoustic wave propagating in such a solid generates scattered waves that propagate in any direction and do not support the main stream of the wave. The

attenuation coefficient of δ_d of ultrasonic waves caused by the scattering depends on the relationship between the wavelength λ and the average grain size D_g . For the most construction materials, condition is performed $D_g \ll \lambda$ ($D_g=20 \div 100$ microns, $\lambda=0,5 \div 6$ mm in the frequency range from 1 MHz to 5 MHz). Scattering in this area is called Rayleigh and occurs on particles with sizes smaller than the acoustic wavelengths. Thus this ratio δ_d is proportional to the third degree of the grain diameter D_g^3 and the fourth degree of the frequency f^4 .

In particular, the coefficient of the attenuation of longitudinal waves δ_l of medium-carbon steel, due to absorption δ_a and scattering δ_d , may be calculated by the simplified formula:

$$\delta = 20f^4 D_g^3 \quad (1)$$

where f - frequency [MHz], D_g - the average grain diameter [mm].

Using the formula [12], we can calculate the average level of structural noises U_{sn} in the near (formula (2)) and the far surface (formula (3)) for the combined areas of the transmitter:

$$U_{sn} = U_0 \frac{\lambda}{2} \sqrt{\frac{\delta C \tau}{\pi S}} e^{-2\delta r} \quad (2)$$

$$U_{sn} = U_0 \frac{1}{2r} \sqrt{\frac{\delta C \tau S}{2\pi}} e^{-2\delta r} \quad (3)$$

whereas U_0 - the amplitude of the transmitted signal, λ - the length of the ultrasonic waves, δ_d - ultrasound scattering coefficient, C - the speed of the ultrasonic waves in the medium, τ - duration of the ultrasonic pulse, S - area of the transducer, δ - the damping coefficient, r - distance from the transducer to the scattering region.

Presented formulae (1) - (3) allow us to investigate the influence of grain size (D_g) and piezoelectric transducer parameters (f , S , τ) on the level of structural noise.

On one hand, the level of structural noise is related with scattered

ultrasonic waves in the structural inhomogeneities in metal produce

$$U_{sn} \sim \sqrt{\delta_d} \sim \sqrt{D_g^3};$$

On the other hand, the structural noise is related with scattered ultrasonic waves attenuation:

$$U_{sn} \sim \exp(-2\delta r) = \exp\left[-\left(0,12f + 20D_g^3 f^4\right)r\right] \quad (4)$$

Measurement Procedure

The amplitude of structural acoustic noises is generally much less than the level of back wall echo, so registration of structural noise requires increasing the amplitude. It is proposed to use the Rayleigh wave signal as reference due to its re-emission in the reception prism. Unlike the back wall echo, the Rayleigh wave is more stable with changes of the contact or the surface roughness and does not depend on the condition of the back wall surface [16].

It is proposed to use the ultrasonic defectoscope DUC-66 and double-crystal transducer P112-5,0-Ø8. For saving and the further processing of the electrical signal to the output «VideoSignal» of defectoscope connected to the digital oscilloscope RIGOL DS1102C, is synchronized with the defectoscope through the synchronization line.

The pulses are generated as a result of the inverse scattering of ultrasound on the inhomogeneous structure, and form the structure noise, which has the form of separated, closely located peaks in the structurescopy's display. Depending on the random phase relationship of individual scattering pulses, they can strengthen or weaken each other.

The type of the amplified signals of structural noise in the control zone between the pulse Rayleigh waves and back wall echo shows the structural noise in the sample (Fig. 1).

The result of structural noise is thanks to the waves interference, therefore our methodology estimates that the integrated characteristic of structural noise is defined as a result of structural noise integration on all working areas after the interpolation of the digitized signal.

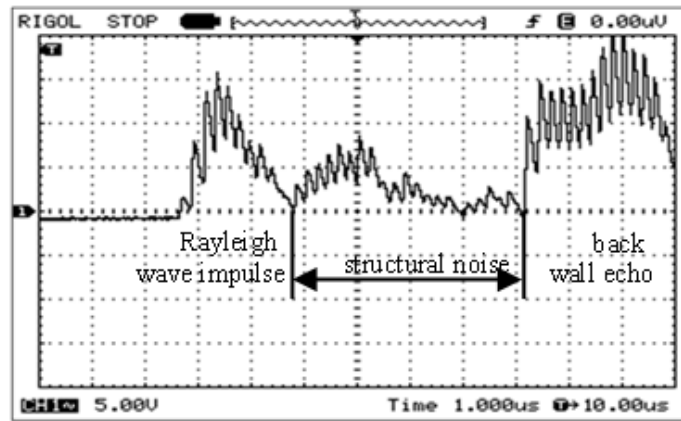


Fig. 1. The Oscillogram of pulses on the oscilloscope screen: the zone of structural noise.

To test the developed methodology of structural noises research, prepared samples from round hire bar of constructional steel (C45E) in the form of disks with a diameter d and height h and with different thermal treatments, that implement different structures with different grain number. The main characteristics of the samples are shown in Table. 1.

Table 1. Characteristics of samples for research.

No of the sample	Type of thermal processing	Temperature of heating under quenching, °C	Number of grain G / average diameter of grain D_g , a μm	Structure
1	Original condition (normalization)	850	5/ 62	perlite + ferrite
2	Water quenching	780	8/ 22	martensite
3	Oil quenching	850	7/ 31	martensite + troostite
4	Quenching+ tempering	850+600	6/ 44	sorbite
5	Original condition (normalization)	850	5/ 62	ferrite + perlite
6	Superheating for annealing	1050	3/ 125	coarse - grained ferrit + perlite

Pictures of flat grinding microstructures of samples surface after etching in 4 percent of HNO_3 aqueous solution for separation of grain boundaries obtained by a microscope Altami c MET 1M shown in Fig. 2.

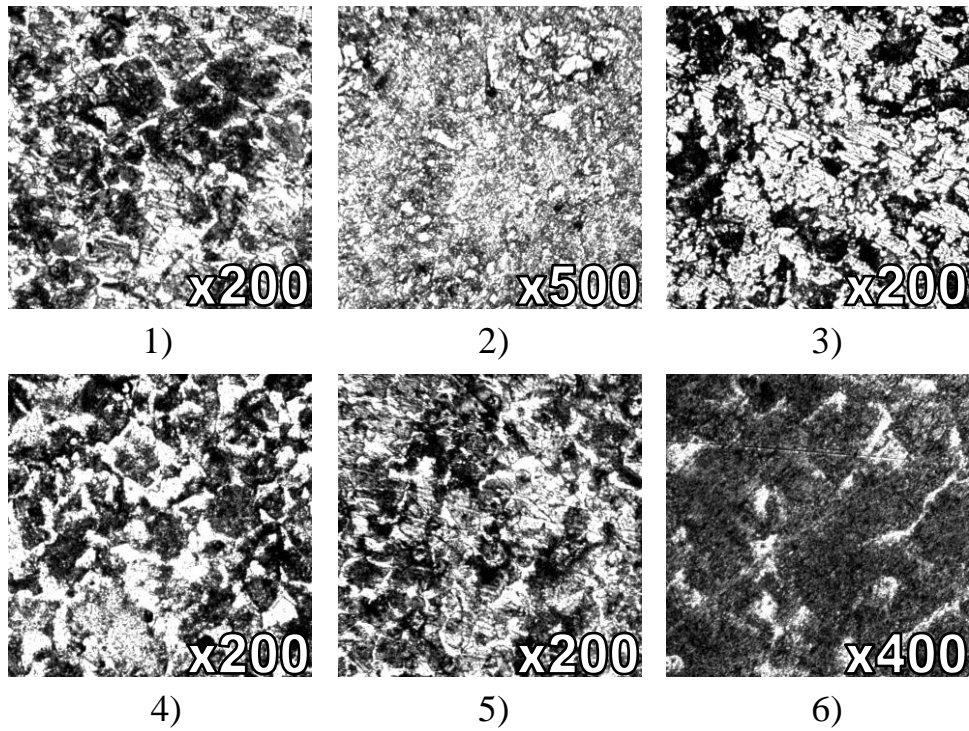


Fig. 2. Metallography of samples: a) the sample number 1; b) the sample number 2; c) the sample number 3; d) the sample number 4; e) the sample number 5; e) sample number 6.

Results and Discussion

Fig. 3 reflects the ratio structural noise U_{sn} - Rayleigh wave for the studied samples. The ratio structural noise $U_{sn} - U_{bp}$ base echo practically coincides with the above diagram. The intervals of vertical deviations correspond with deviations in the level values of structural noise in various areas of the samples. Intervals of vertical deviations corresponding to deviations of structural noise level in various areas of the samples. Note that deviations in the level of structural noise in respect with its average value remains within the deviations in the size of metal sample grain in respect with its average value.

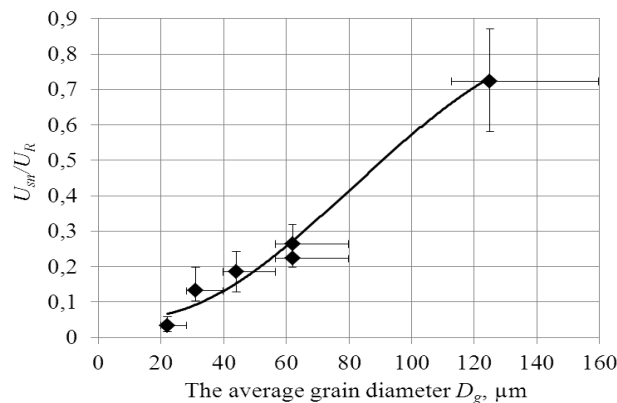


Fig. 3. Graphic relation: structural noise – impulse of Rayleigh wave.

The fact that there is a relation between the level of structural noises and the size of the metal sample grain proves that our methodology can be used for metal structure assessment. In this regard, deviation in the level of structural noises makes it possible for us to state structural inhomogeneity in different areas of metal samples.

The analysis of the results of theoretical and experimental (metallographic and acoustic) research shows that the amplitude of the ultrasonic waves reflected from the structural elements is directly proportional to the size of grains in the heat-treated samples of steel C45E. This dependence agrees with theoretical predictions.

The developed algorithm of the structurescopy, with help of the structural noise, may be automated and used in manufacturing and quality control and also for the maintenance of units currently in operation.

Conclusions

For the first time in the field of ultrasonic structurescopy a new approach is being offered to evaluate the condition of metal structures, and is based on the value of the integral level of structural acoustic noise.

The methodology of structural acoustic noise assessment is based on most the efficient selection of acoustic wave frequencies, as well as control areas, probe pulses (impulse Rayleigh waves), signal processing algorithm.

It was proven that there is a monosemantic ratio between heat-treated samples of steel C45E and the average amplitudes of structural noises.

Summary

For the first time in the field of ultrasonic structurescopy a new approach is being offered to evaluate the condition of metal structures, and is based on the value of the integral level of structural acoustic noise. The methodology of structural acoustic noise assessment is based on most the efficient selection of acoustic wave frequencies, as well as control areas, probe pulses (impulse Rayleigh waves), signal processing algorithm. On the example of steel C45E shows the experimental results of the determining of metal grain size by

acoustical structural noise.

It was proven that there is a monosemantic ratio between heat-treated samples of steel C45E and the average amplitudes of structural noises. This dependence agrees with theoretical predictions.

Acknowledgments

The work was supported by the Program of fundamental investigation URD RAS (project № 12-Y-2-1013), Strategic Development Program of "Kalashnikov Izhevsk State Technical University "for 2012-2016 (project ПСР/М2/Н2.5/МВВ).

References

- [1]. V.V. Murav'ev, E.V. Boyarkin. Nondestructive testing of the structural-mechanical state of currently produced rails on the basis of the ultrasonic wave velocity. Russian Journal of Nondestructive Testing. 2003. M. 39 № 3. p. 189.
- [2]. V.V. Murav'ev, O.V. Muravyeva, E.N. Kokorina. Izv. Vyssh. Uchebn. Zaved. Chern. Metallurg., 2013, № 4, pp. 66–70.
- [3]. V.V. Murav'ev, O.V. Korobeinikova, A.V. Platunov. Izv. Vyssh. Uchebn. Zaved. Chern. Metallurg., 2009, № 6, pp. 44–48.
- [4]. V.V. Murav'ev, O.V. Muravyeva, A.V. Platunov, D.V. Zlobin. In heat-treated steel wires using the electromagnetic-acoustic method. Russian Journal of Nondestructive Testing. 2012. V. 48. № 8. pp. 447-456.
- [5]. V.V. Murav'ev, O.V. Muravyeva, E.N. Kokorina. Quality control of heat treatment of 60c2a steel bars using the electromagnetic-acoustic method. Russian Journal of Nondestructive Testing. 2013. V. 49. № 1. pp. 15-25.
- [6]. V.V. Murav'ev, O.V. Muravyeva, Ye.N. Kokorina. Optimization of magnetization systems of encircling electromagnetic-acoustic transducers of volume waves for nondestructive testing of rolled rod. Sensors and systems. 2013, №2. pp. 2-9.
- [7]. G.A. Budenkov, V.V. Murav'ev, O.V. Korobeinikova. Fundament. Probl. Sovremen. Materialoved. V. 6, 2009, № 3, pp. 111–117.

- [8]. V.V. Murav'ev, O.V. Muravyeva, V.A. Strizhak, A.V. Pryakhin, E.N. Balobanov, L.V. Volkova. Evaluation of residual stresses in rims of wagon wheels using the electromagnetic-acoustic method. Russian Journal of Nondestructive Testing. 2011. V. 47. № 8. pp. 512-521.
- [9]. V.V. Murav'ev, S.Yu. Petrov, A.V. Platunov, E.N. Balobanov, L.V. Volkova, A.A. Ryabov, O.V. Sokolov, T.P. Pechenova, V.V. Kostyuk. Distribution of residual stresses under the electrocontact hardening of loco_motive wheel treads, Tekhnol. Mashinostr., 2011, № 9, pp. 42–45.
- [10]. V.V. Murav'ev, L.V. Volkova, E.N. Balobanov. Estimation of Residual Stresses in Locomotive Wheel Treads Using the Acoustoelasticity Method. Russian Journal of Nondestructive Testing, 2013, V. 49, № 7, pp. 382–386.
- [11]. V.V. Murav'ev, L.V. Volkova. Evaluation of the Interference Value for the Treads of Locomotive Wheels by the Acoustic Elasticity Method. Russian Journal of Nondestructive Testing, V. 49, № 9, pp. 524–529.
- [12]. V.V. Murav'ev, O.V. Muravyeva, A.V. Bayteryakov, A.I. Dedov. Method for determination of acoustic structural noise of metals. Intellekt. Sist. Proizv., 2013, № 1, pp. 143–148
- [13]. L.B. Zuev, V.Ya. Tsellermaer, V.E. Gromov, V.V. Murav'ev. Ultrasonic monitoring of the accumulation of aging damage and recovery of the useful lifetime of industrial parts. Technical Physics. The Russian Journal of Applied Physics. 1997. V. 42. № 9, pp. 1094-1096
- [14]. L.B. Zuev, V.E. Gromov, V.V. Murav'ev. Prikl. Mech. and Technical Physics. 1998, V. 39, № 4, pp. 180-183.
- [15]. L.B. Zuev, V.V. Murav'ev, Yu.S. Danilova. Criterion for fatigue failure in steels. Technical Physics Letters. 1999. V. 25. № 5, pp. 352-353.
- [16]. G.A. Budenkov, O.V. Nedzvetskaya. On calculation of the piezoelectric transducers of rayleigh waves. Russian Journal of Nondestructive Testing. 1992, № 10, pp. 76-81.

STEEL MODIFICATION BY BARIUM AND STRONTIUM

O.I. Nokhrina, I.D. Rozhikhina, V.I. Dmitrienko, M.A. Platonov

Siberian State Industrial University, Novokuznetck, Russia.

E-mail: kafamsf@sibsiu.ru

Steel modification process by the natural materials containing barium and strontium was considered in this work.

The process of barium and strontium reduction by silicon and aluminium with the usage of thermodynamic simulation methods was also examined here.

Influence of steel treatment by barium-strontium modifier on the structure formation and mechanical properties of steel was investigated as well.

The investigated results were realized while 25G2S steel melting in the electric furnace of Joint Stock company “EVRAZ-WSSW” foundry shop.

1) It is hard to improve some properties of traditional materials without using new technologies. One of the main conditions of the development of steel production technologies is the usage of comparatively cheap materials in the form of different complex alloys and mixtures, allowing to control a physico-chemical state of metallic melt and obtain metal products with some improved operational characteristics. And qualitative characteristics of materials used for refinement and modification are to provide stability, effectiveness, economy and ecological security of technologies.

2) Obtaining barium – and strontium containing ligature is power-consuming, laborious and raw material intensive production in ferrous metallurgy. The processes of smelting, pouring, granulation, crushing and packaging of ligature demand both many labor inputs and are accompanied by metal losses. The production data are ecologically harmful and explosive. In this connection the perspective point is the creation of modification technologies allowing steel modification by barium and strontium from natural materials avoiding the stages of ligature production. In natural materials there is barium and strontium in the form of compounds: BaSO_4 , SrSO_4 , BaCO_3 , SrCO_3 .

3) The unique deposit of complex carbonate iron ore containing calcium, barium, strontium is discovered and developed in the north-east of Irkutsk region, Russia [1].

4) Iron ores have the following mineral composition: Sr-Ca-Ba carbonate (70 – 80 %), potash feldspar (10 %), pyroxene (10 – 20 %).

5) Joint Stock Company “NPK Metalltechnoprom” produces barium-strontium modifier BSK-2 according to TU 1717-001-75073896-2005.

This modifier is for steel production, cast iron and non-ferrous alloys and also for welding electrode covering. Chemical analysis results of the barium-strontium modifier are demonstrated in Table 1.

6) X-ray phase analysis results showed that the main compounds containing in the barium-strontium modifier are barium-calcite $\text{BaCa}(\text{CO}_3)_2$, calcite CaCO_3 , calciostrontianite $\text{CaSr}(\text{CO}_3)_2$, dolomite MgCO_3 and siderite FeCO_3 .

7) Differential-thermal analysis was applied to study some phase and structural transitions taking place in iron ore mineral constituents of the barium-strontium modifier.

Table 1. Chemical composition of the barium-strontium modifier, %.

BaO	SrO	CaO	SiO ₂	MgO	K ₂ O	Na ₂ O	Fe ₂ O ₃	MnO	Al ₂ O ₃	TiO ₂	CO ₂
13,0-19,0	3,5-7,5	17,5-25,5	19,8-29,8	0,7-1,1	2,5-3,5	1,0-2,0	1,5-6,5	0,0-0,4	1,9-3,9	0,7-1,1	16,0-20,0

8) The results of DTA demonstrate that there is the dissociation of dolomite, calcite, barium-calcite and calciostrontianite before the temperature reaches 1223 K. Carbonites decomposition of barium and strontium occurs when the temperature is higher than 1223 K, this means that the temperature (1873 – 1923 K) of steelmaking processes is of interest to study the behavior of oxide compound of barium and strontium.

9) Usually the modification is carried out at a final stage of production: either while from the furnace to the ladle or out-of-furnace steel treatment in

the ladle, or while steel casting. Carbon, silicon, aluminium can be considered as reducing agents at different stages of out-of-furnace treatment. The methods of thermodynamic modelling realized in the program complex (“Terra”) were used for determining the conditions of barium and strontium reduction. The analysis of theoretical calculations demonstrated that carbon doesn’t reduce barium and strontium from their oxides under the temperature typical for steelmaking processes (1873 – 1923 K); silicon can reduce barium ($\approx 60\%$), but strontium can’t do it (only 15%); the degree of barium and strontium reduction from their oxides reaches 70 – 50% when aluminium is used. The temperature in the interval of 1873 – 2973 K doesn’t influence greatly upon the reduction degree of these elements (Fig. 1) [2, 3].

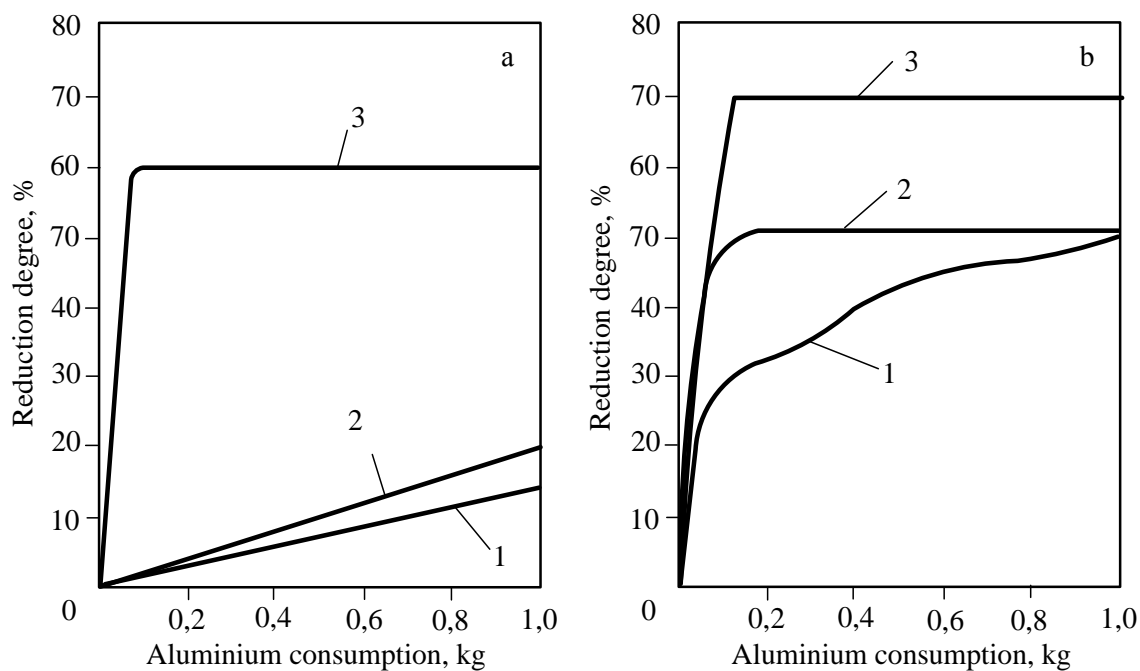


Fig. 1. Variation of strontium reduction degree under the temperatures of 1873 K (1) and 2073 K (2) and of barium – 1873 – 2073 K (3) from their oxides depended on silicon (a) and aluminium (b) consumption.

10) Some laboratory investigations were conducted with metal for studying the process of melted slags interaction containing barium and strontium compounds.

11) Slag forming mixtures (lime, strontium carbonate, barium oxide, barium-strontium modifier) with aluminium powder were added on the surface of liquid steel, deoxidated by silicon preliminarily. During comparative experiments barium and strontium compounds were not added in the slag mixture.

12) The prepared samples were studied using metallographic analysis. The analysis of the results demonstrated that metal treatment by barium and strontium compounds doesn't greatly influence on the formation of nonmetallic on structure inclusions. The presence of barium and strontium compounds affects formation.

13) The sample, that didn't have barium and strontium compounds in the composition of slag forming while smelting, possessed Widmanstatten structure, typical for steels with low mechanical properties, but the samples treated by slagforming mixtures, containing barium and strontium, had the structure being like lamellar pearlite with ferrite isolation on the grain boundaries and separate ferrite isolation in the pearlite grains typical for steels with higher construction strength.

14) The analysis results of chemical composition didn't show the presence of barium and strontium in the samples hypothetically because of their little quantity.

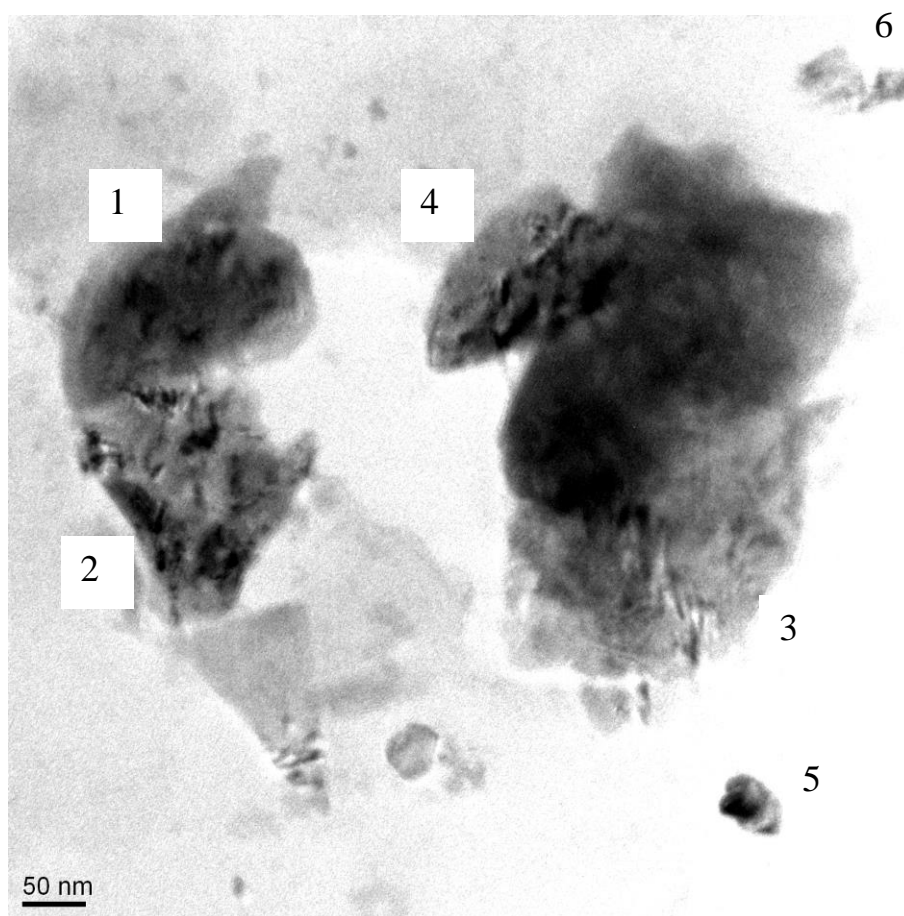
15) These samples were studied by the method of scanning electron microscopy for detecting barium and strontium in steel. The investigation results are presented in Table 2.

Table 2. Relative average values of element analysis results of the samples surface.

Barium, %			Strontium, %		
Ferrite grain	Perlite grain	Interface	Ferrite grain	Perlite grain	Interface
Sample № 4					
0,2	0,05	0,0	0,7	0,85	0,08
Sample № 5					
0,05	0,05	0,05	0,3	0,09	0,0

16) Data from Table 2 show that barium and strontium are located differentially according to structural constituents of metallic matrix. Grains volume of pearlite and ferrite is the zone of preferable barium and strontium location.

17) Steel structure analysis was carried out by the method of the extraction replicates with the usage of transmission electron diffraction microscopy to detect the zones of barium and strontium location in steel (solid solution or inclusions of the second phases). The obtained results demonstrate that the particles, extracted on the replicate, have got small sizes: in the range of 50 – 500 nm, but the analysis of microelectron pattern shows the presence both oxides and carbides of iron and barium and strontium compounds: C_2BaO_4 , $SrFeO_{2,97}$, $Ba_2Fe_6O_{11}$, $BaSrFe_4O_8$, $Ba_3Fe_2O_6$, $Ba_2Fe_{14}O_{22}$ (Fig. 2) in the investigated samples.



1, 2 – $SrCO_3$; 3 – Fe_3O_4 ; 4 – $BaSrFe_4O_8$; 5 – $Ba_3Fe_2O_6$; 6 – $Ba_2Fe_{14}O_{22}$

Fig. 2. Fragment of an electron-microcopy analysis by the method of electron replicates.

18) The conducted investigations confirmed that barium and strontium participate in the forming of structural constituents actively at the moment of crystallization. The presence of barium and strontium in the grain volume demonstrates the interaction of these elements with the metal melt and the influence on structural formation of metal matrix. The presence of complex compounds containing barium and strontium shows at the interaction of the elements of non-metallic inclusions. The detected compounds sizes confirm that the interaction of barium and strontium compounds occurs on a nanolevel.

19) Thus, on the basis of theoretical and experimental investigations they can suggest the following technological foundations of steel modification by the barium-strontium modifier:

- carbonates decomposition of calcium, barium and strontium;
- smelting of the barium-strontium modifier and barium reduction from oxide by silicon under slag deoxidizing;
- calcium, barium and strontium reduction from oxides and carbonites by the aluminium input;
- barium and strontium reduction from aluminium oxides and by silicon dissolved in steel.

References

- [1]. O.I. Nokhrina, V.I. Dmitrienko, I.D. Rozhikhina, M.A. Platonov. Ispolzovanie karbonatita dlya microlegirovaniya stali. *Izv. vuzov. Chernaya Metallurgia*. 2010. № 6. pp. 30 – 40.
- [2]. O.I. Nokhrina, I.D. Rozhikhina, M.A. Platonov, V.I. Dmitrienko. Vosstanovlenie bariya e strontsiya v protsesse obrabotki stali. *Chernie metalli: Ruda e metalli*. Moskva, 2011. №4. pp. 29 – 31.
- [3]. V.I. Dmitrienko, I.D. Rozhikhina, O.I. Nokhrina, R.S. Aizatulov, M.A. Platonov. Issledovanie vosstanovleniya bariya e strontsiya primenitelno k usloviyam vnepechnoi obrabotki stali. *Izv. vuzov. Chernaya Metallurgia*. 2012. № 4. pp. 27 – 29.

MECHANISM OF AIR LAYER STAGNATION FOR HEAT INSULATION PURPOSES

V.V. Sterligov

Siberian State Industrial University Russia

In the high temperature thermotechnical units a brickwork made of refractory materials plays a particularly important role. In furnaces a brickwork influences directly the main process in them – heat transfer to the material being heated [1], and to a lesser extent, a brickwork influences the heat performance of a furnace, heat loss values through it. In boilers, the ‘screen’ tubes take the main part of heat flow, the brickwork role is somewhat limited and is reduced to preventing the heat losses from the boiler’s work (combustion chamber) space. [2]

Recent trends for brickworks and boilers’ masonry, especially water heating ones, are toward the use of the new effective heat insulating materials, e.g. multisiliceous felt (MSF). Magnesian daubing is recommended [2] as a protective coating.

We propose to use air interlayer being produced by some structure of periodic constitution as a insulation layer.

When a furnace or boiler is working, a free (natural) convection [Fig.1] will be developed on the brickwork surface facing the open space.

Intensity of heat exchange is defined by the equation [3]:

$$Nu = C(Gr \cdot Pr)^m, \quad (1)$$

where Nu , Gr , Pr – are Nusselt, Grashof and Prandtl similarity numbers, respectively.

For the case of the most intensive heat exchange $C = 0.135$, $m = 0.33$ [3]. Since Prandtl number for gases is a constant value and from [4] $Pr = 0.71$ for air, then after substitution in the equation (1) we shall obtain such conditions

$$Nu = 0.12 \cdot Gr^{0.33}$$

Getting the α value makes it possible to define the heat flow density by the equation:

$$q_k = 0.12 \cdot \lambda_b \cdot \frac{\sqrt[3]{g \cdot \beta}}{\nu^2} \cdot \sqrt[3]{\Delta t} \cdot \Delta t, [W/m^2] \quad (2)$$

In case of stagnant air interlayer on the surface of the main heat insulation layer, the heat flow density is expressed by the equation:

$$q_t = \frac{t_{CT} - t_{B_{III}}}{\frac{\delta_b}{\lambda_b}} = \frac{\lambda_b \cdot \Delta t}{\delta_b}, [W/m^2] \quad (3)$$

Comparison of heat exchange intensity for the two cases may be received from the ratio:

$$\frac{q_k}{q_r} = 0.12 \cdot \frac{\sqrt[3]{g \cdot \beta}}{\nu^2} \cdot \sqrt[3]{\Delta t} \cdot \delta_b \quad (4)$$

It is evident that when $\frac{q_k}{q_r} > 1$ more heat is taken away by free convection, and conversely, if $\frac{q_k}{q_r} < 1$. It is apparent, that when $\frac{q_k}{q_r} = 1$ it occurs a 'reversal' of the effect, a crisis develops in this situation to which some 'critical' value of air interlayer thickness corresponds as the main acting factor in this process.

Then, having written the condition $\frac{q_k}{q_r} = 1$ on the left side of the equation (4), we obtain

$$\sigma_{kr} = \frac{1}{0.12 \times \sqrt[3]{\frac{g \beta \Delta t}{\nu^2}}} \quad (5)$$

For estimating the order of δ_{kp} magnitude the practical data of working water boiler of KV type were used: $t_{st} = 160^\circ C$, $t_v = 20^\circ C$ and the average temperature of air layer $t_{low} = 90^\circ C$ was calculated. Substitution of these magnitudes into equation (5) gave the magnitude $\delta_{kp} = 3.7 \cdot 10^{-3}$ m, which is a physically real and tangible magnitude.

If it can be possible to produce air layer of the larger thickness, then the effect will be the stronger the larger the layer thickness. Thus, the task is to

produce and hold the stagnant air near the external surface of the main layer of the lining's masonry.

The physical model for stabilization (holding) of the motionless (stagnant) air layer near some surface is heat insulation process being carried out with the use of fir. Coarse hairs, being perpendicular to the surface and located with the great frequency, keep the air layer of the thickness δ equal to the length of coarse hairs. The same system of wire hairs can be made on the masonry layer, using something like steel brush, or frequent voluminous mesh or other structure.

Mathematical interpretation of such a mechanism can be represented if we consider the moving layer of free (natural) convection as a boundary layer on the flat surface, expressed by the Prandtl equation [5].

From the derivation of this equation it follows that there is no gradient of pressure both along the flow or across it, that is $dp/dx = 0$, and $dp/dy = 0$. It means that any resistance to flow movement, resulting in the energy loss, cannot be compensated at the expense of piezometric pressure.

Solving the Prandtl equation for boundary layer is possible by using integral methods on the basis of the momentum conservation law (pressure quantity). Having equated the change of momentum to the acting forces for this case, we shall obtain

$$\frac{d}{dx} \int_0^{\delta} \rho(W_0 - w_x) dy = \tau_w - P_{geom} \quad (6)$$

Distinction of the given case from the real boundary layer is in the boundary conditions, determining the speed of free convection layer $W_x = 0$ with $y = 0$ and $W_x = 0$ with $y = \delta$; for boundary layer $W_x = 0$ with $y = 0$ and $W_x = 0$ with $y = \delta$.

This moving layer can be visualized as the movement in flat slot made by two infinite big planes, so called "Poiseuille problem" that enables the coefficient of friction λ [6] to be determined.

If $W_0 = W_x = 0$, as it follows from boundary conditions, then the left side of the equation (6) will equal 0 and, consequently,

$$\tau_w = P_{geom} \quad (7)$$

In this equation τ_w , $[H/m^2]$, tangential stresses, i.e. friction resistance per unit surface area, and P_{geom} $[H/m^2]$ – geometric pressure being determined by the different degree of heated state (air temperature on the surface of plate and at distance beyond the layer).

$$P_{geom} = H_{gp} p_0 \left(\frac{1}{1 + \alpha t_1} - \frac{1}{1 + \alpha t_2} \right) \quad (8)$$

The equation (7) may be treated in such a way that geometric pressure may transform into dynamic one P_{dyn} , when movement begins in the heated layer, but at the expense of friction resistance or local resistance this movement is suppressed and air is held on the surface making a stagnation layer. Hence it can be written $P_{geom} = P_{din}$

But pressure losses occur on moving

$$\Delta P_{nom} = \zeta \cdot P_{din} = \zeta \cdot P_{geom} \quad (9)$$

It is evident that stagnation condition is the condition when $\Delta P_{nom} \geq P_{geom}$, that is possible in condition

$$\zeta \geq 1 \quad (10)$$

Effect of stagnation at the expense of friction only can be proved if we consider the above mentioned Poiseuille problem for flat slot which can be made by means of thin vertical ribs coated to the heat exchange surface, high enough compared to the distances between them,. The thin narrow channel is formed, as in Poiseuille problem, made by the adjacent ribs, part of heat exchange surface and stagnant environment beyond the ribs.

Losses per friction per 1 m height for this case will account for

$$\Delta P_{mp} = \lambda \cdot P_{din} , \quad (11)$$

with λ – is coefficient of hydraulic resistance. Consequently, the condition of stagnation for this case will be

$$\lambda d_e \geq 1 \quad (12)$$

Friction coefficient for Poiseuille problem [6] is

$$\lambda = 96/Re, \quad (13)$$

where $Re = \frac{wd\lambda}{\nu}$ Reynolds number.

If we use the expression $P_{dyn} = P_{geom}$ for definition of speed, then the problem for definition of d_e value can be solved, and through it the slot size for flow stagnation. For conditions $t_1 = 160^\circ\text{C}$ and $t_2 = 20^\circ\text{C}$ we shall obtain $\delta = 15 \cdot 10^{-3}$ m.

If we take the rib height twice as large as the slot size then we shall obtain 3 cm air layer, that is equal to the thickness of traditional heat insulation daubing. But heat resistance of air layer will be $0.03/0.02 = 1.5$ against $0.03/0.085 = 0.04$ for magnesian layer, that is much more effective.

The same effect may be achieved at the expense of local resistance. The coefficient of hydraulic resistance ζ for local resistance, above all, depends on the type of resistance. And systems of hairs, needles, imitating the fir structure, can be made easily on the surface where free convection is realized. We have carried out the numerical modeling of the hydraulic resistance of system of tube bundle with checkered arrangement – case giving the largest approximation to fir structure. For tubes of 1 mm in diameter and pitch of both bundle direction (along and across) $S/d = 5$, we obtained the coefficient of resistance $\zeta = 1.26$ already for 50 rows. Physical modeling confirmed the initiation of stagnation (arrest) of air layer.

This problem can be solved in terms of similarity theory. The nearest analog here will be Euler number $Eu = \Delta P/w^2\rho$. If we perform the operation $Eu \cdot Fr$, where $Fr = w^2/gl$ - Froude number, then we shall obtain the expression $(\Delta P/w^2\rho) \cdot (w^2/gl) = \Delta P/g\rho l$, the geometric pressure is given in the denominator.

The expression itself is nondimensional ratio of hydraulic resistance (pressure losses) to geometric pressure, i.e. is properly a similarity number, that

has not yet been presented in literature and that we named *Stagnation number*, having designated it as

$$Sg = \Delta P / H \rho g. \quad (14)$$

Hence, the whole problem on estimation of formation conditions of stagnation layer may be solved in the form

$$Sg = f(Gr, Pr) \quad (15)$$

Conclusions

The proposed hypothesis for the possibility of formation of stagnant air layer at free convection at the expense of hydraulic resistance for the purpose of heat insulation is confirmed by numerical modeling and experimental observations. Knowledge of basic laws will enable us to develop the necessary design solutions for the heat insulation that is more effective than traditional refractory heat insulation.

References

- [1]. M.A. Glinkov, G.M. Glinkov. General theory of heat performance of furnaces: Text book for higher school. M.: Metallurgiya, 1990. 232 p.
- [2]. M.A. Mikheev, I.M. Mikheeva. Foundations of heat transfer. M.: Energiya, 1973. 320 p.
- [3]. E.M. Zalkind. Materials for putties and calculation of protection of steam boilers. M.: Energiya, 1972. 184 p.
- [4]. E.I. Kazantsev. Industrial furnaces. M.: Metallurgiya, 1964. 451 p.
- [5]. S.I. Averin, A.N. Minaev, V.S. Shvydki et al. Mechanics of liquid and gas: Text book for higher schools. M.: Metallurgiya, 1987. 304 p.
- [6]. S.S. Kutateladze, A.I. Leontyev. Heat-and-gas exchange and friction in turbulent boundary layer. M.: Energiya, 1972. 344p.

SOLID CARBON-CONTAINING WASTES – A PROMISING FUEL FOR THERMAL-ENERGY UNITS

V.I. Bagryantsev, S.A. Brovchenko, A.P.Podolskii, A.A. Rybushkin, M.V.

Temlyantsev, A.I. Kutsenko

Siberian State Industrial University, Novokuznetsk, Russia.

The prices for energy carriers and electric energy have a tendency to rise annually. The nontraditional, renewable sources of energy such as energy of wind, sun, etc. are rather promising ones in the modern world. Nevertheless they do not find practical application in most of countries because of their climatic features and geographical position. Traditionally, coal, fuel oil and natural gas are the main types of fuel for thermal energy units. At the same time, the economic effectiveness of their application is largely predetermined by the proximity of mineral deposits and transportation expenditures of fuel. In such conditions the interest to a local fuel increases greatly, especially to cheap one, on the basis of technogenic wastes, and the researches on the effective technology development of its combustion become especially actual.

We shall carry out the analysis of the most widely spread types of carbon-containing technogenic wastes [1].

Waste coal.

This type of carbon-containing wastes is characteristic of coal mining countries and regions. In particular, nearly 3 billion tons of solid technogenic and domestic wastes are cumulated in Russia, in Kuzbass, and waste coal forms the main volume in them. The appreciable volumes of these types of wastes are connected with the circumstance that coal content in waste coal may reach 25% and more on realization of the technologies being used at coal dressing plants. Most part of waste coal can be characterized as high-ash, oxidized, fine dispersive, and with a higher humidity. Due to a low specific combustion heat and low gas permeability the coal wastes of these types are not useful for the

combustion by the traditional method, e.g. in fuel-bed firing furnace. As a result the wastes are directed to the waste dumps and form the transfer of large useful territories for the solid waste storage and for sanitary-protection zone of coal mining enterprises.

The repeated efforts of scientists to develop the new types of fuels on the basis of waste coal used the method of pelletizing (production of fuel pellets) or briquetting of dispersed materials (production of fuel briquettes). In both cases the obtained fuel is oriented for combustion in dense-bed firing furnaces which have a number of significant disadvantages: a relatively high chemical and physical incomplete combustion, considerable discharge of harmful substances into atmosphere, etc. In pelletizing and briquetting the choice of a binder and technologies, determining the price and the strength characteristics of the fuel being obtained, play the critical role. From the point of view of heat engineering the pelletizing and briquetting are undesirable processes compared to a fine-dispersion combustion because, when consolidating a dispersed fuel, they decrease its surface of reaction and accordingly, reduce the intensity of heat generation processes.

A rather officially accepted direction is manufacturing of the water-coal fuel (WCF), water-coal suspensions (WCS) or cavitation water-coal fuel (CWCF) [2, 3] on the basis of waste coal. This direction is based on the production of liquid fuel in which the coal containing component is coal slurries being formed in coal dressing and coal hydraulic mining, or grinded coal particles (by dry and wet method) to the size of 0 – 100 mcm. Water is a transporting liquid phase, and special additives and admixtures are introduced in the fuel composition to increase a liquid phase fraction, liquid-mobility of water-coal fuel and to prevent its layering (precipitation of dispersed particles, formation of water interlayers and lenses).

Cavitation water-coal fuel has a number of features [3]. Its manufacture is characterized by a high level of local dynamic compressive and temperature effect on the material treated. Solid parts are ground to the high degree of

dispersion, and a suspension acquires a number of new properties, in particular, a long-term stability and high plasticity with solid phase content up to 70%. A dried fuel transforms to a stable suspension state when water is added, with no mechanical effect; a fuel does not increase in volume on freezing and it restores its properties after defrosting.

The obtained water-coal fuel is burnt by analogy with a liquid fuel with the use of special burner nozzles. Due to the high humidity and ash-content the water-coal suspensions have a limited field of application. They are used mainly as a fuel for thermal-energy units, water and steam boilers.

Water-coal fuel and cavitational water-coal fuel have a number of essential advantages over the pulverized-coal fuel. This type of fuel is fire-and explosion-proof and the presence of water in its composition influences correspondingly the kinetics of burning processes by its intensification. Typical of water-coal fuel is far less discharges of harmful substances into atmosphere, including nitrogen oxides and carbon monoxide as compared to combustion of fuel in a dense layer. Water-coal fuel manufactured by traditional principle have many disadvantages: complex and expensive system of fuel preparation; necessity of realization of special measures on increasing a wear resistance of burners and fuel-supply system (high content of solid particles in water-coal fuel results in the intensive wear of transfer pumps, pipelines, stop and control valves, and burner nozzles as well); complexity of large distance transportation in the conditions of below-zero temperatures, etc. [2, 3].

The promising direction is combustion of pulverized-coal fuel in open flame or in boiling layer (bubble or circulating) [3]. These technologies allow to burn a fine-dispersed, non-watered carbon-containing material. Typical of them is a developed surface of fuel reaction, and it results in the intensification of combustion. Movement of solid particles in a gas flow facilitates its turbulization and increase of emissivity factor, and it intensifies greatly the processes of convectional and radiation heat exchange and reduces a chemical and mechanical incomplete burning.

According to data of papers [3, 4] the combustion feature of a carbon-containing fuel in a boiling layer is that the quantity of solid particles in it makes up 5 – 10% of total mass of layer, this makes it a peculiar muffle, thermally inertial and stable. In these conditions the change of properties and heat engineering characteristics of fuel influences the work of the thermal energy unit to a smaller degree, as compared to a dense layer. In this connection the boiling layer technology is used for combustion of the low grade fuels and wastes of coal mining and waste coal. When this fuel is used the temperature of layer does not exceed 800 – 900⁰C, this practically eliminates the formation of thermal nitrogen oxides. For binding of sulphur oxides (it is important in combustion of high sulphur coals) it is possible to add a sorbent (as a rule, a limestone) [3].

At the same time, when burning a pulverized-coal fuel, some problems connected to the fire-and explosion-safety may arise, depending on the conditions of combustion, that require the development of special protection measures.

The special feature of this method is that all fuel ash goes to the combustion products and is thrown away through a chimney into the atmosphere, polluting it in the absence of dust-cleaning units. Because of this, the dust-cleaning arrangements of dry and wet gas cleaning should necessarily be installed, but depending on the method of cleaning, the complete technological process will rise in prices [2].

Technology of combustion of pulverized-coal fuel in boiling layer is rather sensitive to fractional composition of particles. In excessively fine grinding the particles are carried away by the combustion products, and in excessively coarse grinding, they settle down, forming the analogue of dense layer. Furnaces for fuel burning in boiling layer have a rather developed working space. In manufacturing the large capacity boilers with boiling layer there are some definite complexities connected to the necessity of organization of uniform fuel feeding to a boiling layer of a larger area. These boilers are characterized by a

relatively low heat load per unit area of hearth because of low rates of air supply under the grate, connected to the high carry-over of solid particles [3].

Cinder wastes of boiler plants and heat-electric generation plants. Cinder of boiler plants and heat-electric generation plants are largely considered to be a raw material for the manufacture of building materials, however these wastes may be of specific interest as a fuel or its components. Cinder may contain up to 10 – 15% (and on some cases more than that) of carbon. In fuel-bed firing of a solid fuel a part of it may fall through a boiler grate, fine particles may be carried away by combustion products, a surface of lumps may be slagged, in this case the access of oxygen to a central carbon-containing part of a lump is stopped. All these phenomena form an unburned carbon which is the cause of the high carbon content in cinder wastes. In spite of a rather large volumes of wastes of this type, their large-scale application as a fuel is complicated due to the high instability of composition, namely: carbon content, low combustion heat, need for cinder grinding, etc.

Coke dust (fines).

Coke dust is formed in the process of coke production. It is characterized by a high combustion heat and carbon content, however the volumes of its formation are relatively low. The optimal technology of coke dust utilization is considered to be briquetting [5]. The obtained briquettes are subsequently used as a fuel and a reducing agent in metallurgy.

Wastes of the logging and woodworking industries. The carbon-containing wastes of the logging and woodworking industries are sawdust, wood chips, off-wood, etc. The interest to wastes of this type is predetermined by a number of factors. In particular, according to data [7] Russia has 25% of the world's wood reserves, in this respect, the yield of woodworking wastes in some cases may reach 50 – 80%. A typical sawmill transforms about 60% of wood into planks, here, about 12% goes to sawdust, 6% - to cut ends and 22% - to half log and side

cuts [7]. The volume of sawdust and woodchips in woodworking amounts to 12% from the initial raw

A utilization sphere of the logging and woodworking industries is rather wide. It includes the manufacture of wood fibre-board and chipboard, wood laminate, wood pulp, paper-and-pulp industry, agriculture (fertilizer, fodder additives, litter) etc. A special direction is application of these wastes as fuels. Advantages of wood as a fuel is a low ash content (in most cases less than 1%) and absence of sulphur (only a bark of fir trees has the increased sulphur content) [2, 6]. This type of fuel is more harmless than coal, fuel oil and diesel fuel. At the same time, timber is characterized by a high humidity, sawdust is characterized by susceptibility to spontaneous ignition and small packed density. Taking into consideration the last-mentioned parameters, their transportation to distances more than 20 – 40 km and use as a fuel is economically disadvantageous [7]. For packed density increase the sawdusts are granulated with the aid of special technologies, obtaining the wooden granules (pellets) and briquettes [6].

Agricultural wastes.

The carbon-containing agricultural wastes are a straw, shell of sunflowers, millet seeds, rice, etc. [8]. Straw and shell of seeds have less packed density than sawdust. Therefore the logistics and economic requirements to utilization of agricultural wastes as a fuel for thermal plants, removed from the place of their reaping and storing, predetermine the need of their pelletizing [3].

In contrast to wood wastes the combustion of agricultural wastes have a number of difficulties, specified by their chemical composition. In this respect, nitrogen, being contained in straw, increases the emission of NO_2 . High content of chlorine in straw of oat, barley and rape results in the increased corrosion of heat-exchange equipment. A great content of potassium decreases the ash melting temperature, and this contributes to a formation of slag agglomerates (sinters), preventing the normal boiler performance. Analysis of chemical

composition shows that sinters consists of low-melting eutectic $K_2O - SiO_2$, the formation of which results from the potassium accumulation in a layer [8].

In fact, all technologies of combustion of the fuel made of carbon-containing waste mentioned above find a certain practical application, however their disadvantages restrict the field of their distribution, and principally, reduce the thermal effectiveness of units, operating economy and the ecological safety of their work. In this connection, the development of more universal types and technologies of combustion of solid carbon-containing fuel remains as before a currently central scientific and practical problem having a vital importance for countries and regions with sizeable volumes of technogenic wastes formation.

On the basis of the analysis made, a number of perspective directions, ensuring an increase of thermal and economy effectiveness of use of solid carbon-containing wastes as fuel for thermal-energy units may be determined:

1. maximum reduction of transportation expenses by utilization of fuel on place of waste formation;
2. facilitation in formation of the developed reaction surface of fuel, renunciation of pelletizing and briquetting;
3. conversion to the more modern technologies instead of burning a solid fuel in a dense layer;
4. realization of measures intensifying the heat-exchange processes increasing the combustion effectiveness of low-calorific fuel.

A group of scientists and engineers of Siberian State Industrial University has developed the units and technologies of combustion of different types of carbon-containing fuel from technogenic carbon-containing wastes to generate a thermal energy. For combustion of dispersed carbon-containing wastes the unit is developed the basis of which is a furnace of external combustion. The operation principle of the furnace is based on the combustion of air and solid particle mixture in the flow of high intensive gas-flame vortex, rotating around the horizontal axis at high speed.

As a calorific value of these fuels is much lower than of the traditional ones the processes of combustion and generation of heat are separated: combustion takes place in a separate furnace, a heat exchanger is outside the furnace volume as an independent unit. This solution is supported by a circumstance that some carbon-containing wastes have a high ash content, in some cases up to 40%, and in view of this, the heat-exchanging part should be especially suited to big flows of solid materials. The design of it is dictated by the arresting of ash which is in a dust state.

A diagram of a pilot plant of substandard fuel combustion in a swirling-type furnace is shown on Fig. 1. Diagram of a pilot plant of substandard fuel combustion.

Fuel is supplied to the furnace by air flow from a jet-type mill. A swirl gas flow is produced with fixed blades of a swirling unit when flow of blast air passes through them. To increase the furnace efficiency and to decrease the fuel consumption a preliminary heating of blast air to 100⁰C is provided. Flows of air and solid particle mixture are directed to one side. High intensity of heat and mass-exchange processes in gas-solid fuel system provides the high combustion rates with combustion efficiency of not less than 95%.

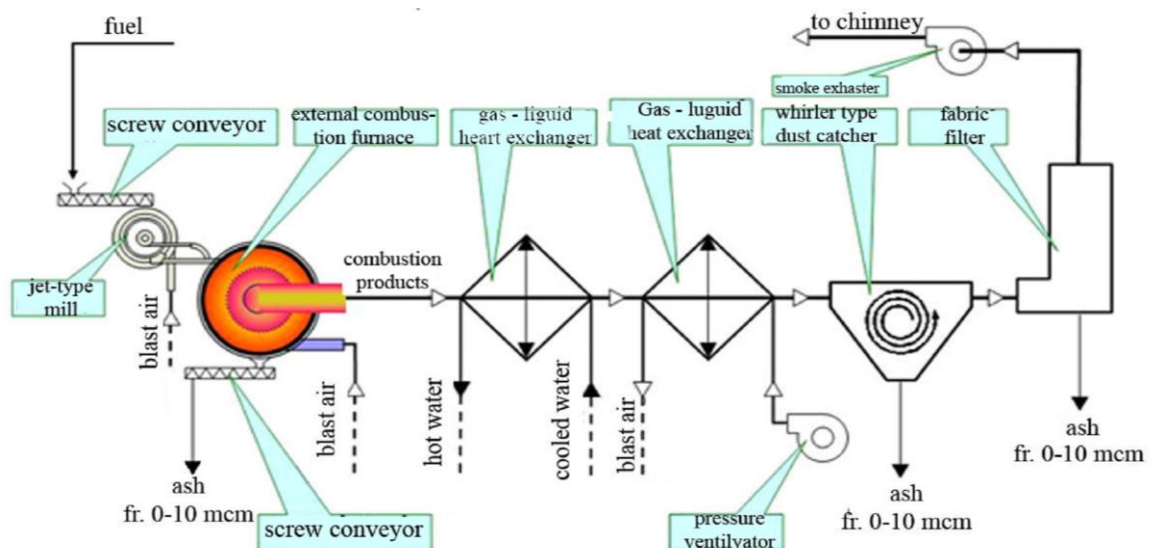


Fig. 1. Diagram of a pilot plant of substandard fuel combustion.

The combustion products at temperature of 1000⁰C are evacuated from the furnace along two gas ducts located at the end faces of the furnace. A fine (fly) ash (of fraction up to 40 mcm) in a suspension state is removed from the furnace together with combustion products. Its share in total ash mass forms up to 70%. A coarser ash (of fraction 40 – 100 mcm) is concentrated along a periphery of a vortex flow and is removed through a slot channel along two chutes to a screw conveyor of ash removal to a block of ash utilization.

It is possible to use as a fuel the waste coals, and wastes of logging and woodworking industries and agricultural and cinder wastes as well. The main requirements to fuels in combustion of coal wastes are the following: granulometric composition with fraction 0 – 10 mm (content of fraction of 0 – 5 mm is not less than 70%), humidity and ash content per working mass are not more than 17 and 45% respectively, devolatilization is not less than 11%, the lowest combustion heat is not less 4000 – 5200 kcal/kg (16.6 – 21.6 mj/kg) Depending on a dispersed composition and a type of fuel used the furnace is provided with the add-on device for its grinding, drying, and in sawdust and shell combustion – with special loading device.

Conclusions

On the basis of the carried out analysis the information about different types of solid technogenic carbon-containing wastes used as a fuel for thermal-energy units has been generalized and systemized, and the advantages and disadvantages of technologies for their combustion have been considered. The most perspective directions, ensuring the increase of heat and economy efficiency of solid carbon-containing wastes as a fuel for the thermal-energy units have been determined.

Acknowledgments

Work is performed according to the basis part of the task assigned by the Ministry of Education and Science of Russia under project No. 2014/213 for state works in the sphere of scientific activities.

References

- [1]. V.I. Bagryantsev, S.A. Kazimirov, A.I. Kutsenko, A.P. Podolskii, A.A. Rybushkin, M.V. Temlyantsev. Practice and prospects of application of solid carbon-containing wastes as fuel for thermal-energy units. Vestnik of Siberian state industrial university, 2013, № 3. pp. 33 – 38.
- [2]. V.G. Lisienko, Ya.M.Shtchelokov, M.G. Ladygichev. Fuel. Rational combustion, control and technological application: Reference book in 3 volumes. Vol. 1 / Edited by V.G. Lisienko. M.: Teploteknik, 2004. 608 p.
- [3]. A.P.Burundukov, S.V. Matuzov. Combustion of waste coal in bubbling bed boiler. Ugol, 2012. № 12. pp. 69 – 72.
- [4]. Yu.P. Korchevoi, A.Yu. Maistrenko, A.I. Topal. Ecologically clean energy technologies. Kiev: Naukova dumka, 2004. 186 p.
- [5]. Yu.V. Shuvalov, Yu.A. Nifontov, A.N. Nikitin. Briquetting of nontraditional types of fuels. Mining information – analytical bulletin. 2005, №9. pp. 161 – 166.
- [6]. V.S. Dubinin, K.M. Lavrukchin, T. A. Stepanova et al. Utilization of wood and vegetation residues for manufacture of the artificial ecologically clean solid fuel for decentralized energy supply of Russia. Industrial power engineering, 2006, № 9. pp. 44 – 47.
- [7]. N.A. Filina, S.Ya. Alibekov. Technology of utilization of wood-and petroleum-containing wastes for generation of thermal energy. Safety of vital activity, 2010. № 10. pp. 32 – 37.
- [8]. P.L. Isjemin, S.N. Kuzmin, D.M. Viryasov et al. Boiler for cinderless combustion of agricultural wastes. Industrial power engineering. 2011, № 11. pp. 55 – 58.

**THE SERVICE LIFE INCREASE OF PERICLASE-CARBON LININGS
OF STEEL-TEEMING LADLES ON THE BASIS OF APPLICATION OF
COATINGS PREVENTING THE REFRACTORY MATERIAL'S
DECARBURIZATION ON HEATING**

M.V. Temlyantsev

Siberian State industrial University, Novokuznetsk, Russia.

Nowadays the carbon-bearing tar-bonded refractory materials, mainly, periclase-carbon and alumino-periclase-carbon ones, in which flaked graphite is carbon component, have gained acceptance both in Russia and abroad for manufacturing the working layer of linings of steel-teeming ladles and ladle-furnace units. For lining of ladle's slag line area the carbon content usually is not more than 15 % in refractory materials. For ladle's wall lining the refractories with carbon content of not more than 10% are used as a rule. While having many advantages, the ladle carbon-bearing refractories have a significant disadvantage – they oxidize (decarburize) at high temperatures in contact with oxygen and other gases-oxidizers.

After manufacturing of the new lining (capital repair) or full replacement of working layer the ladle is subjected to drying and first heating before filling-in the metal. The duration of heating before filling-in the metal is in average from 12 to 24 hours, and temperature of lining's heating is 1000 – 1200⁰C. The heating of the lining is usually done on special drying installations equipped with burners, and heating is actually carried out by the red hot combustion products of gaseous fuel (usually natural gas). In this case, the oxidizing atmosphere of combustion products containing gases-oxidizers: O₂, CO₂, H₂O and in some cases SO₂ is formed in the space of the ladle. The industrial and laboratory experiments [1 – 3] show that on the first heating of new lining a complete decarburized layer to the depth of 10 mm is formed on the surface of the refractory material due to the high temperature oxidation of carbon (graphite) in the atmosphere of combustion products. The decarburized layer of

the refractory material in which carbon (graphite) has burned (oxidized) is characterized by lower strength, higher porosity and low resistance against washout of the melt. In contact with liquid steel the decarburized layer of the refractory material is intensively destructed by the melt and in the process of 1 – 5 fillings the layer fully goes to metal that may result in the contamination of steel by the nonmetal inclusions of lining origin.

For the reduction of decarburization intensity of periclase-carbon refractories at the heating stage, the different measures are realized that are divided into four groups:

- 1) optimization of refractory composition (application of technological binder and carbon substance having the higher resistance to high temperature oxidation, introduction of antioxidants into the composition of refractory);
- 2) applying of the protective coating or glaze on the working surface of a refractory [4];
- 3) reduction of the oxidizing potential of the atmosphere, e.g. in protection of bottom by means of coke loading on its surface or by hermetization of ladle inner space and application of electric drying installations for heating the lining [5];
- 4) realization of low decarburization of temperature realization of low decarburization temperature regimes of heating, consisting in the organisation of temperature change trajectory of refractory's surface at which the time integral from refractory surface temperature will be minimal in the range of intensive oxidation temperatures.

Measures of the first group are realized by the manufacturers of refractories, and, as a rule, have a limited effect and reduce the refractory decarburization intensity only in part.

Measures of the second group may be realized both at plants producing the refractories and by the direct consumers by applying the coating on the new lining of the steel teeming ladle. In so doing, both full and partial protection from carbon burning out can be ensured depending on the type of coating.

Measures of the third group require the production of low oxidizing or reducing atmosphere inside the ladle, i.e. in fact, incomplete fuel burning, that is not always realized, or application of electric drying installations that require the definite capital investments from an enterprise.

Measures of the fourth group make it possible to reduce decarburization only partially but not to eliminate it completely, in this case, they require the availability of automatic control system of ladle lining's heating.

Thus, one of the most effective measures for complete prevention of refractory decarburization is the application of protective coatings. In this connection the complex of investigation concerning the development of effective coating for protection periclase-carbon linings of steel teeming ladles from decarburization at high temperature heating before the intake of the melt [6] has been carried out. The investigations included: analysis of efficiency of coating's application on the piece articles or on new lining; development of requirements to properties and component composition of coatings; development of composition of coating and its industrial testing.

As to the efficiency of coating's application on the working surface of the refractory at the manufacturer's plant or on the new lining before heating, it is necessary to note that on applying the coating on piece refractories, the penetration of oxygen and other gases-oxidizers into the lining's joints upon ladle heating (Fig. 1 a) is possible. In this case, the decarburization of brick edges (Fig. 1 b) takes place which wear out more intensively in the process of service, and the characteristic wear topography of periclase-carbon lining of steel-teeming ladles (Fig. 1 c [4]) provides support for this conclusion. In the case of coating application on new lining the joints are protected from the action of gases-oxidizers and edges of refractories are not decarburized (Fig. 1 d). In this respect, the application of coating on the new lining is accepted as the most efficient one.

Composition and property analysis of different coatings and the experience of their application for protection of graphite and other carbon-bearing articles

from high temperature oxidation show that the coatings can be divided into two groups. The first group includes relatively high-melting coatings that are in hard state in the whole temperature interval of protection and are a gas-tight (or slightly penetrable) barrier for gases-oxidizers. The second group includes relatively low-melting coatings on the basis of glasses which become soft and transform into liquid state in service.

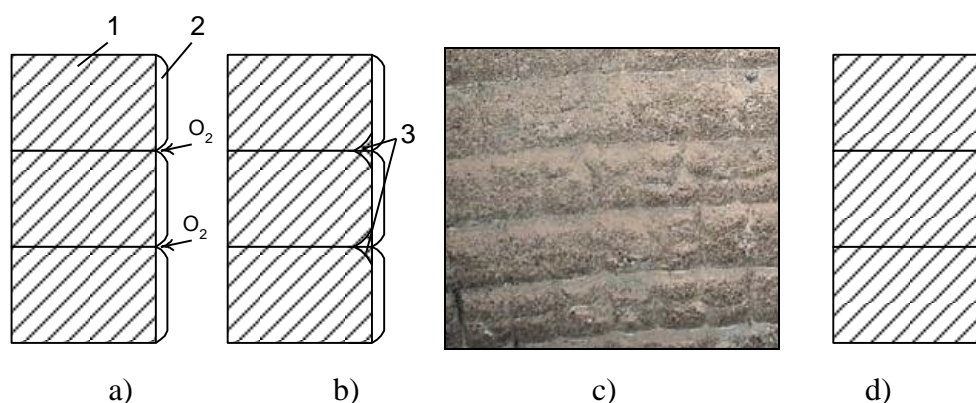


Fig. 1. Variants of protective coating application.

1 – refractory; 2 – protective coating; 3 – decarburized edges of refractory.

In general case, the coatings should meet the following requirements:

- 1) to ensure the sufficient decrease of intensity and complete elimination of periclase-carbon refractory decarburization;
- 2) to retain the protective properties, up to the temperatures of 1100 – 1200⁰C at heating duration up to 24 hours in the combustion products of natural gas being burned with the excess and shortage of oxidizer;
- 3) to possess the strength enough for adhesion with lining on heating (the coating should not flake, crack, exfoliate);
- 4) not to react chemically with a refractory and not to damage it;
- 5) to possess the minimal heat-insulation effect (to have the emissivity factor of the order of 0.7 – 0.8 and possible higher coefficient of heat conductivity);
- 6) the coating should not decrease the steel quality and contaminate it with nonmetallic inclusions;
- 7) the coating should not result in the high wear out of lining in contact with slag and metal melt;

- 8) the coating should be technologically effective in applying on vertical surface of steel-teeming ladle's lining;
- 9) do not contain rare and expensive components;
- 10) should be nontoxic, flameproof, do not emit harmful or noxious substances on heating.

The new coating on the basis of aggregate of silicate composition (fraction less than 0.5), and binder – liquid glass and additives was developed as result of the theoretical analyses and series of laboratory experiments.

The protective properties of the coating were studied in laboratory and industrial conditions. The aggregate and binder were mixed to the consistency of thick sour cream and were applied on the surface of the tar-bonded periclase-carbon refractories on the basis of melted periclase and flaked graphite with carbon content of 8-10%, the thickness of coating did not increase 1 mm.

In laboratory conditions the experiments were carried out with the samples of cross dimensions 14x18x50 mm cut from bricks. Heating of samples was done in electric resistance furnace SUOL – 0.25.1/12.5-II with heaters from silicon carbide in the atmosphere of air. The samples were heated up to the temperature of 800, 900, 1000, 1100, 1200⁰C and were held at constant temperatures for 1, 2 and 3 hours. The sample's temperature was steadily measured by chromel-alumel thermocouple and the readings were registered by the device "Termodat 19E2".

In carrying the industrial experiments one half of the brick was protected by the coating, the second half was left open. Brick was placed to the steel-teeming ladle and the heating of lining was done according to the operating regimes at the enterprise.

After the speeded up cooling on air the samples were cut and a metallographic section of the surface zone of the refractory was made. The depth of the decarburized layer was defined as the distance from the surface to the unchanged zone of the refractory.

The investigation of microstructure of laboratory samples protected by the coating has that the decarburized layer is completely absent in them. Industrial experiments have verified the results of the laboratory ones. Fig. 2 shows the microstructure photograph of brick cross section.



Fig. 2. Cross section of brick, the left half of which was protected by the coating, but the right half was in direct contact with oxidizing atmosphere.

Figure 2 illustrates visually the positive effect from application of the coating. The left half has a clearly marked damaged decarburized layer (of light colour) of the depth up to 7 – 10 mm.

As a result of the carried out experiments it was determined that the mechanism of the protective action of the coating is the following. At temperatures of the order of 600 – 700⁰C corresponding to the temperature interval of the beginning of the intensive carbon burning out, the softening of the coating of silicate composition takes place. With the further temperature rise the coating begins to spread along the refractory's surface and to cover it with complete viscous film obstructing the penetration of gases-oxidizers to the surface of the refractory. At maximum temperatures of heating 1100 – 1200⁰C the viscosity of the coating remains enough for preserving its protective properties on vertical areas of the lining.

The industrial application of the coating for the protection of the lining of 130-ton steel teeming ladles ensured the increase of remanent thickness of lining by 12.5 – 22.5 mm, and average resistance of ladle by 10 heats. Reclamations

for quality of metal, from the ladles, the lining of which was protected by the devised coating were absent.

Conclusions

The coating has been devised which protect effectively the new periclase-carbon linings from the decarburization on the first heating. The application of the coating assures the increase of service life (resistance) of lining of working layer of steel-teeming ladles.

References

- [1]. M.V. Matveev, M.V. Temlyantsev. Investigation of periclase-carbon refractory's decarburization on heating the steel teeming ladle's lining before melt receiving. *Izvestiya vusov. Chernaya metallurgiya*. 2010. № 10. pp. 60-62.
- [2]. M.V. Matveev, M.V. Temlyantsev. Decarburization of periclase-carbon refractories in heat treatment of steel teeming ladle's lining. *Metallurg*. 2010. № 8. pp. 60-62.
- [3]. M.V. Temlyantsev, M.V. Matveev, E.N. Temlyantseva. Investigation of different factor's influence on decarburization of periclase-carbon ladle's refractories. *Izvestiya vusov. Chernaya metallurgiya*. 2011. № 10. pp. 32-36.
- [4]. F.V. Mozhzherin, V.A. Musevich, A.P. Duka et al. Evolution of design and resistivity of linings of 150 ton steel-teeming ladle refractories. *Novye ogneupory*. 2009. № 1. pp. 5 – 14.
- [5]. I.M. Bershitsky, A.V. Tarapyshekin. Energy saving and ecologically safe units for electric drying and heating the lining of ladles. *Stal*. 2010. № 2. pp. 24-25.
- [6]. M.V. Temlyantsev, M.V. Matveev, R.E. Kostyuchenko, M.Yu. Lositskaya. On applications of coating protection of periclase-carbon ladle's refractories from decarburization on heating the ladle's lining. *Vestnik of Russian academy of natural sciences. West-Siberian department: Collection of scientific papers*. Novokuznetsk: SibSIU, 2011. V. 13. pp. 130– 133.

RESEARCH ON THE INFLUENCE OF ANCHORS AND HANGING TRANSPORT DEVICES IN UNDERGROUND DIGGING ON THE STRAIN OF THE ROOF ROCKS

V.R. Nogikh, I.M. Krasnoperova, O.A. Petrova

Siberian State Industrial University, Novokuznetsk, Russia.

Abstract

The regularities of the distribution of stresses and strains of roof rock under the influence of anchors and transport devices hung on them. It is substantiated the following recommendations to improve the stability of the roof rocks under alternating loads on the anchor under the influence of transported loads: securing the anchor into the hole should be within 70% of the length of the bolt.

Keywords: anchor, underground digging, rock, weight transported loads, diesel wagon haulage, anchor tension, stresses, strains.

In underground mining of mineral deposits one of the actual tasks is to ensure the sustainability of transport developments in the maintenance of their maintenance-free status for the entire period of operation. On today's high productive mines not only increased the intensity of traffic stream, but also increased the size and weight of transported equipment. In accordance with the concept of progressive development of transport systems for mining transportation of bulky equipment weighing more than 30 tons as the main direction the introduction of hanging monorail railway with diesel wagon haulage is performed.

When operating monorail and diesel wagon railway uneven periodically scope load variation on the supports occur, vibration of monorails supporters and rocks in the vicinity of mine, which leads to lower opening strength and rock strength of the cyclical impact of alternating loads.

Thereupon, actual studies are aimed at creating a system full-strength "mine opening - rocks - roof bolting of the first and second levels - special lining - suspended monorail railway - rolling-stock monorail railway", hereinafter

referred to as "Multifunction system geological mass- timbering- transport "(MSGTT).

More generally, the scheme of interaction elements MSGTT is shown in fig. 1, which shows the projection of the development working with the location it bolting, vehicles and rocks.

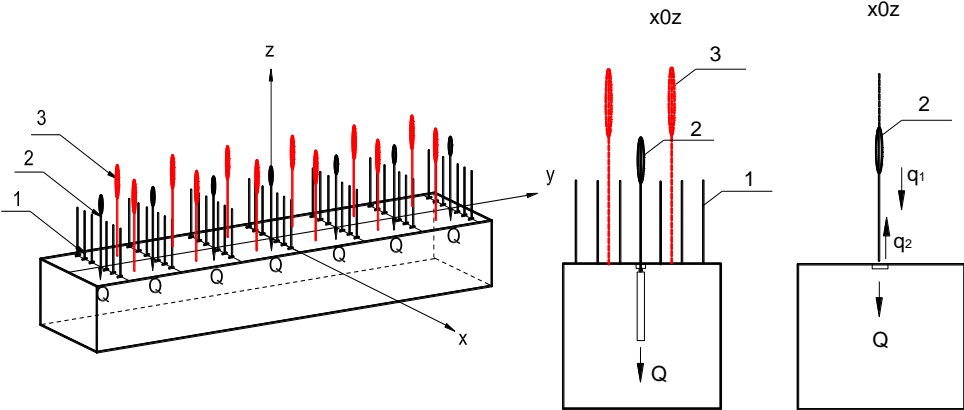


Fig. 1. Scheme of interaction elements "Multifunction system geological mass-timbering- transport "(MSGTT): a - axonometry, b - cross section mine opening, c - scheme anchors when moving mine diesel locomotive (1 - the first level anchor; 2 - the second level anchor; 3 - anchor for hanging monorail).

Fig. 1 illustrates one embodiment of a transport securing passport production. Anchors of the first level (1) are fixed in the roof during mine opening. Anchors of second level (2), usually up to rope 6 m further set after generating species or the need for reinforcement, for example in the purification zone of waste. For installation (suspension) of hanging diesel wagon road adjudge one or two anchors along the axis of the alignment of road (3).

In the normal operating condition all of the anchors are fixed at the top and at the bottom by means of washers and screw nut tightened with a force of $q_1=q_2$. When driving monorail train the load Q is transferred on the supporting anchor, corresponding to the mass of the train. This load is redistributed to the length of the underground digging. If the weight of the train, attributable to the anchor does not exceed its initial thrust ($q_2-Q > 0$), according to manufacturer's

operating instructions of the vehicles it is possible to use hanging diesel wagon transport.

In fact, load during operation affects not only support anchors, but also neighboring anchors and stressedly-deformed state and the stability of the roof rocks. Currently there are no analytical solutions and methods that take into account the effect of complex load mass on neighboring cells lining. Therefore an algorithm calculating the displacements, strains and stresses, taking into account the combined effect of mass monorail trains on all elements lining transport development and stressedly-deformed state and the stability of the roof rocks was developed.

In the basis of the algorithm for calculating the geomechanical parameters of rocks there is a superposition method, according to which one can determine the effect of weight train carriages with a load on each element of the lining, and then calculate the total effect of the mass of all trains [1].

To determine the effect of a singular anchor on the distribution of displacements, stresses and strains of rock anchors we suggest the following design diagram (Fig. 2). At the top of the underground digging it is set an anchor carrier (2) which is secured in rock by means of the wedge lock or adhesive. The tension anchors at the top are performed by means of washers and nuts in the bottom of the anchor. Thrust force $q_2=q_1$.

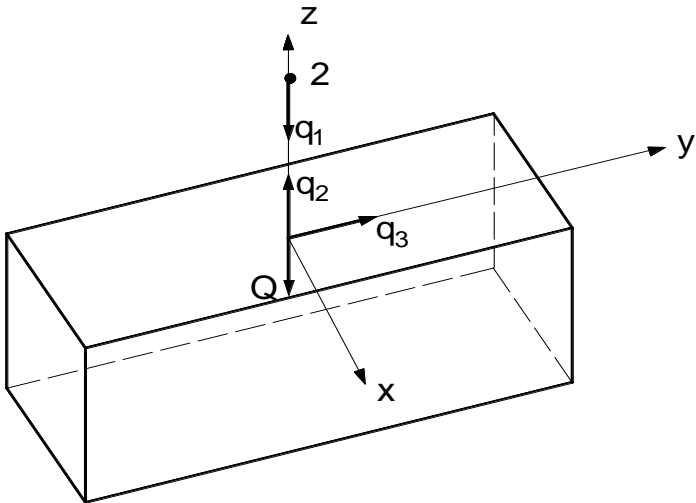


Fig. 2. Scheme of the load distribution on the anchor influenced tension nut (q_2) and weight of transported load (Q).

Statement of the problem: it is required to establish the impact of the anchor efforts $q_2=q_1$ and load transported on the Q values of the displacements of the roof rocks, stresses and strains, as well as changes in the strength of the rocks under the influence of these stresses and strains.

Task solution is proposed by using the known solutions by Mindlin [2]. According to the scheme of Fig. 2 for securing the lock anchor point 2 at a distance c from the top of the mine opening, where c - fixed length in the rocks of the roof anchor and arbitrary values of the coordinates x , y , z calculated vertical and horizontal displacement, vertical and horizontal stresses, tangential stresses. For modeling the stressedly-deformed state (SDS) elements MSKKT a computer program was developed in which geomechanical parameters are calculated at a predetermined pitch of the coordinates x , y and z . The results of calculations are processed in the form of graphs using standard office software.

To investigate the parameters set targets (SDS) and a program of numerical experiments was developed (Fig. 3). In the modeling the effect of ground pressure occurring in the vicinity of mine opening was not taken to the account. The solution of such idealized problem revealed patterns of interaction with rocks roof anchors under the following operating conditions established in resin-grouted roof bolt holes (Fig. 3):

- 1) under tension (outward thrust) using washers and nuts;
- 2) with a tension through suspension monorial load trains;
- 3) fixing with an anchor in the borehole over the entire length or at individual points (locks);
- 4) the system interacts with rocks roof anchors for different modes of operation.

According to the results for each task, given in Fig. 3, we receive appropriate results confirming the feasibility of the concept MSGTT as identified principles polyfunctionality elements and systems in general, the emergence of elements of the system, the consistency of the interaction of system components at inclusion of new elements, the possibilities of continuous

improvement of system elements, high adaptability of the system elements to a wide range of geological and mine technical conditions.

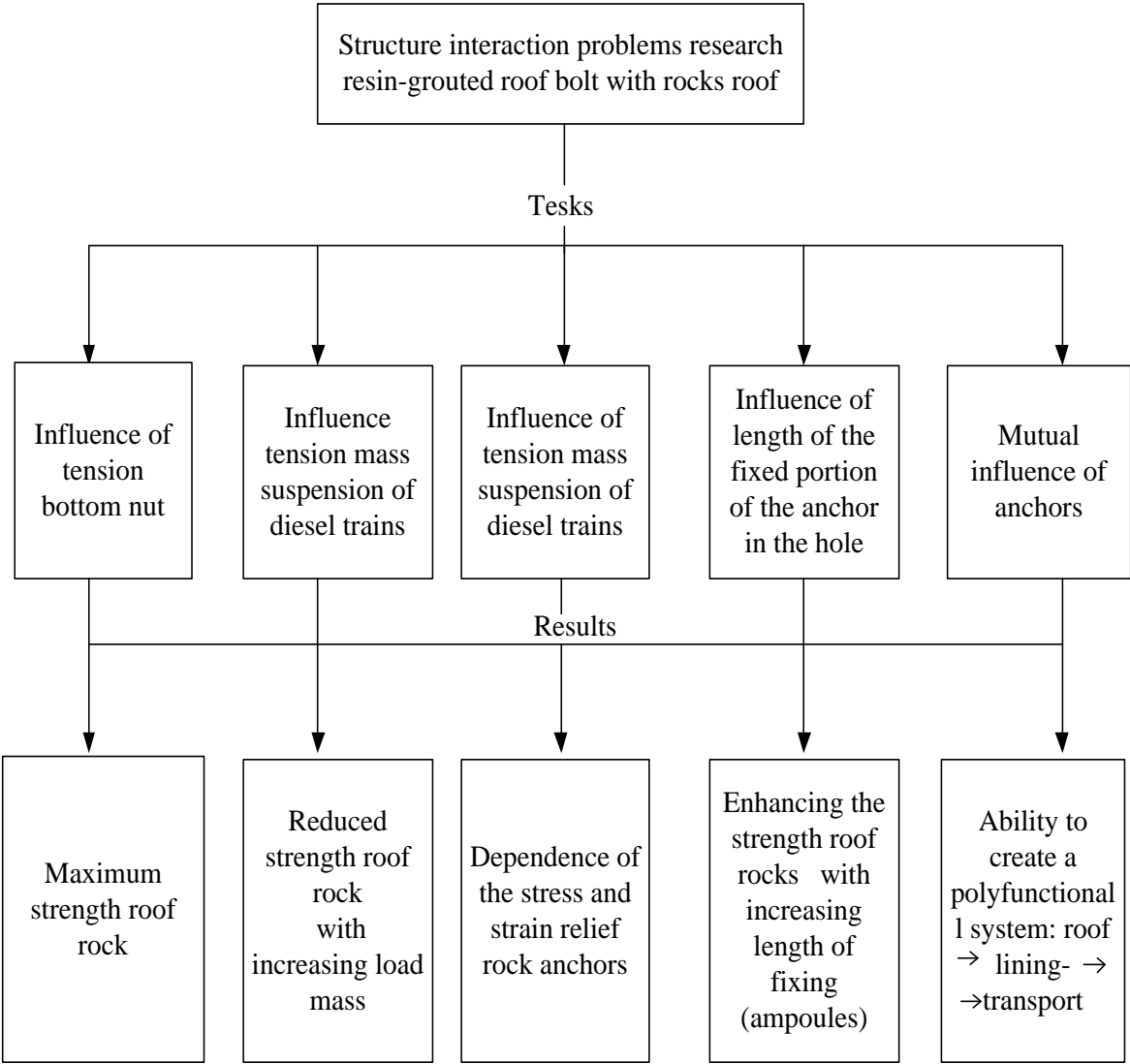


Fig. 3. Classification of tasks interaction studies with rocks roof anchors in the vehicle mines.

At the first stage of the research we study the patterns of interaction of the single anchor (Fig. 4) with the rocks of the roof. We modeled the impact of mass suspension monorial train and initial outward thrust anchor on the distribution of displacements of roof rock, as well as vertical, horizontal and shear stresses. The investigation of the distribution of these parameters under different conditions of the securing of the anchor in the hole along its length is new.

As initial conditions, we take the following: the width of 6 m, 3 m height, the roof rock of siltstone presented with a compressive strength of 30 MPa, a

modulus of elasticity $E = 6240 \text{ MPa}$, Poisson's ratio $\nu = 0,3$, the shear modulus $G = 2,400 \text{ MPa}$, anchor is located in the middle of mine digging.

In planning and performing research raw data varied within the limits specified in Table 1.

Table 1. Characteristics and variation limits of input data for calculating the parameters.

Parameter	Dimension	Adopted value in the base case	Variation limits	Pitch in simulation
Anchor length	m	2	2-6	1,0
Outward thrust anchor installation	kN	60	60-200	20
Number of vials for securing the anchor in the hole	kol	1	1-3	1
Tensile strength of rocks under compression	MPa	30	30-90	30
Shear modulus	MPa	2400	2400-7200	2400

Fig. 4 shows the distribution of vertical and horizontal displacements arising under the influence of generation installed in the roof resin-grouted roof bolt 2.0 m long with a tension of 60 kN. Tensioning is effected by a nut on the lower end of the anchor. The top the anchor is secured with an adhesive at the length of 0.2 m.

Two characteristic zones are clearly distinguished on the vertical axis: compression at lower part of the roof anchor for generating vertical displacements $w > 0$ and stretching the upper part of the anchor when $w < 0$. Horizontal displacements confirm that the entire length of the hole in the top of the development under the influence of vertical compressive displacement v rock movement occurs horizontally from the axis of the anchor ($v > 0$). This pattern can lead to cracking of the contact rock anchor adhesive polymer composition and slip the anchor rod for this fracture. Above the anchor under

the influence of its tension, on the contrary, there is a horizontal movement axis of the rock to the anchor.

We should highlight the impact of a stuck anchor at the top of the hole, where there is intense deformation of rocks.

The presence of zones of tension and compression of the roof rocks under the influence in the hole and secured with a nut strutted anchor is also confirmed by the nature of the distribution of vertical stress σ_{vert} (Fig. 5).

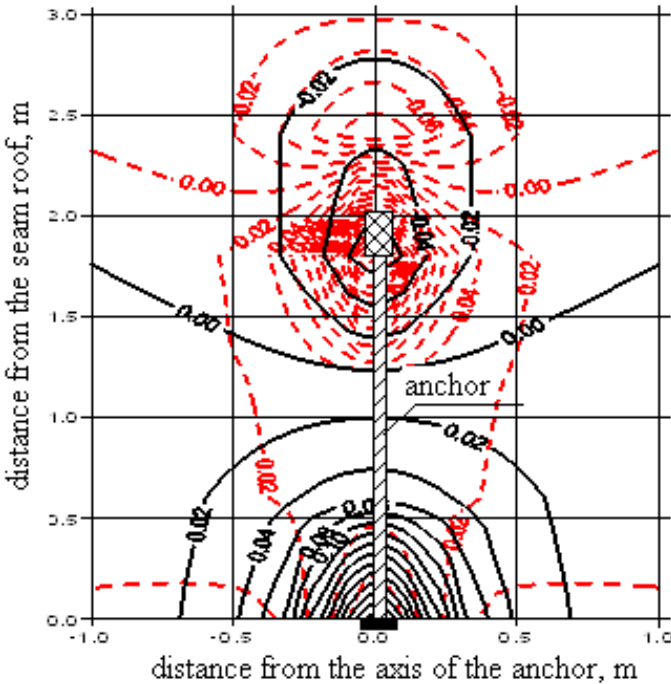


Fig. 4. Distribution of vertical w (solid black line) and horizontal v (red dotted line) displacement (mm) of the roof influenced by rock anchor a length of 2 m to 60 kN with a tension of a lock in the upper portion, $\sigma_{\text{com}} = 30$ MPa.

In the entire length of compressed rock anchor, which is confirmed by the sign $\sigma_{\text{vert}} < 0$.

Above the Anchor in the rocks there is a zone of strain ($\sigma_{\text{vert}} > 0$).

According to the graphs in Figures 4 and 5, it can be concluded that the role of the anchor consists in forming the entire length thereof and compression zones of the bundle above the castle rock anchor. This pattern is confirmed by other authors, for example [3-5].

Quite different operating conditions of the anchor when used for suspended transport. For fixed anchor cargo there may be a situation in which the weight of the load is larger than the initial tension of the anchor. In this case, under the influence of compressive load mass of rocks in the bottom of the roof rock is zero, the anchor will be attached at the top and hang freely in the hole, and on the lower end of the force Q is applied, equal to the proportion of the weight of cargo transported, distributed on the anchor.

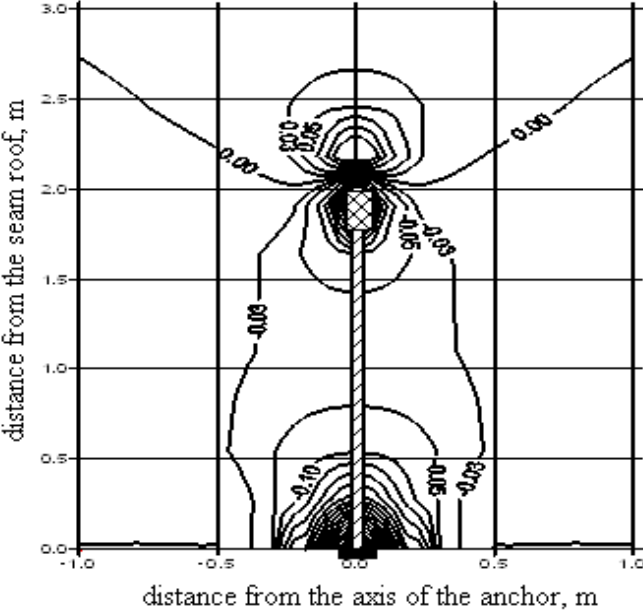


Fig. 5. Contours of vertical stress distribution (σ_{vert} , MPa) under the influence of roof rock anchors, 2 m long with tension 60 kN with a lock at the top, $\sigma_{\text{com}} = 30$ MPa, $\sigma_{\text{vert}} < 0$ compression.

The results of calculation of vertical displacements of the roof rocks under the influence of the anchor in the rocks with the thrust of the roof and the bottom nut free operation with suspension at the lower end of the anchor load are shown in Fig. 6. From a comparison of vertical displacement distribution graphs in Figures 4 and 6 that the tension anchor with washer and nut creates a zone of compression along the length of the roof rocks anchor. Application to the anchor of load Q, exceeding its initial thrust, leads to the formation of the rocks of the roof over the entire length of the roof anchor subsidence and stretching strain.

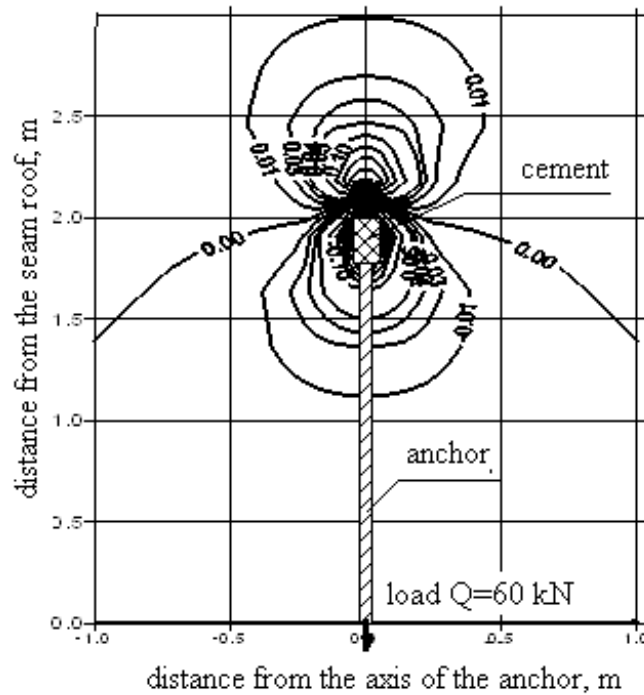


Fig. 6. Graphs of distribution of vertical displacement (mm) of the roof rocks under the influence of anchor 2 m long with tension 60 kN with a lock at the top and bottom suspension transported load $Q = 60 \text{ kN}$, $\sigma_{\text{com}} = 30 \text{ MPa}$.

This is confirmed by the distribution of vertical displacement graphs axis anchor at different operating conditions: a thrust from below with a nut and thrust without suspension bottom transported material (Fig. 7). At the disposal of the anchor nut at the bottom of the roof rocks occur compressive deformation, which prevent rock foliation, create additional cracks and reduce the stability of the roof. The scheme of deformation of rocks under the influence of the weight of transported cargo is completely different. In the upper part of the hole state rock influenced by the kind of load on the anchor is almost unchanged.

At the bottom of the tensile deformation of the roof occur which lead to the immediate destruction of the roof rock as the rock strength tensile 8-20 times smaller than in compression. [6].

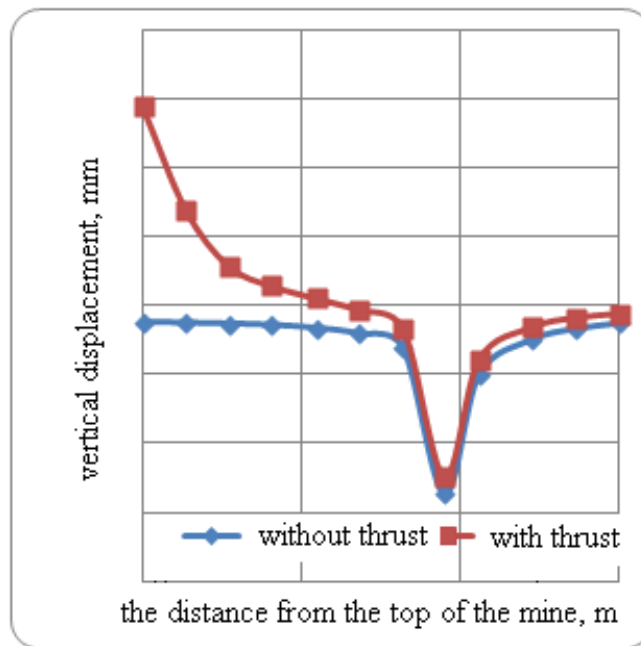


Fig. 7. Graphs of the distribution of vertical displacement (mm) of the roof rocks under the influence of anchor 2 m long with tension 60 kN with a lock at the top, $\bar{\sigma}_{com} = 30$ MPa.

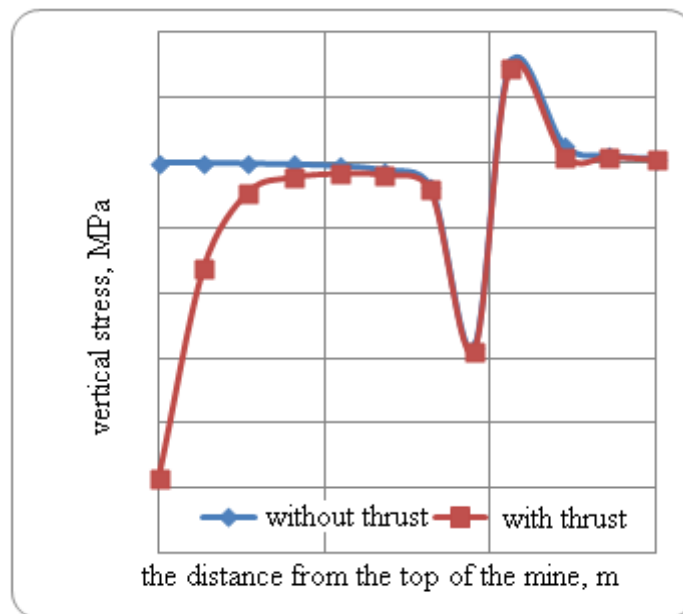


Fig. 8. Graphs of the distribution of vertical stress (MPa) in the rocks under the influence of roof anchors, 2 m long with tension 60 kN with a lock at the top, $\bar{\sigma}_{com} = 30$ MPa.

The revealed pattern of roof rock deformation under the influence of the full thrust of the anchor in the rocks of the roof and the suspension on the lower end of the transported cargo is confirmed by the results of the distribution of vertical stress (Fig. 8).

To solve the third task specified in Fig. 3, i.e. the establishment of parameters SDS depending roof rock relief anchor and the calculation of displacements and stresses of roof rocks in the vicinity of the anchor at the disposal of the anchor within 60 - 200 kN.

It is established that the nature of the distribution of stresses and displacements is almost unchanged with increasing tension anchor within 60 - 200 kN. For comparison, Figures 8 and 9 show the vertical stress at different anchor tightening applications. It is revealed that stress changes directly proportional to the tension, i.e.

$$\sigma_{\text{vert}} = \alpha Q \tag{3.7}$$

where σ_{vert} -vertical stress, MPa; Q – tension of the anchor, MPa; α - coefficient of proportionality, for the conditions of Table 3.1, $\alpha = 0,16$.

It should be noted that the tension anchor within 60 - 200 kN by the transported load, vertical tensile stresses up the anchor comprise 0.3 - 1.0 MPa (Figures 8 and 9), i.e. increased insignificantly. Therefore, it can be stated that the impact of sustainable roofing distributed mass transported cargo cannot cause significant destruction. As shown in Fig. 7, only local dumped at elevated fracture may occur. This conclusion is valid in the absence of the influence of the reference rocks roof rock pressure.

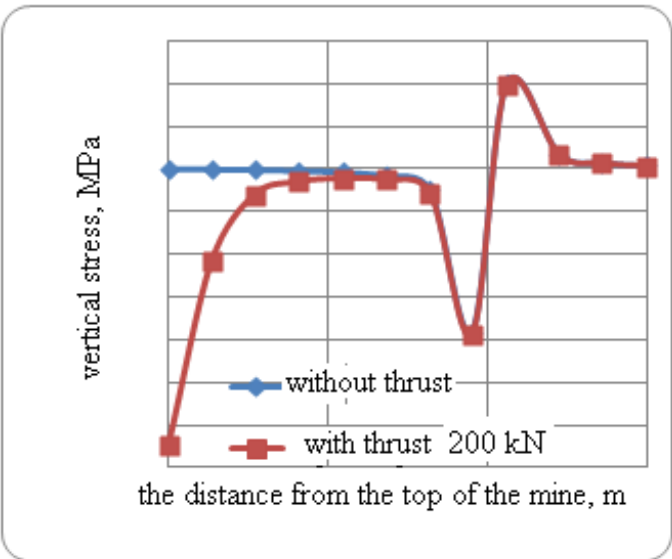


Fig. 9. Graphs of the distribution of vertical stress (MPa) in the rocks under the influence of roof anchors, 2 m long with tension 200 kN with a lock at the top, $\sigma_{\text{com}} = 30$ MPa.

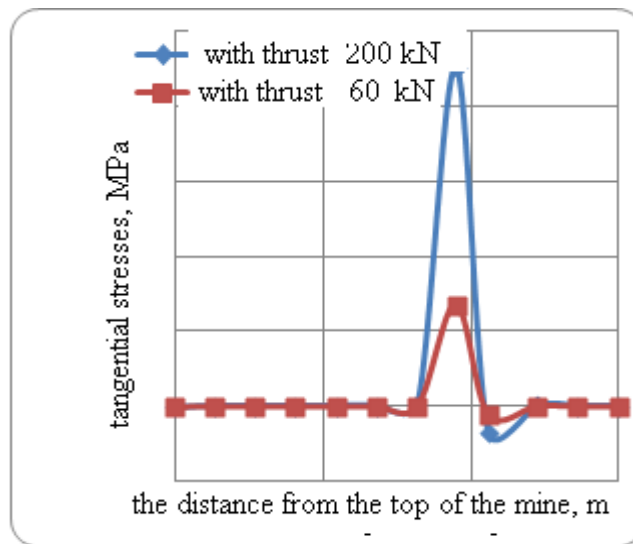


Fig. 10. Graphs of the distribution of tangential stresses (MPa) in the rocks under the influence of roof anchors, 2 m long with tension 60 and 200 kN with a lock at the top, $\sigma_{cx} = 30$ MPa.

According to the results of numerical simulation it is revealed that the most dangerous areas in the top of the mine criteria for strength and stability of the rocks are zones with high tangential stresses. It follows from the graphs of Fig. 10, which shows the variation of tangential stresses in the rocks along the axis of the anchor. The maximum tangential stresses are revealed at the points of fixing anchor with rocks. The values of these stresses are increased in proportion to its tension. It's typical that, a dangerous portion is localized within the range 200-300 mm in the upper part of the hole.

During mine diesel locomotive movement such limit tangential stresses in the roof hubs may lead to the gradual destruction of rock formation under the influence of horizontal displacements of the crack gap between the anchor and the hole wall, the displacement of the anchor for these cracks and falling out of the roof rocks. Such phenomena have been repeatedly observed in practice [7]. Apparently, the main reason to pull anchor type SK with a mechanical lock should include excess of maximum stress with respect to the limit set by the strength of the passport, the destruction of rocks at the contact and lock hole.

Due to the high probability of failure of rocks in the area of securing the anchor lock researches on the distribution of tangential stresses at the disposal of the anchor in the hole at several points (locks), including the fixing of the anchor along the entire length were conducted(Fig. 11).

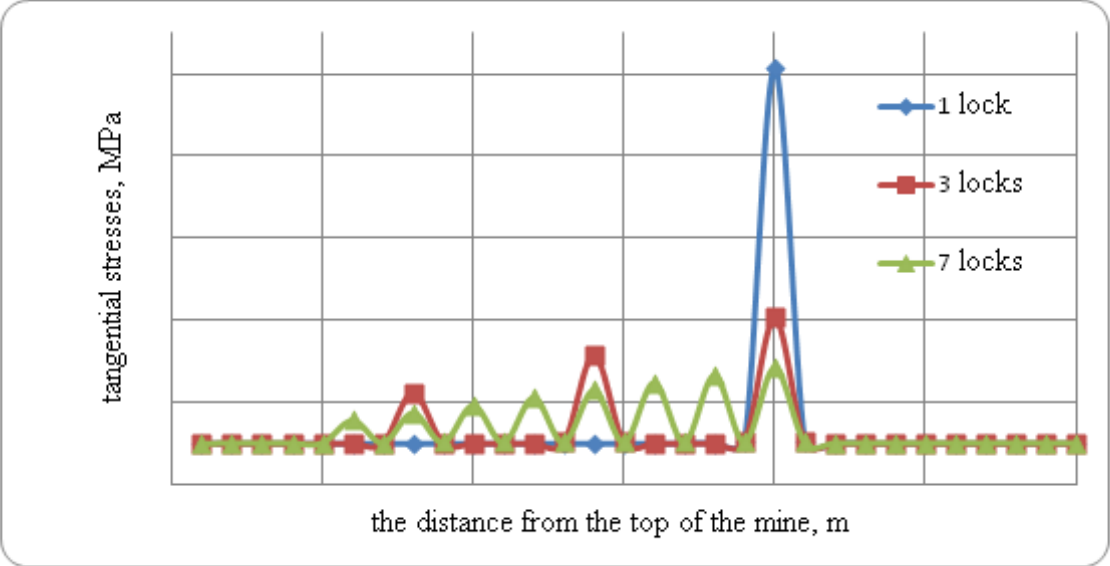


Fig. 11. Graphs of the distribution of tangential stresses (MPa) in the rocks under the influence of roof anchors, 2 m long with tension 200 kN with a different number of fixing points in the hole, $\bar{\sigma}_{com} = 30$ MPa.

The graphs in Figure 11 show that with increasing amounts of thrust points (locks) of the anchor in the hole tangential stresses are reduced. The pattern of distribution of tangential stresses is not only in reducing the absolute values, but also by reducing their length of anchor as it approaches to the digging.

This pattern gives us an important practical conclusion that to improve the operational reliability of the anchors in the workings of transport by reducing the likelihood of displacement of anchors on the cracks in the adhesive composition of the gap between the anchor and the walls of the hole, it is necessary to hold the anchor securing the interval from the top of the anchor for the development of at least 70% bolt length (Figures 12, 13).

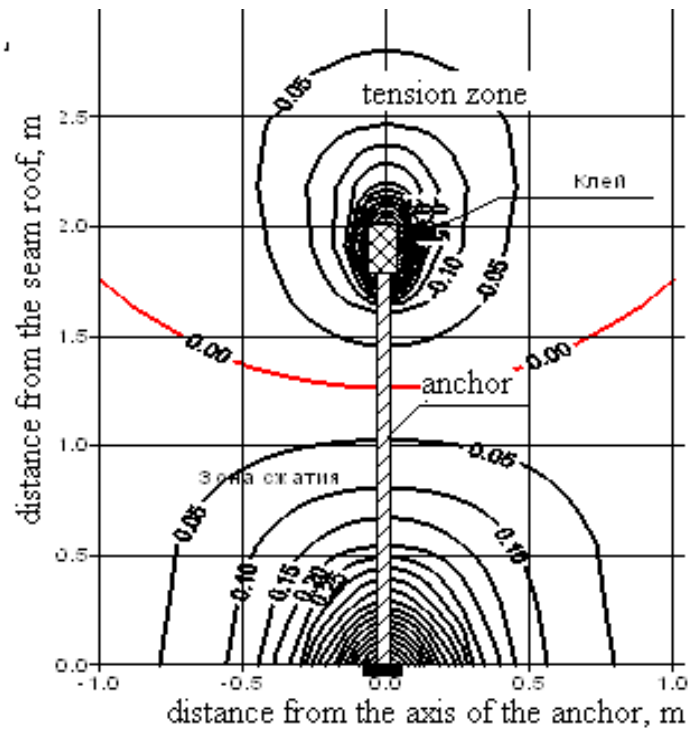


Fig. 12. Contours of vertical displacement distribution when attaching the anchor 2.0 m long by 0.2 m length of the drill hole bottom, the thrust on the nut 200 kN.

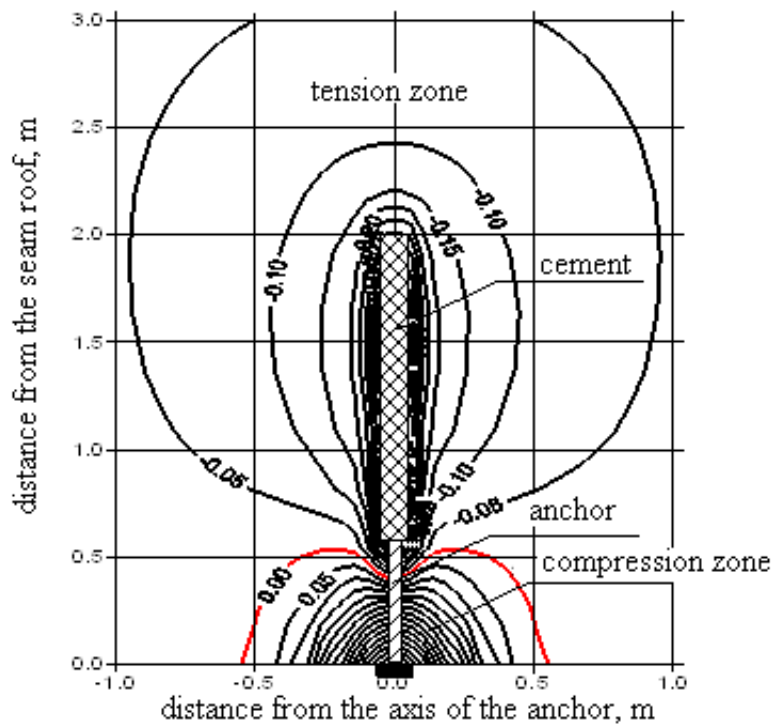


Fig. 13. Contours of vertical displacement distribution when attaching the anchor length of 2.0 m at a length of 1.4 m from the bottom of the hole, the thrust on the nut 200 Kn.

To assess the nature of the distribution of vertical displacements of the roof rocks by a single and multilock anchor securing in the hole the corresponding simulation was carried out (Figures 12, 13) and the following conclusions and recommendations were made:

1) Border of zones of subsidence and lifting rocks under the influence of the set anchor fixed at one point at the top of the hole is located at the height of approximately $2/3$ the length of the anchor, starting from the top of the mine, while with multipoint fixed anchor this boundary is located at the height of approximately $2/3$ of the distance between roof generation and lower lock;

2) Volume of the stretching zone of rocks in the upper part of the anchor increases in proportion with the length of the fixed portion of the anchor.

3) The single anchor role is in the formation of compression zones throughout its length and the rock splitting above the anchor lock. Attaching the transported cargo to the anchor exceeding initial thrust anchor, leads to the formation of roof subsidence and tensile strain of the rocks within the length of the roof anchor;

4) The pattern of distribution of tangential stresses means not only in reducing the absolute values of tangential stresses in the rocks of the roof with a multipoint anchor securing the in the hole, but also in reducing the stress on the length of the anchor as you approach from the bottom of the hole to develop;

5) To improve the operational reliability of the anchors in the workings of transport by reducing the likelihood of displacement of anchors on the cracks in the adhesive composition of the gap between the anchor and the walls of the hole, it is recommended to fix the anchor in the interval from the top of the anchor for the mine of at least 70 % of the length of the bolt.

6) The boundary zones of subsidence and lifting rocks under the influence of the established anchor fixation with a single point at the top of the hole is located at a height of approximately $2/3$ the length of the anchor, starting from the top of the development, while multipoint anchor fixing this boundary is

located at a height of approximately $2/3$ of the distance between roof generation and lower lock

7) The amount of stretch zone rocks in the upper part of the anchor increases in proportion to the length of the fixed portion of the anchor.

This work was financially supported by the Ministry of Education and Science of Russian Federation. Project number 2708.

References

- [1]. S.P. Timoshenko, G. Goodyer. Theory of elasticity. M.: Science, 1975. 576 p.
- [2]. K. Brebbia. Application of the boundary element method in engineering/ Theory of elasticity. M.: Mir, 1985. 248 p.
- [3]. A.M. Nikitina, V.N. Fryanov. Geomechanical sustainability mining in a nonuniform virgin coal. Novokuznetsk: SibSIU, 2009. 199 p.
- [4]. J.A. Zlatickaia, V.N. Fryanov. Geomechanical substantiation parameters hazardous areas and technologies of hardening of rocks in the vicinity of underground workings. Novokuznetsk: SibSIU, 2006. 160 p.
- [5]. V.A. Voloshin. Geomechanical stability forecast of developing entry in areas of geological disturbances and increased rock pressure: dissertation for the academic degree. SibSIU. Novokuznetsk: 2002. 24p.
- [6]. G.G. Shtumpf, Y.A.Rijkov, V.A. Shalamanov, A.I. Petrov. Physicotechnical properties of rocks and coals of Kuznetsk Basin: hand-book. M.: Nedra, 1994. 447 p.
- [7]. A.V. Remezov, V.G. Haritonov and other .Anchoring in Kuzbass mines and its further development: Tutorial. Kemerovo: Kuzbassvuzizdat, 2005. 471 p.

Contents

Physical materials science of modern materials

Guijie Hao, Huaiwu Zhang, Xiaoli Tang <i>Electrical pulse annealing improves soft magnetic properties of nanometer CoNbZr films in GHz frequency range.....</i>	11
S.V. Raikov, E.V. Kapralov, E.S. Vashchuk, E.A. Budovskikh, V.E. Gromov, Yu. F. Ivanov, K.V. Sosnin <i>Structure – phase states and wear resistance of deposition surface of deposition surface formed o steel by electric arc method.....</i>	19
Wei Li, Yao Shen, Wei Zeng <i>Effect of electric pulse on the annealing behaviors of submicron grained metals</i>	28
V.A. Starenchenko, Yu.V. Solov`eva, S.V. Starenchenko <i>Strees relaxion in Ni_3Ge single cristals with the anomalous temperature trengthening.....</i>	41
Zhang Tengfei, Li Qiulin, Han Yecong, Gao Minrui, Liu Wei <i>Investigation on the agglomeration behavior of primary silicon in hypereutectic Al-Si alloy melt under electromagnetic vibration</i>	48
V. Stolyarov <i>Features of electroplastic deformation and electropulse treatment for TiNi alloys.</i>	58
V.E. Gromov, V.A. Kuznetsov, S.V. Konovalov, G. Tang, G. Song <i>Method of current amplitude estimation of pulse generator.....</i>	65
G.M. Poletaev, N.A. Kulabukhova, M.D. Starostenkov, S.V. Dmitriev <i>Interatomic potentiels in the systems Pd-H and Ni-H.....</i>	70
N.A. Kozyrev, N.E. Kryukov, R.E. Krykov, V.F. Igushev, I.I. Kovalevskii <i>Possibilities of application of carbon-fluorine cantaining additions in submerged-arc welding.....</i>	83
S.A. Barannikova, O.A. Stolboushkina, D.A. Kosinov, S.V. Konovalov, V.E. Gromov <i>Hydrogen absorption effect on the plastic deformathion localizator of low carbon steel.....</i>	93

V.A. Feodorov, P.M. Kuznetsov <i>Features surface topology of Fe-Si Alloy in the laser radiation exposure...</i>	104
E.V. Starovatskay, L.P. Mishliaev, I.V. Tsiryapkina <i>Materials structure description by fractal complex.....</i>	110
Yu.F. Ivanov, E.A. Petrikova, A.V. Tkachenko, A.D. Teresov, A.A. Klopotov <i>Structure and properties of surface alloy formed by high –intensity electron beam treatment of the film (Ti or TiCu)/substrate (AlSi).....</i>	118
V.D. Sarychev, S.A. Nevskii, E.V. Cheremushkina, V.E. Gromov <i>Biphase filtration model of plastic deformation.....</i>	128
V.V. Muraviev, O.V. Muravieva, A.V. Baiteryakov, A.I. Dedov <i>The methodology of determining acoustical structural noise of steel.....</i>	137
A.M. Guriev, S.G. Ivanov, M.A. Guriev, Mei Shunqi, Gong Wenbang <i>Surface hardening of steels with boron.....</i>	149
B.D. Iyngdenov, A.M. Guriev, V.A. Butukhanov, Mei Shunqi, Zhou Qinhu <i>Phase composition of gradient structures on carbon steels after boronizing</i>	154
V.E. Gromov, K.V. Volkov, Yu.F. Ivanov, K.V. Morozov, S.V. Konovalov, K.V. Alsaraeva, O.A. Semina <i>Formation fine structure of the superior quality rails.....</i>	160
V.A. Feodorov, T.N. Plushnikova, S.A. Sidorov, A.V. Yakovlev <i>The influence of acid and hydrogen-charging media on the mechanical properties of amorphous and nanocrystalline alloys.....</i>	164
S. Panin, I. Vlasov, V. Sergeev, V. Naidfeld, M. Kalashnikov, O. Bogdanov, B. Ovechkin <i>Influence of Zr⁺ ion-beam surface treatment of 30CrMnSiNi2 steel on its structure and mechanical properties.....</i>	171
G. Poletaev, D. Dmitrienko, A. Soskov, V. Mikrokov, M. Starostenkov <i>Molecular Dynamics Research of structure of triple junction of tilt Boundaries and mixed type grain Boundaries in Nickel.....</i>	183
E.V. Protopopov, Yu. A. Seleznev, A.N. Cherepanov, V.Ya. Chinokalov, D.V. Foigt, L.A. Ganzer <i>Properties of cast and rolled steel after nanopowder inoculation.....</i>	190

N.A. Koneva, N.A. Popova, E.L. Nikonenko, M.V. Fedorisheva, E.V. Kozlov <i>Influence of high- temperature annealing on the formation of nanoparticles of the γ' phase based on the Ni –Al superalloy.....</i>	195
V.A. Stepanov, E.I. Isaev <i>ION-INDUCED Plastic deformatihon in solids.....</i>	204
N.V. Koptseva, J.J. Efimova, O.A. Nikitenko, M.P. Baryshnikov, M.S. Zherebtsov <i>Carbon steel ultrafine structure formation in high – speed deformation at elevated temperatures.....</i>	216
S.V. Feiler, E.V. Protopopov, E.V. Polevoy, V.P. Dement`ev <i>Study of electromagnetic stirring in the continuous casting of rail steel segregated processes to development.....</i>	224
Yu. F. Ivanov, E.A. Petrikova, A.D. Teresov, O.V.Krysina, A.A. Klopotov <i>Surface alloys synthesized by high-intensity pulsed electron beam treatment of film-substrate systems: structure and properties.....</i>	230
A. Evstigneev, A. Debelyak, V. Muravyev, S. Lonchakov, V.Pitcyk <i>Evolution of structural changes in zones of local catastrophic destruction of pipeline systems of processing of oil products.....</i>	236
S.Z. Lonchakov, O.V. Bashkov, V.I. Muravyov, A.V. Frolov <i>Research of defects concentrators of tension by parametrs of acoustic issue at development of damages.....</i>	259
V.V. Rubanik, Y.V. Isarenko, V.V. Rubanik. <i>Electrotermic treatment of wire.....</i>	271
I. Vlasov, S. Panin, V. Sergeev, O. Bogdanov, P. Maruschak, B. Ovechkin. <i>Effect of ION_ARC Vacuum Beam treatment by Zr^+ on a structure and faligue durability of 30CrMnSiNi2 steel.....</i>	282
V.V. Muraviev, A.J. Kotolomov, A.V. Baiteryakov, A.I. Dedov <i>The determing of metal grain size by acoustical structural noise</i>	291

Applied aspects of modern technologies of material working

O.I. Nokhrina, I.D. Rozhikhina, V.I. Dmitrienko, M.A. Platonov <i>Steel modification by barium and strontium.....</i>	299
V.V. Sterligov <i>Mechanism of air layer stagnation for heat insulation purposes.....</i>	305
V.I. Bagryantsev, S.A. Brovchenko, A.P. Podolskii, A.A. Rybushkin, M.V. Temlyantsev, A.I. Kutsenko <i>Solid carbon – containing wastes – a promising fuel for thermal – energy units</i>	311
M.V. Temlyantsev. <i>The service life increase of periclase – carbon linings of steel – teeming ladles on the bases of application of coatings preventing the refractory materials decarburization on heating.....</i>	321
V.R. Nogikh, I.M. Krasnoperova, O.A. Petrova <i>Research on the influence of anchors and hanging transport devices in underground digging on the strain of the roof rocks.....</i>	328

Scientific Education

**External fields processing and treatment technology and
preparation of nanostructure of metals and alloys**

Book of the International workshop articles

1-7 October, 2014

Edition in Chief: Professor Sc. D. (Physics & Mathematics) V. E. Gromov

Technical editing, desing: V.E. Khomicheva

Publishing Licence from 10.04.14

Format 60×84 1/16. Offset. Press.

Volume 22,3 print sheets. 100 copies. Order 199.

Siberian State Industrial University

654007 Novokuznetsk, Kirov str., 42

Printed in SibSIU Publishing Center